GEOCHEMICAL AND MINERALOGICAL IMPACTS OF SULFURIC ACID ON CLAYS BETWEEN PH 5.0 AND -3.0

A Thesis Submitted to the College of
Graduate Studies and Research
In Partial Fulfillment of the Requirements
For the Degree of Doctor of Philosophy
In the Department of Geological Sciences
University of Saskatchewan
Saskatoon

By
SEAN A. SHAW

PERMISSION TO USE

In presenting this thesis in partial fulfillment of the requirements for a Postgraduate degree from the University of Saskatchewan, I agree that the Libraries of this University may make it freely available for inspection. I further agree that permission for copying of this thesis in any manner, in whole or in part, for scholarly purposes may be granted by the professor or professors who supervised my thesis work or, in their absence, by the Head of the Department or the Dean of the College in which my thesis work was done. It is understood that any copying or publication or use of this thesis or parts thereof for financial gain shall not be allowed without my written permission. It is also understood that due recognition shall be given to me and to the University of Saskatchewan in any scholarly use which may be made of any material in my thesis.

Requests for permission to copy or to make other use of material in this thesis in whole or part should be addressed to:

Head of the Department of Geological Sciences
University of Saskatchewan
114 Science Place
Saskatoon, Saskatchewan
Canada
S7N 5E2

ABSTRACT

Natural and constructed clay liners are routinely used to contain waste and wastewater. The impact of acidic solutions on the geochemistry and mineralogy of clays has been widely investigated in relation to acid mine drainage systems at pH > 1.0. The impact of sulfuric acid leachate characterized by pH < 1.0, including potentially negative pH values on the geochemistry and mineralogy of clays is, however, not clear.

To address this deficiency a series of batch and diffusion cell studies, investigating the geochemical and mineralogical impacts of H_2SO_4 solutions (pH 5.0 to -3.0), were conducted on three mineralogically distinct clays (Kc, Km, and BK). Batch testing was conducted at seven pH treatments (5.0, 3.0, 1.0, 0.0, -1.0, -2.0 and -3.0) using standardized sulfuric acid solutions for four exposure periods (14, 90, 180, and 365 d). Aqueous geochemical, XRD, and Si and Al XANES analyses showed: increased dissolution of aluminosilicates with decreasing pH and increasing exposure period; preferential dissolution of aluminosilicate Al-octahedral layers relative to Si-tetrahedral layers; formation of an amorphous silica-like phase that was confined to the surface layer of the altered clay samples at pH $\leq$ 0.0 and t $\geq$ 90 d; and precipitation of anhydrite and a Al-SO_4-rich phase (pH $\leq$ -1.0, t $\geq$ 90 d).

The diffusive transport of H_2SO_4 (pH =1.0, -1.0, and -3.0) through the Kc and Km clays for 216 d was examined using single reservoir, constant concentration, diffusion cells. The diffusive transport of H^+ within the cells was modeled using 1-D transport models that assumed no absorption, linear absorption, and non-linear absorption of H^+. The absorption isotherms were calculated from the pH 5.0, 3.0, and 1.0 batch experiment results, which were assumed representative of H^+ absorption at pH < 1.0. However, model results indicated that the batch test results can not account for the observed H^+ consumption in all cells and greatly underestimate the amount of H^+ consumption in the pH -1.0 and -3.0. In the Kc and Km diffusion cells, above-background Ca, Al, Fe, and Si aqueous concentrations were associated with depth intervals characterized by decreased pH values. Respective peak concentrations of 325, 403, 176, 11.7, and 1.38 x 10^3 μmol g^{-1} (Kc) and 32.4, 426, 199, 7.2, and 1.22 x 10^3 μmol g^{-1} (Km) were measured in the pH -3.0 cells. XRD results showed that the elevated concentrations corresponded to the loss

of carbonates and montmorillonite peaks and decreased peak intensities for illite and kaolinite in depth intervals with pH $\leq$ 1.0, in the Kc and Km pH -1.0 and -3.0 cells.

The combined results of these studies indicated that the long-term diffusion of H_2SO_4 through clays at pH < 1.0 will result in a large amount of primary phase dissolution; however, this will be accompanied by precipitation of soluble Ca and Al sulfate salts and amorphous silica, especially at pH $\leq$ 0.0. Additionally, the presence of even a small amount of carbonate will serve to greatly buffer the diffusive transport of H_2SO_4 through clays, even at a source pH of -3.0.

ACKNOWLEDGEMENTS

The contents of this thesis represent the collaborative work undertaken by numerous individuals over the course of this research project.

I am greatly appreciative of the guidance and mentoring of my supervisor Dr. M. Jim Hendry. The enthusiasm, knowledge, support, and creative leeway he has provided throughout this entire process have, in no small part, allowed me to become a better researcher.

I am grateful to Dr. Derek Peak for helping to push my research into an area I had never considered, investing weeks of his personal time to assist me with sample analyses and providing invaluable knowledge and insight into the complicated world of synchrotron research.

I would also like to thank Dr. S. Lee Barbour for his time and patience through many discussions and brainstorming sessions over various aspects of my research.

I would like to thank the members of my committee for their participation in my thesis, Drs. Kevin Ansdell, Pan, Derek Peak, S. Lee Barbour and the external examiner Dr. x.

I would like to thank my wife, Megan, for her moral and emotional support through both the high and low points that I have encountered throughout the course of my research.

I would finally like to thank my family, in particular my mother, Rita, for providing encouragement and moral and financial support over the past ten years spent working my way through B.Sc., M.Sc., and Ph.D. degrees.

TABLE OF CONTENTS

	Page
PERMISSON TO USE	**i**
ABSTRACT	**ii**
ACKNOWLEDGEMENTS	**iv**
TABLE OF CONTENTS	**v**
LIST OF FIGURES	**ix**
LIST OF TABLES	**xii**
1.0 INTRODUCTION	**1**
1.1 Overview	**1**
1.2 Research objectives	**2**
1.3 Literature review	**5**
1.4 References	**13**
2.0 GEOCHEMICAL AND MINERALOGICAL IMPACTS OF H_2OS_4 ON CLAY BETWEEN PH 5.0 AND -3.0	**20**
2.1 Abstract	**20**
2.2 Introduction	**20**
2.3 Materials and methods	**22**
2.3.1 Clay samples	**22**
2.3.2 Clay characterization	**22**
2.3.3 Batch experiments	**24**
2.3.4 Aqueous geochemistry	**25**
2.3.5 Geochemical modeling	**25**
2.3.6 Solid phase mineralogy	**26**
2.3.7 Global dissolution rates	**26**
2.4 Results	**27**
2.4.1 Characterization of unaltered clays	**27**
2.4.2 Aqueous geochemistry	**30**
2.4.2.1 Al	**30**
2.4.2.2 Si	**31**

2.4.2.3 Ca **32**
2.4.2.4 SO_4 **33**
2.4.3 Mineralogical changes as a function of pH **34**
2.4.3.1 Kc clay **34**
2.4.3.2 Km clay **36**
2.4.3.3 BK clay **36**
2.4.4 Global dissolution rates **37**
2.5 Discussion **38**
2.5.1 Mineral dissolution **38**
2.5.2 Global dissolution rates **40**
2.5.3 Ca and SO_4 geochemistry **43**
2.5.4 Conceptual model **44**
2.6 Conclusions **46**
2.7 Acknowledgements **46**
2.8 References **47**
3.0 APPLICATION OF SI AND AL X-RAY ABSORPTION NEAR EDGE STRUCTURE TO ACIDIC DISSOLUTION OF MIXED CLAYS BETWEEN PH 1.0 AND -3.0 **53**
3.1 Abstract **53**
3.2 Introduction **53**
3.3 Materials and methods **55**
3.3.1 Sample descriptions **55**
3.3.2 Altered sample preparation **55**
3.3.3 XANES analyses **56**
3.4 Results and discussion **58**
3.4.1 Si XANES study **58**
3.4.1.1 K and $L_{2,3}$-edge peak assignment **58**
3.4.1.2 K-edge standard spectra **60**
3.4.1.3 $L_{2,3}$-edge standard spectra **61**
3.4.1.4 Altered samples **65**
3.4.2 Al XANES study **68**

3.4.2.1 K and $L_{2,3}$-edge peak assignment **68**

3.4.2.2 K-edge standard spectra **68**

3.4.2.3 $L_{2,3}$-edge standard spectra **70**

3.4.2.4 Altered samples **77**

3.4.3 Conceptual model **79**

3.5 Conclusions **80**

3.6 Acknowledgements **82**

3.7 References **83**

4.0 DIFFUSIVE TRANSPORT OF ACID THROUGH CLAY BETWEEN PH 1.0 AND -3.0 **88**

4.1 Abstract **88**

4.2 Introduction **88**

4.3 Materials and methods **91**

4.3.1 Clay samples **91**

4.3.2 Diffusion cell design **91**

4.3.3 Experiment design **92**

4.3.4 Clay recovery **93**

4.3.5 Aqueous geochemistry **93**

4.3.6 X-ray diffraction analyses **94**

4.3.7 Si K-edge XANES analyses **94**

4.3.8 Transport modeling **95**

4.4 Results and discussion **97**

4.4.1 Acid buffering **97**

4.4.2 Metal mobilization **103**

4.4.3 Secondary phase precipitation **106**

4.4.4 Transport modeling **109**

4.5 Conclusions **112**

4.6 Acknowledgements **113**

4.7 References **113**

5.0 SUMMARY AND CONCLUSIONS **118**

5.1 Characterization of the mineralogical effects of H_2SO_4 on clays **118**

5.2 Characterization of the geochemical effects of H_2SO_4 on clays 120

5.3 Determine the long-term impact of H_2SO_4 diffusion through clays 121

5.4 Global Conclusions 122

6.0 RECOMMENDATIONS FOR FUTURE WORK 125

APPENDIX 1: Supplementary data for clays 128

APPENDIX 2: Supplementary data for chapter 2 134

APPENDIX 3: Supplementary data for chapter 3 157

APPENDIX 4: Supplementary data for chapter 4 165

APPENDIX 5: Negative pH supplementary data 194

LIST OF FIGURES

Figure 1.1: Conceptual model of the differences between a) dilute solutions (I < 0.5 M) and b) concentrated solutions (I > 0.5 M).

Figure 2.1: XRD diffractograms of the unaltered whole rock Kc (A), Km (B) and BK (C) samples, where Q = quartz, S = smectite, K = kaolinite, I = illite, D = dolomite, P = plagioclase, Sd = siderite and C = cristobalite. All Kc and BK scans represent glycolated samples.

Figure 2.2: Aqueous phase Al (A-C), Si (D-F), Ca (G-I) and SO_4 (J-L) concentrations (mol L^{-1} g^{-1}) for the 14d (○), 90d (△), 180d (◇) and 365d (□) exposure periods in the Kc (left), Km (center) and BK (right) batch experiments. Error bars (one standard deviation) for all measured parameters are smaller than the plotted symbols.

Figure 2.3: Percent of Al and Ca mass mobilized (wt %) and mass percent of added SO_4 mobilized to the aqueous phase in the Kc (A, D), Km (B, E) and BK (C, F) batch experiments, for the 14d (○), 90d (△), 180d (◇) and 365d (□) exposure periods. SO_4 values represent the amount initially added to each respective batch experiment.

Figure 2.4: XRD diffractograms of unaltered, 1.0, 0.0, -1.0 and -3.0 pH treatments for the Kc, Km and BK clay media samples in the 90, 180 and 365d exposure periods, where Q = quartz, S = smectite, K = kaolinite, I = illite, D = dolomite, P = plagioclase, Sd = siderite, C = cristobalite and A = anhydrite. All Kc and BK scans represent glycolated samples.

Figure 2.5: Calculated log apparent global dissolution rates (mol m^{-2} s^{-1}) for Al (R_{Al}) and Si (R_{Si}) for the 14d (○), 90d (△), 180d (◇) and 365d (□) exposure periods in the Kc (A, D), Km (B, E) and BK (C, F) batch experiments.

Figure 2.6: Dissolution rates for A) smectite (▼) and B) illite (▲) and kaolinite (✕) and compared to the 180d R_{Al} of Kc (□), Km (◇) and BK (○) batch experiments. Smectite dissolution rates are taken from Amram and Ganor (2005) and represent exposure periods between 100 and 242d. Illite dissolution rates are taken from Kohler et al. (2005) and represent exposure periods between 103 and 196d. Kaolinite dissolution rates are taken from Cama et al. (2002) and represent exposure periods between 102 and 144d.

Figure 2.7: Conceptual model of the geochemical and mineralogical evolution of clay interaction with H_2SO_4 solutions between pH 5.0 and -3.0. (after Pesquera et al., 1992).

Figure 3.1: Si K-edge TEY and Si $L_{2,3}$-edge FY spectra of standard silicate minerals.

Figure 3.2: Enlargement of peak A region for selected Si $L_{2,3}$-edge FY spectra.

Figure 3.3: Si K-edge TEY (solid) and FY (dashed) spectra of unaltered (UA) and altered a) Kc, b) Km, and c) BK samples altered in H_2SO_4 solutions of pH 1.0, 0.0, -1.0, and -3.0 for durations of 14 and 365 day.

Figure 3.4: Si $L_{2,3}$-edge FY spectra of unaltered (UA) and altered a) Kc, b) Km, and c) BK samples altered in H_2SO_4 solutions of pH 1.0, 0.0, -1.0, and -3.0 for durations of 14 and 365 day.

Figure 3.5: Al K-edge TEY and Al $L_{2,3}$-edge FY spectra of Al-containing standard minerals.

Figure 3.6: Enlargement of peak A region for phyllosilicate Al $L_{2,3}$-edge FY spectra.

Figure 3.7: Al K-edge TEY spectra of unaltered (UA) and altered a) Kc, b) Km, and c) BK samples altered in H_2SO_4 solutions of pH 1.0, 0.0, -1.0, and -3.0 for durations of 14 and 365 day.

Figure 3.8: Al $L_{2,3}$-edge FY spectra of unaltered (UA) and altered a) Kc, b) Km, and c) BK samples altered in H_2SO_4 solutions of pH 1.0, 0.0, -1.0, and -3.0 for durations of 14 and 365 day.

Figure 3.9: Conceptual model of phyllosilicate dissolution under extremely acidic conditions between pH 5.0 and -3.0. Modified from Shaw and Hendry (accepted).

Figure 4.1: Depth profiles for Kc a) pH and 1:100 total soluble pore-water extracts for b) Ca, c) SO_4, d) Al, e) Fe, and f) Si for Kc_1 (□), Kc_{-1} (○), and Kc_{-3} (△).

Figure 4.2: Depth profiles for Km a) pH and 1:100 total soluble pore-water extracts for b) Ca, c) SO_4, d) Al, e) Fe, and f) Si for Km_1 (□), Km_{-1} (○), and Km_{-3} (△).

Figure 4.3: XRD diffractograms of unaltered and selected depth interval samples from the a) Kc pH -1.0, b) Kc pH -3.0, c) Km pH -1.0, and d) Km pH -3.0 cells, where Q = quartz, S = smectite, K = kaolinite, I = illite, D = dolomite, P = plagioclase, Sd = siderite, C = cristobalite and A = anhydrite. All Kc samples were glycolated.

Figure 4.4: Si K-edge TEY (solid) and FY (dashed) spectra of unaltered (UA) and altered samples taken from discreet depth intervals from a) Kc_1 and Kc_{-1}, and b) Kc_{-3}.

Figure 4.5: Si K-edge TEY (solid) and FY (dashed) spectra of unaltered (UA) and altered samples taken from discreet depth intervals from a) Km_1 and Km_{-1}, and b) Km_{-3}.

Figure 4.6: Ca and SO_4^{2-} depth profile concentrations for 1:1 pore-water extracts for the Kc (a & b) and Km (c & d) pH 1.0 (□), -1.0 (○), and -3.0 (△) cells.

Figure 4.7: Comparison of measured (●) and modeled H^+ activity (aH^+) profiles assuming no absorption (dashed line) and non-linear absorption (solid line) for Kc a) pH 1.0, b) pH -3.0, and c) pH -3.0 cells.

Figure 4.8: Comparison of measured (●) and modeled H^+ activity (aH^+) profiles assuming no absorption (dashed line) and non-linear absorption (solid line) for Km a) pH 1.0, b) pH -3.0, and c) pH -3.0 cells.

Figure 5.1: Conceptual model of phyllosilicate dissolution under extremely acidic conditions between pH 5.0 and -3.0.

LIST OF TABLES

Table 1.1: Mineral dissolution reaction series. Adapted from Blowes and Ptacek (1994).

Table 2.1: Mineralogical content of Kc, Km and BK whole rock (< 63 μm) and clay (< 2 μm) fractions, determined by semi-quantitative XRD methods.

Table 2.2: Sequential extraction results for the Kc, Km and BK samples. Fractions include 1) exchangeable; 2) carbonate bound; 3) Fe hydroxide/organic bound; and 4) residual (aluminosilicates)

Table 3.1: Mineralogical content of Kc, Km and BK whole rock and clay fractions, determined by semi-quantitative XRD methods. From Shaw and Hendry (accepted).

Table 3.2: Chemical formula and Si order of silicates and Al-containing minerals examined in Si K- and $L_{2,3}$-edge and Al K- and $L_{2,3}$-edge XANES.

Table 4.1: Geochemistry of the unaltered Kc and Km clay samples (after Shaw and Hendry, accepted).

Table 4.2: Average C and S values calculated from Kc and Km pH 5.0, 3.0, and 1.0 batch tests results, conducted by Shaw and Hendry (accepted). The S values for pH 1.0 were assumed to represent the pH -1.0 and -3.0 values for both clays.

Table 4.3: Linear and non-linear absorption isotherm equations determined for Kc and Km clays for pH 1.0, -1.0, and -3.0 using calculated S and C values in Table 2.

1.0 INTRODUCTION

1.1 Overview

The Alberta Oil Sands represent the second largest proven reserve of oil in the world, behind only Saudi Arabia. These deposits contain approximately 1.6 trillion barrels of bitumen of which 174 billion barrels are proven reserves that are recoverable using current technology (ADE, 2005). Forecasts are that 1.9 million barrels per day will be produced by 2010 with production increasing to 3.6 million barrels per day by 2020 (ADE, 2005).

Elemental sulfur (S^0) is recovered as a by-product of sour gas and oil sands production. The recovered S^0 is typically stored in large, above-ground blocks that are susceptible to the ingress of atmospheric oxygen and precipitation, resulting in the creation of sulfuric acid (H_2SO_4) rich leachate. These solutions are characterized by elevated sulfate (SO_4) and extremely low pH (pH < 0.5). The leachate within the block that has not been diluted by mixing with infiltrating meteoric water could be characterized by negative pH values. Generally S^0 blocks are considered to be temporary, existing for only weeks 0r months until they are remelted and shipped to market. However, the geographical and economical factors associated the Alberta Oilsands suggests that these blocks may exist for many years before it is economical to ship them to market Therefore, the long-term effects of H_2SO_4 on the underlying geologic media are of paramount concern.

Natural and constructed clay liners are routinely used to contain waste and wastewater. The impact of acidic solutions on the geochemistry and mineralogy of clays has been widely investigated in relation to acid mine drainage (AMD) problems but these generally are for systems with pH values greater than 1.0. AMD systems primarily evolve within mine tailing settings from the oxidization of sulfide minerals that produces elevated H_2SO_4 concentrations. These systems are typically characterized by primary mineral dissolution (e.g. Blowes and Ptacek, 1994; Jambor et al., 2002), mobilization and transport of metals to the aqueous environment (e.g. Dubrovsky et al., 1985; Jurjovec et al., 2002), precipitation of secondary mineral phases (e.g. Alpers et al., 1994; Moncur et al., 2005) and metal sorption processes (e.g. Blowes and Ptacek, 1994; McGregor et al., 1998). Few studies involve more acidic (pH < 1.0) conditions (Blowes et al., 1991;

Nordstrom et al., 2000; Jamieson et al., 2005; Moncur et al., 2005). The impact of H_2SO_4 leachate characterized by pH values less than 1.0 and potentially less than zero on the geochemistry and mineralogy of clays are, however, not clear.

1.2 Research Objectives

The goal of this research is to develop an understanding of the long-term geochemical and mineralogical impact of H_2SO_4 on clays. This research study focuses on the geochemical and mineralogical interactions that occur between clays typically used as engineered barriers in mine settings and H_2SO_4 solutions between pH 5.0 and -3.0. The main objectives of the research are to determine: (i) the mineralogical alterations resulting from the interaction of clays with H_2SO_4 solutions between pH 5.0 and -3.0; (ii) the aqueous geochemistry of the major elemental constituents associated with these interactions and, iii) the long-term geochemical and mineralogical impacts of H_2SO_4 diffusion through clay liners. To achieve these objectives the following steps were taken:

1. Three mineralogically distinct clays, typically used as natural or engineered barriers in mining applications, were selected for this study so that the results would be applicable to a wide range of clay types. Kc clay, which was rich in montmorillonite, illite, kaolinite, and dolomite, was selected for its use as the engineered barrier beneath the existing above ground S^0 blocks in the Alberta Oilsands. Km clay was rich in kaolinite and illite and was chosen because of its very low carbonate content and potential use as a barrier for future S^0 blocks in the Alberta Oilsands. Finally, the BK, a pure Na-montmorillonite, was selected to provide a basis of comparison for the more complex, mixed, Kc and Km clays.
2. The mineralogy and geochemistry of the three unaltered clay samples was characterized. Characterization included: whole sample acid digests, cation exchange capacities, B.E.T. surface area, whole rock and clay fraction mineral compositions, sequential extractions and total carbonate contents.
3. The mineralogical and geochemical impacts of H_2SO_4 on the clay samples were determined as a function of solution pH and exposure time through a series of batch experiments.

4. A conceptual model of the mineralogical and geochemical interactions between clays and acidic solutions was developed between pH 5.0 and -3.0 using the results of the current and previous studies.
5. Characterization of the dissolution of phyllosilicates and the formation of new phases caused by H_2SO_4 interaction with clays for both variable pH and exposure times was measured using x-ray diffraction (XRD) and x-ray absorption near edge structure (XANES) analyses.
6. Characterization of the mineralogical and geochemical impacts of H_2SO_4 transport through clays, as a function of source pH, was measured through a series of long-term diffusion cell experiments.
7. A one-dimensional transport model was used in an attempt to simulate the observed diffusion of hydronium ions (H^+) through clay between pH 1.0 and -3.0 for cases of zero adsorption and non-linear consumption of H^+.

The findings of this research are presented in the form of three manuscripts submitted to peer-reviewed scientific journals (Chapters 2-4). All laboratory studies, synchrotron studies, data analyses, and manuscript preparations were preformed by the author.

Chapter 2 presents the results of an examination of the mineralogical and geochemical impact of H_2SO_4 solutions on clays. A series of batch experiments were conducted over a pH range of 5.0 to -3.0 and exposure periods of 14 to 365 d. Previous studies have mainly focused on individual mineral phases and pH values > 1.0. This was the first study to consider the interactions between multimineralic clay samples and pH values <1.0. Results of these batch experiments showed increased dissolution of aluminosilicates with decreasing pH and increasing exposure period with smectite being more susceptible to dissolution then illite and kaolinite, the precipitation of an amorphous silica phase occurred at pH ≤ 0.0, and anhydrite precipitated in Ca-rich clays at pH ≤ -1.0. Calculated dissolution rates suggested that two reaction mechanisms control aluminosilicate dissolution in all three clays, with a more pH dependent mechanism occurring between pH 5.0 and 1.0 and a near pH independent mechanism between pH 0.0 and -3.0. A stepwise conceptual model of the impact of sulfuric acid on aluminosilicate

geochemistry and mineralogy between pH 5.0 and -3.0 was proposed. This manuscript was accepted by *Appl. Geochem.* (Shaw and Hendry, accepted) for publication, in January 2008, and is currently awaiting publication.

The results of a synchrotron radiation based study of the chemical and structural changes experienced by Si and Al due to H_2SO_4 interaction with clays are presented in Chapter 3. Through a comparison of the altered Kc, Km, and BK clays with a series of known silicate and phyllosilicate standards, it was shown that the acidic alteration of clays could be described. The Si XANES results indicated the preferential dissolution of the phyllosilicates (pH $\leq$ 1.0, t $\geq$ 14 d), the persistence of quartz at pH $\geq$ -3.0 and t $\geq$ 365 d, and the formation of an amorphous silica-like phase that was confined to the surface layer of the altered clay samples at pH $\geq$ -1.0 and t $\geq$ 90 d). The Al XANES results demonstrated dissolution of Al-octahedral layers (pH $\leq$ 1.0, t $\geq$ 14 d), the persistence of four-fold relative to six-fold coordinated Al, and the precipitation of an Al-SO_4-rich phase (pH $\leq$ -1.0, t $\geq$ 90 d). The study demonstrated that Si and Al XANES provides both surface and bulk sensitive information on the chemical and structural changes of Si and Al that cannot be attained using conventional mineralogical analyses. An existing conceptual model of phyllosilicates dissolution under extremely acidic conditions was modified to include the results of this study. This manuscript has been submitted to *Geochim. Cosmochim. Acta* (Shaw et al., in submission) and is currently being reviewed.

Chapter 4 presents the results of an investigation of the diffusive transport of H_2SO_4 in clays between pH 1.0 and -3.0. Single reservoir, constant concentration, diffusion cell experiments were conducted on Kc and Km clays with H_2SO_4 reservoir solutions of pH 1.0, -1.0, and -3.0 over a period of 216 d. Results of these experiments showed above-background pH values to depths of 80, 193, and 210 mm in the pH 1.0, -1.0, and -3.0 Kc cells, respectively, and 138, $\geq$ 288, and $\geq$ 288 mm in the Km cells , respectively. Associated with these lower pH regions were elevated Ca, Al, Fe, Si, and SO_4 concentrations associated with acidic dissolution of primary carbonate and aluminosilicate phases in all cells. XRD results confirmed the removal of carbonate and montmorillonite peaks and the decrease of illite and kaolinite peaks. Si K-edge TEY

XANES results confirmed the dissolution of phyllosilicates at depths with pH < 1.0 in all cells. The diffusive transport of H^+ within the cells was modeled using a series of one-dimensional transport simulations that assumed no absorption and non-linear absorption of H^+. Absorption isotherms were assumed to be representative of the consumption of H^+ through acidic mineral dissolution reactions and were calculated from a series of batch tests between pH 5.0 and 1.0, previously conducted on the Kc and Km clays (Chapter 2). Model results indicate that the batch test results are unable to account for the observed H^+ consumption in all cells. Possible explanations for the model discrepancies included underestimation of H+ consumption or overestimation of the effective diffusion coefficient. The results of this study indicate that, despite the extreme pH values considered, diffusion of H_2SO_4 solutions with pH < 1.0 will be greatly attenuated through the addition of a strong acid neutralizing mineral phase, such as dolomite, to the clay. This manuscript has is being prepared for submission to *Appl. Geochem.* (Shaw and Hendry, in prep.).

The overall Summary and Conclusions of this thesis and Recommendations for Future Work are presented in Chapters 5 and 6. Appendix 1 contains supplementary data for the geochemical characterization of the unaltered Kc, Km, and BK clays studied in this thesis. The raw data, geochemical analyses results, and mineralogical analyses data collected for the investigations summarized in Chapter 2 are presented in Appendix 2. The data collected for use in Chapter 3, including all raw XANES spectra results, are summarized in Appendix 3. Appendix 4 includes the raw measurement data, geochemical analyses, mineralogical analyses, and associated transport model results used for the investigations presented in Chapter 4. Finally, Appendix 5 presents supporting data used in the calculation and application of negative pH measurements used throughout the experiments presented in this thesis.

1.3 Literature Review

1.3.1 Acid mine drainage

Acid-mine drainage systems are characterized by the production of acidity and SO_4 through the oxidation of sulfide minerals (Jambor, 1994) and have been well studied

for over twenty years (e.g. Dubrovsky et al., 1985; Morin et al., 1988; Blowes and Ptacek, 1994; Schuring et al., 1997; Shaw et al., 1998; Al et al., 2000; Kashir and Yanful, 2001; Jurjovec et al., 2002; Dold and Fontbote, 2002; Sracek et al., 2004; Brookfield et al., 2006). Morin et al. (1988) demonstrated the capacity of geologic media, including clay minerals, to buffer the acidity of AMD affected waters through series of mineral dissolution reactions. The proposed mineral reaction series was subsequently refined by Blowes and Ptacek (1994), and is summarized in Table 1.1.

Table 1.1. Mineral dissolution reaction series. Adapted from Blowes and Ptacek (1994).

Phase	Dissolution Reaction	Buffering pH
Carbonate	$CaCO_3 + H^+ \leftrightarrow Ca^{2+} + HCO_3^-$	6.5 to 7.5
Siderite	$FeCO_3 + H^+ \leftrightarrow Fe^{2+} + HCO_3^-$	4.8 to 6.3
Al-Hydroxides	$Al(OH)_3 + H^+ \leftrightarrow Al^{3+} + 2H_2O$	4.0 to 4.3
Fe-Hydroxides	$Fe(OH)_3 + H^+ \leftrightarrow Fe^{3+} + 2H_2O$	2.0 to 3.5
Silicates	$Al_2Si_2O_5(OH)_4 + 6H^+ \leftrightarrow 2Al^{3+} + 2H_4SiO_4 + H_2O$	< 1.5

The migration of acidic solutions through geologic media results in a dynamic set of geochemical interactions including primary mineral dissolution, secondary mineral precipitation, metal co-precipitation/sorption (Blowes and Ptacek, 1994; McGregor et al., 1998; Bigham and Nordstrom 2000). As acidic waters are continuously introduced from the source the buffering capacity of each successive mineral in the reaction series is overcome, which leads to the development of pH horizons. In addition, mobilized metals are transported down-gradient to areas of higher pH, resulting in the precipitation of secondary minerals and co-precipitation and sorption reactions (Blowes and Ptacek, 1994; Jurjovec et al., 2002). As the low pH front intercepts these secondary phases they potentially re-dissolve and re-mobilize metals into the pore water. Most AMD studies are characterized by pH values >1.0 (e.g. Al et al., 2000; Blowes et al., 2003; Hammarstrom et al., 2003; Sidenko and Sherriff, 2005; Gunsinger et al., 2006), while few studies involve more acidic (pH < 1.0) conditions. These latter studies include those at Heath Steele, New Brunswick, Canada (pH≥ 0.80; Blowes et al., 1991), Sherridon, Manitoba,

Canada (pH≥ 0.67; Moncur et al., 2005), and Iron Mountain, California (pH≥ -3.6; Nordstrom et al., 2000).

1.3.2 Concentrated Solutions

The concentration (c) and activity (α) of a species in solution can be equated using a species specific activity coefficient (γ) (Stumm and Morgan, 1996):

$$\alpha = c\,\gamma \qquad [1.1]$$

In infinitely dilute solutions (ionic strength < 0.1 M), activity coefficients of individual species are equal to unity. As solutions become more concentrated the direct interaction between ions increase and the activity coefficient diverges from unity (Stumm and Morgan, 1996). Conceptually, each ion in a dilute solution is surrounded by a series of water molecules (hydration shells). As the solute increases in concentration a decreasing number of water molecules are available (Figure 1.1). Numerical solutions can account for the difference between concentration and activity to an ionic strength < 0.5 M, while a poor correlation exists at I > 0.5 M (Stumm and Morgan, 1996).

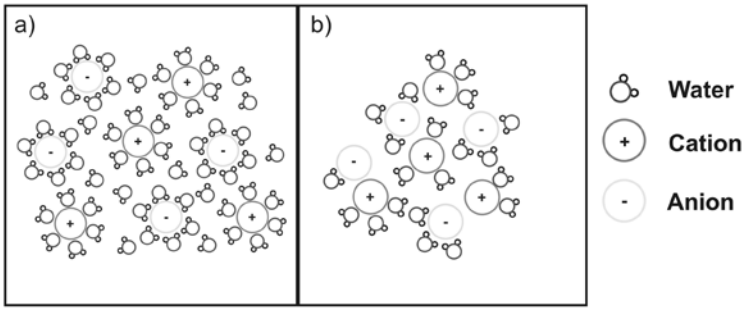

Figure 1.1: Conceptual model of the differences between a) dilute solutions (I < 0.5 M) and b) concentrated solutions (I > 0.5 M).

A set of empirical equations based on statistical thermodynamics have been developed in order to better estimate the activity of ions in concentrated solutions. Collectively these equations are termed Pitzer equations (Meinrath, 2002). Pitzer equations account for the direct interaction of ions in concentrated solutions including

cation-cation, anion-anion, cation-anion, cation-cation-anion, and anion-anion-cation interactions. The empirical datasets utilized in the development of these equations have an associated level of statistical uncertainty, which limit their predictive capabilities (Meinrath, 2002). Currently, literature datasets are confined to a small number of species (Ba, Ca, Fe, H_2O, H^+, K, Li, Mg, Mn, Na, Sr, Br, Cl, CO_3 and SO_4) limiting the application of Pitzer equations to a small number of systems (Plummer et al., 1988).

1.3.3 Negative pH measurements

The pH of a solution is defined as (Stumm and Morgan, 1996):

$$pH = -\log \{H^+\} = -\log [H^+] - \log \gamma_H \qquad [1.2]$$

where:

$\{H^+\}$ = H^+ activity
$[H^+]$ = H^+ concentration
γH = activity coefficient

By convention the measurement of pH is limited to $1 < pH < 13$, a range over which there is a reproducible method to measure pH in low ionic strength solutions ($I < 0.1$ M) using a standard glass electrode. However, in concentrated solutions ($I > 0.1$ M), liquid junction potentials develop between the electrode and the solution impeding the ability to achieve reproducible results between individual solutions (Stumm and Morgan, 1996). Nordstrom et al, (2000) developed a method to measure $pH < 1.0$ using standardized H_2SO_4 solutions and a standard reference electrode. Briefly, the theoretical pH values of standardized solutions are calculated using a Pitzer equation based computer program (PHRQPITZ; Plummer et al., 1988). The potential (mV) of the standardized solutions are measured with a standard glass electrode and a calibration curve is generated from the results. Application of this method to the extremely acidic mine waters located at Iron Mountain, California, resulted in reproducible measurements to a maximum pH of -3.6 (Nordstrom et al., 2000).

1.3.4 Acidic mineral dissolution rates

The bulk of proton promoted mineral dissolution rate calculations have been determined through small-scale, laboratory based, investigations (e.g. Zysset and Schindler, 1996; Gautelier et al., 1999; Cama et al., 2002; Hradil and Hostomosky, 2002; Brandt et al., 2003; Amram and Ganor, 2005; Metz et al., 2005). Several studies have shown laboratory determined rates to be orders of magnitudes higher than those determined through direct field investigations (Schnoor, 1990; Velbel 1993; White and Brantley, 1995, 2003). Previous aluminosilicate dissolution studies show a general decrease in reaction rates with increasing exposure period (e.g. Kalinowski and Schweda, 1996; Hradil and Hostomsky, 2002; Brandt et al., 2003; Kohler et al., 2003; White and Brantley, 2003; Kohler et al., 2005). White and Brantley (2003) suggest the decrease in dissolution rates with increasing time are a result of several intrinsic processes including: decreased surface area, depletion of reactive sites, precipitation of secondary products, and extrinsic processes resulting from the controlled systems used in laboratory experiments. Salmon and Malmstrom (2006) demonstrate that rates calculated for multimineralic samples, such as those in the current investigation, are between one and two orders of magnitude lower than the rates for freshly prepared monomineralic samples typically used in aluminosilicate dissolution studies. To date, studies have focused on aluminosilicate dissolution rates at pH > 1.0, while few studies have considered systems characterized by pH < 1.0 (e.g. Hradil and Hostomosky, 2002; Cama et al., 2002).

The dissolution reaction of clays treated with H_2SO_4 solutions in the experiments may be written as follows (Qafoku et al., 2004):

$$clay\ (smectite,\ illite,\ kaolinite,\ etc...) + H^+ + SO_4 \rightarrow Al + Si + Fe + Ca \ldots \qquad [1.3]$$

As clay is comprised of several individual mineralogical phases, the dissolution and precipitation rates calculated from the amount of release and uptake of Al and Si from the aqueous phase can be written as the sum of the rate expressions that represent the rates for each individual mineralogical phase (Qafoku et al., 2004). For example the release rate of Si may be written as:

$$\frac{\delta Si}{\delta t} = (k_{H_3O^+ - quartz}\left[H_3O^+\right]^a + k_{SO_4 - quartz}\left[SO_4\right]^b) +$$
$$(k_{H_3O^+ - smectite}\left[H_3O^+\right]^a + k_{SO_4 - smectite}\left[SO_4\right]^b) + \quad [1.4]$$
$$(k_{H_3O^+ - kaolinite}\left[H_3O^+\right]^a + k_{SO_4 - kaolinite}\left[SO_4\right]^b) + ...$$

The global dissolution rate (R_x) of clay can be calculated using the following equation (after Zysset and Schindler, 1996):

$$R_{Al/Si} = \frac{d[X]}{dtA} = \left\{\left[X\right]_{t=1} - \left[X\right]_{t=0}\right\} / dt \quad [1.5]$$

In equation [5], *dt* is the exposure length in seconds, $[X]_{t=1}$ is the dissolved ion concentration (mol L^{-1} g^{-1}) normalized to the initial mass of clay placed in the flask, *A* is the B.E.T. surface area of the clay sample, and $[X]_{t=0}$ is the initial dissolved concentration of the ion of interest. If the dissolution reaction is far from equilibrium, the reaction rate of proton promoted mineral dissolution is typically been described by the following rate law (Zysset and Schindler, 1996):

$$R = k\,[H^+]^n \quad [1.6]$$

where *R* is the mineral dissolution rate, *k* is the reaction constant, $[H^+]$ is the proton concentration, and *n* is the reaction order. This equation can be transformed into:

$$\log R = \log k - n\,pH \quad [1.7]$$

from which *n*, or pH dependence of the reaction, can be determined from a plot of log R versus pH, where the slope of the straight line is equal to *n*.

1.3.5 Si and Al XANES

X-ray absorption near edge structure (XANES) provides information on the electronic interactions between the element of interest and surrounding atoms and provides useful information on oxidation states and coordination geometry (Brown and Sturchio, 2002). Silicates are characterized by silica surrounded by oxygen atoms in tetrahedral coordination (^{4}Si) and, due to the charge (+ 4) on Si, silicate tetrahedrons link only in corner sharing bonds. Silicates reference can be grouped, according to the number

of oxygen atoms that are shared in the tetrahedral linkages, as nesosilicates (zero, Q^0), sorosilicates (one, Q^1), cyclosilicates and inosilicates (two, Q^2), phyllosilicates (three, Q^3), or tectosilicates (four, Q^4). Previous studies have used Si XANES and energy-loss near-edge structure (ELNES) analyses to determine the number of shared oxygen atoms, or degree of polymerization, in various silicates using both K-edge (e.g. Li et al., 1995a; Chaboy et al., 1995; Bantignies et al., 1997; Gilbert et al., 2003) and $L_{2,3}$-edge (Li et al., 1994; Poe et al., 1997; Garvie and Buseck, 1999) XANES.

Researchers have also used aluminum (Al) K-edge XANES and electron energy-loss spectroscopy analyses (Li et al., 1995b; Ildefonse et al., 1998; Doyle et al., 1999; Kato et al., 2001; Yoon et al., 2004) and to a lesser extent $L_{2,3}$-edge XANES (Chen et al., 1993; Zou et al., 1999; Hu et al., 2008; Weigel et al., 2008) to examine the coordination of Si and Al in silicates. The majority of K-edge XANES studies focus on fingerprinting the four-fold and six-fold Al coordination of mineral phases (Li et al., 1995b; Cabaret et al., 1996; Mottana et al., 1997; Ildefonse et al., 1998; Doyle et al., 1999; Kato et al., 2001; van Bokhoven et al., 1999; Gehlen et al., 2002; Yoon et al., 2004). Aluminum $L_{2,3}$-edge XANES is extremely chemically sensitive as it is dominated by the interactions between the ejected 2p electron of Al and unoccupied Al orbitals of s+d character; while the ligands surrounding the Al and the coordination number of those ligands both have a large effect on these electronic transitions.

1.3.6 Diffusive transport

Fick's first law for one-dimensional transport in saturated soils can be applied in cases where advection is negligible, such as in low permeable clays, and solute transport is dominated by diffusive transport (Shackelford, 1991):

$$J_D = -D_0 \tau n \frac{dc}{dx} \qquad [1.8]$$

where J_D is the diffusive mass flux of solute (M L^{-2} T^{-1}), c is mass concentration of the solute (M L^{-3}), x is the distance of transport (L), τ is the dimensionless tortuosity factor, n is the total porosity of the clay, and D_o is the aqueous diffusion coefficient (L^2 T^{-1}) of the species of interest in free water. According to Shackelford (1991), the effective diffusion coefficient in soil (D^*) can be utilized in order to account for the tortuosity factor:

$$D^* = D_0 \tau \qquad [1.9]$$

Therefore, Fick's first law can be expressed as:

$$J_D = -D^* \mathrm{n} \frac{dc}{dx} \qquad [1.10]$$

The diffusive transport of a solute through clay is controlled both by the diffusive flux and chemical and/or biological reactions that retard the solutes movement. An adsorption isotherm can be used to characterize these interactions by developing a relationship between the mass of species adsorbed to the soil solid, S (M M^{-1}) and the concentration in solution, c. The slope of the adsorption isotherm is referred to as the distribution function. A typical relationship used to describe non-linear distribution functions is the Freundlich isotherm, defined by Fetter (1988) as follows:

$$S = K_d c^b \qquad [1.11]$$

where *b* is a fitting coefficient.

In the case where the adsorption isotherm is linear the slope is described as the distribution function (K_d). In this case the attenuation provided by adsorption is independent of concentration and this gives rise to a dimensionaless retardation factor, R_d defined as follows:

$$R_d = 1 + \left(\frac{\rho_b}{\mathrm{n}} \right) (\mathrm{K_d}) \qquad [1.12]$$

where ρ_b (M L^{-3}) is the dry bulk density, n is the porosity, and K_d is the distribution coefficient.

The use of the dimensionless retardation factor (R_d) allows the rate of transport for an attenuated species to be expressed as a ratio of the rate of transport for a non-reactive solute (such as chloride). Therefore, in a diffusion dominated system (such as a

clay liner) Fick's second law can be used to calculate the rate diffusion (Shackelford, 1991):

$$\frac{\partial c}{\partial t} = \frac{D^*}{Rd}\frac{\delta^2 c}{\delta x^2} \qquad [1.13]$$

It is important to note that in this form of Fick's second law, it is assumed that there is the porosity of the domain is uniform and that the effective porosity for diffusion (e.g. Ficks' First Law) is the same as the porosity describing the accessible pore-space available to the species of interest. The use of an adsorption relationship is also predicated on the assumption that the adsorption process is 'instantaneous' (e.g. 'fast' relative to chemical kinetics) and reversible.

1.4 References

Al, T.A., Martin, C.J. and Blowes, D.W., 2000. Carbonate-mineral/water interactions in sulfide-rich mine tailings. *Geochim. Cosmochim. Acta* 64, 3933-3948.

Alpers C. N., Blowes D. W., Nordstrom D. K., and Jambor J. L., 1994. Secondary minerals and acid mine-water chemistry. In: The Environmental Geochemistry of Sulfide Mine-Wastes, Short Course Handbook 22 (eds. D.W. Blowes and J.L. Jambor), pp. 248-270.

Amram, K. and Ganor, J., 2005. The combined effect of pH and temperature on smectite dissolution rate under acidic conditions. *Geochim. Cosmochim. Acta* 69, 2535-2546.

Bantignies J. F., Cartier Dit Moulin C., and Dexpert H., 1997. Wettability contrasts in kaolinite and illite clays: characterization by infrared and x-ray absorption spectroscopies. *Clays and Clay Minerals* 45, 184-193.

Bigham, J.M. and Nordstrom, D.K., 2000. Iron and aluminum hydroxysulfates from acid sulfate waters. Reviews in Mineralogy and Geochemistry 40, 351-403.

Blowes, D.W. and Ptacek, C.J., 1994. Acid-neutralization mechanisms in inactive mine tailings. In: Blowes, D.W. and Jambor, J.L. (Eds.), The Environmental Geochemistry of Sulfide Mine-Wastes, Short Course Handbook 22, pp. 271-292.

Blowes, D.W., Ptacek, C.J. and Jurjovec, J., 2003. Mill tailings: Hydrogeology and geochemistry. In: Blowes, D.W., Jambor, J.L. and Ritchie, A.I.M. (Eds.), The

Environmental Geochemistry of Sulfide Mine-Wastes, Short Course Handbook 31, pp. 95-116.

Blowes, D.W., Reardon, E.J., Jambor, J.L. and Cherry, J.A., 1991. The Formation and Potential Importance of Cemented Layers in Inactive Sulfide Mine Tailings. *Geochim. Cosmochim. Acta* 55, 965-978.

Brandt, F., Bosbach, D., Krawczyk-Barsch, E., Arnold, T. and Bernhard, G., 2003. Chlorite dissolution in the acid pH-range: A combined microscopic and macroscopic approach. *Geochim. Cosmochim. Acta* 67, 1451-1461.

Brookfield, A.E., Blowes, D.W. and Mayer, K.U., 2006. Integration of field measurements and reactive transport modeling to evaluate contaminant transport at a sulfide mine tailings impoundment. *J. Contam. Hydrol.* 88, 1-22.

Brown G. E. and Sturchio N. C., 2002. An overview of synchrotron radiation applications to low temperature geochemistry and environmental science. In: Applications of Synchrotron Radiation in Low-Temperature Geochemistry and Environmental Sciences, Reviews in Mineralogy and Geochemistry (eds. Fenter et al.) Mineralogical Society of America and the Geochemical Society 49, 1-115.

Cabaret D., Sainctavit P., Ildefonse P., and Flank A. M., 1996. Full multiple-scattering calculations on silicates and oxides at the Al K edge. *J. Phys.: Condens. Matter* 8, 3691-3704.

Cama, J., Metz, V. and Ganor, J., 2002. The effect of pH and temperature on kaolinite dissolution rate under acidic conditions. *Geochim. Cosmochim. Acta* 66, 3913-3926.

Chaboy J., Benfatto M., and Davoli I., 1995. Theoretical-analysis of X-ray-absorption spectra at the silicon K and L(2,3) edges of crystalline and amorphous SiO_2. *Phys. Rev. B* 52, 10014-10020.

Chen J. M., Rosenberg R. A., Simons J. K., and Tan K. H., 1993. X-ray-absorption near-edge structure of single-crystal sapphire using synchrotron-radiation - the interatomic-distance correlation. *Japan. J. Appl. Phys. Part 1* 32, 788-790.

Dold, B. and Fontbote, L., 2002. A mineralogical and geochemical study of element mobility in sulfide mine tailings of Fe oxide Cu-Au deposits from the Punta del Cobre belt, northern Chile. *Chem. Geol.*189, 135-163.

Doyle C. S., Traina S. J., Ruppert H., Kendelewicz T., Rehr J. J., and Brown G. E. , 1999. XANES studies at the Al K-edge of aluminum-rich surface phases in the soil environment. *J. Synchrotron Rad.*. 6, 621-623.

Dubrovsky, N.M., Cherry, J.A., Reardon, E.J. and Vivyurka, A.J., 1985. Geochemical Evolution of Inactive Pyritic Tailings in the Elliot Lake Uranium District. *Can. Geotech. J.* 22, 110-128.

Fetter, C. W., 1988. Applied hydrogeology, 2nd ed., Merrill Publishing Company; Columbus, 592p.

Garvie L. A. J. and Buseck P. R., 1999. Bonding in silicates: Investigation of the Si L_{-2},L_{-3} edge by parallel electron energy-loss spectroscopy. *Amer. Mineral*. 84, 946-964.

Gautelier, M., Oelkers, E. H. and Schott, J., 1999. An experimental study of dolomite dissolution rates as a function of pH from -0.5 to 5 and temperature from 25 to 80C. *Chem. Geol.* 157, 13-26.

Gehlen M., Beck L., Calas G., Flank A. M., Van Bennekom A. J., and Van Beusekom J. E. E., 2002. Unraveling the atomic structure of biogenic silica: Evidence of the structural association of Al and Si in diatom frustules. *Geochim.. Cosmochim. Acta* 66, 1601-1609.

Gilbert B., Frazer B. H., Naab F., Fournelle J., Valley J. W., and De Stasio G., 2003. X-ray absorption spectroscopy of silicates for in situ, sub-micrometer mineral identification. *Amer. Mineral.* 88, 763-769.

Gunsinger, M.R., Ptacek, C.J., Blowes, D.W., Jambor, J.L. and Moncur, M.C., 2006. Mechanisms controlling acid neutralization and metal mobility within a Ni-rich tailings impoundment. *Appl. Geochem*. 21, 1301-1321.

Hammarstrom, J.M., Sibrell, P.L. and Belkin, H.E., 2003. Characterization of limestone reacted with acid-mine drainage in a pulsed limestone bed treatment system at the Friendship Hill National Historical Site, Pennsylvania, USA. *Appl. Geochem.* 18, 1705-1721.

Hradil, D. and Hostomsky, J., 2002. Effect of composition and physical properties of. natural kaolinitic clays on their strong acid weathering rates. *Catena* 49, 171-181.

Hu Y. F., Xu R. K., Dynes J. J., Blyth R. I. R., Yu G., Kozak L. M., and Haung P. M., 2008. Coordination nature of aluminum (oxy)hydroxides formed under the influence of tannic acid studied by X-ray absorption spectroscopy. *Geochim. Cosmochim. Acta.* 72, 1959-1969.

Ildefonse P., Cabaret D., Sainctavit P., Calas G., Flank A. M., and Lagarde P., 1998. Aluminum X-ray absorption near edge structure in model compounds and Earth's surface minerals. *Phys. Chem. Min.* 25, 112-121.

Jambor, J.L., 1994. Mineralogy of sulfide-rich tailings and their oxidation products. In: Blowes, D.W. and Jambor, J.L. (Eds.), The Environmental Geochemistry of Sulfide Mine-Wastes, Short Course Handbook 22, pp. 59-102.

Jambor, J. L., Dutrizac, J. E., Groat, L. A., and Raudsepp, M., 2002. Static tests of neutralization potentials of silicates and aluminosilicate minerals. *Environ. Geol.* 43, 1-117.

Jamieson H. E., Robinson C., Alpers C. N., Nordstrom D. K., Poustovetov A., and Lowers H. A., 2005. The composition of coexisting jarosite-group minerals and water from the Richmond mine, Iron Mountain, California. *Can. Mineral.* 43, 1225-1242.

Jurjovec, J., Ptacek, C.J. and Blowes, D.W., 2002. Acid neutralization mechanisms and metal release in mine tailings: A laboratory column experiment. *Geochim. Cosmochim. Acta* 66, 1511-1523.

Kalinowski, B. E. and Schweda, P. 1996. Kinetics of muscovite, phlogopite, and biotite dissolution and alteration at pH 1-4, room temperature. *Geochim. Cosmochim. Acta* 60, 367-385.

Kashir, M. and Yanful, E.K., 2001. Hydraulic conductivity of bentonite permeated with acid mine drainage. *Can. Geotech. J.* 38, 1034-1048.

Kato Y., Shimizu K., Matsushita N., Yoshida T., Yoshida H., Satsuma A., and Hattori T., 2001. Quantification of aluminum coordinations in alumina and silica-alumina by AlK-edge XANES. *Phys. Chem. Chem. Phys.* 3, 1925-1929.

Kohler, S.J., Dufaud, F. and Oelkers, E.H., 2003. An experimental study of illite dissolution kinetics as a function of pH from 1.4 to 12.4 and temperature from 5 to 50 degrees C. *Geochim. Cosmochim. Acta* 67, 3583-3594.

Kohler, S.J., Bosbach, D. and Oelkers, E.H., 2005. Do clay mineral dissolution rates reach steady state? *Geochim. Cosmochim. Acta* 69, 1997-2006.

Li D., Bancroft G. M., Kasrai M., Fleet M. E., Secco R. A., Feng X. H., Tan K. H., and Yang B. X., 1994. X-ray-absorption spectroscopy of silicon dioxide (SiO_2) polymorphs - the structural characterization of opal. *Amer. Mineral.* 79, 622-632.

Li D., Bancroft G. M., Fleet M. E., and Feng X. H., 1995a. Silicon K-edge XANES spectra of silicate minerals. *Phys. Chem. Min.* 22, 115-122.

Li D. E., Bancroft G. M., Fleet M. E., Feng X. H., and Pan Y., 1995b. Al K-Edge XANES Spectra of Aluminosilicate Minerals. *Amer. Mineral.* 80, 432-440.

McGregor R. G., Blowes D. W., Jambor J. L., and Robertson W. D., 1998. Mobilization and attenuation of heavy metals within a nickel mine tailings impoundment near Sudbury, Ontario, Canada. *Environ. Geol.* 36, 305-319.

Meinrath, G., 2002. Extended traceability of pH: an evaluation of the role of Pitzer's equations. *Anal. Bioanal. Chem.* 374, 796-805.

Metz, V., Amram, K. and Ganor, J., 2005. Stoichiometry of smectite dissolution reaction. *Geochim. Cosmochim. Acta* 69, 1755-1772.

Moncur, M.C., Ptacek, C.J., Blowes, D.W. and Jambor, J.L., 2005. Release, transport and attenuation of metals from an old tailings impoundment. *Appl. Geochem.* 20, 639-659.

Morin, K.A., Cherry, J.A., Dave, N.K., Lim, T.P. and Vivyurka, A.J., 1988. Migration of acidic groundwater seepage from uranium-tailings impoundments, 1. Field study and conceptual hyrodgeochemical model. *J. Contam. Hydro.* 2, 271-303.

Mottana A., Robert J. L., Marcelli A., Giuli G., DellaVentura G., Paris E., and Wu Z. Y., 1997. Octahedral versus tetrahedral coordination of Al in synthetic micas determined by XANES. *Amer. Mineral.*82, 497-502.

Nordstrom, D.K., Alpers, C.N., Ptacek, C.J. and Blowes, D.W., 2000. Negative pH and extremely acidic mine waters from Iron Mountain, California. *Env. Sci. Technol.* 34, 254-258.

Plummer, L.N., Parkhurst, D.L., Fleming, G.W. and Dunkle, S.A., 1988. A computer program incorporating pitzer's equations for calculation of geochemical reactions in brines. U.S. Geological Survey Water-Resources Investigations Report 88-4153.

Poe, B., Seifert, F., Sharp, T. and Wu, Z., 1997. ELNES spectroscopy of mixed Si coordination minerals. *Phys. Chem. of Mineral.* 24, 477-487.

Qafoku, N.P., Ainsworth, C.C., Szecsody, J.E. and Qafoku, O.S., 2004. Transport-controlled kinetics of dissolution and precipitation in the sediments under alkaline and saline conditions. *Geochim. Cosmochim. Acta* 68, 2981-2995.

Salmon, S.U. and Malmstrom, M.E., 2006. Quantification of mineral dissolution rates and applicability of rate laws: Laboratory studies of mill tailings. *Appl. Geochem.* 21, 269-288.

Schnoor, J. L., 1990. Kinetics of chemical weathering: a comparison of laboratory and field rates. In: Stumm, W. (Ed.), Aquatic Chemical Kinetics. Wiley, New York, pp. 475-504.

Schuring, J., Kolling, M. and Schulz, H.D., 1997. The potential formation of acid mine drainage in pyrite-bearing hard-coal tailings under water-saturated conditions: An experimental approach. *Environ.Geol.* 31, 59-65.

Shackelford, C. D., 1991a. Laboratory diffusion testing for waste disposal – A review. *J. Contam. Hydrol.* 7, 177-217.

Shackelford, C. D. and Daniel, D. E., 1991b. Diffusion in saturated soil. I: Background. *J. Geotech. Eng.* 117, 467-484.

Shaw, S. C., Groat, L. A., Jambor, J. L., Blowes, D. W., Hanton-Fong, C. J., and Stuparyk, R. A., 1998. Mineralogical study of base metal tailings with various sulfide contents, oxidized in laboratory columns and field lysimeters. *Environ. Geol.* 33, 209-217.

Shaw, S. A. and Hendry M. J., accepted. Geochemical and mineralogical impacts of H_2SO_4 on clays between pH 5.0 and -3.0. *Appl. Geochem.*

Shaw S. A., Peak, D. and Hendry M. J., in submission. Application of Si and Al x-ray absorption near edge structure to acidic dissolution of mixed clays between pH 1.0 and -3.0. *Geochim. Cosmochim. Acta*

Shaw, S. A. and Hendry M. J., in prep. Diffusive transport of sulfuric acid in clay between pH 1.0 and -3.0 *Appl. Geochem.*

Sidenko, N.V. and Sherriff, B.L., 2005. The attenuation of Ni, Zn and Cu, by secondary Fe phases of different crystallinity from surface and ground water of two sulfide mine tailings in Manitoba, Canada. *Appl. Geochem.* 20, 1180-1194.

Sracek, O., Choquette, M., Gelinas, P., Lefebvre, R. and Nicholson, R.V., 2004. Geochemical characterization of acid mine drainage from a waste rock pile, Mine Doyon, Quebec, Canada. *J. Contam. Hydro.* 69, 45-71.

Stumm, W. and Morgan, J. J. 1996. Aquatic Chemistry: Chemical equilibrium and rates in natural waters, 3rd ed. John Wiley & Sons, New York, 1022p.

van Bokhoven J. A., Sambe H., Ramaker D. E., and Koningsberger D. C., 1999. Al K-edge near-edge X-ray absorption fine structure (NEXAPS) study on the coordination structure of aluminum in minerals and Y zeolites. *J. Phys. Chem. B.* 103, 7557-7564.

Velbel, M. A. 1993. Constancy of silicate mineral weathering ratios between natural and experimental weathering: implications for hydrologic control of differences in absolute rate. *Chem. Geol.* 105, 89-99.

Weigel, C., Calas G., Cormier L., Galoisy, L., and Henderson, G. S., 2008. High resolution Al $L_{2,3}$-edge x-ray absorption near edge structure spectra of Al-containing crystals and glasses: coordination number and bonding information from edge components. *J. Phys. Condens. Matter.* 20, 135219.

White, A.F. and Brantley, S.L., 1995. Chemical weathering rates of silicate minerals: An overview. Chemical Weathering Rates of Silicate Minerals 31, 1-22.

White, A.F. and Brantley, S.L., 2003. The effect of time on the weathering of silicate minerals: why do weathering rates differ in the laboratory and field? *Chem. Geol.* 202, 479-506.

Yoon T. H., Johnson S. B., Benzerara K., Doyle C. S., Tyliszczak T., Shuh D. K., and Brown G. E., 2004. In-situ characterization of aluminum-containing mineral-microorganism aqueous suspensions using scanning transmission X-ray microscopy. *Langmuir* 20, 10361-10366.

Zou Z., Hu Y. F., Sham T. K., Huang H. H., Xu G. Q., Seet C. S., and Chan L., 1999. XAFS studies of Al/TiNx films on Si(100) at the Al K- and L_{-3},L_{-2}-edge. *J. Synchrotron Rad* 6, 524-525.

Zysset, M. and Schindler, P.W., 1996. The proton promoted dissolution kinetics of K-montmorillonite. *Geochim. Cosmochim. Acta* 60, 921-931.

2.0 GEOCHEMICAL AND MINERALOGICAL IMPACTS OF H2SO4 ON CLAYS BETWEEN PH 5.0 AND -3.0.

2.1 Abstract

Natural and constructed clay liners are routinely used to contain waste and wastewater. The impact of acidic solutions on the geochemistry and mineralogy of clays has been widely investigated in relation to acid mine drainage systems at pH > 1.0. The impact of sulfuric acid leachate characterized by pH < 1.0 and potentially negative pH values on the geochemistry and mineralogy of clays is, however, not clear. Thus, laboratory batch experiments were conducted on three natural clay samples with different mass ratios of smectite, illite and kaolinite to investigate the impact of sulfuric acid on the geochemistry and mineralogy of aluminosilicates from pH 5.0 to -3.0. Batch testing was conducted at seven pH treatments (5.0, 3.0, 1.0, 0.0, -1.0, -2.0 and -3.0) using standardized sulfuric acid solutions for four exposure periods (14, 90, 180, and 365 d). Aqueous geochemical and XRD analyses showed: increased dissolution of aluminosilicates with decreasing pH and increasing exposure period, that smectite ($[Na, Ca]_{0.3}[Al, Mg]_2SiO_4O_{10}[OH]_2$) was more susceptible to dissolution than illite ($[K, H_3O][Al, Mg, Fe]_2[Si, Al]_4O_{10}[OH]_2$) and kaolinite ($Al_2Si_2O_5[OH]_4$), precipitation of an amorphous silica phase occurred at $pH \leq 0.0$, and anhydrite precipitated in Ca-rich clays at pH≤ -1.0. In addition, global dissolution rates were calculated for the clays and showed good agreement to literature smectite, illite and kaolinite dissolution rates, which suggests global dissolution rates for complex clays could be determined from monomineralic studies. A stepwise conceptual model of the impact of sulfuric acid on aluminosilicate geochemistry and mineralogy between pH 5.0 and -3.0 is proposed.

2.2 Introduction

Interactions between acidic solutions and geologic media have been well studied in acid mine drainage (AMD) settings for over twenty years, in both field (e.g. Dubrovsky et al., 1985; Morin et al., 1988; Blowes and Jambor, 1990; Blowes and Ptacek, 1994; Al et al., 2000; Dold and Fontbote, 2002; Sracek et al., 2004; Brookfield et al., 2006) and laboratory (Schuring et al., 1997; Shaw et al., 1998; Kashir and Yanful, 2001; Jurjovec et al., 2002; Newbrough and Gammons, 2002; Acero et al., 2006) based

studies. AMD systems are characterized by the production of sulfuric acid (H_2SO_4) through the oxidation of sulfide minerals (Jambor, 1994). Blowes and Ptacek (1994) demonstrated the capacity of geologic media to buffer the acidity of AMD affected waters through a series of mineral dissolution reactions including; carbonates (pH 4.8 to 7.5), metal hydroxides (pH 4.3 to 3.5), and aluminosilicates (pH < 3.5).

Most AMD studies are characterized by pH values > 1.0 (e.g. Al et al., 2000; Blowes et al., 2003; Hammarstrom et al., 2003; Sidenko and Sherriff, 2005; Gunsinger et al., 2006), while few studies involve more acidic (pH < 1.0) conditions. These studies include those at Heath Steele, New Brunswick, Canada (pH $\geq$ 0.80; Blowes et al., 1991), Sherridon, Manitoba, Canada (pH $\geq$ 0.67; Moncur et al., 2005), and Iron Mountain, California (pH $\geq$ -3.6; Nordstrom et al., 2000). Observations by Moncur et al. (2005) indicate the complete dissolution of carbonates and metal hydroxides, the near depletion of some aluminosilicates (biotite, chlorite, and smectite), and depletion of more stable aluminosilicates (albite, cordierite, and amphibole). Nordstrom and Alpers (1999) note the occurrence of large deposits of hydrated Fe and Al sulfates in the extremely acidic conditions at Iron Mountain including; melanterite ($Fe^{II}SO_4 \bullet 7H_2O$), romerite ($Fe^{II}Fe^{III}_2[SO_4]_4 \bullet 14H_2O$), rhomboclase ($H_3OFe^{III}[SO_4]_2 \bullet 3H_2O$), and halotrichite-bilinite ($Fe^{II}[Al,Fe^{III}]_2[SO_4]_4 \bullet 22H_2O$). However, overall the geochemical and mineralogical interactions between H_2SO_4 solutions with pH < 1.0 and clays are not understood.

Low pH measurements (pH < 1.0) characterize H_2SO_4-rich leachate from zero-valent sulfur (S^0) that is recovered as a by-product of oil and gas production. The recovered S^0 is typically stored in large, above-ground, blocks that are susceptible to the ingress of atmospheric oxygen and atmospheric precipitation, resulting in the production of H_2SO_4. Long-term storage requirements (circa 500 years) have led to the consideration of developing below-ground storage strategies, in part to mitigate the production of acidic leachate. However, production of leachate within these storage environments could potentially be characterized by even greater concentrations of H_2SO_4 and negative pH values, due to a decrease in the amount of dilution by precipitation.

The goal of this study is to understand the geochemical interactions that occur between clays typically used as liner material in mine settings and H_2SO_4 solutions between pH 5.0 and -3.0. The specific objectives of this study are to: (i) determine the

mineralogical alteration of clays exposed to H_2SO_4 solutions between pH 5.0 and -3.0; (ii) determine the aqueous geochemistry of the major elemental constituents (Al, Ca, Si and SO_4) resulting from these interactions and, (iii) determine the general geochemical reaction mechanisms and global dissolution rates associated with these interactions. To address these objectives, three mineralogically distinct clays, typically used for natural liners and covers in mining applications, were selected for study. Results of this study should be applicable to a wide range of clay types. These objectives were met using a series of constant pH batch experiments conducted over several exposure periods for each clay sample.

2.3 Materials and methods

2.3.1 Clay samples

The three clay samples tested were: the Cretaceous Clearwater (Kc), Cretaceous McMurray (Km) and Barakade 90 (BK). The Kc and Km clays were obtained from the Syncrude Canada Limited (SCL) Mildred Lake mine site, located 60 km north of Fort McMurray, Alberta, Canada and the BK clay was obtained from BPM Minerals LLC in northern Wyoming, USA. The Kc and Km clays are from the Mannville Group, a Cretaceous deposit that overlays much of the Western Canadian Sedimentary Basin. The Kc clay comprises the constructed containment liner beneath the SCL above ground S^0 storage blocks, while the Km has been considered for use in liner construction. The BK sample is a powdered Wyoming sodium-bentonite typically used as a backfill for slurry walls, a mixture component of seepage barriers and containment liners and as a grout material (Mitchell, 1993).

2.3.2 Clay characterization

Mineralogy of the whole rock (< 63 μm) and clay size (< 2 μm) fractions for each sample were determined by X-ray diffraction (XRD) using Ni-filtered Cu K-α radiation at 1.6 KVA from a FR-580 Enraf-Nonius X-ray generator. Expandable clays were identified by solvating samples with ethylene glycol (Moore and Reynolds, 1989).

Whole-rock Al and Ca masses were determined by total digestion using HCl/HNO_3 microwave digestion followed by quantification using inductively-coupled

plasma mass spectroscopy (ICP-MS, Perkin Elmer Elan 5000); with an average sample replicate precision of ± 1.9 % (rsd). This method did not allow for quantification of the total Si concentration due to evaporative losses in the digestion process.

Sequential extractions were conducted on the whole-rock samples, in triplicate, to determine percentage of Al and Ca partitioned between; i) the water soluble and exchangeable fractions (Tessier et al., 1979), the carbonate bound fraction (Tessier et al., 1979), the Fe hydroxide fraction (Hall et al., 1996), organic bound fraction (Tessier et al., 1979), and residual fraction (Hall et al., 1996). Extractions were conducted by homogenizing the bulk sample, collecting a 1.0 g aliquot into a HDPE vial, and adding the prescribed amount of extraction solution. At the end of each extraction, the vials were centrifuged (10-15 minutes; 3000 g) to separate the liquid and solid phases. When specified the solid residue was rinsed with a 10 mL aliquot of nanopure water, centrifuged (10 min; 3000 g), and the recovered rinse solution was added to the extract solution. The solid phase was reserved for the next extraction and the liquid phase was filtered through a 0.45 µm cellulose-nitrate membrane, pre-conditioned with 10 mL of nanopure water, collected into a 20 mL HDPE bottle, acidified with ultra-pure H_2SO_4 (5 % v/v), and then refrigerated (4°C). Inductively-coupled atomic emission spectroscopy (ICP-AES, Spectro Cirros, CDD) was used to quantify a full suite of cations. However, only Al concentrations, with an average sample replicate precision of ± 1.9 % (rsd), are discussed in this study. Ca was determined using atomic adsorption spectroscopy (AAS, Varian X5) which had an average sample replicate precision of ± 1.7 % (rsd).

Cation exchange capacity (CEC) was determined for the whole-rock fraction of each clay using the method of Hendershot and Duquette (1986). The concentrations of Ca, Mg, Na and K were determined by atomic adsorption spectroscopy (AAS, Varian X5) with an average sample replicate precision of ± 1.7 % (rsd).

The surface areas of the whole-rock Kc, Km, and BK samples were determined by evaluating one-point nitrogen adsorption data according to the BET-equation. Measurements were made using an accelerated surface area and porosimetry analyzer (Model ASAP 2000, Micromeritics Instrument Corp.).

2.3.3 Batch experiments

The Kc, Km, and BK batch experiments each consisted of seven constant pH treatments (5.0, 3.0, 1.0, 0.0, -1.0, -2.0 and -3.0). Solutions were standardized using anhydrous Na_2CO_3 as a primary standard, accounting for density differences, and pH values were determined using the method of Nordstrom et al. (2000). Batch experiments were conducted over exposure periods of 14, 90, 180, and 365 days (d). The pH was attained and maintained using standardized H_2SO_4 or NaOH solutions as required. All batch experiments for the 14 d exposure period were conducted in duplicate to address variability in the method; no duplicate samples were analyzed for the other exposure periods.

For all batch experiments, 5 g of the homogenized whole-rock sample and 100 g of standardized H_2SO_4 solution were added to a 125 mL Erlenmeyer flask and covered with perforated Parafilm to minimize evaporative losses. Sample blanks for each pH treatment were conducted in an identical manner, omitting the addition of clay. Each clay slurry was hand shaken daily for one minute over the duration of the experiments. Batch experiments were conducted at room temperature (22 to 25°C).

The pH of each clay slurry was measured daily using an Orion glass combination electrode (Model 9102BN) and was adjusted with a measured mass of standardized H_2SO_4 solution, until no further change was recorded in 24 hours, after which time pH measurements were taken on a weekly basis. The pH electrode was calibrated with pH 7.00, 4.00 and 1.00 buffers for samples with pH > 1.0. Samples with a pH < 1.0 were calibrated using the method described by Nordstrom et al. (2000), which had an average standard deviation of ±0.2 pH units. Determinations of Eh were made using a Cole-Parmer platinum ORP electrode (Model 05990-55) and electrode accuracy was checked with *Zobell's* solution (Nordstrom, 1977).

At the end of each exposure period, the clay slurries were transferred into HDPE vials and centrifuged (10-15 minutes; 3000 g) to separate the liquid and solid phases, which were subsequently stored for analyses. Mass balance calculations indicated that between three and five percent by weight (wt %) of clay slurry was lost from each flask over the duration of the batch experiments. This loss was attributed to clay slurry being retained on the electrodes after each measurement and not from evaporation. It was,

therefore, assumed that the geochemical composition of the remaining clay slurry was not altered.

2.3.4 Aqueous geochemistry

Solutions from the batch testing were filtered through 0.45 µm cellulose-nitrate membranes, pre-conditioned with 10mL aliquots of nanopure water (approximately 17.5 µS/cm), and collected into separate bottles for cation (125 mL HDPE) and anion (20 mL HDPE) analyses, acidified with ultra-pure H_2SO_4 (5 % v/v, cations only) when required, and refrigerated at approximately 4°C prior to analyses. Samples were diluted by weight when required (due to an instrument limitation on the allowable matrix acidity) prior to analyses using nanopure water. Samples were analyzed for a full suite of cations and anions (Al, Ba, Be, B, Ca, Cd, Cr, Co, Cu, Fe, K, Pb, Mg, Mn, Mo, Na, Ni, P, Si, Ag, Sr, Ti, V, Zn, Zr, Cl, NO_3, and SO_4); however, only the major constituents pertinent to the current study are discussed. These included; Al, Ca, Si, and SO_4. Inductively-coupled plasma atomic emission spectroscopy (ICP-AES, Spectro Cirros, CDD) was used to quantify Al and Si concentrations, which had an average sample replicate precision of ± 1.9 % (rsd). Ca was determined using atomic adsorption spectroscopy (AAS, Varian X5); with an average sample replicate precision of ± 1.7 % (rsd). Anion samples were analyzed for SO_4 using ion chromatography (IC, Dionex IC25/DX-320) with an average sample replicate precision of ± 3.4 % (rsd).

2.3.5 Geochemical modeling

Geochemical speciation calculations were conducted on the analytical results of the liquid phase samples for pH treatments $\geq$ 0.0 (I < 1.7M) using the equilibrium geochemical speciation program PHREEQC (version 2.15, Parkhurst and Appelo, 1999). The thermodynamic database MINTEQ (Allison et al., 1991) was used with this program. The illite solid phase thermodynamic data from the PHREEQC thermodynamic database was added to the MINTEQ database because it was absent from the original database. Speciation calculations for sample pH treatments < 0.0 (I > 1.7M) were not conducted, as convergence to a solution could not be achieved using available thermodynamic databases. Although the PHRQPITZ thermodynamic database (Plummer et al., 1988),

present in PHREEQC, was developed specifically for high ionic strength solutions and has been modified for use in AMD case studies (Ptacek and Blowes, 2000) it lacked the requisite thermodynamic datasets for Si and Al, the dominant dissolved ions measured in this study. The authors understand that PHREEQC and the MINTEQ database are not structured to be compatible with the high ionic strength solutions considered in this study and they have been employed to approximate the geochemical speciation in these solutions for qualitative purposes only.

2.3.6 Solid phase mineralogy

Mineral identification in the Kc, Km, and BK samples recovered from each batch experiment was accomplished using Ni-filtered Cu K-α radiation at 1.6 KVA with a Sol-X energy dispersive X-ray detector (Bruker AXS D8-Advance). All Kc and BK samples were solvated with ethylene glycol prior to analysis because they contained expandable mineral phases (Moore and Reynolds, 1989). Expandable minerals were not present in the Km samples. All reported angular notations are referred to in degrees 2-theta.

2.3.7 Global dissolution rates

The dissolution reaction of the Kc, Km, and BK clays exposed to H_2SO_4 solutions may be presented as (Qafoku et al., 2004):

$$clay\ (smectite,\ illite,\ kaolinite,\ etc...) + H^+ + SO_4 \rightarrow Al + Si + Fe + Ca \ldots \quad [3.1]$$

As clays are comprised of several mineral phases, the global dissolution and precipitation rates, calculated from the release and uptake of Al and Si from the aqueous phases, can be presented as the sum of the rate expressions representing the rates for individual mineralogical phases (Qafoku et al., 2004). For example, the release rate of Si may be written as:

$$\begin{aligned}\frac{\delta Si}{\delta t} = &(k_{H_3O^+-quartz}\left[H_3O^+\right]^a + k_{SO_4-quartz}\left[SO_4\right]^b) + \\ &(k_{H_3O^+-smectite}\left[H_3O^+\right]^a + k_{SO_4-smectite}\left[SO_4\right]^b) + \\ &(k_{H_3O^+-kaolinite}\left[H_3O^+\right]^a + k_{SO_4-kaolinite}\left[SO_4\right]^b) + \ldots\end{aligned} \quad [3.2]$$

The dissolved Al and Si concentrations in each batch experiment and the constant pH conditions in each treatment were combined to calculate the global Al (R_{Al}) and Si (R_{Si}) dissolution rates for each of the three clays (after Zysset and Schindler, 1996):

$$R_{Al/Si} = \frac{d[X]}{dtA} = \{[X]_{t=1} - [X]_{t=0}\} / dtA \qquad [3.3]$$

In [3.3], *dt* is the length of the exposure period (s), $[X]_{t=1}$ is the dissolved Al or Si mass (mol g^{-1}) normalized to the initial mass of clay placed in the flask and accounting for solution density, *A* is the BET surface area of the whole-rock sample (m^2 g^{-1}), and $[X]_{t=0}$ is the initial dissolved Al or Si concentration (mol L^{-1} g^{-1}), which are equal to 7.7 x 10^{-3} and 8.1 x 10^{-3} mol L^{-1} in each batch experiment. The aqueous concentration of Al and Si measured at the end of each exposure period was used to determine the mass in the aqueous phase. Therefore, these values represented the difference between the masses of Al and Si released into solution due to mineral dissolution and surface desorption reactions and the masses removed due to secondary mineral precipitation and absorption reactions and can be considered as the global dissolution rates.

If the dissolution reaction is far from equilibrium, the pH dependence of the global reaction rate of proton promoted dissolution of the clay can be described by the rate law (Zysset and Schindler, 1996):

$$R = k\,[H^+]^n \qquad [3.4]$$

where *R* is the global dissolution rate (mol m^{-2} s^{-1}), *k* is the reaction constant, $[H^+]$ is the proton activity (mol L^{-1}) and *n* is the reaction order. This equation can be transformed into:

$$\log R = \log k - n\,pH \qquad [3.5]$$

from which the reaction order, or pH dependence, can be determined from a plot of log global dissolution rate versus pH, where the slope of the straight line is equal to *n* in [3.5].

2.4 Results

2.4.1 Characterization of unaltered clays

X-ray diffraction analyses showed that the Kc whole rock mineralogy (Table 2.1) was dominated by quartz, with substantial amounts of illite, kaolinite, plagioclase, and

dolomite. Analyses of the clay fraction, which accounted for 40 wt % of the Kc sample, indicated near equal percentages of smectite, illite and kaolinite (Table 2.1). Strong peaks for smectite, illite, kaolinite, quartz, plagioclase, and dolomite were evident in the diffractograms of the unaltered and glycolated whole rock sample (Fig. 2.1a). Strong secondary peaks for illite, quartz, kaolinite, and plagioclase were also observed (Fig. 2.1a).

Total digestion of the unaltered Kc yielded Al and Ca concentrations of 2.8 x 10^3 and 4.1 x 10^2 μmol g^{-1}. Sequential extraction results suggested that the majority of solid phase Al was present in the residual fraction, while Ca was predominantly in the Fe-hydroxide/organic fraction (Table 2.1). The CEC and surface area were 28.5 meq 100 g^{-1} and 40 m^2 g^{-1} (Table 2.1).

Table 2.1. Mineralogical content of Kc, Km and BK whole rock (< 63 μm) and clay (< 2 μm) fractions, determined by semi-quantitative XRD methods.

Mineral Phase	Composition (weight %)					
	Kc		Km		BK	
	< 63μm	*< 2μm*	*< 63μm*	*< 2μm*	*< 63μm*	*< 2μm*
Quartz	54	18	30	5	4	4
Smectite	2	23	0	1	79	79
Kaolinite	12	22	43	61	0	0
Illite	10	29	20	29	0	0
Plagioclase	11	0	1	1	5	5
Chlorite	3	8	1	2	0	0
Cristobalite	0	0	0	0	12	12
Dolomite	9	0	0	0	0	0
Siderite	0	0	4	3	0	0
CEC (meq 100 g^{-1})	28.5		20.3		83.0	
BET (m^2 g^{-1})	29.3		22.9		28.1	

(W = Ca, Na, H; X = Al, Mg, Fe, Zn; Y = K, H; Z = Al, Fe, Li, Mg)

Unaltered Km whole rock mineralogy was dominated by kaolinite, with considerable amounts of quartz and illite, and a minor amount of siderite (Table 2.1). Analysis of the clay fraction, which represented approximately 25 wt % of the clay, indicated amounts of illite and kaolinite and no smectite (Table 2.1). The whole-rock sample was characterized by dominant illite, kaolinite, quartz, and siderite peaks (Figure 2.1b), with secondary illite, quartz and kaolinite peaks also present (Fig. 2.1b).

Total digestion of the unaltered Km yielded Al and Ca concentrations of 2.5 x 10^3 and 3.9 x 10^1 μmol g^{-1}. Sequential extraction results indicated that, similar to the Kc sample, Al was mostly in the residual fraction, while the majority of Ca was in the Fe-hydroxide/organic fraction (Table 2.2). The CEC and surface area were 20.3 meq $100g^{-1}$ and 25 m^2 g^{-1} (Table 2.1).

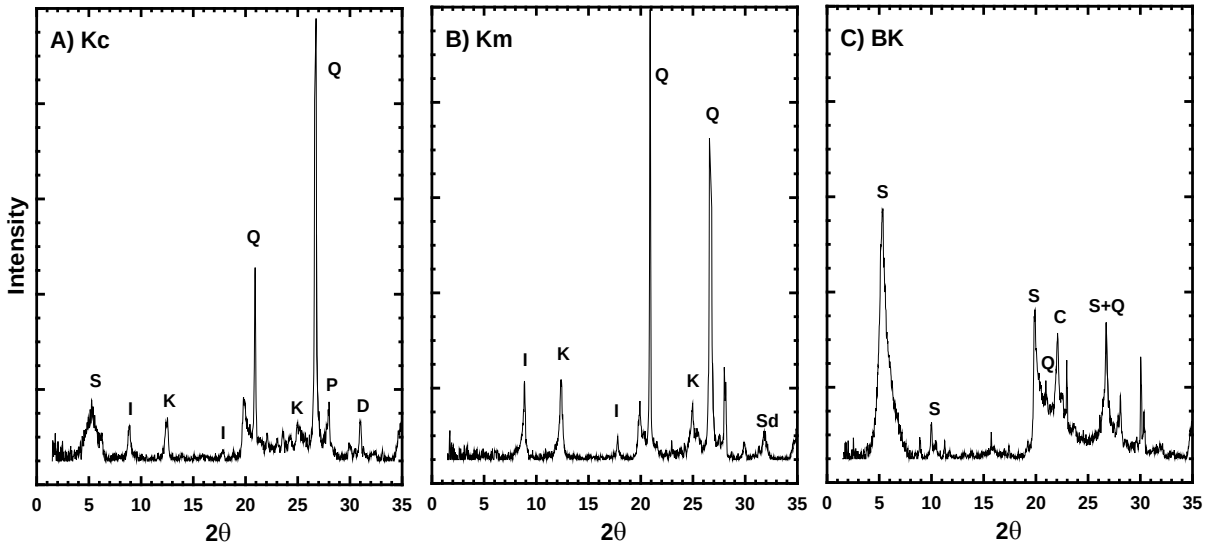

Figure 2.1. XRD diffractograms of the unaltered whole rock Kc (A), Km (B) and BK (C) samples, where Q = quartz, S = smectite, K = kaolinite, I = illite, D = dolomite, P = plagioclase, Sd = siderite and C = cristobalite. All Kc and BK scans represent glycolated samples.

The mineral distributions in the clay-size fraction are equivalent to those in the whole rock fraction for the BK sample (Table 2.1). Smectite is the most abundant mineral phase, with lesser amounts of cristobalite, plagioclase and quartz. Unaltered BK demonstrated strong peaks for smectite, cristobalite, and a dual smectite-quartz, with secondary peaks for smectite and quartz in glycolated samples (Fig. 2.1c). In addition, a peak at 8.9° was attributed to the presence of a small amount of illite.

Total digestion of unaltered BK yielded total Al and Ca concentrations of 4.4 x 10^3 and 3.5 x 10^2 μmol g^{-1}. Sequential extraction results demonstrated that Al and Ca content were predominantly partitioned in the residual fraction (Table 2.2). The CEC and surface area were 83.0 meq 100 g^{-1} and 60 m^2 g^{-1} (Table 2.1).

Table 2.2. Sequential extraction results for the Kc, Km and BK samples. Fractions include 1) exchangeable; 2) carbonate bound; 3) Fe hydroxide/organic bound; and 4) residual (aluminosilicates)

Clay Media	Element	Fraction (weight %)			
		Exchangeable	Carbonate	Fe-hydroxide/ Organic	Residual
Kc	**Al**	0.02	0.00	3.78	96.2
	Ca	11.9	31.1	45.9	11.1
Km	**Al**	0.08	0.02	1.00	98.9
	Ca	22.8	6.40	66.5	4.24
BK	**Al**	0.06	0.16	2.10	97.7
	Ca	18.9	29.3	11.9	39.9

2.4.2 Aqueous geochemistry

2.4.2.1 Al

Dissolved Al concentrations in the Kc, Km, and BK batch experiments increased with decreasing pH and increasing exposure period (Fig. 2.2a-c). Between 14 d and 365 d, the concentration of Al in the Kc, Km, and BK experiments ranged from 5.5×10^{-6} to 2.0×10^{-2}, 3.2×10^{-7} to 1.5×10^{-2} and 7.9×10^{-8} to 2.3×10^{-2} mol L^{-1} g^{-1}, respectively. These concentrations correspond to the mobilization of a maximum of 59, 49, and 43 wt % Al, respectively (Fig. 2.3a-c). Speciation calculations predicted that the aqueous solutions for Kc, Km, and BK were saturated with respect to montmorillonite (SI = 0.8 to 5.3) in the 5.0 pH treatments and undersaturated (SI = -21 to -4.0) in the 0.0 to 3.0 pH treatments. Speciation calculations also predicted supersaturation with respect to kaolinite (SI = 2.9 to 6.2) in the 5.0 pH treatments and undersaturation (SI = -18 to -1.7) between the 0.0 and 3.0 pH treatments in the Kc, Km, and BK batch experiments. Further, calculations suggested slight undersaturation to slight supersaturation with respect to illite in the Kc 5.0 pH treatment (SI = -0.2 to 0.7) and undersaturation in the remaining Kc, Km, and BK treatments (SI = -0.4 to -32).

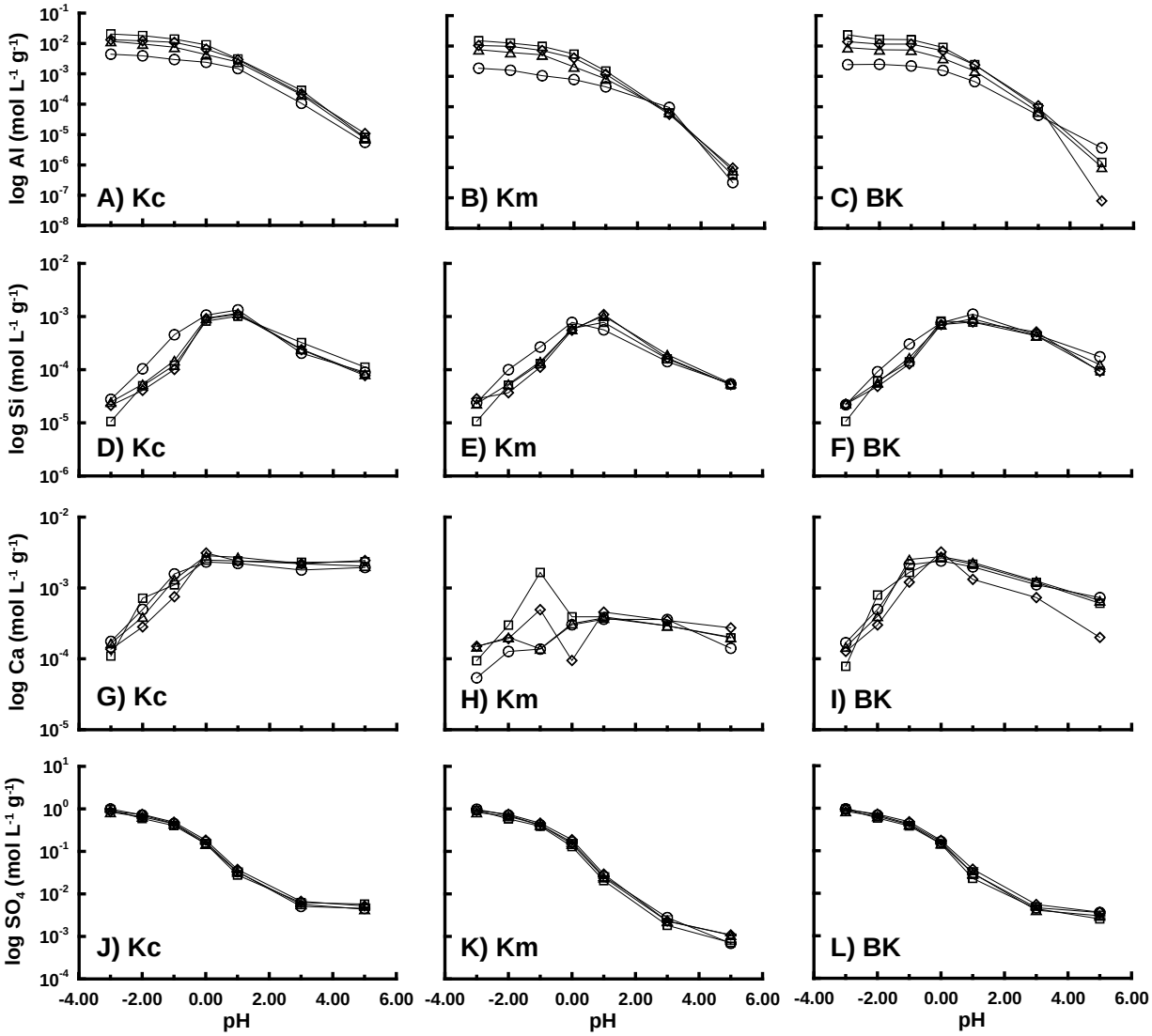

Figure 2.2. Aqueous phase Al (A-C), Si (D-F), Ca (G-I) and SO_4 (J-L) concentrations (mol L^{-1} g^{-1}) for the 14d (○), 90d (△), 180d (◇) and 365d (□) exposure periods in the Kc (left), Km (center) and BK (right) batch experiments. Error bars (one standard deviation) for all measured parameters are smaller than the plotted symbols.

2.4.2.2 Si

Dissolved Si concentrations increased with decreasing pH to peak values in the 1.0 pH treatments for each exposure period in the Kc, Km, and BK batch experiments. An exception occurred for the Km 14 d and BK 365 d exposure periods, which both peaked in the 0.0 pH treatments (Fig. 2.2d-f). Subsequently, Si concentrations decreased to minimum concentrations between pH 1.0 and -3.0 for all three batch experiments. Speciation calculations indicated saturation to supersaturation with respect to both quartz

(SI = 0.4 to 2.0) and cristobalite (SI = 0.0 to 1.6) for all of the Kc, Km, and BK aqueous solutions. Speciation calculations also suggested that the aqueous solutions of all four exposure periods in the Kc, Km, and BK experiments were saturated to supersaturated with respect amorphous silica (SI = 0.1 to 0.7) for the pH 1.0 and 0.0 treatments and slightly undersaturated (SI = -0.8 to -0.1) for the pH 5.0 and 3.0 treatments.

2.4.2.3 Ca

In the Kc batch experiments, dissolved Ca concentrations increased slightly with decreasing pH, attaining maximum values between the 5.0 and 0.0 pH treatments, in the 14, 90, 180, and 365 d exposure periods (Fig. 2.2g). Subsequently, concentrations decreased, with decreasing pH, to minimum values in the -3.0 pH treatments. Dissolved Ca concentrations in the Km batch experiments initially increased to maximum values between pH 5.0 and 1.0 and subsequently decreased to minimum concentrations in the -3.0 pH treatments, for each exposure period (Fig. 2.2h). However, unlike the Kc batch experiments, the trend in measured concentrations was not consistent for all four exposure periods, with minimum and maximum values of 5.4×10^{-5} (14 d; -3.0 pH) and 1.6×10^{-3} mol L^{-1} g^{-1} (365 d; -1.0 pH) (Fig. 2.2g). The aqueous Ca concentrations in the BK batch experiments also increased between pH 5.0 and 0.0, with peak concentrations observed in the 0.0 pH treatment. Concentrations then decreased between pH 0.0 and -3.0 to minimum values in all four exposure periods (Fig. 2.2i).

The measured aqueous concentrations equate to a maximum mobilization of Ca into the aqueous phase of between 55 and 75 wt % and a minimum mobilization of < 3 wt % for the Kc batch experiments (Fig. 2.3d). The percentage of Ca mobilized to the Km aqueous phases varied from 11 to 100 wt %, generally increasing in value between pH 5.0 and 1.0 and then decreasing between pH 1.0 and -3.0 for each exposure period (Fig. 2.3e). The percentage of mobilized Ca in the BK batch experiments increases between pH 5.0 and 0.0, with maximum values between 64 and 81 wt %, and decreases between pH 0.0 and -3.0, for all four exposure periods (Fig. 2.3f).

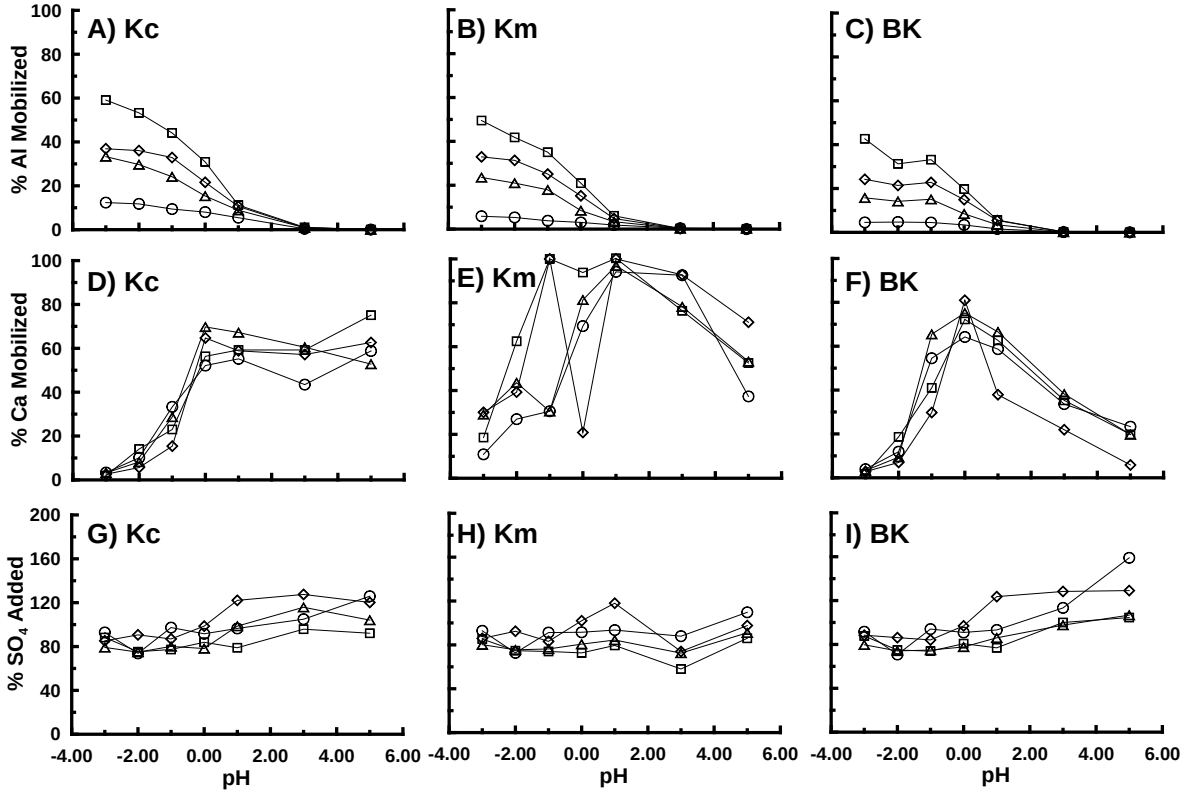

Figure 2.3. Percent of Al and Ca mass mobilized (wt %) and mass percent of added SO_4 mobilized to the aqueous phase in the Kc (A, D), Km (B, E) and BK (C, F) batch experiments, for the 14d (○), 90d (△), 180d (◇) and 365d (□) exposure periods. SO_4 values represent the amount initially added to each respective batch experiment.

2.4.2.4 SO_4

In all three batch experiments, dissolved SO_4 concentrations increased with decreasing treatment pH for all four exposure periods. Concentrations ranged from 4.3 x 10^{-3} to 1.0, 6.9 x 10^{-4} to 9.8 x 10^{-1} and 2.5 x 10^{-3} mol L^{-1} g^{-1} to 9.7 x 10^{-1} mol L^{-1} g^{-1} in the Kc, Km, and BK aqueous phases, respectively (Fig. 2.3j-l). These concentrations corresponded to between 75 to 128 wt %, 58 to 110 wt %, and 71 to 159 wt % of the total SO_4 added to the Kc, Km, and BK batch experiments, respectively, where the aqueous phase wt % generally decreased with decreasing pH (Fig 2.3g-i). Speciation calculations indicated gypsum (SI = 0.1 to 0.4) and anhydrite (SI = -0.1 to 0.2) were in a state of near equilibrium in the Kc batch experiments. Conversely, speciation calculation results indicate that the aqueous phase was undersaturated with respect to both gypsum (SI = -0.5 to -1.3) and anhydrite (SI = -0.7 to -1.5) throughout the Km batch experiments.

Finally, speciation calculations indicate slight undersaturation to saturation with respect to gypsum (SI = -1.0 to 0.0) in the 5.0 and 3.0 pH treatments and saturated to supersaturated conditions in the 1.0 and 0.0 pH treatments (SI = 0.0 to 0.4), for each exposure period. Conversely, calculation results for anhydrite (SI = -1.2 to 0.0) demonstrate slightly undersaturated to saturated conditions prevailed between the 5.0 and 1.0 pH treatments, while a state of saturation to slight supersaturation existed for the 0.0 pH treatments (SI = 0.0 to 0.2), for all four exposure periods.

2.4.3 Mineralogical changes as a function of pH

2.4.3.1 Kc clay

The intensity of the main Kc smectite peak (5.3°) decreased between the unaltered and 1.0 pH treatment, and was not observed in any of the lower pH treatments following all four exposure periods (Fig. 2.4). The primary illite and kaolinite peaks decreased in intensity with decreasing pH and, unlike smectite, persisted even at the most extreme conditions examined (365 d; -3.0 pH). A comparison of the primary illite and kaolinite peaks (Fig. 2.4) suggested that kaolinite decreased to a greater extent than illite between pH 1.0 and -1.0. The intensities of the peak for quartz appeared relatively unchanged during the entire Kc batch experiment (Fig. 2.4). Further, a broad band of background intensity, which increased with decreasing pH, developed between 18° and 30° in pH treatments $\leq$ 0.0 for each exposure period (Fig. 2.4). Two distinct peaks (25.5° and 31.4°; Fig. 2.4) were observed for pH -1.0 and -3.0 for each exposure period. These were attributed to the presence of anhydrite in the altered Kc solid phase. An unidentified peak (9.8°) was observed in each -3.0 pH treatment (Fig. 2.4). The peak associated with dolomite decreased below background intensity levels at pH treatments$\leq$ 5.0 in each of the examined exposure periods (data not shown). Conversely, the primary plagioclase peak remained unchanged for all pH treatments and exposure periods while the intensity of the secondary plagioclase peak increased with both increasing exposure period and decreasing pH.

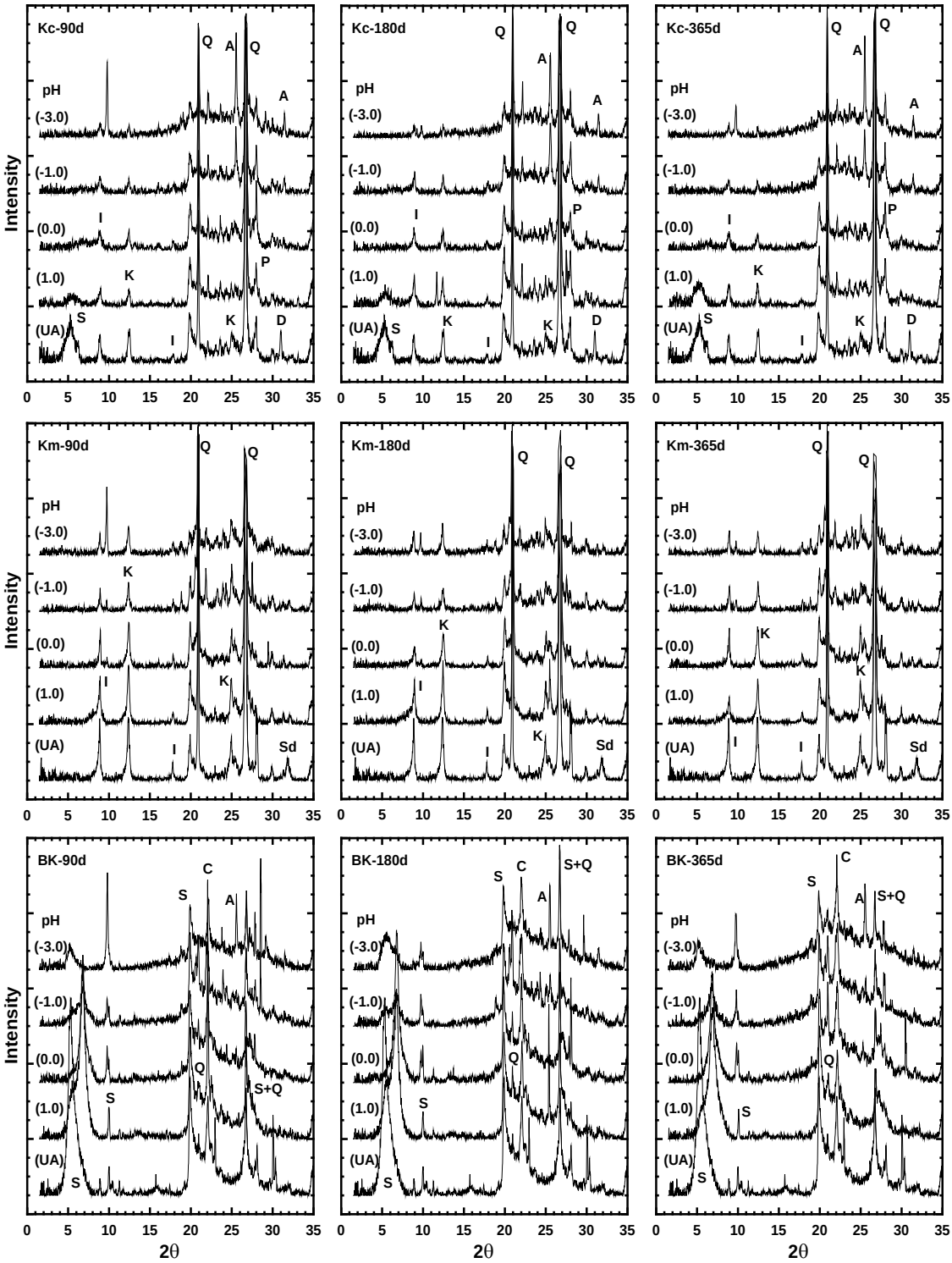

Figure 2.4. XRD diffractograms of unaltered, 1.0, 0.0, -1.0 and -3.0 pH treatments for the Kc, Km and BK clay media samples in the 90, 180 and 365d exposure periods, where Q = quartz, S = smectite, K = kaolinite, I = illite, D = dolomite, P = plagioclase, Sd = siderite, C = cristobalite and A = anhydrite. All Kc and BK scans represent glycolated samples.

2.4.3.2 Km clay

As was the case for the XRD results for the Kc samples, illite and kaolinite peak intensities decreased with decreasing treatment pH, indicating the progressive dissolution of both mineral phases in the Km batch experiments (Fig. 2.4). In contrast to the Kc results, the preferential dissolution of kaolinite over illite was not clearly evident, possibly due to the large wt % of kaolinite in the unaltered Km clay. A band of intensity between 18° and 30°, which increased with increasing exposure period and decreasing pH, was also observed in the Km diffractograms. The intensities of these bands were less than those observed in the Kc diffractograms (Fig. 2.4). The peak associated with siderite declined below background intensity levels in the 5.0 pH treatment of all four exposure periods (data not shown). Three unidentified peaks (9.8°, 18.8°, and 21.9°) were observed in the -1.0 and -3.0 pH diffractograms for each exposure period (Fig. 2.4).

2.4.3.3 BK clay

The smectite basal peak (5.3°) intensity for BK decreased between the unaltered and 1.0 pH diffractograms for each successively lower pH treatment (Fig. 2.4). The basal peak shifted from 5.3° to approximately 6.8° between the 1.0 and -1.0 pH treatments in the 90, 180, and 365 d experiments (Fig. 2.4). A minor shoulder, centered at approximately 5.3°, was also evident in each of the 1.0 and -1.0 pH treatments. Further, the secondary smectite peak at 26.6° decreased with decreasing treatment pH, while the 10.0° peak intensity remained relatively unchanged between the 1.0 and -1.0 pH treatments and increased in the -3.0 pH treatment diffractograms for each exposure period (Fig. 2.4). Similar to the results observed in the Kc and Km batch experiments, the intensity of the quartz (21.0°) and cristobalite (22.0°) peaks remained relatively unaltered in each BK batch experiment (Fig. 2.3) and an increasingly intense band, between 18 and 30°, was observed with decreasing pH and increasing exposure time (Fig. 2.4). A distinct peak at 25.5° was observed in the pH -1.0 and -3.0 diffractograms for the 180 and 365 d exposure periods. These peaks were attributed to the presence of anhydrite (Fig. 2.3). As was the case for the Km results, an unidentified peak was observed at 18.9° in the -1.0 and -3.0 pH treatments of the 90, 180, and 365 d exposure periods, respectively (Fig. 2.4). In addition, an unidentified peak (9.8°) was observed to overlap with the secondary

smectite peak (10.0°) in the pH 0.0, -1.0, and -3.0 diffractograms, for each exposure period (Fig. 2.4).

2.4.4 Global dissolution rates

The R_{Al} in each exposure period of the Kc, Km, and BK batch experiments were estimated using [3.3] and plotted as log R_{Al} vs. pH (Fig. 2.5a-c). The R_{Al} increased with decreasing pH and decreased with increasing exposure period in all three batch experiments. Further, these data suggested two distinct linear relationships between R_{Al} and pH, typically ranging from pH 5.0 to 0.0 and pH 0.0 to -3.0, for all three batch experiments. Reaction orders were obtained by fitting a straight line to the log R_{Al} versus pH plot over both regions for the Kc (n = 1.20 to 1.33; 0.15 to 0.25), Km (n = 1.50 to 1.81; 0.24 to 0.33) and BK (n = 1.17 to 1.72; 0.09 to 0.21) batch experiments, respectively.

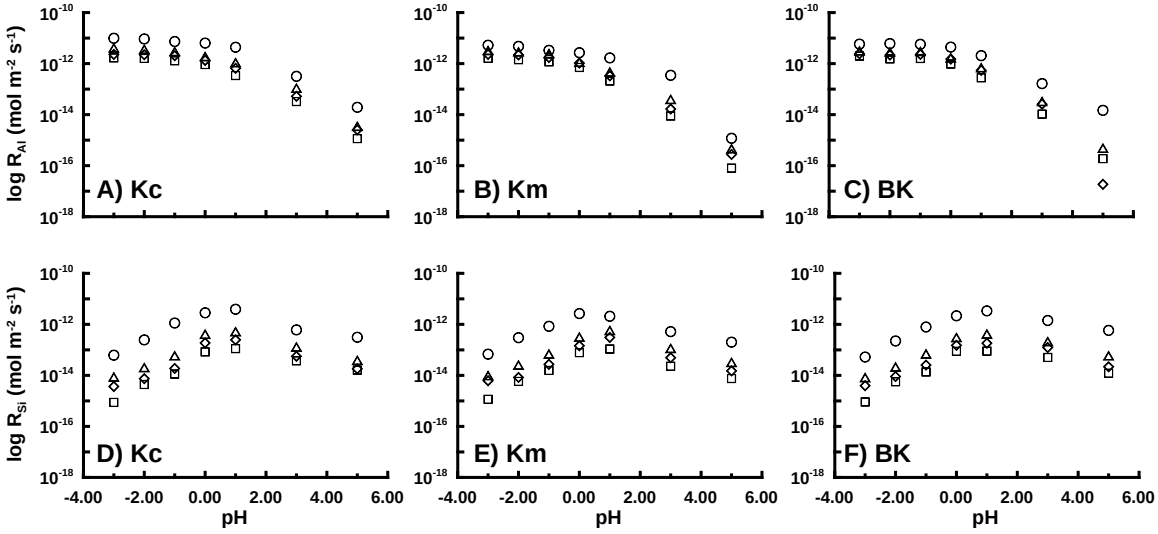

Figure 2.5. Calculated log apparent global dissolution rates (mol m^{-2} s^{-1}) for Al (R_{Al}) and Si (R_{Si}) for the 14d (○), 90d (△), 180d (◇) and 365d (□) exposure periods in the Kc (A, D), Km (B, E) and BK (C, F) batch experiments.

The R_{Si} values were estimated using [3.3] for each exposure period in all three batch experiments (Fig. 2.5d-f). For each exposure period, the R_{Si} steadily increased between pH 5.0 and 1.0 and then decreased between pH 1.0 and -3.0. Moreover, R_{Si} decreased with increasing exposure period in all three batch experiments. Reaction orders

were determined by linear regression for the two linear regions for the Kc (n = 0.49 to 0.65; -1.07 to -1.27), Km (n = 0.58 to 0.76; -0.90 to -1.17) and BK (n = 0.44 to 0.53; -1.05 to -1.19) batch experiments, respectively.

2.5 Discussion

2.5.1 Mineral dissolution

Most of the Al was sequestered in the residual fractions of the Kc, Km, and BK samples, suggesting that the majority of the total Al was bound within the aluminosilicate framework, which is consistent with the work of Tessier et al. (1979). Moreover, the observed decrease in the peak intensities of smectite, illite and kaolinite with decreasing pH in the Kc, Km, and BK diffractograms (Fig. 2.4) and the considerable increases in dissolved Al concentrations with decreasing pH (Fig. 2.2a-c) indicated the dissolution of aluminosilicates from all three samples with decreasing pH.

The decrease in peak intensities and shift in peak positions observed in the Kc, Km, and BK diffractograms suggested that smectite crystallinity was affected more than illite and kaolinite (Fig. 2.4). Jozefaciuk and Bowanko (2002) observed a similar trend in smectite, illite and kaolinite diffractograms after treatment with 0.1, 1.0 and 5.0 M HCl (pH = 1.0, 0.0 and -1.9). In addition, the observed shift of the primary smectite peak (5.3° to 6.8°) and persistence of the secondary peak (10.0°) suggested alteration of smectite structure between the 1.0 and -1.0 pH treatments for all exposure periods of the BK batch experiments (Fig. 2.4). However, the product of smectite alteration indicated in the BK diffractograms could not be identified from the available data.

The observed CEC and surface area measurements of the unaltered Kc, Km, and BK samples (Table 2.1) are consistent with the observation of Meunier (2005) that the relative magnitude of CEC and specific surface area of aluminosilicates follows smectite >> illite > kaolinite. Komadel et al. (1996) and Gates et al. (2002) observe that smectite is more susceptible to dissolution with decreasing pH through increased absorption of hydronium ions (H^+) on exchange sites and interaction over a larger surface area. These observations were consistent with the results of the current study. However, the mobilization of only 43 wt % of the BK solid phase Al and the persistence of smectite peaks in the BK diffractograms suggested that although a significant amount of smectite

underwent dissolution it was not completely removed during any of the four exposure periods. The preferential dissolution of kaolinite over illite that was observed between pH 1.0 and -1.0 in the Kc XRD results (Fig. 2.4) is consistent with the findings of Hradil and Hostomsky (2002). These authors noted a decrease in dissolution rates with increasing illite content in kaolinite samples. Therefore, these observations suggested that the dissolution of the main aluminosilicate phases in the batch experiments followed the order smectite >> kaolinite > illite in the current study.

Previous studies of pure phase aluminosilicate dissolution suggest that aqueous Si concentrations initially exceed Al values by an order of magnitude due to the preferential dissolution of fine-grained amorphous silica phases present as surface coatings or cementing layers (Zysset and Schindler, 1996; Brandt et al., 2003; Kohler et al., 2003; Metz et al., 2005; Amram and Ganor, 2005). A similar difference between measured aqueous Al and Si concentrations was observed in the pH 5.0 and 3.0 Kc, Km, and BK batch experiments (Fig. 2.2a-f) in the 5.0 and 3.0 pH treatments for each batch experiment. Additionally, although the Kc, Km, and BK samples contained large percentages of quartz, we assumed, based on previous studies (Barrios et al., 1995; Breen et al., 1997; Madejova et al., 1998; Belver et al., 2002; Komadel, 2003; Wu and Ming, 2006), that quartz remained relatively intact even in the most acidic (pH = -3.0, 5.3 M) treatments. As a result, the data suggested that the majority of the dissolved Si in each batch experiment was derived from the dissolution of aluminosilicates.

The decrease in aqueous Si concentrations and continued increase in dissolved Al concentration between pH 1.0 and -3.0 (Fig. 2.2a-f) in each batch experiment were similar to the trends described by Van Rompaey et al. (2002), who studied the dissolution of smectite in H_2SO_4 solutions between 0.1 and 1.0 M ($-0.1 < pH < 1.0$) over exposure periods from 1 to 8 hours. Therefore, as the majority of dissolved Si appears to have originated from aluminosilicate dissolution the decreased aqueous Si concentrations suggested precipitation of a Si-rich phase in each batch experiment. A Si-rich precipitate, expressed as a broad band of intensity between 18° and 30° in the Kc, Km, and BK diffractograms (Fig. 2.4), was observed at pH treatments ≤ 0.0. Qualitative comparison of the intensities of the band demonstrated that the relative amount of Si-rich precipitate formed in each batch experiment followed the trend BK > Kc >> Km. This trend

corresponded to the percentage of smectite in the unaltered Kc, Km, and BK samples and suggested that amorphous silica forms more readily from smectite-rich clays than illite and kaolinite-rich clays in systems with pH $\leq$ 0.0. Additionally, this trend corresponded to the increased susceptibility of smectite, relative to illite and kaolinite, to dissolution with decreasing pH, as previously discussed.

The formation of a Si-rich amorphous phase was noted in previous studies involving the progressive dissolution of aluminosilicates in HCl (0.2 to 8.0 M; pH 1.0 to -3.2) and H_2SO_4 (2.0 to 16 M; pH < -10 to -0.7) solutions (Mendioroz et al., 1987; Pesquera et al., 1992; Vincente et al., 1996; Madejova et al., 1998; Gates et al., 2002; Nguetnkam et al., 2005). Several studies conclude that at pH < 1.0 Al-octahedral layers preferentially dissolve leaving behind relatively unaffected Si-tetrahedral layers, which subsequently polymerize, forming a hydrous amorphous Si phase (Mendioroz et al., 1987; Pesquera et al., 1992; Gates et al., 2002; Belver et al., 2002; Komadel, 2003; Tyagi et al., 2006). Mendioroz et al. (1987) and Pesquera et al. (1992) observe the deposition of amorphous silica onto the residual smectite sample at HCl concentrations > 1 M (pH < 0.0), and note that the amount deposited increases with decreasing pH. These observations are consistent with the observed increased intensity amorphous silica measured in the Kc, Km, and BK diffractograms with decreasing pH in the current study (Fig. 2.4).

2.5.2 Global dissolution rates

Previous pure phase aluminosilicate dissolution studies show a general decrease in reaction rates with increasing exposure period (e.g. Kalinowski and Schweda, 1996; Hradil and Hostomsky, 2002; Brandt et al., 2003; Kohler et al., 2003; White and Brantley, 2003; Kohler et al., 2005). These findings supported the trends in calculated R_{Al} and R_{Si} values with increasing exposure period between pH 5.0 and 1.0 in the current study (Fig. 2.5a-f). White and Brantley (2003) suggest the decrease in dissolution rates with increasing time are a result of several intrinsic processes including: decreased surface area, depletion of reactive sites and precipitation of secondary products and extrinsic processes resulting from the controlled systems used in laboratory experiments. The greatest decrease in R_{Al} and R_{Si} occurred between the 14 and 90 d experiments in all

three batch experiments (Fig. 2.5a-f). These findings indicated rapid dissolution of an Al and Si bearing phase at early times. This observation is supported by several monomineralic studies that show initially high dissolution rates resulting from the presence of ultrafine particles, highly reactive sites and strained areas on larger grains (e.g. Chou and Wollast, 1984; Knauss and Wolery, 1989; Casey and Bunker, 1990; White and Brantley, 1995; Brandt et al., 2003).

Salmon and Malmstrom (2006) demonstrate that rates calculated for multimineralic samples, such as those in the current investigation, are between one and two orders of magnitude lower than the rates for freshly prepared monomineralic samples typically used in aluminosilicate dissolution studies. However, a comparison of long-term smectite dissolution rates from the literature (100 to 242 d; 25°C; Amram and Ganor, 2005) with the 180 d R_{Al} values from the smectite-rich Kc and BK batch experiments from the current study demonstrated good agreement between monomineralic dissolution rates and multimineralic global dissolution rates (Fig. 2.6a). Additionally, a similar comparison of long-term illite (103 to 192 d, 25 °C; Kohler et al., 2005) and kaolinite (102 to 144 d, 25 °C; Cama et al., 2002) dissolution rates from the literature to the R_{Al} values of the illite and kaolinite-rich samples in the current study (Kc and Km, 180 d) demonstrated good agreement between monomineralic and multimineralic dissolution rates at pH values > 1.0 (Fig. 2.6b). The lower monomineralic kaolinite dissolution rates at pH < 1.0 may be attributed to the different acid matrices used in each study, as Hamer et al. (2003) demonstrate in their study of the effectiveness of different acids in promoting chlorite dissolution. In the current study H_2SO_4 was used and Cama et al. (2002) used $HClO_4$. In contrast to the conclusions of Salmon and Malmstrom (2006), these observations suggested that monomineralic dissolution rates could be used to determine the global dissolution rates of the more complex clays considered in the current study.

A definitive shift in the relationship between R_{Si} and pH was observed at pH < 1.0 (Fig. 2.5d-f) and expressed in the altered reaction orders for all three clays, which corresponded to the observed decrease in aqueous Si concentrations at the same pH (Fig. 2.2d-f). Additionally, these observations correlated well with the appearance of amorphous silica in the Kc, Km, and BK XRD results at pH $\leq$ 0.0, which suggested that

the precipitation of amorphous silica was strongly pH dependent. A similar definitive shift in the relationship between R_{Al} values and treatment pH was evident at pH < 1.0 (Fig. 25a-c) and was expressed by the substantial decrease in reaction orders from between 1.17 and 1.81 to between 0.09 and 0.33. These results suggested that the dissolution mechanism for all three samples at pH > 1.0 was strongly pH dependent, while at pH < 1.0 it independent of pH. Given the large concentrations of protons associated with solutions at pH < 1.0 proton saturation of surface sites may explain the observed shift in reaction orders, in keeping with the work of Wieland and Stumm (1992) and Ganor et al. (1995). Cama et al. (2002) conclude that kaolinite dissolution between pH 0.5 and 4.5 is controlled by two independent and parallel reaction pathways, both involving fast adsorption of protons to surface sites followed by a slow hydrolysis step. While the premise of this model appears to fit the current study, with the observed shift in global reaction rates at pH < 1.0, we do not have sufficient data to comment on these mechanisms. Above HCl concentrations of 6 M (pH < -2.2), Pesquera et al. (1992) conclude that the deposition of amorphous silica begins to inhibit the dissolution of the remaining clay sample. The observed shift of R_{Al} values to near pH independence, between pH 1.0 and -3.0 in all three batch experiments, could have been a result of dissolution inhibition caused by the increased amorphous silica deposition previously suggested to occur at pH ≤ 0.0.

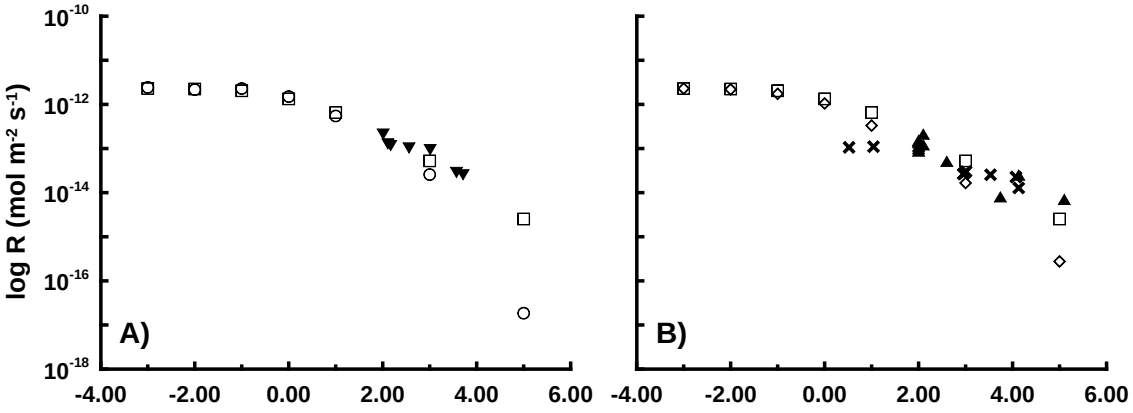

Figure 2.6. Dissolution rates for A) smectite (▼) and B) illite (▲) and kaolinite (✕) and compared to the 180d R_{Al} of Kc (□), Km (◇) and BK (○) batch experiments. Smectite dissolution rates are taken from Amram and Ganor (2005) and represent exposure periods between 100 and 242d. Illite dissolution rates are taken from Kohler et al. (2005) and represent exposure periods between 103 and 196d. Kaolinite dissolution rates are taken from Cama et al. (2002) and represent exposure periods between 102 and 144d.

2.5.3 Ca and SO_4 geochemistry

The total dissolved mass of Ca was an order of magnitude less in the Km aqueous phases relative to Kc and BK samples because the Kc contained dolomite and both Kc and BK had considerable Ca (18.9 meq 100 g^{-1}) on exchange sites associated with smectite. The mobilization of greater than 100 wt % of the SO_4 originally added to each batch experiment suggested the dissolution of an S-bearing phase at pH $\geq$ 1.0 in all three batch experiments, however, no S-bearing phases were identified in the unaltered Kc, Km or BK clays. The relatively constant aqueous Ca concentrations, observed between the 5.0 and 0.0 pH treatments in the Kc batch experiments, coupled with the calculated state of gypsum and anhydrite saturation, suggested that dissolved Ca concentrations were controlled by the presence of a Ca-SO_4 mineral phase. However, no characteristic peaks were observed in the Kc diffractograms for these pH treatments possibly because of the high detection limits associated with XRD analyses for these phases. Conversely, the aqueous Ca concentrations and speciation calculation results suggested the absence of such a control mechanism in both the Km and BK batch experiments, over the same range of pH treatments.

The decrease in aqueous Ca concentrations for the Kc and BK samples between pH 0.0 and -3.0, and the decrease in the aqueous wt % of SO_4 initially added to the batch experiment indicated the possible precipitation of a Ca and SO_4-enriched phase. This was supported by the corresponding diffractograms that indicated the presence of anhydrite in the -1.0 and -3.0 pH treatments for both the Kc and BK batch experiments, with characteristic peaks observed at 25.5° (Kc and BK) and 31.3° (Kc) that are in keeping with Moore and Reynolds (1989). With the extremely high SO_4 concentrations in all three batch experiments, SO_4 should not have been the limiting factor in anhydrite precipitation. Alternatively, Iller (1979) and Mendioroz et al. (1987) observe scavenging of cations, including Ca, during amorphous silica formation from the acidic dissolution of clay at pH < 1.0. However, the incorporation of Ca within the precipitated amorphous silica phase observed in the Kc, Km, and BK samples could not be confirmed with the available data in this study.

The presence of several unidentified peaks in the -1.0 and -3.0 diffractograms from the Kc (9.8), Km (9.8°, 18.8° and 21.9°) and BK (9.8°) batch experiments indicated the

precipitation of one or more secondary phases. Moore and Reynolds (1989) suggest that zeolites are characterized by peaks within this range (e.g. barrerite, mordenite, stilbite). However, zeolites typically form from clay exposed to extremely alkaline conditions and not the extreme acidic conditions present in this study (Belver et al., 2002; Ramirez et al., 2005). Given the large aqueous metal and SO_4 concentrations that characterized the -1.0 and -3.0 pH treatments, the formation of an Al-SO_4-rich mineral phase may be a more probable explanation for these unidentified peaks. In particular, the primary (9.8°) and secondary peaks (18.9°) of aluminite ($Al_2[SO_4][OH]_4 \cdot 7H_2O$), commonly associated with AMD settings, closely matched two of the unidentified peaks (Bigham and Nordstrom, 2000; Hammarstrom et al., 2005). The peak at 21.9° may reflect the presence of cristobalite (Moore and Reynolds, 1989).

2.5.4 Conceptual model

Based on the findings of the current study, the stepwise process of aluminosilicate dissolution and the subsequent precipitation of amorphous silica observed with decreasing pH are summarized in Figure 2.7. The unaltered aluminosilicate structure, the main mineral phase of the Kc, Km, and BK clays (Table 2.1), consists of alternating Al-octahedral and Si-tetrahedral layers and inter-layer cations that account for the CEC of aluminosilicates. Between pH 5.0 and 3.0 cations are mobilized from the aluminosilicate inter-layer by substitution reactions with H^+ ions from the H_2SO_4 solution and any carbonate phases present will undergo dissolution, resulting in an increase in aqueous Ca concentrations. As the pH decreases to between 3.0 and 1.0 the Al-octahedral and Si-tetrahedral layers start to undergo dissolution, with fine-grained SiO_2 phases preferentially dissolving and leading to a marked increase in aqueous Si concentrations relative to Al values. Al-octahedral layers are preferentially dissolved at pH $\leq$ 1.0, substantially increasing the aqueous Al concentrations, and mobilizing the relatively stable Si tetrahedra to solution. At pH $\leq$ 0.0 Si -tetrahedra begin to polymerize and precipitate forming an amorphous silica phase. Additionally, the high concentrations of aqueous metals and SO_4 result in the observed precipitation of SO_4-rich phases at pH $\leq$ -1.0.

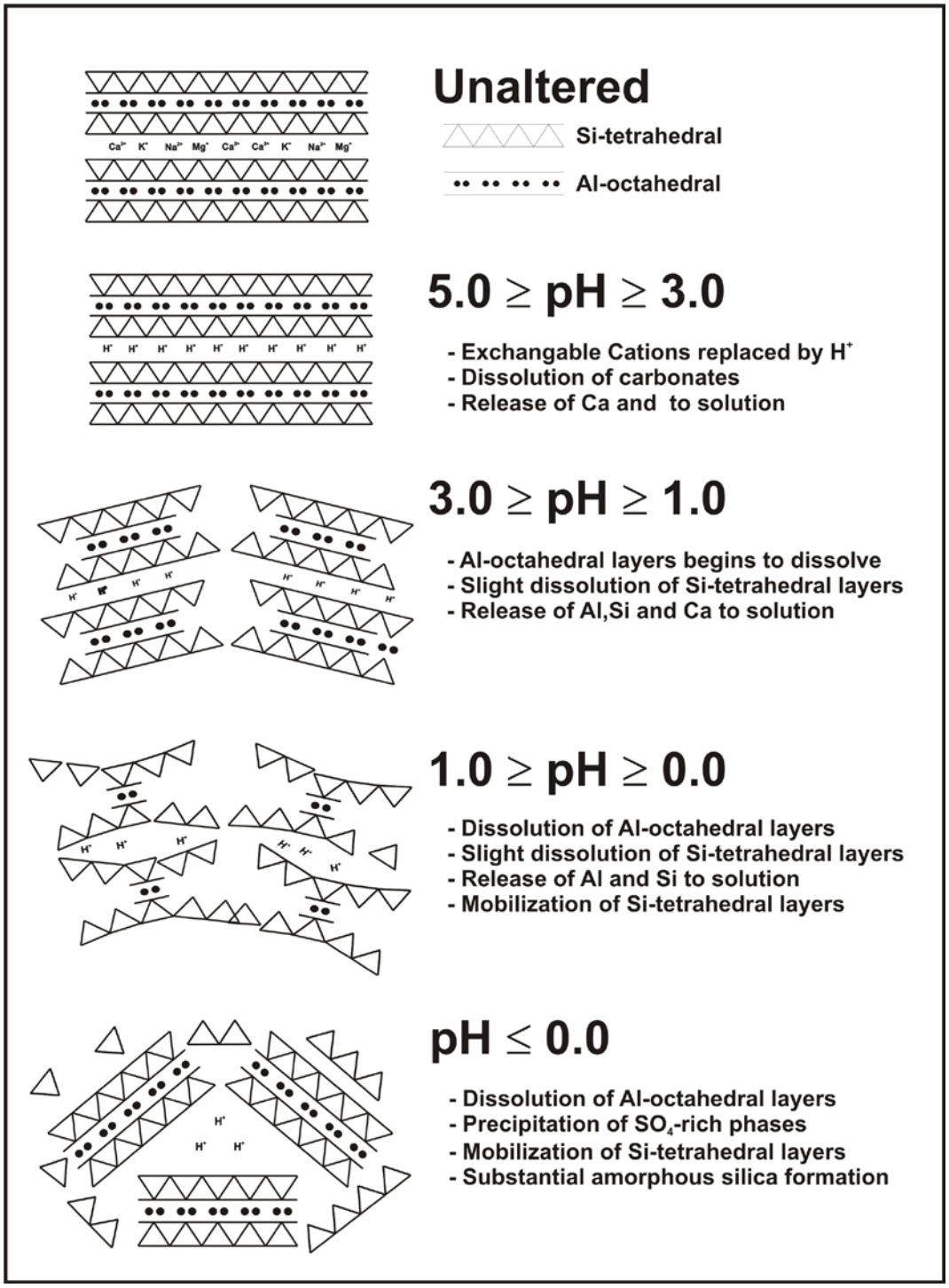

Figure 2.7. Conceptual model of the geochemical and mineralogical evolution of clay interaction with H_2SO_4 solutions between pH 5.0 and -3.0. (after Pesquera et al., 1992).

2.6 Conclusions

The dissolution of aluminosilicates in three clay samples between pH 5.0 and -3.0 were examined using constant-pH batch experiments. Each batch experiment involved seven standardized H_2SO_4 solutions (pH = 5.0, 3.0, 1.0, 0.0, -1.0, -2.0 and -3.0) conducted over four exposure periods (14, 90, 180, and 365 d). All batch experiments used 5 g of clay and 100 g of acid solution.

A conceptual model of aluminosilicate dissolution was developed to explain the reaction processes that occur with increased H_2SO_4 strength between pH 5.0 and -3.0. The dissolution process was characterized by the preferential dissolution of aluminosilicate Al-octahedral layers at pH values $\leq$ 1.0, while the corresponding Si-tetrahedral layers remained relatively unaltered. At pH $\leq$ 0.0 the Si-tetrahedra precipitated, forming an amorphous silica phase. XRD results indicated the presence of an increased amount of amorphous silica with decreasing pH and R_{Si} values indicated an increased rate of precipitation with decreasing pH. The deposition of amorphous silica followed the trend BK > Kc > Km and suggested that smectite-rich clays formed amorphous silica more readily. In addition, an anhydrite precipitate was observed in the Ca-rich Kc and BK experiments and an undefined secondary phase, possibly aluminite, precipitated in all three batch experiments at pH $\leq$ -1.0.

Data showed that between pH 5.0 and -3.0 the crystallinity of the smectite-rich clay was more susceptible to the effects of H_2SO_4 solutions than illite and kaolinite, although kaolinite-rich clays were characterized by higher R_{Al} values. R_{Al} values suggested that two reaction mechanisms control aluminosilicate dissolution in all three clays, with a pH dependent mechanism occurring between pH 5.0 and 1.0 and a near pH independent mechanism between pH 0.0 and -3.0.

2.7 Acknowledgements

The authors would like to thank T. Al and V. Reddy of the University of New Brunswick's Microscopy and Microanalysis facility for their assistance with the XRD analysis and D. Quirt of Areva Resources Canada Inc. for helpful discussions. We are also grateful for the numerous helpful comments provided by the two reviewers. Funding for this study was provided by Syncrude Canada Limited and NSERC.

2.8 References

Acero, P., Ayora, C., Torrento, C. and Nieto, J.M., 2006. The behavior of trace elements during schwertmannite precipitation and subsequent transformation into goethite and jarosite. *Geochim. Cosmochim. Acta* 70, 4130-4139.

Al, T.A., Martin, C.J. and Blowes, D.W., 2000. Carbonate-mineral/water interactions in sulfide-rich mine tailings. *Geochim. Cosmochim. Acta* 64, 3933-3948.

Allison, J.D., Brown, D.S. and Novo-Gradac, K.J., 1991. MINTEQA2/PRODEFA2, A geochemical assessment model for environmental systems: Version 3.0 User's Manual. United States Environmental Protection Agency.

Amram, K. and Ganor, J., 2005. The combined effect of pH and temperature on smectite dissolution rate under acidic conditions. *Geochim. Cosmochim. Acta* 69, 2535-2546.

Barrios, M.S., Gonzalez, L.V.F., Rodriguez, M.A.V. and Pozas, J.M.M., 1995. Acid Activation of a Palygorskite with Hcl - Development of Physicochemical, Textural and Surface-Properties. *Appl.Clay Sci.* 10, 247-258.

Belver, C., Munoz, M.A.B. and Vicente, M.A., 2002. Chemical activation of a kaolinite under acid and alkaline conditions. *Chem. Mat.* 14, 2033-2043.

Bigham, J.M. and Nordstrom, D.K., 2000. Iron and aluminum hydroxysulfates from acid sulfate waters. *Rev. Mineral. Geochem.* 40, 351-403.

Blowes, D.W. and Jambor, J.L., 1990. The Pore-Water Geochemistry and the Mineralogy of the Vadose Zone of Sulfide Tailings, Waite-Amulet, Quebec, Canada. *Appl. Geochem.* 5, 327-346.

Blowes, D.W. and Ptacek, C.J., 1994. Acid-neutralization mechanisms in inactive mine tailings. In: Blowes, D.W. and Jambor, J.L. (Eds.), The Environmental Geochemistry of Sulfide Mine-Wastes, Short Course Handbook 22, pp. 271-292.

Blowes, D.W., Ptacek, C.J. and Jurjovec, J., 2003. Mill tailings: Hydrogeology and geochemistry. In: Blowes, D.W., Jambor, J.L. and Ritchie, A.I.M. (Eds.), The Environmental Geochemistry of Sulfide Mine-Wastes, Short Course Handbook 31, pp. 95-116.

Blowes, D.W., Reardon, E.J., Jambor, J.L. and Cherry, J.A., 1991. The Formation and Potential Importance of Cemented Layers in Inactive Sulfide Mine Tailings. *Geochim. Cosmochim. Acta* 55, 965-978.

Brandt, F., Bosbach, D., Krawczyk-Barsch, E., Arnold, T. and Bernhard, G., 2003. Chlorite dissolution in the acid pH-range: A combined microscopic and macroscopic approach. *Geochim. Cosmochim. Acta* 67, 1451-1461.

Breen, C., Zahoor, F.D., Madejova, J. and Komadel, P., 1997. Characterization and catalytic activity of acid-treated, size-fractionated smectites. *J. Phys. Chem. B* 101, 5324-5331.

Brookfield, A.E., Blowes, D.W. and Mayer, K.U., 2006. Integration of field measurements and reactive transport modelling to evaluate contaminant transport at a sulfide mine tailings impoundment. *J. Contam. Hydro.* 88, 1-22.

Cama, J., Metz, V. and Ganor, J., 2002. The effect of pH and temperature on kaolinite dissolution rate under acidic conditions. *Geochim. Cosmochim. Acta* 66, 3913-3926.

Casey, W.H. and Bunker, B., 1990. Leaching of Mineral and Glass Surfaces during Dissolution. *Rev. Mineral.* 23,397-426.

Chou, L. and Wollast, R., 1984. Study of the Weathering of Albite at Room-Temperature and Pressure with a Fluidized-Bed Reactor. *Geochim. Cosmochim. Acta* 48, 2205-2217.

Dold, B. and Fontbote, L., 2002. A mineralogical and geochemical study of element mobility in sulfide mine tailings of Fe oxide Cu-Au deposits from the Punta del Cobre belt, northern Chile. *Chem. Geol.* 189, 135-163.

Dubrovsky, N.M., Cherry, J.A., Reardon, E.J. and Vivyurka, A.J., 1985. Geochemical Evolution of Inactive Pyritic Tailings in the Elliot Lake Uranium District. *Can. Geotech. J.* 22, 110-128.

Ganor, J., Mogollon, J.L. and Lasaga, A.C., 1995. The Effect of Ph on Kaolinite Dissolution Rates and on Activation-Energy. *Geochim. Cosmochim. Acta* 59, 1037-1052.

Gates, W.P., Anderson, J.S., Raven, M.D. and Churchman, G.J., 2002. Mineralogy of a bentonite from Miles, Queensland, Australia and characterisation of its acid activation products. *Appl. Clay Sci.* 20, 189-197.

Gunsinger, M.R., Ptacek, C.J., Blowes, D.W., Jambor, J.L. and Moncur, M.C., 2006. Mechanisms controlling acid neutralization and metal mobility within a Ni-rich tailings impoundment. *Appl. Geochem.* 21, 1301-1321.

Hall, G.E.M., Gauthier, G., Pelchat, J.C., Pelchat, P. and Vaive, J.E., 1996. Application of a sequential extraction scheme to ten geological certified reference materials for the determination of 20 elements. *J. Anal. At. Spectrom.* 11, 787-796.

Hamer, M., Graham, R.C., Amrheim, C. and Bozhilov, K.N., 2003. Dissolution of ripidolite (Mg, Fe-chlorite) in organic and inorganic acid solutions. *Soil Sci. Soc. Am. J.* 67, 654-661.

Hammarstrom, J.M., Sibrell, P.L. and Belkin, H.E., 2003. Characterization of limestone reacted with acid-mine drainage in a pulsed limestone bed treatment system at the

Friendship Hill National Historical Site, Pennsylvania, USA. *Appl. Geochem*. 18, 1705-1721.

Hammarstrom, J.M., Seal, R.R., Meier, A.L. and Kornfeld, J.M., 2005. Secondary sulfate minerals associated with acid drainage in the eastern US: recycling of metals and acidity in surficial environments. *Chem. Geol.* 215,407-431.

Hendershot, W.H. and Duquette, M., 1986. A Simple Barium-Chloride Method for Determining Cation-Exchange Capacity and Exchangeable Cations. *Soil Sci. Soc. Am. J.* 50, 605-608.

Hradil, D. and Hostomsky, J., 2002. Effect of composition and physical properties of. natural kaolinitic clays on their strong acid weathering rates. *Catena* 49, 171-181.

Iller, R.K., 1979. *The chemistry of silica.* Wiley, New York.

Jambor, J.L., 1994. Mineralogy of sulfide-rich tailings and their oxidation products. In: Blowes, D.W. and Jambor, J.L. (Eds.), The Environmental Geochemistry of Sulfide Mine-Wastes, Short Course Handbook 22, pp. 59-102.

Jozefaciuk, G. and Bowanko, G., 2002. Effect of acid and alkali treatments on surface areas and adsorption energies of selected minerals. *Clays Clay Miner*. 5, 771-783.

Jurjovec, J., Ptacek, C.J. and Blowes, D.W., 2002. Acid neutralization mechanisms and metal release in mine tailings: A laboratory column experiment. *Geochim. Cosmochim. Acta* 66, 1511-1523.

Kalinowski, B.E. and Schweda, P., 1996. Kinetics of muscovite, phlogopite, and biotite dissolution and alteration at pH 1-4, room temperature. *Geochim. Cosmochim. Acta* 60, 367-385.

Kashir, M. and Yanful, E.K., 2001. Hydraulic conductivity of bentonite permeated with acid mine drainage. *Can. Geotech. J.* 38, 1034-1048.

Knauss, K.G. and Wolery, T.J., 1989. Muscovite Dissolution Kinetics as a Function of Ph and Time at 70-Degrees-C. *Geochim. Cosmochim. Acta* 53, 1493-1501.

Kohler, S.J., Bosbach, D. and Oelkers, E.H., 2005. Do clay mineral dissolution rates reach steady state? *Geochim. Cosmochim. Acta* 69,1997-2006.

Kohler, S.J., Dufaud, F. and Oelkers, E.H., 2003. An experimental study of illite dissolution kinetics as a function of pH from 1.4 to 12.4 and temperature from 5 to 50 degrees C. *Geochim. Cosmochim. Acta* 67, 3583-3594.

Komadel, P., 2003. Chemically modified smectites. *Clay Miner.* 38,127-138.

Komadel, P. et al., 1996. Dissolution of hectorite in inorganic acids. *Clays Clay Miner.* 44, 228-236.

Madejova, J., Bujdak, J., Janek, M. and Komadel, P., 1998. Comparative FT-IR study of structural modifications during acid treatment of dioctahedral smectites and hectorite. *Spectrochim. Acta, Part A* 54, 1397-1406.

Mendioroz, S., Pajares, J. A., Benito, I., Pesquera, C., Gonzalez, F., and Blanco, C., 1987. Texture evolution of montmorillonite under progressive acid treatment - change from H-3 to H2 type of hysteresis. *Langmuir* 3, 676-681.

Metz, V., Amram, K. and Ganor, J., 2005. Stoichiometry of smectite dissolution reaction. *Geochim. Cosmochim. Acta* 69, 1755-1772.

Meunier, A., 2005. Clays. Springer, New York.

Mitchell, J.K., 1993. Fundamentals of soil behavior. Wiley, New York.

Moncur, M.C., Ptacek, C.J., Blowes, D.W. and Jambor, J.L., 2005. Release, transport and attenuation of metals from an old tailings impoundment. *Appl. Geochem.* 20, 639-659.

Moore, D.M. and Reynolds, R.C., 1989. X-ray diffraction and the identification and analysis of clay minerals. Oxford University Press, Oxford.

Morin, K.A., Cherry, J.A., Dave, N.K., Lim, T.P. and Vivyurka, A.J., 1988. Migration of acidic groundwater seepage from uranium-tailings impoundments, 1. Field study and conceptual hyrodgeochemical model. *J. Contam. Hydro.* 2, 271-303.

Newbrough, P. and Gammons, C.H., 2002. An experimental study of water-rock interaction and acid rock drainage in the Butte mining district, Montana. *Env. Geol.* 41, 705-719.

Nguetnkam, J.P. et al., 2005. Assessment of the surface areas of silica and clay in acid-leached clay materials using concepts of adsorption on heterogeneous surfaces. *J. Colloid Interface Sci.* 289, 104-115.

Nordstrom, D.K., 1977. Thermochemical Redox Equilibria of Zobells Solution. *Geochim. Cosmochim. Acta* 41, 1835-1841.

Nordstrom, D.K. and Alpers, C.N., 1999. Negative pH, efflorescent mineralogy, and consequences for environmental restoration at the Iron Mountain Superfund site, California. Proc. Nat. Acad. Sci. U.S.A. 96, 3455-3462.

Nordstrom, D.K., Alpers, C.N., Ptacek, C.J. and Blowes, D.W., 2000. Negative pH and extremely acidic mine waters from Iron Mountain, California. *Env. Sci. Technol.* 34, 254-258.

Parkhurst, D.L. and Appelo, C.A.J., 1999. User's guide to PHREEQC (Version 2) - A computer program for speciation, batch-reaction, one-dimensional transport, and inverse geochemical calculations. Report 99-4259: 310 p.

Pesquera, C., Gonzalez, F., Benito, I., Blanco, C., Mendioroz, S. and Pajares, J., 1992. Passivation of a Montmorillonite by the Silica Created in Acid Activation. *J. Mater.Chem.* 2, 907-911.

Plummer, L.N., Parkhurst, D.L., Fleming, G.W. and Dunkle, S.A., 1988. A computer program incorporating pitzer's equations for calculation of geochemical reactions in brines. U.S. Geological Survey Water-Resources Investigations Report 88-4153.

Ptacek, C.J. and Blowes, D.W., 2000. Prediction of sulfate mineral solubility in concentrated waters. *Rev. Miner.* 40, 513-540.

Qafoku, N.P., Ainsworth, C.C., Szecsody, J.E. and Qafoku, O.S., 2004. Transport-controlled kinetics of dissolution and precipitation in the sediments under alkaline and saline conditions. *Geochim. Cosmochim. Acta* 68, 2981-2995.

Ramirez, S. et al., 2005. Alteration of the Callovo-Oxfordian clay from Meuse-Haute Marne underground laboratory (France) by alkaline solution. I. A XRD and CEC study. *Appl. Geochem.* 20, 89-99.

Salmon, S.U. and Malmstrom, M.E., 2006. Quantification of mineral dissolution rates and applicability of rate laws: Laboratory studies of mill tailings. *Appl. Geochem.* 21, 269-288.

Schuring, J., Kolling, M. and Schulz, H.D., 1997. The potential formation of acid mine drainage in pyrite-bearing hard-coal tailings under water-saturated conditions: An experimental approach. *Env. Geol.* 31, 59-65.

Shaw, S. C., Groat, L. A., Jambor, J. L., Blowes, D. W., Hanton-Fong, C. J., and Stuparyk, R. A., 1998. Mineralogical study of base metal tailings with various sulfide contents, oxidized in laboratory columns and field lysimeters. *Environ. Geol.* 33, 209-217.

Sidenko, N.V. and Sherriff, B.L., 2005. The attenuation of Ni, Zn and Cu, by secondary Fe phases of different crystallinity from surface and ground water of two sulfide mine tailings in Manitoba, Canada. *Appl. Geochem.* 20, 1180-1194.

Sracek, O., Choquette, M., Gelinas, P., Lefebvre, R. and Nicholson, R.V., 2004. Geochemical characterization of acid mine drainage from a waste rock pile, Mine Doyon, Quebec, Canada. *J. Contam. Hydro.* 69,45-71.

Tessier, A., Campbell, P.G.C. and Bisson, M., 1979. Sequential Extraction Procedure for the Speciation of Particulate Trace-Metals. *Anal. Chem.* 51, 844-851.

Tyagi, B., Chudasama, C.D. and Jasra, R.V., 2006. Determination of structural modification in acid activated montmorillonite clay by FT-IR spectroscopy. *Spectrochim. Acta, Part A* 64, 273-278.

Van Rompaey, K., Van Ranst, E., De Coninck, F. and Vindevogel, N., 2002. Dissolution characteristics of hectorite in inorganic acids. *Appl. Clay Sci.* 21, 241-256.

Vicente, M.A., Suarez, M., LopezGonzalez, J.D.D. and BanaresMunoz, M.A., 1996. Characterization, surface area, and porosity analyses of the solids obtained by acid leaching of a saponite. *Langmuir* 12, 566-572.

White, A.F. and Brantley, S.L., 1995. Chemical weathering rates of silicate minerals: An overview. Chemical Weathering Rates of Silicate Minerals 31, 1-22.

White, A.F. and Brantley, S.L., 2003. The effect of time on the weathering of silicate minerals: why do weathering rates differ in the laboratory and field? *Chem. Geol.* 202, 479-506.

Wieland, E. and Stumm, W., 1992. Dissolution Kinetics of Kaolinite in Acidic Aqueous-Solutions at 25-Degrees-C. *Geochim. Cosmochim. Acta* 56, 3339-3355.

Wu, P.X. and Ming, C., 2006. The relationship between acidic activation and microstructural changes in montmorillonite from Heping, China. *Spectrochim. Acta, Part A* 63, 85-90.

Zysset, M. and Schindler, P.W., 1996. The proton promoted dissolution kinetics of K-montmorillonite. *Geochim. Cosmochim. Acta* 60, 921-931.

3.0 APPLICATION OF SI AND AL X-RAY ABSORPTION NEAR EDGE STRUCTURE TO ACIDIC DISSOLUTION OF MIXED CLAYS BETWEEN PH 1.0 AND -3.0

3.1 Abstract

Although widely investigated in relation to acid mine drainage systems at pH > 1.0, we know little about the impact of sulfuric acid (H_2SO_4) on the geochemistry and mineralogy of clays at pH < 1.0 (including negative pH values). Thus, laboratory batch experiments were conducted on three mixed clay samples with different mass ratios of phyllosilicates (smectite, illite and kaolinite) to investigate the impact of H_2SO_4 from pH 1.0 to -3.0 for exposure periods of 14, 90, 180, and 365 days. Si and Al K- and $L_{2,3}$-edge x-ray absorption near edge structure (XANES) spectroscopy were employed on these samples to determine the chemical and structural changes that occur during acidic dissolution of phyllosilicates that cannot be distinguished using x-ray diffraction analyses. A series of silicate, phyllosilicate, and Al-bearing standard compounds were also studied to provide an explanation for the observed changes in the clay samples. The Si XANES results indicated the preferential dissolution of the phyllosilicates (pH≤ 1.0, t ≥ 14 d), the persistence of quartz even at pH ≥ -3.0 and t ≥ 365 d, and the formation of an amorphous silica-like phase that was confined to the surface layer of the altered clay samples at pH≤ 0.0 and t ≥ 90 d). Al XANES results demonstrated dissolution of Al -octahedral layers (pH≤ 1.0, t ≥ 14 d), the persistence of four -fold relative to six-fold coordinated Al, and the precipitation of an Al-SO_4-rich phase (pH≤ -1.0, t≥ 90 d). An existing conceptual model of phyllosilicates dissolution under extremely acidic conditions was modified to include the results of this study.

3.2 Introduction

Large amounts of zero-valent sulfur (S^0) are recovered as a by-product of oil production in the Alberta Oil Sands, located near Fort McMurray, Alberta, Canada. This S^0 is typically stored in large, above-ground, blocks that are susceptible to the ingress of atmospheric oxygen and precipitation. These conditions lead to the production of a sulfuric acid (H_2SO_4) rich leachate that is flushed through the S^0 blocks due to precipitation events and is routinely characterized by extremely low pH measurements

(pH < 0.5). The acidity of this leachate is expected to be even greater for leachate directly beneath the block that has not been diluted by precipitation, which could be characterized by negative pH values. While the majority of S^0 blocks are only in existence for weeks to months, due to geographical and economical factors, S^0 blocks in the Alberta Oilsands have been in use for several years. Therefore, the long-term effects of H_2SO_4 production on the surrounding environment are of paramount concern.

Interactions between H_2SO_4 solutions and geologic media have been well studied in acid mine drainage (AMD) settings for over twenty years (e.g., Dubrovsky et al., 1985; Morin et al., 1988; Blowes and Jambor, 1990; Blowes and Ptacek, 1994; Al et al., 2000; Kashir and Yanful, 2001; Dold and Fontbote, 2002; Jurjovec et al., 2002; Sracek et al., 2004; Gunsinger et al., 2006). Most AMD studies are characterized by pH values > 1.0, while only a few studies involve more acidic (pH < 1.0) conditions (Blowes et al., 1991; Nordstrom et al., 2000; Moncur et al., 2005). Generally, the geochemical and mineralogical interactions between H_2SO_4 solutions with pH < 1.0 and clays are poorly understood.

Through a series of long-term (14 to 365 d) batch experiments, Shaw and Hendry (accepted) investigated the impact of H_2SO_4 solutions between pH 5.0 and -3.0 on three mixed clays (Kc, Km, and BK) with different phyllosilicate ratios (montmorillonite, illite, and kaolinite) typically used in as liner materials in mine settings. They found that dissolved Al concentrations increase substantially between pH 1.0 and -3.0 to peak values of 2.3×10^{-2} mol L^{-1} g^{-1}, while Si values increase to a peak of 1.2×10^{-3} mol L^{-1} g^{-1} at pH 0.0 and then decrease between pH 0.0 and -3.0. The authors indicate that peak Al and Si concentrations represent mobilization of between 40 and 60 % of total Al from the Kc, Km, and BK solid phases. Furthermore, through X-ray diffraction (XRD) analyses Shaw and Hendry (accepted) demonstrate; i) the loss of montmorillonite crystal structure at pH ≤ 1.0; ii) a considerable decreases in illite and kaolinite peak intensities at pH ≤ 1.0; iii) precipitation of amorphous silica (a-SiO_2) at pH ≤ 0.0, and iv) precipitation of anhydrite and possibly aluminite ($Al_2[SO_4][OH]_4 \cdot 7H_2O$) at pH ≤ -1.0. Previous acidic dissolution studies of phyllosilicates conducted at pH ≥ 1.0 indicate that Al -octahedral layers preferentially dissolve, while the associated Si-tetrahedral layers remain relatively

unaffected (Mendioroz et al., 1987; Pesquera et al., 1992; Gates et al., 2002; Belver et al., 2002; Komadel, 2003; Tyagi et al., 2006).

From the work of Shaw and Hendry (accepted) we have learned, via aqueous geochemistry and XRD analyses, that when mixed clays are in contact with H_2SO_4, extensive dissolution of phyllosilicates and the formation of new, non-crystalline, poorly crystalline, or short-range ordered phases occurs. The objective of this research is to use x-ray absorption near edge structure (XANES) spectroscopy to study the effects of H_2SO_4 concentration and exposure period on the dissolution of phyllosilicates and the formation of new phases, to better characterize their structure and infer possible controlling mechanisms. These objectives were achieved using Si and Al XANES at the K- and $L_{2,3}$-edges.

3.3 Materials and Methods

3.3.1 Sample descriptions

The three clay samples tested were: Cretaceous Clearwater (Kc), Cretaceous McMurray (Km), and Barakade 90 (BK). The Kc and Km clays were obtained from the Syncrude Canada Limited (SCL) Mildred Lake mine site, located 60 km north of Fort McMurray, Alberta, Canada (57° 4’ 30” N, 111° 39’ 0” W). The BK clay was obtained from BPM Minerals LLC in northern Wyoming, USA (44° 49’ 16” N, 108° 22’ 34” W). The Kc and Km samples are comprised of several mineral phases, including substantial amounts of quartz, montmorillonite, kaolinite, and illite, while BK is primarily composed of montmorillonite and quartz (Table 3.1). Representative silicate and aluminum mineral standards were selected to serve as a basis of comparison to the three clay samples investigated in the current and are listed in Table 3.2.

3.3.2 Altered sample preparation

Batch experiments were conducted by treating each clay sample for between 14 and 365 d with four different standardized H_2SO_4 solutions (pH = 1.0, 0.0, -1.0, and -3.0). Treatments consisted of 5 g of homogenized clay (< 63 µm) and 100 g of standardized H_2SO_4. The pH of each clay slurry was measured daily using an Orion glass combination electrode (Model 9102BN) and was adjusted with standardized H_2SO_4 or NaOH solution

until no further change was recorded in 24 hours, after which time pH measurements were taken on a weekly basis. The pH electrode was calibrated with pH 7.0, 4.0 and 1.0 buffers for samples with pH > 1.0. Samples with a pH < 1.0 were calibrated using the method described by Nordstrom et al. (2000), which had an average standard deviation of ±0.2 pH units. At the end of each respective exposure period, the clay solids were separated from the acid solution by centrifugation, air dried at room temperature, and stored in HDPE vials for future analyses.

Table 3.1. Mineralogical content of Kc, Km and BK whole rock and clay fractions, determined by semi-quantitative XRD methods. From Shaw and Hendry (accepted).

Mineral Phase	Composition (weight %)					
	Kc		Km		BK	
	< 63µm	*< 2µm*	*< 63µm*	*< 2µm*	*< 63µm*	*< 2µm*
Quartz	53.9	17.8	30.4	4.8	3.5	3.5
Smectite	1.8	23.0	0.3	0.5	79.4	79.4
Kaolinite	11.5	22.4	42.6	61.3	0.0	0.0
Illite	9.5	29.1	20.3	28.9	0.0	0.0
Plagioclase	10.8	0.0	1.0	0.5	5.2	5.2
Chlorite	3.4	7.7	1.3	1.5	0.0	0.0
Cristobalite	0.0	0.0	0.0	0.0	11.8	11.8
Dolomite	9.3	0.0	0.0	0.0	0.0	0.0
Siderite	0.0	0.0	4.3	2.6	0.0	0.0

3.3.3 XANES analyses

Si K-edge XANES measurements were preformed at the University of Wisconsin Synchrotron Radiation Center (Madison, WI) using the Canadian Synchrotron Radiation Facility double crystal monochromator beamline (DCM; Yang et al., 1992). Al K-edge, Al $L_{2,3}$-edge, and Si $L_{2,3}$-edge XANES measurements where conducted at the Canadian Light Source (Saskatoon, Canada) using the high resolution spherical grating monochromator beamline (SGM; Regier et al., 2007) and the variable line spacing plane grating monochromator beamline (VLS-PGM; Hu et al., 2007). Continuous Si K-edge spectra were collected on the DCM beamline over the region of 1825 to 1890 eV using step intervals of 0.5 eV (1825 to 1840 eV) and 0.25 eV (1840 to 1890 eV) with a one second dwell time for each point. Al K-edge spectra were collected on the SGM beamline over the region of 1555 to 1595 eV using step an interval of 0.1 eV with a one second dwell time for each point. The medium energy grating (25 to 125 eV) of the VLS-PGM

was used to collect continuous spectra over the regions of 76 to 86 eV (Al $L_{2,3}$-edge) and 100 to 120 eV (Si $L_{2,3}$-edge) using 50 μm entrance and exit slits, a step size of 0.1 eV, and a one second dwell time for each point. Surface sensitive total electron yield (TEY) and bulk sensitive fluorescence yield (FY) were measured simultaneously on all three beamlines. The photon energy resolution value for the DCM was 0.25 eV and 0.1 eV for the SGM and PGM beamlines.

Table 3.2. Chemical formula and Si order of silicates and Al-containing minerals examined in Si K- and $L_{2,3}$-edge and Al K- and $L_{2,3}$-edge XANES.

Silicate	Idealized Formula	Polymerization
H_4SiO_4	H_4SiO_4	Nesosilicate (Q^0)
Kaolinite	$(MgCaNaK)_{.05}(AlFeTi)_4(SiAl)_4O_{10}(OH)_8$	Phyllosilicate (Q^3)
Montmorillonite	$(Na,Ca)_{0.3}(Al,Mg)_2Si_4O_{10}(OH)_2 \cdot nH_2O$	Phyllosilicate (Q^3)
Illite	$(MgCaK)_{1.52}(AlFeMgTi)_4(SiAl)_4O_{20}(OH)_4$	Phyllosilicate (Q^3)
Muscovite	$KA1_2[A1Si_3O_{10}](OH)_2$	Phyllosilicate (Q^3)
Chlorite	$(Mg, A1, Fe)_{12}(Si, A1)_8O_{20}(OH)_{16}$	Phyllosilicate (Q^3)
Talc	$Mg_3Si_4O_{10}(OH)_2$	Phyllosilicate (Q^3)
Hydrous amorphous Al-silicate (Al-SiO_2)	$(Al_2O_3)(SiO_2)_{1.5}(H_2O)_{2.5}$	Tectosilicate (Q^4)
Hydrous amorphous silica (a-SiO_2)	SiO_2	Tectosilicate (Q^4)
Quartz	SiO_2	Tectosilicate (Q^4)
$AlPO_4$	$AlPO_4$	
α-Al_2O_3	Al_2O_3	
γ-Al_2O_3	Al_2O_3	
Hydrous amorphous Al-oxide (HAO)	Al_2O_3	
Halotrichite	$FeAl_2(SO_4)_4 \cdot 22H_2O$	
$Al_2(SO_4)_3$	$Al_2(SO_4)_3 \cdot 16H_2O$	

Sample preparation consisted of grinding the samples to a fine powder with an agate mortar and pestle and placing them on carbon tape supported with a stainless steel sample holder. Duplicate spectra were obtained for each sample and averaged. All DCM spectra were normalized to the incident photon flux (I_0), which was monitored by a Samson-type ionization chamber filled with nitrogen gas at 1.0 torr pressure. All SGM and PGM spectra were normalized to the incident photon flux (I_0) by monitoring the current emitted from a gold or nickel mesh located downstream from the last refocusing mirror. For the K-edge spectra, a first-order polynomial baseline was taken and than normalized to an edge step of one for Si (1826 to 1836 eV; 1880 to 1890 eV) and Al (1555 to 1560 eV; 1590 to 1595 eV). For the Si and Al $L_{2,3}$-edge spectra, a spline was

applied to the pre-edge, to account for the distortions caused by self-absorption, and a linear fit of the background was subtracted. Additionally, all $L_{2,3}$-edge spectra were normalized to the peak with maximum intensity for ease of visual comparison. The apparent energy positions of edge features were determined by their apparent maximum. It is worth noting that the raw Al $L_{2,3}$-edge spectra were all shifted 1 eV lower compared to existing literature spectra, as such all our spectra have been calibrated to the corundum standard presented by Ildefonse et al. (1998) so that our energies are consistent.

3.4 Results and Discussion

3.4.1 Si XANES study

3.4.1.1 K and $L_{2,3}$-edge peak assignment

The Si K- and $L_{2,3}$-edge XANES spectra of several reference silicates are presented in Figure 3.1a & 3.1b and major peak features are labeled according to Garvie and Buseck (1999). The major peak features in the K-edge FY spectra were characterized by reduced intensities relative to the TEY spectra, which can be attributed to self-absorption effects caused by the high Si concentrations (Stohr, 1992). Otherwise, the FY and TEY spectra were identical and; therefore, only the TEY spectra are presented in Figure 3.1a. The $L_{2,3}$-edge TEY spectra were poorly resolved relative to the FY spectra due to surface charging; therefore, only the FY spectra are presented in Figure 3.1b. For the Si K-edge spectra, Li et al. (1994) attribute peak C to the transition of electrons from the Si 1s state to Si 3p state, peaks D and F to the effects of multiple scattering from distant atom shells, and peaks E and G to the transition of Si 1s electrons to the Si 3d state (meaning medium to long-range order in silicates). Several studies demonstrate that peaks C and G are characteristic of ^{4}Si (Li et al., 1994; Cabaret et al., 2001; Levelut et al., 2001). The $L_{2,3}$-edge peak A region was characterized by a double feature, split by approximately 0.6 eV, which is attributed to the spin orbital interactions of the Si 2p orbitals (Li et al., 1994). Li et al. (1994) also assign the high intensity of peak B to the transition of Si 2p electrons to the t_2 state, while attributing peak C to transitions to the empty 3d orbital.

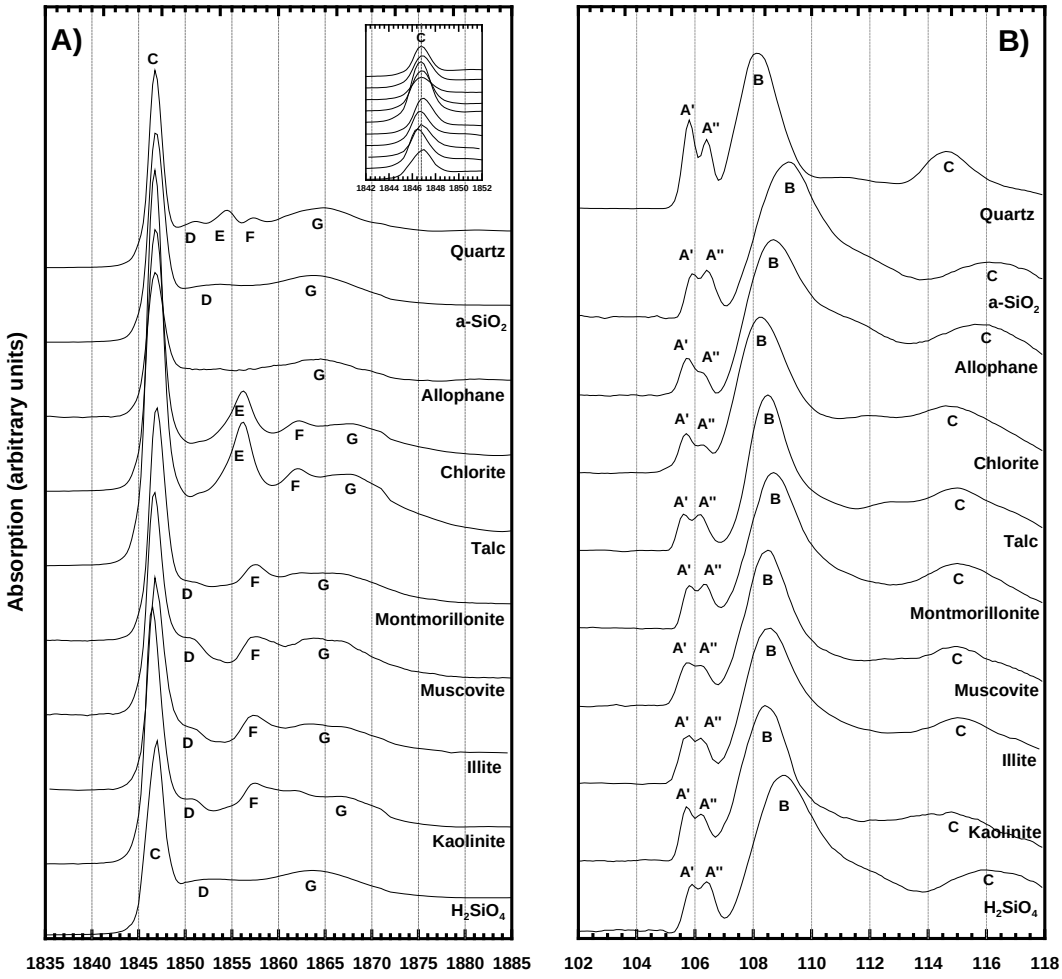

Figure 3.1. Si K-edge TEY (A) and Si $L_{2,3}$-edge FY (B) spectra of standard silicate minerals.

In natural materials, silica is surrounded by oxygen atoms in tetrahedral coordination (^{4}Si) and, due to the charge (+ 4) on Si, silicate tetrahedrons link only in corner sharing bonds. Previous studies have utilized Si XANES and energy-loss near-edge structure (ELNES) analyses to determine the number of shared oxygen atoms, or degree of polymerization, in various silicates using both K-edge (e.g. Li et al., 1995a; Chaboy et al., 1995; Bantignies et al., 1997; Gilbert et al., 2003) and $L_{2,3}$-edge (Li et al., 1994; Poe et al., 1997; Garvie and Buseck, 1999). The silicate reference standards (Table 3.2) can be classified based on the number of oxygen atoms that are shared in the tetrahedral linkages as nesosilicates (zero, Q^0), sorosilicates (one, Q^1), cyclosilicates and inosilicates (two, Q^2), phyllosilicates (three, Q^3), or tectosilicates (four, Q^4). The Si standards presented in Figures 3.1a and 3.1b are grouped according to the number of

shared oxygen atoms, from the bottom spectra upwards (nesosilicate, phyllosilicate, tectosilicate; Fig. 3.1a & b). Additionally, the phyllosilicate spectra were also ordered by increasing Si tetrahedral structure and chemical composition (1:1, 2:1 trioctahedral, 2:1 dioctahedral, and 2:1:1) and the tectosilicates are presented in terms of increasing order and chemical composition (Fig. 3.1a & b).

3.4.1.2 K-edge standard spectra

In the Si K-edge TEY standard spectra, silicic acid (H_4SiO_4) was characterized by peak C shifted to higher energy (1847.00 eV) than the other standards and an absence of peaks D and F (Fig. 3.1a). The short-range ordered hydrous aluminum silicate and pure silicate precipitates (Al-SiO_2 and a-SiO_2; Fig. 3.1a) were characterized by peak C at 1847.75 eV, weakly present peaks E and G weakly consistent with ^{4}Si, and lack of other major peak features, which indicated that little medium to long-range order was present. Conversely, the spectrum for quartz, which consists of long-range ordered SiO_4 units, was characterized by features for all of the major peaks (Fig. 3.1a). For the phyllosilicate standards some substantial differences were evident, which corresponded to both structural and chemical differences. Peak C was shifted to lower energy for the 1:1 standard (kaolinite; 1846.50 eV) relative to the remaining phyllosilicate standards (1846.75 to 1847.00 eV), which was also observed for another 1:1 phyllosilicate (dickite; data not shown). Additionally, although structurally similar, muscovite was shifted to lower energy relative to illite, which could be attributed to the greater amount of Si present in the illite Si-tetrahedral layer (Fig. 3.1a; Li et al., 1995). Finally, peak E was substantially more intense and shifted to lower energy for talc and chlorite compared to the remaining phyllosilicate standards (Fig. 3.1a). The observed shift was potentially the result of chemical variations as both talc and chlorite were characterized by trioctahedral, Mg-rich, layers, while the remaining phyllosilicates were typified by dioctahedral, Al-rich, layers. Based on these observed differences between the Si K-edge spectra of the various silicate standards, we can attempt to explain the observed alterations of our clay samples upon exposure to H_2SO_4 solutions between pH 1.0 and -3.0.

3.4.1.3 $L_{2,3}$-edge standard spectra

The Si $L_{2,3}$ standard spectra (Fig. 3.1b) were characterized by three peaks, peak A that consisted of a well resolved peak doublet (105.5 to 107.0 eV), a broad and intense peak B (107.5 to 111.5 eV), and a broad peak C (113.5 to 118 eV). All of the examined standards were characterized by ^{4}Si and the energy shifts between standards were well correlated for peaks A' and B, which likely corresponds to the assignment of both peaks to transitions of the Si 2p electrons (Li et al., 1994). Al-SiO_2 and H_4SiO_4 lacked medium and long-range order, as demonstrated in the Si K-edge results, and were likely characterized by substantial incorporation of H_2O within their overall structure. Based simply on ligand theory, water ligands are expected to have a higher energy transition for lowest unoccupied molecular orbits (LUMO) than hydroxide (OH^-) or oxygen (O^{2-}) in a spectrochemical series (Shriver et al., 1994). This corresponded to the higher energy position of peaks A' and B observed for a-SiO_2, Al-SiO_2, and H_4SiO_4 (Fig. 3.1b). In addition, a comparison of the a-SiO_2, Al-SiO_2 and phyllosilicate spectra indicated that the inclusion of Al within the silicate system also shifted peak B to lower energies (Fig. 3.1b). Based upon valence bond theory, the O^{2-} ligand is expected to be slightly stronger in the Si-O-Al bond than in the Si-O-Si bond, which decreases the lowest energy electronic transition of the complex and results in the observed shift to lower energies in the Al containing silicate spectra.

The relative intensities of peaks A' and A'' changes from A' being much larger in quartz, allophane, and kaolinite, to being roughly equal for the other silicate standards (Fig. 3.2a & b). According to Garvie and Buseck (1999), the observed relationship is likely related to changes in the symmetries of the $2p_{1/2}$ and $2p_{3/2}$ orbitals that makes their transition less favorable. Additionally, The splitting between peaks A' and A'' appeared to become generally more well resolved with an increase in the number of shared oxygen atoms (Fig. 3.2a & b) For the phyllosilicate standard spectra, the energy position of peak A', and by extension peak B, was relatively similar for kaolinite, illite, muscovite, and chlorite, shifted to higher energy for montmorillonite, and to lower energy for talc (Fig. 3.1b). For Q^4 silicates, peak A' was shifted to lower energy for crystalline quartz compared to a-SiO_2 and Al-SiO_2.

The peaks of montmorillonite were potentially shifted to higher energies, relative to the other phyllosilicates, due to a combination of: (i) characteristically low Al substitution within the Si-tetrahedral layers; (ii) increased strain on the Si-O-Al bonds that results from its octahedral structure, and (iii) hydrogen-bonding networks with interlayer water. In contrast, illite and muscovite are characterized by Al substitution within the Si-tetrahedral layer and K as an inner-sphere complex in the Si-tetrahedral layers instead of H_2O, while the trioctahedral structure of talc results in a much less strained configuration than dioctahedral structure. Additionally, there are OH^- groups associated with kaolinite that are filling holes in the hexagonal sheet structure. These structural characteristics of illite, muscovite, talc, and kaolinite potentially lower the Si-O bond energy and result in the observed shift of peaks A' and B to lower energies in the corresponding standard spectra relative to montmorillonite. In summary, both increasing crystallinity and increasing substitution of Al within the Si tetrahedron lower the energies of peaks A and B in ^{4}Si silicates.

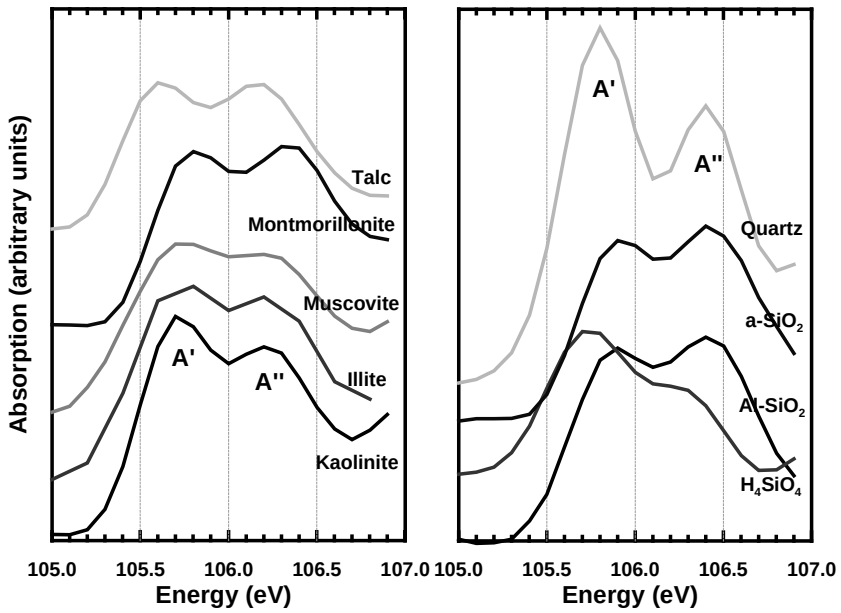

Figure 3.2. Enlargement of peak A region for selected Si $L_{2,3}$-edge FY spectra.

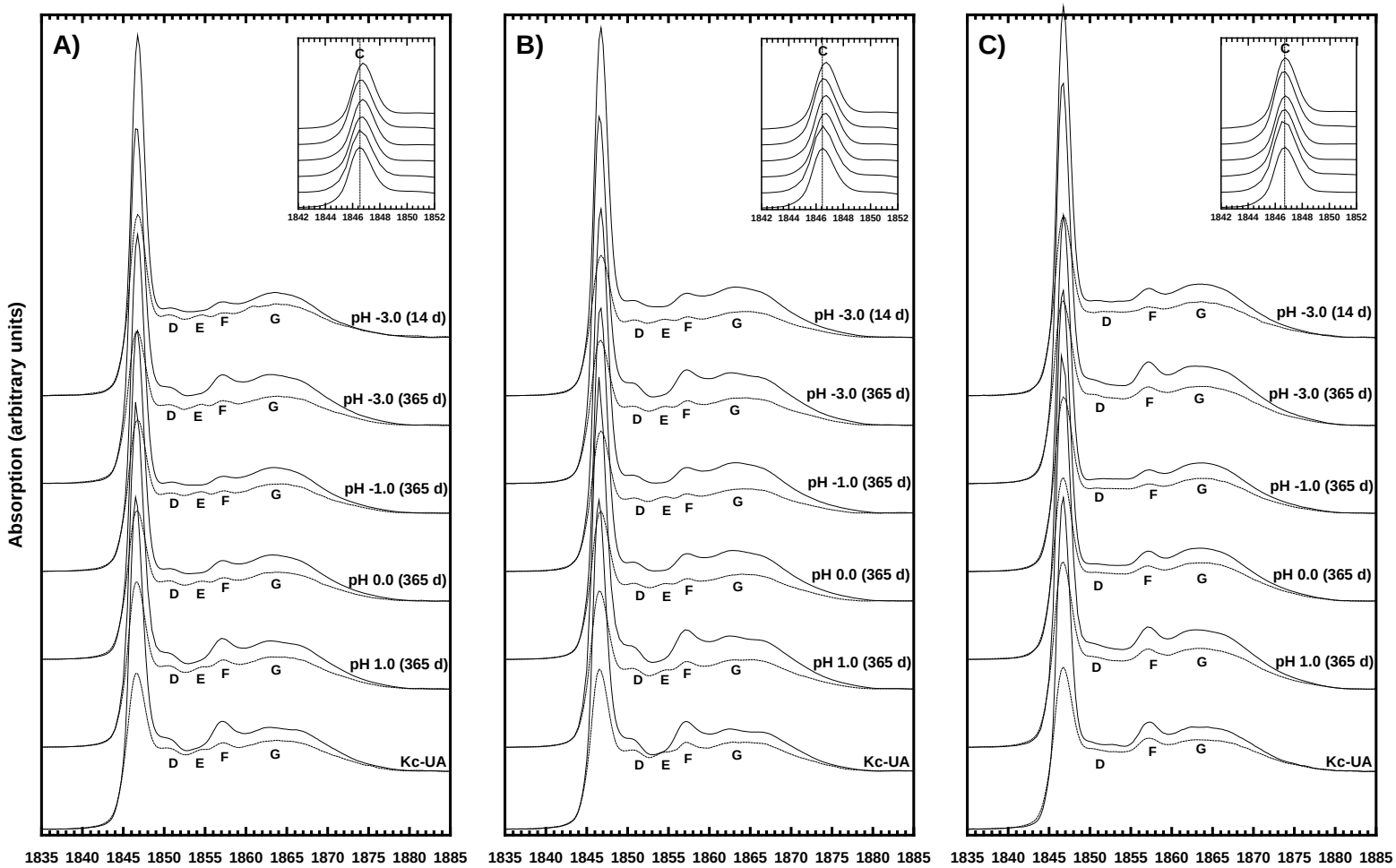

Figure 3.3. Si K-edge TEY (solid) and FY (dashed) spectra of unaltered (UA) and altered a) Kc, b) Km, and c) BK samples altered in H_2SO_4 solutions of pH 1.0, 0.0, -1.0, and -3.0 for durations of 14 and 365 day.

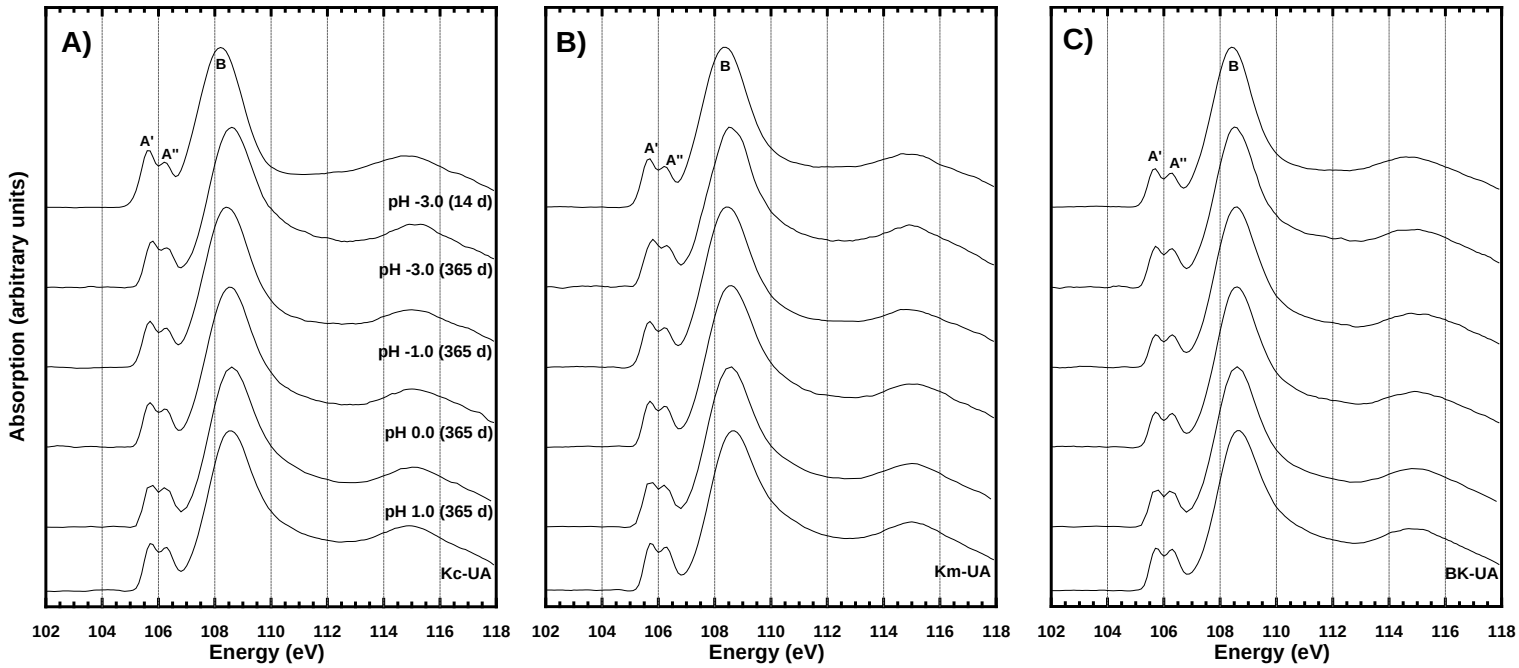

Figure 3.4. Si $L_{2,3}$-edge FY spectra of unaltered (UA) and altered a) Kc, b) Km, and c) BK samples altered in H_2SO_4 solutions of pH 1.0, 0.0, -1.0, and -3.0 for durations of 14 and 365 day.

3.4.1.4 Altered samples

The Si K-edge TEY and FY spectra for the Kc, Km, and BK batch experiments are presented in Figure 3.3a to 3.3c, while the corresponding Si $L_{2,3}$-edge FY spectra are illustrated in Figure 3.4a to 3.4c. The major peak features of the unaltered Kc and Km TEY spectra correlated well with the kaolinite standard spectrum (Fig. 3.1a), while the unaltered BK TEY spectrum (Fig. 3.3c) was best matched to montmorillonite (Fig. 3.1a). These observations were in good agreement with the mineralogical composition of the unaltered Kc, Km, and BK samples (Table 3.1). The Kc and Km Si K-edge FY spectra, representative of the sample bulk, indicated a combination of strong quartz-like and phyllosilicate-like peak signatures, while the BK spectra remained well matched to the montmorillonite standard (Fig. 3.3a & b). The Kc, Km, and BK Si $L_{2,3}$-edge spectra were characterized by equally intense peaks A' and A'', separated by 0.6 eV, and could not be differentiated from the major peak features. Wu et al., (1998) suggests that the major peak features in Si $L_{2,3}$-edge spectra are mainly controlled by short-range interactions with the first oxygen shell. This finding suggested that the mineralogical differences between the unaltered Kc, Km, and BK samples (Table 3.1) were not detected in the Si $L_{2,3}$-edge spectra owing to the similar short-range Si structure of phyllosilicates, which was previously observed in the standard spectra (Fig. 3.1b).

The Si K-edge TEY and FY spectra demonstrated a clear alteration of the Kc, Km, and BK Si structure with increased treatment acidity and duration (Fig. 3.3a-c). In both the TEY and FY spectra, a substantial decrease in the intensities of peaks D and F and increase in the intensity of peak E were observed at pH $\leq$ 0.0 and t $\geq$ 90 d, for all three samples (Fig. 3.3a-c). Additionally, the onset energy increased from 1846.50 to 1846.75 eV at pH $\leq$ 0.0 and t $\geq$ 90d, in the Kc and Km TEY and FY spectra, but remained unchanged in the BK spectra (Fig. 3.3a & b). In the Si $L_{2,3}$-edge spectra of all three altered samples, the peak A'/peak A'' intensity ratio increased with increased treatment acidity and duration, but was more pronounced for the Kc and Km spectra (Fig. 3.4a-c). The position of peak B shifted to lower energies in the Kc (pH $\leq$ -1.0, $\geq$ 90 d; 108.60 to 108.20 eV), Km (pH $\leq$ 1.0, $\geq$ 14 d; 108.70 to 108.40 eV), and BK (pH = -3.0, $\geq$ 14 d; 108.60 to 108.40 eV) spectra (Fig. 3.4a-c). However, the energy position of peak A' remained unchanged for all altered Kc, Km, and BK samples.

In the Kc and Km Si K-edge FY spectra, the alteration of peaks C, D, E, and F suggested the development of a quartz-like peak signature (Fig. 3.3a & b). Previous acidic dissolution studies demonstrate the unreactive nature of quartz, even under the most acidic conditions examined in the current study (Barrios et al., 1995; Breen et al., 1997; Madejova et al., 1998; Belver et al., 2002; Komadel, 2003; Wu and Ming, 2006). Moreover, the intensities of the main quartz peaks in the Kc, Km, and BK XRD diffractograms, collected by Shaw and Hendry (accepted), remain relatively constant with decreasing pH and increasing exposure time. Together, these observations suggested that the dissolution of phyllosilicates led to a relative increase in amount of quartz in the altered Kc and Km samples. A quartz-like signature was not evident in the BK Si K-edge FY spectra (Fig. 3.3c); instead the altered spectra were loosely similar to the standard montmorillonite spectrum. This difference can be attributed to the low quartz and substantial montmorillonite content of BK (Table 3.1), which was shown to be present even at pH -3.0 and 365 d through XRD analyses (Shaw and Hendry, accepted). In the Kc, Km, and BK Si K-edge TEY spectra, the shift of peak C to higher energies was indicative of an increase in Si polymerization from Q^3 to Q^4 (Li et al., 1995a), while the decreased intensity of peaks D and F suggested a decrease in the medium-range Si order (Neuville et al., 2004). Together the observed changes produced Si K-edge TEY spectra that took on a-SiO_2-like peak features with increased treatment acidity and duration (Fig. 3.3a-c). These results correlated well to those of Shaw and Hendry (accepted), where decreasing dissolved Si concentrations and growth of a broad amorphous peak in the Kc, Km, and BK XRD diffractograms were attributed to the precipitation of an a-SiO_2 phase at pH$\leq$ 0.0 and t $\geq$ 14 d. Moreover, the precipitation of a -SiO_2 has been observed in previous studies involving the acidic dissolution of monomineralic phyllosilicate phases, such as montmorillonite and kaolinite, at pH$\leq$ 0.0 (Mendioroz et al., 1987; Pesquera et al., 1992; Gates et al., 2002; Belver et al., 2002; Komadel, 2003; Tyagi et al., 2006). Therefore, the Si K-edge TEY and FY spectra showed the preferential dissolution of phyllosilicates within the Kc, Km, and BK samples, while the FY spectra suggested the formation of an a-SiO_2-like precipitate that was confined to the sample surfaces.

Garvie and Buseck (1999), through a comprehensive ELNES study of silicates show that the onset energy of peak A' generally increases with an increase in Si

polymerization. In the current study, the Kc, Km, and BK Si $L_{2,3}$-edge spectra are surface sensitive (Kasrai et al., 1996) and, thus, the observed alterations should generally correspond to the previous Si K-edge TEY discussion. In contrast to the K-edge TEY results, where increased Si polymerization was observed, the energy position of peak A' for the altered Kc, Km, and BK $L_{2,3}$-edge FY spectra remained unchanged. The apparent contradiction with the findings of Garvie and Buseck (1999) can be attributed to the excellent energy resolution achieved in the current study. In previous ELNES (e.g. Garvie and Buseck, 1999) and XANES (e.g. Li et al., 1994) studies the split between peaks A' and A'' is not well resolved, this means that earlier arguments that an increase in the energy position of peak A' is equal to increased Si polymerization are not directly applicable to our data. Moreover, as the Si $L_{2,3}$-edge FY spectra for the standard minerals suggested, the onset energy of peak A' was affected not only by the degree of polymerization, but also was sensitive to the chemical environment surrounding the SiO_4 unit, such as the substitution of Al, H_2O, or OH^- for O^{2-} in the lattice.

Given the sensitivity of the Si $L_{2,3}$-edge spectra, the observed shift of peak B to lower energies with decreasing pH and increasing exposure time, in the Kc, Km, and BK samples, is indicative of a fundamental change in the Si structure chemistry. These changes could potentially be controlled by one of two mechanisms, or a combination of both: 1) mineralogical changes in phyllosilicates, such as (i) a decrease in the strain on the Si-O-Al bonds, or (ii) an increase in the amount of tetrahedrally coordinated Al (^{4}Al); 2) ^{4}Al could have increased due to incorporation within the a-SiO_2 precipitate, a mechanism previously documented in pure-phase phyllosilicate acidic dissolution studies (Iller, 1979; Mendioroz et al., 1987). The involvement of one or more of these proposed mechanisms could not be determined from the available Si XANES data. Therefore, to gain additional understanding of the acidic dissolution of the Kc, Km, and BK samples, Al K-edge and $L_{2,3}$-edge XANES spectroscopy was next employed to probe the effects of increasing treatment acidity and duration on Al structure within our mixed phyllosilicate samples.

3.4.2 Al XANES study

3.4.2.1 K- and $L_{2,3}$-edge peak assignment

The Al K- and $L_{2,3}$-edge XANES of the reference mineral phases are presented in Figure 3.5a and 3.5b and are labeled according to the convention set out by Ildefonse et al. (1998). Only the Al K-edge TEY spectra were presented as the corresponding FY spectra were nearly identical to the TEY results. The Al $L_{2,3}$-edge TEY spectra were significantly affected by surface charging, as was observed by Weigel et al. (2008); therefore, only the Al $L_{2,3}$-edge FY spectra were presented. The Al K-edge onset energy (peak A' or A) result from electron transitions from the 1s to 3p Al orbitals (Cabaret et al., 1996). Additionally, Cabaret et al. (1996) and Wu et al. (1999) demonstrate that major peak features above the initial peak result from multiple scattering and medium-range Al order. In the Al $L_{2,3}$-edge spectra, peak A results from the excitation of Al 2p electrons to Al 3s and 3d orbitals (Hu et al., 2008; Weigel et al., 2008). Weigel et al. (2008) indicate that, similar to the Si $L_{2,3}$-edge spectra, the onset edge is split by spin-orbit coupling, which results in the separation of the 2p core state into $2p_{1/2}$ (L_2-edge; A') and $2p_{3/2}$ levels (L_3-edge; A''), which comprise the peak A region (Fig. 3.5b).

3.4.2.2 K-edge standard spectra

Previous studies demonstrate that Al K-edge XANES is diagnostic of the Al atoms coordinating environment, as it distinguishes between ^{4}Al and six-fold coordinated Al (^{6}Al) based on the onset energy position (Li et al., 1995b; Cabaret et al., 1996; Ildefonse et al., 1998; Doyle et al., 1999; van Bokhoven et al., 1999; Yoon et al., 2004). Specifically, the onset energy is shifted approximately 1.5 eV lower for ^{4}Al than ^{6}Al phases. In the current study, Al K-edge standards with ^{6}Al were generally characterized by two major peak features, approximately 10 eV in width; peak A situated between 1567.1 and 1567.7 eV and peak B between 1569.8 and 1571.5 eV (Fig. 3.5a). Conversely, the onset energy (peak A') for ^{4}Al standards occurred at approximately 1565.5 eV (Fig. 3.5a). Several previous studies attribute this shift to a change in the average Al-O bond length, from 1.9 Å for ^{6}Al phases to 1.7 Å for ^{4}Al phases (Kato et al., 2001; Weigel et al., 2008).

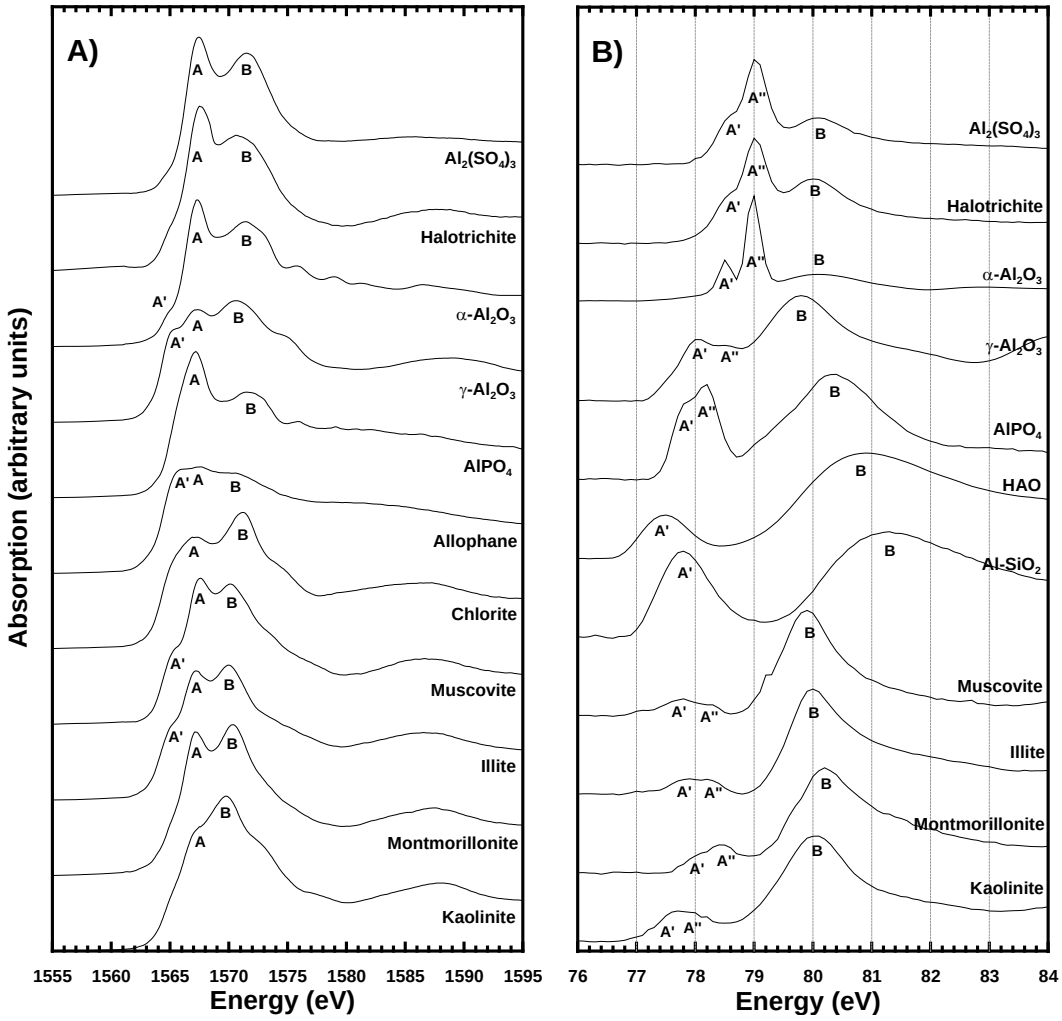

Figure 3.5. Al K-edge TEY and Al $L_{2,3}$-edge FY spectra of Al-containing standard minerals.

Corundum (α -Al_2O_3), synthetic aluminum sulfate ($Al_2[SO_4]_3$), and halotrichite are characterized by ^{6}Al surrounded by oxygen, which was evident from the position of peak A in the corresponding spectra (Fig. 3.5a). There was little difference between the synthetic and natural aluminum sulfate standards; however, halotrichite demonstrated a slight shoulder at peak A', associated with a small amount of ^{4}Al, and peak B was more intense and shifted to higher energy for $Al_2[SO_4]_3$. In contrast to α-Al_2O_3, γ-Al_2O_3 contained a substantial amount of ^{4}Al, estimated to be approximately 30 % by Bouchet Colliex (2003), which was expressed through the near-equally intense peaks A', A, and B (Fig. 3.5a). Conversely, $AlPO_4$, a solely ^{4}Al mineral, was shifted to higher energy than other ^{4}Al phases, which is attributed to the larger electronegativity of P compared to Si or

Al (Ildefonse et al., 1998). The position of peak A' for $AlPO_4$ in the current study (1567.2 eV) was significantly higher than that observed by Hu et al. (2008; 1566.1). Additionally, our spectra was better resolved with a clear splitting of peaks A and B, which Hu et al. (2008) assign to the amorphous nature of their standard. The Al-SiO_2 standard exhibited both ^{4}Al and ^{6}Al, but with little resolution was evident between peaks A', A, and B (Fig. 3.5a). The remaining standards consisted of 1:1 (kaolinite), 2:1 (montmorillonite, illite, muscovite), and 2:1:1 (chlorite) phyllosilicates. Kaolinite consists of a single Al-octahedral layer associated with a phyllosilicate sheet. The other phyllosilicate standards are characterized by an Al-octahedral layer bonded to two phyllosilicate sheets, and in the case of chlorite an additional Al layer. Peak B was substantially more intense relative to peak A for kaolinite and chlorite when compared to the remaining phyllosilicate standards (Fig. 3.5a). Theoretical calculations by Wu et al. (1999) and direct observations by Neuville et al. (2004) demonstrate that the intensity of peak B increases relative to peak A with an increase in the amount of Al in the silicate. Due to their 1:1 and 2:1:1 structures, both kaolinite and chlorite contain relatively more Al than montmorillonite, illite, and muscovite. The shift of peak B to slightly higher energy in the chlorite spectrum, compared to the other phyllosilicates, potentially is due to the incorporation of an additional Al-octahedral layer between the 2:1 stacking. The separation between peaks A and B was approximately 3.2 eV for montmorillonite and 2.5 eV for the remaining 2:1 phyllosilicates and kaolinite standard spectra. Illite, muscovite, and chlorite exhibited slight features associated with peak A', which suggested all three were comprised of a minor amount of ^{4}Al.

3.4.2.3 $L_{2,3}$-edge standard spectra

Relatively little information exists on the Al $L_{2,3}$-edge XANES of minerals; however, two recent studies have utilized high resolution XANES spectroscopy at the Al $L_{2,3}$-edge (Hu et al., 2008; Weigel et al., 2008). These studies provide some fundamental explanations for the shape and position of features in Al $L_{2,3}$-edge XANES spectra that are consistent with the current study. In general, the Al $L_{2,3}$-edge spectrum is dominated by the interactions between the ejected 2p electron of Al and unoccupied Al orbitals of s+d character. However, the ligands surrounding the Al and the coordination number of

those ligands both have a large effect on these electronic transitions. For this reason the Al $L_{2,3}$-edge is extremely chemically sensitive. In general, the $L_{2,3}$-edge spectra in the 76 to 84 eV range is dominated by two separate regions, which are termed peak A and peak B in this study (Fig. 3.5b) following the convention set by Weigel et al. (2008) and other researchers (Mo and Ching 2001). The Peak A region was often split into two or three distinct peaks (A', A'', A'''; Fig. 3.5b) due to spin-orbit coupling that allowed for resolution between the Al L_2- and L_3-edges (Wiegel et al., 2008). Additionally, the position and intensities of the peak A region were related to coordination number (^{4}Al is lower in energy than ^{6}Al) and the nature of the Al-O bond in structurally similar standards. Weigel et al. (2008) estimate that, using the Pauling electrostatic bond valance principle, the onset energy of peak A increases with increasing ionic character of the Al-O bond. Peak B was generally shifted to higher energy in ^{4}Al standards, but was also strongly affected by site distortions, which shifted it to lower energies (Fig. 3.5b). Asymmetry in peak B was ascribed to multiple coordinated Al (^{4}Al, ^{5}Al, ^{6}Al) all being present in a given standard. Finally, the observed variation in relative intensities of peaks A and B was related to selection rules transitions and; therefore, symmetries of the orbitals involved, with peak B typically being stronger in tetrahedral compounds due to s-p hybridization changing the selectivity rules (Shriver et al. 1994). However, distortion in the Al sites, being either tetrahedral or octahedral, also causes the relative intensity of peak B to increase (Weigel et al. 2008).

The major spectral features of the Al $L_{2,3}$-edge standard spectra (Fig. 3.5b) can be explained using the above discussion. Aluminum sulfate, halotrichite, and α-Al_2O_3 are generally characterized by ^{6}Al surrounded by oxygen, with an intense peak A clearly split into A' and A" and a weaker peak B. The α-Al_2O_3 standard spectrum in the current study is in good agreement with that of Weigel et al. (2008), who found that the width at half maximum of peaks A' and A" was generally characteristic of edge-sharing ^{6}Al compounds. As observed in the Al K-edge results (Fig. 3.5a), there was little difference between the peak positions of the synthetic ($Al_2[SO_4]_3$) and natural (halotrichite) $AlSO_4$ standards, while both had a more intense peak B (with a pronounced tail) and much broader A' and A" peaks than α-Al_2O_3 (Fig. 3.5b). However, for halotrichite, there was a slight broadening of the peak A region and an increased peak B intensity, relative to the

reagent, which was consistent with the small amount of ^{4}Al observed in the Al K-edge data (Fig. 3.5a). In contrast with α-Al_2O_3, γ- Al_2O_3 contains substantial ^{4}Al, which caused peaks A' and A" to broaden and shift to lower energy and peak B to increase in intensity and also shift to lower energy (Fig. 3.5b). Additionally, peak B appeared to contain a second component (~81.5 eV), which would be consistent with substitution of a substantial amount of ^{4}Al into the Al_2O_3 mineral structure. The γ-Al_2O_3 spectrum was in good agreement with that published by Hu et al (2008). The peak A region of the $AlPO_4$ standard spectra in Figure 4b can be resolved into A' and A" peaks. Weigel et al. (2008) also observe this clear splitting but Hu et al. (2008) do not, and attribute its absence to the amorphous nature of their $AlPO_4$ standard. Moreover, the position of peak B for $AlPO_4$ (80.40 eV; Fig. 3.5b) appears generally similar to that observed in Weigel et al. (2008; 80.45 eV), but substantially lower than that observed by Hu et al. (2008; 81.2 eV) The peak A region was shifted to lower energy than observed for α-Al_2O_3, which was consistent with a switch from ^{6}Al to ^{4}Al dominant coordination (Weigel et al., 2008). The strong Peak B was also consistent with ^{4}Al and the relatively symmetrical shape suggested a single type of coordination was present. The hydrous aluminum oxide standard (HAO) was extremely similar in synthesis method to the short range order Al (hydr)oxide studied by Hu et al. (2008) and, based upon theory and Al K-edge results (Fig. 3.5a), contained substantial ^{4}Al. Qualitatively, the corresponding spectra were quite similar with a broad peak A, due to unresolved L_2- and L_3-edges, and both were shifted to a lower energy than $AlPO_4$ (Fig. 3.5b). Additionally both spectra had a broad and intense peak B; however, in the current study, the position of peak B was shifted to higher energies than observed by Hu et al. (2008), which could be duet to slightly more ^{4}Al or ^{5}Al present in our sample, distortions in the bonding environments, or other unknown factors. The Al-SiO_2 spectrum (Fig. 3.5b) was similar in shape to the aluminosilicate glasses presented in Weigel (2008). However, both peaks A and B were shifted to slightly higher energies, potentially due to the presence of ^{6}Al, which was previously observed in the Al K-edge results for Al-SiO_2 (Fig. 3.5a).

The remaining standards were all considerably more complex in structure, with an octahedral layer of ^{6}Al linked to a phyllosilicate sheet, and have not previously been studied with Al $L_{2,3}$-edge XANES. The overall shape of all these clay minerals was

similar: a weak peak A region and an intense asymmetrical peak B, with similar intensities for all samples (Fig. 3.5b). The energy position of peak B increased from 79.9 to 80.2 eV among the muscovite, illite, kaolinite, and montmorillonite spectra. In the illite and muscovite spectra, the position of peak B was the lowest of the phyllosilicate standards (Fig. 3.5b), which was likely due to ^{4}Al substitution into the Si-tetrahedral layers. In kaolinite, peak B was similar in position, but more intense, to the α-Al_2O_3, Al_SO_4, and halotrichite standards. Based on the kaolinite structure, Al was expected to be present as predominantly ^{6}Al. However, the Al-O bonds in kaolinite were significantly more distorted than in the α-Al_2O_3 standard due to oxygen atoms being coordinated to the Si-tetrahedral layer, and protonated Al-O bonds that participate in extensive hydrogen bonding. For montmorillonite, peak B was more asymmetric and was shifted to higher energy than observed for kaolinite, which could be related to changes in the Al-O bonding environment for montmorillonite. Both axial oxygens of the Al-octahedral layer are coordinated to Si layers, and Mg substitution imparts an excess negative charge on the montmorillonite dioctahedral layer (Sparks, 1995), which substantially change the Al-O bond properties relative to kaolinite. Moreover, Mg substitution occurs preferentially at one of the Al crystallographic positions, which may explain the asymmetry of peak B. This highlights the complexity and sensitivity of the Al $L_{2,3}$-edge: coordination number and bond distortions both contribute to the observed positions and shapes of the spectral features.

The Peak A region, although weak in intensity, also contains much useful information. To facilitate discussion, the 76.0 to 79.0 eV region of the phyllosilicate standards was enlarged in Figure 3.6. For all standards, there was separation of the Al $L_{2,3}$-edge into two peaks (A' and A"). In kaolinite and montmorillonite, this splitting was less pronounced and the combined width of the peaks was less than muscovite and illite, which was consistent with the ^{4}Al observed in the Al K-edge results (Fig. 3.5a). Peak intensity was also substantially higher in kaolinite and montmorillonite, where only ^{6}Al was present. Additionally, the onset energy of montmorillonite was shifted to much higher energies than observed for the other phyllosilicates (Fig. 3.6). According to Weigel et al. (2008), one of the major reasons for the Al $L_{2,3}$-edge to shift to higher energies is the increasing ionic character of the Al-O bond, which could alternatively be

stated as the increasingly electronegative character of oxygen. As montmorillonite is a 2:1 clay mineral, it was expected that the bonding character of Al-O would be less ionic than for kaolinite, since axial Al-O bonds are linked to Si and not hydrogen. However, approximately one of every eight Al atoms in the dioctahedral layer of montmorillonite is replaced by Mg, which results in oxygen ligands that are actually more electronegative than those in the ideal unsubstituted system (or kaolinite). For illite and muscovite, peak A was broader, shifted to lower energies, and had a more pronounced splitting than montmorillonite (Fig. 3.6). Both minerals were characterized by mixed ^{4}Al and ^{6}Al coordinated environments. The ^{4}Al was present as a substitution in the phyllosilicate sheets of these minerals. Alternatively, the substitution of Fe into the Al-octahedral layer might have also lowered the onset energy. Weigel et al. (2008) did not observe electronic effects associated with Fe substitution; however, it is possible that in a crystalline material with a defined structure replacing Mg with a much better electron acceptor, such as Fe, could partially account for the observed shift to lower energies for illite and muscovite relative to montmorillonite.

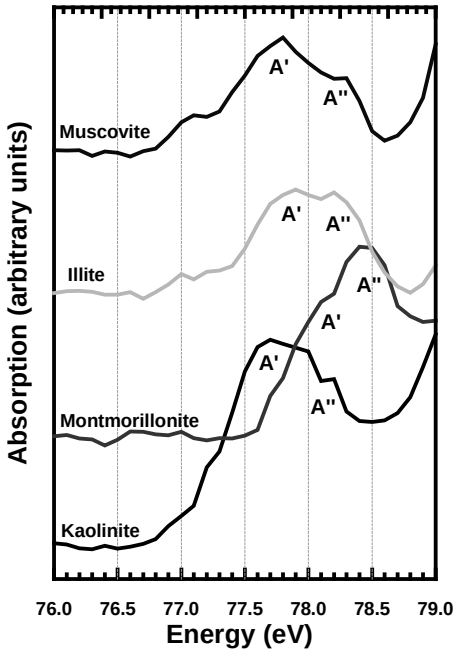

Figure 3.6. Enlargement of peak A region for phyllosilicate Al $L_{2,3}$-edge FY spectra.

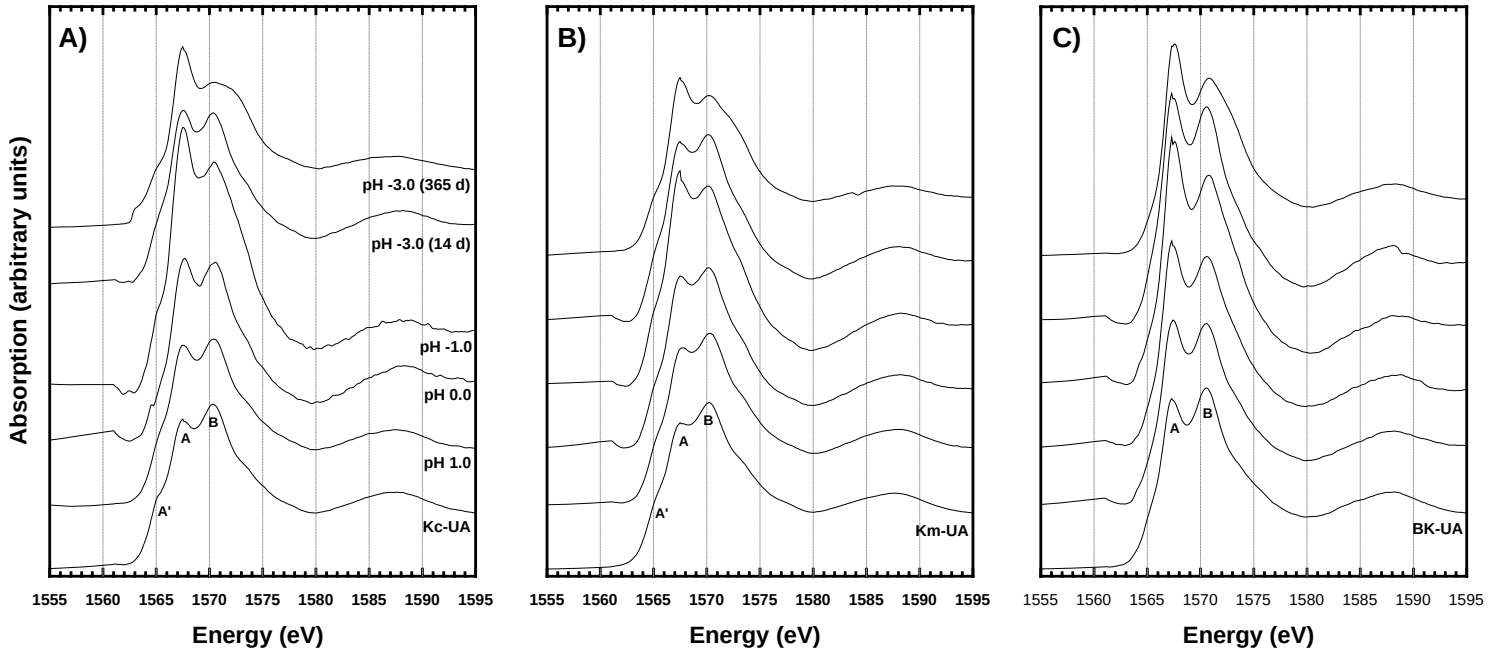

Figure 3.7. Al K-edge TEY spectra of unaltered (UA) and altered a) Kc, b) Km, and c) BK samples altered in H_2SO_4 solutions of pH 1.0, 0.0, -1.0, and -3.0 for durations of 14 and 365 days.

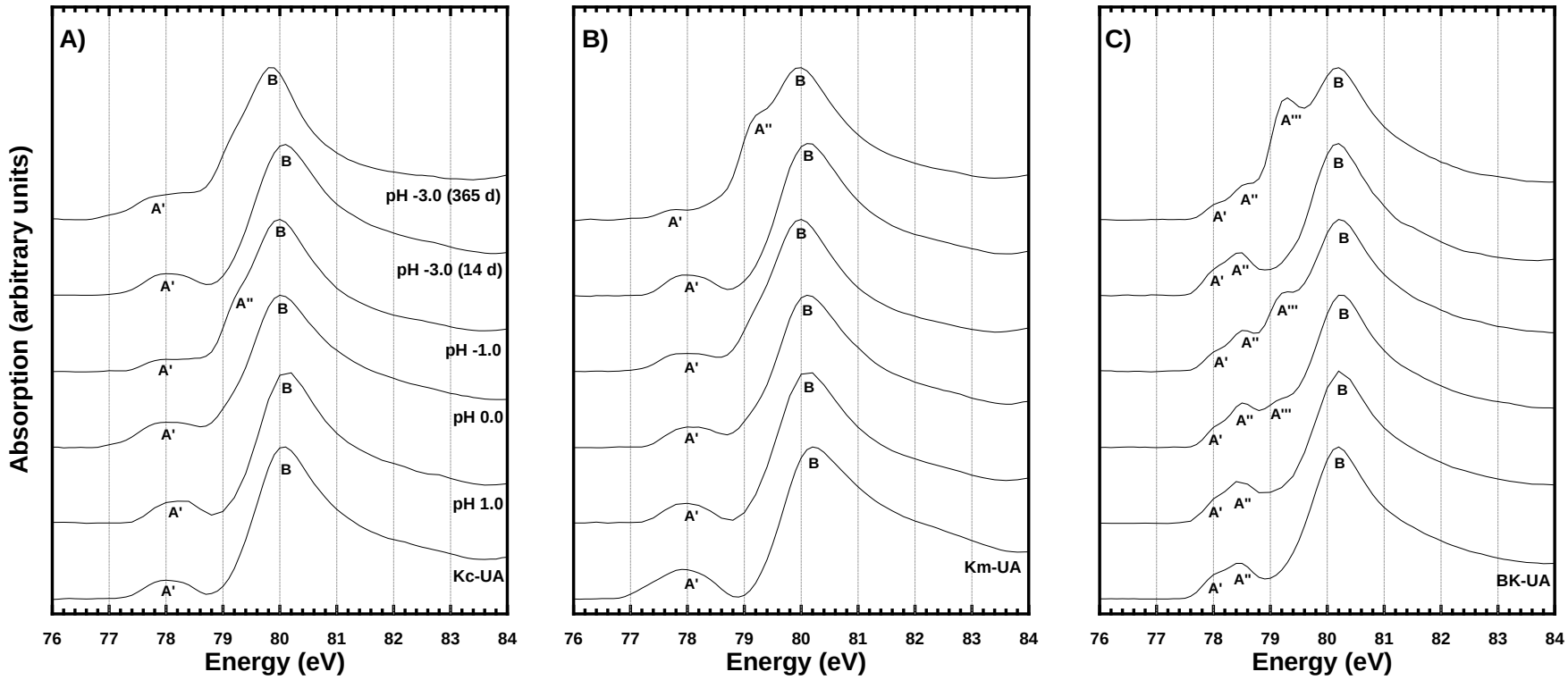

Figure 3.8. Al $L_{2,3}$-edge FY spectra of unaltered (UA) and altered a) Kc, b) Km, and c) BK samples altered in H_2SO_4 solutions of pH 1.0, 0.0, -1.0, and -3.0 for durations of 14 and 365 day.

3.4.2.4 Altered samples

The Kc, Km, and BK unaltered and altered Al K-edge TEY spectra are illustrated in Figures 3.7a to 3.7c, while the complimentary Al $L_{2,3}$-edge FY spectra are presented in Figures 3.8a to 3.8c. Similar to the Si K-edge XANES results, the unaltered Al K-edge spectra for each sample was well correlated to the peak features observed for the standard phyllosilicate spectra. Moreover, the Kc and Km spectra were also distinguished by small shoulders corresponding to ^{4}Al (peak A'; Fig. 3.7a & b), which likely corresponded to the substantial illite contents (Table 3.1). The Kc, Km, and BK Al $L_{2,3}$-edge spectra were similar to the peak features observed for the phyllosilicate standards (Fig. 3.8), a poorly resolved peak A and a much broader and intense peak B at approximately 78.0 and 80.2 eV (Fig. 3.5b).The Kc and Km Al $L_{2,3}$-edge spectra were characterized by a single, unresolved, peak A (Fig. 3.8a & b); however, peak A was broader and shifted to a slightly lower energy relative to Kc. Conversely, in the BK spectrum, peak A was separated into two poorly resolved features that had much higher intensities than the Kc and Km peaks (Fig. 3.8c). These observations suggested that the unaltered Kc and Km Al $L_{2,3}$-edge spectra were represented by a mix of the phyllosilicate standard spectra, with the greater kaolinite content of Km responsible for the observed shift to lower energy and increased width of peak A compared to Kc. Furthermore, the BK spectrum was well correlated to the major peak features previously discussed for the montmorillonite standard spectra.

The Al K-edge spectra of the Kc, Km, and BK samples indicated a substantial alteration of the Al structure with increasing treatment acidity and duration (Fig. 3.7a-c).The intensity of peak A increased and peak B decreased at pH$\leq$ 1.0 and t $\geq$ 14 d in all three samples, but was most pronounced for the BK samples (Fig. 3.7a-c). The intensity of peak A' slightly increased with decreasing pH and increasing exposure period for the Kc and Km Al K-edge spectra. Furthermore, the width of peak B increased considerably between pH -1.0 and -3.0 (365 d) in the Kc and Km spectra, and to a lesser extent for the BK spectra (Fig. 3.7 a-c). In the Kc and Km Al $L_{2,3}$-edge spectra, peak A remained as a single unresolved feature and exhibited a decreased intensity with increased treatment acidity and duration (Fig. 3.8a & b). In contrast, peaks A' and A'' remained clearly resolved, and the intensities relatively unchanged, in the BK spectra (Fig. 3.8c).

However, the position of the peak A region remained unchanged in the altered spectra of all three samples. The intensities of peak A'' (Kc and Km) and A''' (BK) progressively increased and eventually merged with peak A' (Kc and Km) and peak A'' (BK) at pH ≤ 0.0 and t ≥ 90 d. Peak B shifted to lower energy in the Kc (80.1 eV to 79.9 eV; pH ≤ 0.0, t ≥ 90 d) and Km (80.2 eV to 80.0 eV; pH ≤ 1.0, t ≥ 90 d), while remaining unchanged in the BK (80.2 eV) spectra (Fig. 3.8a-c).

In the Al K-edge spectra, the increased peak A/peak B ratio with increased treatment acidity and duration suggested that the amount of Al decreased relative to the Si content in the Kc, Km, and BK samples, a mechanism that Wu et al. (1999) and Neuville et al. (2004) describe in detail. Furthermore, the relative increase in the intensity of peak A' in the Kc and Km samples was well correlated to the persistence of illite, relative to montmorillonite and kaolinite, observed by Shaw and Hendry (accepted) through XRD analyses. As discussed for the Al K-edge standard spectra, illite is characterized by ^{4}Al that occurs through substitution within the Si-tetrahedral layer. These conclusions are consistent with those of Shaw and Hendry (accepted), who through aqueous and XRD analyses show the preferential dissolution of montmorillonite, illite, and kaolinite. They are also consistent with the previously discussed Si XANES results that indicated an increased polymerization of the Si structure through the dissolution of phyllosilicates. Additionally, the absence of peak A' from the altered BK spectra (Fig. 3.7c) showed that incorporation of Al within the Si-tetrahedral layer of the a-SiO_2 precipitate, as proposed in Section 3.1.3, did not occur at measurable amounts, at least in the BK samples.

Weigel et al. (2008) demonstrate that in Al $L_{2,3}$-edge FY spectra the energy position of the peak A region shifts to lower energy in minerals characterized by greater ^{4}Al than ^{6}Al. However, despite the increase in ^{4}Al expected by increased illite from XRD analyses (Shaw and Hendry, accepted) and in the Al K-edge results of this study, the position of peak A remains unchanged in the altered Kc, Km, and BK Al $L_{2,3}$-edge spectra (Fig. 3.8a-c). However, the average energy position of the peak A region in the phyllosilicate standard spectra were nearly identical for kaolinite and illite and shifted to higher energy by only 0.5 eV for montmorillonite (Fig. 3.6). Coupled with the unresolved and broad nature of the peak A region previously noted for Kc and Km spectra, the

increased illite content would not be expressed in a shift of the peak A region to lower energy. Conversely, the shift of peak B to lower energy (-0.2 eV) was diagnostic of the increased illite content in the Kc and Km spectra with increasing treatment acidity and duration (Fig. 3.8a & b). The absence of a similar shift in the BK spectra further supports this conclusion as BK initially contained no measurable ^{4}Al minerals, which was evident from the Al K-edge spectra and XRD results of Shaw and Hendry (accepted).

The Kc, Km, and BK batch experiments are have significant aqueous SO_4 concentrations at pH $\leq$ 1.0, which vary between 2.0 x 10^{-2} and 1.0 umol L^{-1} g^{-1} (Shaw and Hendry, accepted). In addition, Shaw and Hendry (accepted), through mass balance calculations and XRD analyses, propose that aluminite ($Al_2[SO_4][OH]_4 \bullet 7H_2O$), or a similar Al-$SO_4$ phase, precipitates in all three samples at pH $\leq$ 0.0. In the Al K-edge results, the altered Kc, Km, and BK spectra and the $Al_2[SO_4]_3$ and halotrichite standard spectra showed a strong visual match for the pH -3.0 (365d) samples. Furthermore, peaks A'' (Kc and Km) and A''' (BK) developed at pH $\leq$ 0.0 at approximately 79.3 eV (Fig. 3.8a-c), which roughly equaled the position of peak A'' in the ^{6}Al standard spectra of α-Al_2O_3, $Al_2[SO_4]_3$, and halotrichite (Fig. 3.5b) but were characterized by substantially lower intensities. These results appeared to confirm the formation of a new Al phase in the Kc, Km, and BK samples at pH $\leq$ 0.0 and t $\geq$ 90 d, which is likely an Al-SO_4 phase.

3.4.3 Conceptual model

The current study builds on the conceptual model for the dissolution of phyllosilicates in H_2SO_4 solutions developed by Shaw and Hendry (accepted) for pH 5.0 to -3.0. The model of Shaw and Hendry (accepted) describes the preferential dissolution of Al-octahedral layers at pH values $\leq$ 1.0 and the mobilization of the Si -tetrahedral layers into the aqueous phase, while an a-SiO_2 phase forms at pH $\leq$ 0.0. In the current study, Si K-edge TEY, FY, and Al K-edge TEY spectra showed the preferential dissolution of phyllosilicates within the Kc, Km, and BK samples at pH $\leq$ 0.0 and t $\geq$ 90 d. Additionally, the Si K-edge FY spectra suggested the formation of an a-SiO_2-like precipitate that was confined to the Kc and Km sample surfaces, but observed throughout the BK sample surface and bulk at pH $\leq$ 0.0 and t $\geq$ 90d. The formation of an Al-SO_4-rich phase was also proposed by Shaw and Hendry (accepted), which was well correlated to

the observed development of an Al-SO_4-like peak signature in the Al K-edge and $L_{2,3}$-edge spectra of all three phyllosilicate samples. Therefore, the results of the current study can be used to modify the conceptual model originally presented by Shaw and Hendry (accepted). Specifically, the results indicated the preferential dissolution of the phyllosilicate Al-octahedral layers at pH $\leq$ 1.0, persistence of ^{4}Al relative to ^{6}Al during Al-octahedral dissolution, dissolution of Si-tetrahedral layers at pH $\leq$ 0.0, and the precipitation of an Al-SO4-rich phase at pH $\leq$ 0.0 (Fig. 3.9).

3.5 Conclusions

The Si and Al K- and $L_{2,3}$-edge spectra in the current study, along with aqueous geochemical and XRD evidence (Shaw and Hendry, accepted) show the effects of acidic dissolution, with increased treatment acidity and duration, on the Si and Al structure of phyllosilicates contained within the Kc, Km, and BK mixed clay samples. The Si K-edge TEY and FY results indicate increased Si polymerization. Additionally, Si K-edge TEY spectra indicate decreased medium and long-range Si order at the sample surface, while Si K-edge FY results demonstrate an increase in Si order within the sample bulk. Combined the Si K-edge XANES results suggest the progressive dissolution of the phyllosilicates from the Kc, Km, and BK samples and the subsequent formation of an a-SiO_2-like precipitate confined to the surface of the samples. The Si $L_{2,3}$-edge XANES results suggest that the previous contention of Garvie and Buseck (1999) that the energy position of peak A was diagnostic of the degree of Si polymerization was not applicable to the better resolved data in the current study. Furthermore, comparison of the standard Si $L_{2,3}$-edge spectra with current bond energy theory indicated that the energy position of peak B is dependent on the relative strain imparted on the Si-O-M bond (where M is some metal) by the connecting metal. The shift of peak B to lower energies in the altered Kc, Km, and BK Si $L_{2,3}$-edge spectra indicated an increase in the relative amount of ^{4}Al substituted within the SiO_4 unit and was attributed to the increased amount of illite, which is more resistant to acidic dissolution than montmorillonite or kaolinite (Shaw and Hendry, accepted).

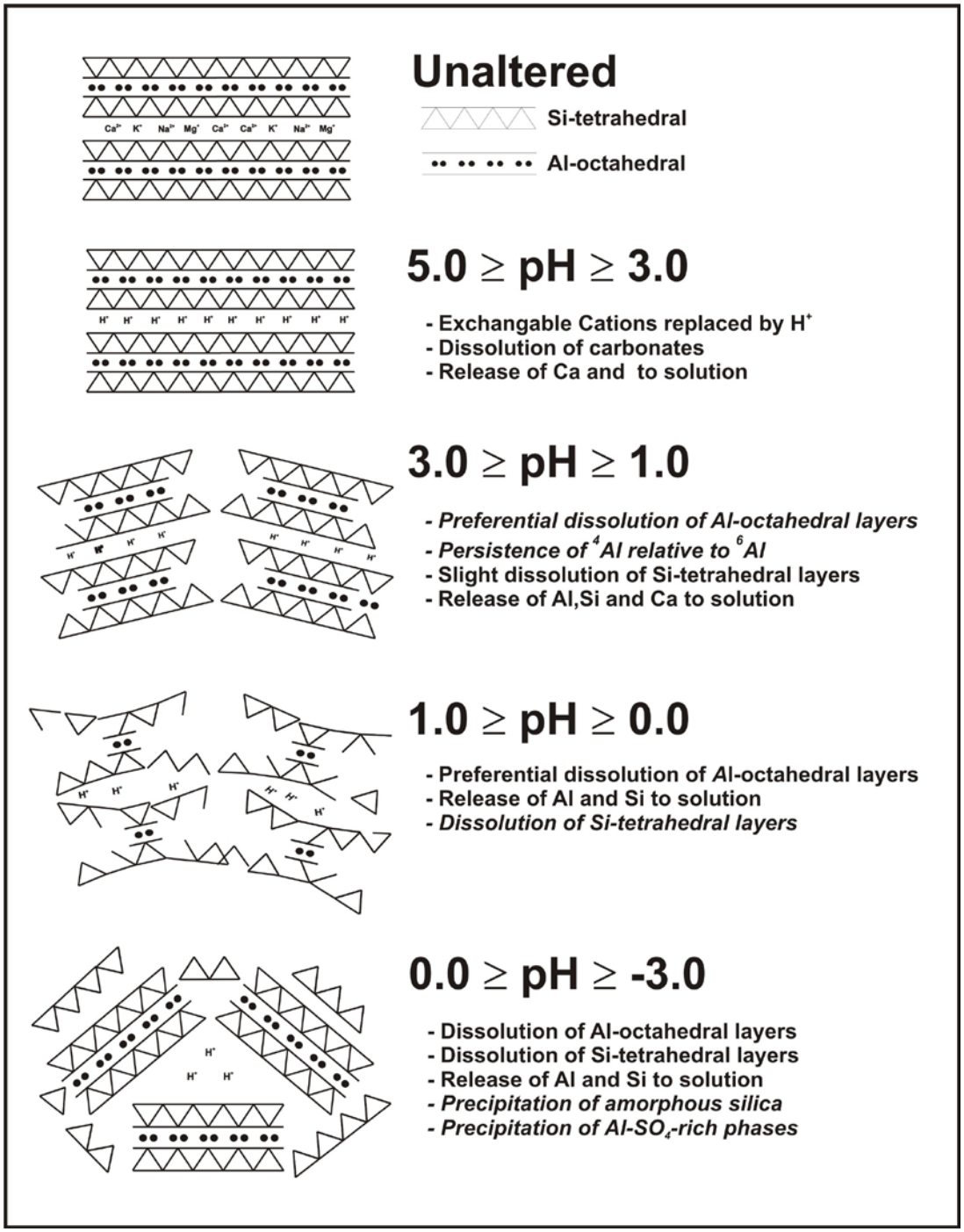

Figure 3.9. Conceptual model of phyllosilicate dissolution under extremely acidic conditions between pH 5.0 and -3.0. Modified from Shaw and Hendry (accepted).

The Al K-edge XANES confirm the progressive dissolution of the Al-octahedral layer suggested by the Si K-, $L_{2,3}$-edge XANES results and previously acquired aqueous geochemical data (Shaw and Hendry, accepted). Increased dissolution of Al relative to Si

structure was indicated by the increased peak A/peak B ratio in the Al K-edge spectra with increasing treatment acidity and duration. Preferential dissolution of montmorillonite and kaolinite in the Kc and Km samples, indicated by Shaw and Hendry (accepted) and observed in the Si $L_{2,3}$-edge results, was supported by the increased ^{4}Al content, relative to ^{6}Al, observed in the Al K- and $L_{2,3}$-edge spectra for Kc and Km. The formation of a new ^{6}Al phase at pH $\leq$ 0.0 and t $\geq$ 90 d was clearly evident in altered Kc, Km, and BK samples through a broadening of peak B in the Al K-edge spectra and growth of peaks A'' (Kc and Km) and A''' (BK) in the Al $L_{2,3}$-edge spectra.

The acidic dissolution of a substantial amount of the initial mixed clay material will have significant negative effect on the long-term integrity of clay linters rich in phyllosilicates. However, the observed precipitation of equally substantial amounts of secondary phases, such as a-SiO_2 and Al-SO_4, could serve to counter-balance the negative effects caused by the acidic dissolution. This study is the first to utilize Si and Al XANES analyses as a analytical tool for understanding the effects of acidic dissolution on mixed clay samples and demonstrates the additional information not obtainable through conventional geochemical methods. An existing conceptual model was modified to illustrate the processes involved during the acidic dissolution of phyllosilicates between pH 5.0 and -3.0.

3.6 Acknowledgements

The authors thank Lucia Zuin and Robert Blyth for their assistance with analyses conducted at the Canadian Light Source, Astrid Jurgensen and Narayana Apparthurai for their assistance with analyses conducted at the Synchrotron Radiation Center (DMR-0537588) and Yongfeng Hu for the many valuable discussions of the data. Funding was provided by Syncrude Canada Limited and NSERC through a Collaborative Research and Development Grant. A portion of the research was performed at the Canadian Light Source, which is supported by NSERC, NRC, CIHR, and the University of Saskatchewan.

3.7 References

Al, T. A., Martin, C. J., and Blowes, D. W., 2000. Carbonate-mineral/water interactions in sulfide-rich mine tailings. *Geochim. Cosmochim. Acta*. 64, 3933-3948.

Bantignies, J. F., Cartier Dit Moulin, C., and Dexpert, H., 1997. Wettability contrasts in kaolinite and illite clays: characterization by infrared and x-ray absorption spectroscopies. *Clays and Clay Minerals*. 45, 184-193.

Barrios, M. S., Gonzalez, L. V. F., Rodriguez, M. A. V., and Pozas, J. M. M., 1995. Acid activation of a palygorskite with HCl - Development of physicochemical, textural and surface-properties. *Appl. Clay Sci.* 10, 247-258.

Belver, C., Munoz, M. A. B., and Vicente, M. A., 2002. Chemical activation of a kaolinite under acid and alkaline conditions. *Chem. Mater* 14, 2033-2043.

Blowes, D. W. and Jambor, J. L., 1990. The pore-water geochemistry and the mineralogy of the vadose zone of sulfide tailings, Waite-Amulet, Quebec, Canada. *Appl. Geochem.* 5, 327-346.

Blowes, D. W., Reardon, E. J., Jambor, J. L., and Cherry, J. A., 1991. The formation and potential importance of cemented layers in inactive sulfide mine tailings. *Geochim. Cosmochim. Acta* 55, 965-978.

Blowes, D. W. and Ptacek, C. J., 1994. Acid-neutralization mechanisms in inactive mine tailings. In: *The Environmental Geochemistry of Sulfide Mine-Wastes, Short Course Handbook 22* (eds. D.W. Blowes and J.L. Jambor), Mineralogical Association of Canada Short Course 22, pp. 271-292.

Bouchet, D., and Colliex, C., 2003. Experimental study of ELNES at grain boundaries in alumina: intergranular radiation damage effects on Al-L_{23} and O-K edges. *Ultramicroscopy* 96, 139-152.

Breen, C., Zahoor, F. D., Madejova, J., and Komadel, P., 1997. Characterization and catalytic activity of acid-treated, size-fractionated smectites. *J. Phys. Chem. B* 101, 5324-5331.

Cabaret, D., Sainctavit, P., Ildefonse, P., and Flank, A. M., 1996. Full multiple-scattering calculations on silicates and oxides at the Al K edge. *J. Phys.Condens. Matter* 8, 3691-3704.

Chaboy J., Benfatto M., and Davoli I., 1995. Theoretical-analysis of X-ray-absorption spectra at the silicon K and L(2,3) edges of crystalline and amorphous SiO_2. *Phys. Rev. B* 52, 10014-10020.

Dold, B. and Fontbote, L., 2002. A mineralogical and geochemical study of element mobility in sulfide mine tailings of Fe oxide Cu-Au deposits from the Punta del Cobre belt, northern Chile. *Chem. Geol.* 189, 135-163.

Doyle, C. S., Traina, S. J., Ruppert, H., Kendelewicz, T., Rehr, J. J., and Brown, G. E., 1999. XANES studies at the Al K-edge of aluminum-rich surface phases in the soil environment. *J. Synchrotron Rad.* 6, 621-623.

Dubrovsky, N. M., Cherry, J. A., Reardon, E. J., and Vivyurka, A. J., 1985. Geochemical evolution of inactive pyritic tailings in the Elliot Lake Uranium District. *Can. Geotech. J.* 22, 110-128.

Garvie, L. A. J. and Buseck, P. R., 1999. Bonding in silicates: Investigation of the Si L_{-2},L_{-3} edge by parallel electron energy-loss spectroscopy. *Amer. Mineral*. 84, 946-964.

Gates, W. P., Anderson, J. S., Raven, M. D., and Churchman, G. J., 2002. Mineralogy of a bentonite from Miles, Queensland, Australia and characterization of its acid activation products. *Appl. Clay Sci*. 20, 189-197.

Gilbert, B., Frazer, B. H., Naab, F., Fournelle, J., Valley, J. W., and De Stasio, G., 2003. X-ray absorption spectroscopy of silicates for in situ, sub-micrometer mineral identification. *Amer. Mineral*. 88, 763-769.

Gunsinger, M. R., Ptacek, C. J., Blowes, D. W., Jambor, J. L., and Moncur, M. C., 2006. Mechanisms controlling acid neutralization and metal mobility within a Ni-rich tailings impoundment. *Appl. Geochem.* 21, 1301-1321.

Hu, Y. F., Zuin, L., Wright, G., Igarashi, R., McKibben, M., Wilson, T., Chen, S. Y., Johnson, T., Maxwell, D., Yates, B. W., Sham, T. K., and Reininger, R., 2007. Commissioning and performance of the VLS-PGM Beamline at the Canadian Light Source. *Rev. Sci. Instrum.* 78, 083109.

Hu, Y. F., Xu, R. K., Dynes, J. J., Blyth, R. I. R., Yu, G., Kozak, L. M., and Haung, P. M., 2008. Coordination nature of aluminum (oxy)hydroxides formed under the influence of tannic acid studied by X-ray absorption spectroscopy. *Geochim. Cosmochim. Acta.* 72, 1959-1969.

Ildefonse, P., Cabaret, D., Sainctavit, P., Calas, G., Flank, A. M., and Lagarde, P., 1998. Aluminum X-ray absorption near edge structure in model compounds and Earth's surface minerals. *Phys. Chem. Min.* 25, 112-121.

Iller, R.K., 1979. *The chemistry of silica.* Wiley, New York.

Jurjovec, J., Ptacek, C. J., and Blowes, D. W., 2002. Acid neutralization mechanisms and metal release in mine tailings: A laboratory column experiment. *Geochim.. Cosmochim. Acta* 66, 1511-1523.

Kashir, M. and Yanful, E. K., 2001. Hydraulic conductivity of bentonite permeated with acid mine drainage. *Can. Geotech. J.* 38, 1034-1048.

Kasrai, M., Lennard, W. N., Brunner, R. W., Bancroft, G. M., Bardwell, J. A., and Tan, K. H., 1996. Sampling depth of total electron and fluorescence measurements in Si L- and K-edge absorption spectroscopy. *Appl. Surf. Sci.* 99, 303-312.

Kato, Y., Shimizu, K., Matsushita, N., Yoshida, T., Yoshida, H., Satsuma, A., and Hattori, T., 2001. Quantification of aluminum coordinations in alumina and silica-alumina by AlK-edge XANES. *Phys. Chem. Chem. Phys.* 3, 1925-1929.

Komadel, P. 2003. Chemically modified smectites. *Clay Min.* 38, 127-138.

Levelut, D., Cabaret, D., Benoit, M., Jund, P., and Flank, A. M., 2001. Multiple scattering calculations of the XANES Si K-edge in amorphous silica. *J. Non. Cryst. Solids*. 293-295, 101-104.

Li, D., Bancroft, G. M., Kasrai, M., Fleet, M. E., Secco, R. A., Feng, X. H., Tan, K. H., and Yang, B. X., 1994. X-ray-absorption spectroscopy of silicon dioxide (SiO_2) polymorphs - the structural characterization of opal. *Amer. Mineral.* 79, 622-632.

Li, D., Bancroft, G. M., Fleet, M. E., and Feng, X. H., 1995a. Silicon K-edge XANES spectra of silicate minerals. *Phys. Chem. Min.* 22, 115-122.

Li, D. E., Bancroft, G. M., Fleet, M. E., Feng, X. H., and Pan Y., 1995b. Al K-Edge XANES Spectra of Aluminosilicate Minerals. *Amer. Mineral.* 80, 432-440.

Pesquera, C., Gonzalez, F., Benito, I., Blanco, C., Mendioroz, S., and Pajares, J., 1992. Passivation of a Montmorillonite by the Silica Created in Acid Activation. *J. Mater. Chem.* 2, 907-911.

Poe, B., Seifert, F., Sharp, T., and Wu, Z., 1997. ELNES spectroscopy of mixed Si coordination minerals. *Phys. Chem. Minerals*. 24, 477-487.

Madejova, J., Bujdak, J., Janek, M., and Komadel, P., 1998. Comparative FT-IR study of structural modifications during acid treatment of dioctahedral smectites and hectorite. *Spectrochim. Acta A* 54, 1397-1406.

Mendioroz, S., Pajares, J. A., Benito, I., Pesquera, C., Gonzalez, F., and Blanco, C., 1987. Texture evolution of montmorillonite under progressive acid treatment - change from H-3 to H2 type of hysteresis. *Langmuir* 3, 676-681.

Mo, S. D., and Ching, W. Y., 2001. X-ray absorption near-edge structure in alpha-quartz and stishovite: Ab initio calculation with core-hole interaction. *Appl. Sci. Let.* 78, 3809-3811.

Moncur, M.C., Ptacek, C.J., Blowes, D.W. and Jambor, J.L., 2005. Release, transport and attenuation of metals from an old tailings impoundment. *Appl. Geochem*. 20, 639-659.

Morin, K. A., Cherry, J. A., Dave, N. K., Lim, T. P., and Vivyurka, A. J., 1988. Migration of acidic groundwater seepage from uranium-tailings impoundments, 1. Field study and conceptual hyrodgeochemical model. *J. Contam. Hydrol.* 2, 271-303.

Neuville, D. R., Cormier, L., and Massiot, D., 2004. Al environment in tectosilicates and peraluminous glasses: A 27Al MQ-MAS NMR, Raman, and XANES investigation. *Geochim. Cosmochim. Acta.* 68, 5071-5079.

Nordstrom, D.K., Alpers, C.N., Ptacek, C.J. and Blowes, D.W., 2000. Negative pH and extremely acidic mine waters from Iron Mountain, California. *Environ. Sci. Technol.* 34, 254-258.

Regier, T., Paulsen, J., Wright, G., Coulthard, I., Tan, K., Sham, T. K., and Blyth, R. I. R., 2007. Commissioning of the spherical grating monochromator (SGM) soft x-ray spectroscopy beamline at the Canadian Light Source. *AIP Proc. for the 9th International Conference on Synchrotron Radiation Instrumentation* 879, 473-476.

Sparks, D. L. 1995. *Environmental soil chemistry*. Academic Press, San Diego.

Sracek, O., Choquette, M., Gelinas, P., Lefebvre, R., and Nicholson, R. V., 2004. Geochemical characterization of acid mine drainage from a waste rock pile, Mine Doyon, Quebec, Canada. *J. Contam. Hydrol.* 69, 45-71.

Shaw, S. A. and Hendry, M. J., accepted. Geochemical and mineralogical impacts of H_2SO_4 on clays between pH 5.0 and -3.0. *Appl. Geochem*.

Shriver, D. F., Atkins, P., and Langford, C. H., 1994. *Inorganic Chemistry. 2nd ed.* W.H. Freeman and Company, New York City.

Stohr, J., 1992 *NEXAFS Spectroscopy*. Springer-Verlag, New York.

Tyagi, B., Chudasama, C.D. and Jasra, R.V., 2006. Determination of structural modification in acid activated montmorillonite clay by FT-IR spectroscopy. *Spectrochim. Acta, Part A* 64, 273-278.

van Bokhoven, J. A., Sambe, H., Ramake,r D. E., and Koningsberger, D. C., 1999. Al K-edge near-edge X-ray absorption fine structure (NEXAPS) study on the coordination structure of aluminum in minerals and Y zeolites. *J. Phys. Chem. B.* 103, 7557-7564.

Weigel, C., Calas, G., Cormier, L., Galoisy, L., and Henderson, G. S., 2008. High resolution Al $L_{2,3}$-edge x-ray absorption near edge structure spectra of Al-containing

crystals and glasses: coordination number and bonding information from edge components. *J. Phys. Condens. Matter.* 20, 135219.

Wu, Z. Y., Jollet, F., and Seifert, F., 1998. Electronic structure analysis of α-SiO_2 via x-ray absorption near-edge structure at the Si K, $L_{2,3}$ and O K edges. *J. Phys. Condens. Matter*. 10, 8083-8092.

Wu, Z., Romano, C., Marcelli, A., Mottana, A., Cibin G. Ventura, G. D., Giuli, G., Courtial, P., and Dingwell, D. B., 1999. Evidence for Al/Si tetrahedral network in aluminosilicate glasses from Al K-edge x-ray-absorption spectroscopy. *Phys. Rev. B.* 60, 9216-9219.

Wu, P. X. and Ming, C., 2006. The relationship between acidic activation and microstructural changes in montmorillonite from Heping, China. *Spectrochim. Acta, Part A* 63, 85-90.

Yang, B. X., Middleton, F. H., Olsson, B. G., Bancroft, G. M., Chen, J. M., Sham, T. K., Tan, K., and Wallace, D. J., 1992. Double-Crystal Monochromator Beam Line on the Aladdin 1-Gev Storage Ring. *Rev. Sci. Instrum* 63, 1355-1358.

Yoon, T. H., Johnson, S. B., Benzerara, K., Doyle, C. S., Tyliszczak, T., Shuh, D. K., and Brown, G. E., 2004. In-situ characterization of aluminum-containing mineral-microorganism aqueous suspensions using scanning transmission X-ray microscopy. *Langmuir* 20, 10361-10366.

4.0 DIFFUSIVE TRANSPORT OF SULFURIC ACID IN CLAYS

4.1 Abstract

The diffusive transport of H_2SO_4 (at pH =1.0, -1.0, and -3.0) through two mineralogically distinct clays (Kc and Km) was examined using single reservoir, constant concentration, diffusion cells. At the end of the 216 day test period, geochemical analyses indicated diffusion of above-background concentrations of H^+ to depths of 80, 193, and 210 mm in the pH 1.0, -1.0, and -3.0 Kc cells and 138,≥ 288, and ≥ 288 mm in the Km cells, respectively. Elevated Ca, Al, Fe, and Si concentrations were associated with elevated H^+ values in all Kc and Km cells. Peak Ca, Al, Fe, and Si concentrations of 325, 403, 176, 11.7, and 1.38 x 10^3 μmol g^{-1} (Kc) and 32.4, 426, 199, 7.2, and 1.22 x 10^3 μmol g^{-1} (Km) were measured in the pH 1.0, -1.0, and -3.0 cells. XRD results showed that these elevated concentrations corresponded to the loss of carbonate and montmorillonite peaks and decreased peak intensities for illite and kaolinite in depth intervals with pH ≤ 1.0 in the Kc and pH -1.0 and -3.0 in the Km cells. Si K-edge XANES results were well correlated to XRD results and demonstrated decreased phyllosilicate peak features over the same depth intervals. The diffusive transport of H^+ within the cells was modeled using a one-dimensional transport model derived from absorption isotherms from a series of previously conducted batch tests between pH 5.0 and 1.0 on the Kc and Km clays. Model results suggested that the batch test results can approximate the observed H^+ consumption in the pH 1.0; however, they greatly underestimate the amount of H^+ consumption in the pH -1.0 and -3.0 cells. The results of this study indicate that, despite the extreme pH values considered, diffusion of H_2SO_4 solutions with pH < 1.0 will be greatly attenuated in the presence of a strongly neutralizing mineral phase, such as dolomite, within the clay.

4.2 Introduction

The presence of acid in geologic media, derived from either natural weathering or mining-induced processes, can control solute migration and the stability of minerals. Generally, there is a negative correlation between pore-water pH and dissolved constituent concentrations, such as Al, Fe, and most divalent metals (Cu, Zn, Ni, Co), which leads to increased mobility in the aqueous environment. Metal mobility results

from the dissolution of minerals caused by their decreased stability in the presence of acid (Blowes and Ptacek, 1994).

The most significant body of literature addressing the interactions between acid and geologic media is related to acid mine drainage (AMD) (e.g. Dubrovsky et al., 1985; Blowes and Jambor, 1990; Blowes and Ptacek, 1994; Schuring et al., 1997; Al et al., 2000; Kashir and Yanful, 2001; Jurjovec et al., 2002; Moncur et al., 2005). These settings are typically characterized by pH < 5.0 and elevated dissolved sulfate (SO_4) and metal concentrations, produced through oxidation of sulfide minerals (Blowes et al., 2003). Studies demonstrate that the release of hydronium ions (H^+) and dissolved metals in AMD systems are typically lower than predicted for the amount of acid introduced into the affected system (Dubrovsky, 1986; Morin et al., 1988; Blowes et al., 2003). Morin et al. (1988) were the first to describe these processes through a series of acid-neutralizing reactions governed by the relative solubility of mineral phases present in the geologic media of interest. Subsequent refinements demonstrate a sequence of reactions that controls the pore-water pH, which consist of the dissolution and precipitation of carbonates, hydroxides, and the dissolution of phyllosilicates (Blowes and Jambor, 1990; Blowes and Ptacek, 1994; Jurjovec et al., 2002). Blowes and Ptacek (1994) demonstrate that carbonate, Al-hydroxide, Fe-hydroxide, and phyllosilicate buffering reactions maintain the pH of affected pore-waters at values ranging from, 4.8 to 7.5, 4.0 to 4.3, 2.5 to 3.5, and 1.5, respectively. Additionally, attenuation of mobilized metals can occur through either secondary mineral precipitation or sorption to mineral surfaces (Blowes and Ptacek, 1994). Jurjovec et al. (2002) demonstrate that carbonate dissolution occurs relatively rapidly, while phyllosilicate dissolution is kinetically limited and varies widely among the phyllosilicates (Jambor et al., 2002).

Most AMD settings are characterized by pH > 1.0 (e.g. Al et al., 2000; Blowes et al., 2003; Hammarstrom et al., 2003; Sidenko and Sherriff, 2005; Gunsinger et al., 2006), and relatively few studies involve more acidic (pH < 1.0) conditions. These very low pH environments include Heath Steele, New Brunswick, Canada (pH ≥ 0.80; Blowes et al., 1991), Sherridon, Manitoba, Canada (pH ≥ 0.67; Moncur et al., 2005), and Iron Mountain, California (pH ≥ -3.6; Nordstrom et al., 2000). The authors of these studies indicate complete dissolution of carbonates, hydroxides, significant degradation of

phyllosilicates, and precipitation of large amounts of hydrated Fe and Al sulfates associated with these extreme pH conditions.

Another environment similar to AMD is the long-term storage of zero-valent sulfur (S^0) that is recovered as a by-product from oil and gas production. The recovered S^0 is typically stored in large, above-ground, unsaturated blocks situated on engineered clay liners. These S^0 blocks are susceptible to the ingress of atmospheric oxygen and precipitation that can produce sulfuric acid (H_2SO_4). The H_2SO_4-rich leachate discharging from the base of these unsaturated S^0 blocks is routinely characterized by pH < 1.0. While the majority of S^0 blocks are deconstructed after a few weeks to months, geographical and economical factors in the Alberta Oilsands can result in the blocks being maintained for decades. Therefore, the long-term effects of H_2SO_4 production on the surrounding environment are of concern. In a study of the geochemical effects of H_2SO_4 on mixed clays between pH 5.0 and -3.0, Shaw and Hendry (accepted) observe increasing dissolution of phyllosilicates and preferential dissolution of the associated Al-octahedral layer, with decreasing pH and increasing exposure time. Additionally, these authors note the precipitation of amorphous silica, gypsum/anhydrite, and an Al-SO_4 phase at pH < 1.0. Warren and Dudas (1992a), in an investigation of a 25 year old S^0 block, observe acid infiltration into the surrounding calcareous till to depths 600 mm and pH values between 1.6 and 6.8. The authors also show the complete removal of carbonates, preferential dissolution of the Al-octahedral layer of smectites, and the formation of a substantial amount of Fe-oxyhydroxides and gypsum (Warren and Dudas, 1992b). Beyond these investigations, studies on the impact of long-term S^0 storage on the surrounding environment are absent from the scientific literature.

The goal of the current study was to improve our understanding of the geochemical effects of H_2SO_4 diffusion through clays, between pH 1.0 and -3.0. The specific objectives of this study were to: (i) define the geochemical controls on the diffusive transport of H_2SO_4 through clay, (ii) describe the effects of diffusive transport on the primary and secondary mineralogy of the clays, and (iii) simulate the diffusive transport of H_2SO_4 through clay. These objectives were met through a series of diffusion

cell experiments conducted on simulated compacted clay liners at pH values of 1.0, -1.0, and -3.0. To make the results applicable to a wide range of clays, two mineralogically distinct clays, typically used for natural liners and covers in mining applications, were tested. The modeling effort was limited to diffusive-retardation modeling.

4.3 Materials and methods

4.3.1 Clay samples

The two clay samples tested were obtained from the Syncrude Canada Limited (SCL) Mildred Lake mine site, located 60 km north of Fort McMurray, Alberta, Canada. The Kc and Km clays were from the Mannville Group, a Cretaceous deposit that overlays much of the Western Canadian Sedimentary Basin. The Kc clay was used in the construction of the containment liners beneath the SCL above ground S^0 storage blocks, while the Km has been considered for use in liner construction. The mineralogy characterization of the unaltered Kc and Km clays are summarized in Table 4.1.

Table 4.1. Geochemistry of the unaltered Kc and Km clay samples (after Shaw and Hendry, accepted).

Mineral Phase	Composition (weight %)			
	Kc		Km	
	< 63µm	***< 2µm***	***< 63µm***	***< 2µm***
Quartz	53.9	17.8	30.4	4.8
Smectite	1.8	23.0	0.3	0.5
Kaolinite	11.5	22.4	42.6	61.3
Illite	9.5	29.1	20.3	28.9
Plagioclase	10.8	0.0	1.0	0.5
Chlorite	3.4	7.7	1.3	1.5
Dolomite	9.3	0.0	0.0	0.0
Siderite	0.0	0.0	4.3	2.6
Total Carbonate (%)	3.3		0.0	
CEC (meq $100g^{-1}$)	28.5		20.3	
Surface Area ($m^2\ g^{-1}$)	29.3		22.9	

4.3.2 Diffusion cell design

The diffusive transport of the acidic solutions through the clays was investigated using six constant source single-reservoir diffusion cells constructed from PVC pipe.

Each cell had an inner diameter of 76 mm and a path length of 300 mm. Approximately 2.4 kg of homogenized, unaltered Kc or Km (< 0.063 mm) was mixed with nanopure water (~17.5 μS mm^{-1}) to achieve saturated conditions. To simulate the conditions found in liners beneath S^0 blocks (data not shown), the cells were uniformly packed to a dry bulk density of 1400 kg m^{-3}. Additionally, the average dry bulk density (ρ_b) and water content (θ) were 1.62 and 0.44 for Kc and 1.68 and 0.42 for Km. The specifications are consistent with previous field measurements of the compacted clay liner beneath an existing S^0 block (unpublished data). A nylon screen/PVC filter plate combination was placed between the top of the packed clay and the H_2SO_4 reservoir (365 cm^3 volume) in each diffusion cell. The column was vented to the atmosphere through the reservoir.

4.3.3 Experimental design

Synthetic H_2SO_4 reservoir solutions were prepared from trace-grade H_2SO_4 (JT Baker) and nanopure water to concentrations of 0.10, 2.3, and 5.2 mol L^{-1} (with ionic strengths of 0.19, 4.6, and 10.3 M, respectively). The pH values of these solutions were determined using the method of Nordstrom et al. (2000) and were equal to 1.0, -0.9 and -2.8, respectively. Approximately 100 g of the H_2SO_4 solutions were added to the each respective diffusion cell reservoir, through sealable access ports, using a large gauge stainless steel needle. For simplicity, the six diffusion cells, Kc pH 1.0, -1.0, and -3.0 and Km pH 1.0, -1.0, and -3.0, are referred to as Kc_1, Kc_{-1}, Kc_{-3}, Km_1, Km_{-1}, and Km_{-3}. The pH of the clay profile in each diffusion cell were measured, on a weekly basis, using a spear-tip pH probe (Orion 8163BN) through re-sealable observation ports at 30, 90, and 240 mm along the length of the diffusion cell wall. The diffusion cell experiments were conducted for 216 d, which was approximately equal to the time required for the pH front to breakthrough ($pH \leq 4.0$) the 90 mm observation port in the Kc_{-3} cell. Reservoir pH was monitored, on a daily basis, using a glass-body combination pH electrode. Solutions were collected and replaced with fresh solutions when pH values decreased by$\geq$ 0.2 units. The reservoir solutions were collected into 125 mL HDPE bottles and stored at approximately 4°C for quantitative analysis.

4.3.4 Clay recovery

At the conclusion of each experiment, the diffusion cell reservoir was disassembled and the clay was extruded through the cell top using a hydraulic jack. The extruded clay was sectioned into 11-20 sub-samples using a stainless steel wire. The pH and Eh of the top and bottom of each sub-sample was immediately measured with a spear-tipped glass combination electrode (Orion; Model #8163BN) using the method of Nordstrom et al. (2000). The sub-samples were then double sealed in plastic bags and stored at 4°C for aqueous geochemistry and solid phase mineralogy analyses.

4.3.5 Aqueous geochemistry

Attempts to recover pore-water solutions from the clay sub-samples using both centrifugation and piston-squeezing methods were unsuccessful. As a result, water extracts were used to estimate the aqueous geochemistry of the *in-situ* pore-waters. It is likely that readily soluble secondary phases formed within the clay sub-samples, given the large amount of SO_4 that was introduced into the diffusion cells. The possibility that these phases would undergo partial dissolution and increase the measured ion concentrations was considered. Therefore, both 1:1 and 1:100 (solid: liquid) pore-water extractions were conducted. 1:1 extracts were selected to best approximate the typical pore-water solution. These extractions could result in only partial dissolution of any readily soluble secondary phases present in the clay samples. The 1:100 extracts were conducted to ensure the complete dissolution of these phases and were considered representative of the total soluble (aqueous + water soluble phases) amounts of the major aqueous constituents.

The 1:1 and 1:100 extracts were conducted by homogenizing the clay sub-sample, collecting either a 40 g or 1 g aliquot into a 125 mL HDPE bottle, and adding either 40 or 100 g of nanopure water. For sub-samples with $pH \leq 1.0$, a standardized H_2SO_4 solution of equal pH was used instead of nanopure to approximate the ionic strength of the *in-situ* pore-water. All extraction bottles were continuously agitated at room temperature (22 to 25°C) for 24 hours to ensure adequate dissolution of all soluble phases and centrifuged (15 min; 3000 g) to separate the liquid and solid phases. The collected liquid phases were filtered through a 0.45 µm cellulose-nitrate membrane, pre-conditioned with 10 mL of

nanopure water, collected into separate bottles for cation (125 mL HDPE) and anion (20 mL HDPE) analyses, acidified with trace-grade H_2SO_4 (5 % v/v, cations only), and refrigerated at approximately 4°C for further analyses.

Atomic absorption spectroscopy (AAS, Varian X5) was used to quantify Al, Fe, Si, Ca, Mg, and Na for the 1:1 water extracts, while ion chromatography (IC, Dionex IC25/DX-320) was used to quantify SO_4^{2-} concentrations. The sample replicate precisions for these elements were ± 3.5, 2.0, 5.0, 2.4, 2.2, 1.8, and 4.2, respectively. For the 1:100 extracts, inductively coupled plasma atomic emission spectroscopy (ICP-AES, Spectro Cirros CDD) was used to quantify Al, Fe, Si, Ca, Mg, Na, and SO_4^{2-} concentrations, which had average sample replicate precisions of ± 2.6, 1.8, 2.1, 3.8, 2.3, 1.5, and 0.9 %, respectively. All concentrations were normalized to the dry weight of clay used in each extract and are reported as μmol g^{-1}.

4.3.6 X-ray diffraction analyses

Mineral identification was performed on selected air-dried sub-samples from the Kc and Km cells. Analyses were performed using Ni-filtered Cu K-α radiation at 1.6KVA with a Sol-X energy dispersive x-ray detector (Bruker AXS D8-Advance). All Kc samples were solvated with ethylene glycol prior to analysis as they contained expandable mineral phases (Moore and Reynolds, 1989). All reported angular notations were referred to in degrees 2-theta (°).

4.3.7 Si K-edge XANES analyses

Si K-edge XANES measurements were performed at the University of Wisconsin Synchrotron Radiation Center (Madison, WI) using the Canadian Synchrotron Radiation Facility double crystal monochromator beamline (DCM; Yang et al., 1992). Continuous Si K-edge spectra were collected over the region of 1825 to 1890 eV using step intervals of 0.5 eV (1825 to 1840 eV) and 0.25 eV (1840 to 1890 eV) with a one second dwell time for each point. Surface sensitive total electron yield (TEY) and bulk sensitive fluorescence yield (FY) were measured simultaneously on all three beamlines. The photon energy resolution value was 0.25 eV.

Sample preparation consisted of grinding the samples to a fine powder with a agate mortar and pestle and placing them on carbon tape supported with a stainless steel sample holder. Duplicate spectra were obtained for each sample and averaged. All spectra were normalized to the incident photon flux (I_0), which was monitored by a Samson-type ionization chamber filled with nitrogen gas at 1.0 torr pressure. A first-order polynomial baseline was taken and then normalized to an edge step of one for Si (1826 to 1836 eV; 1880 to 1890 eV.

4.3.8 Transport modeling

Fick's first law for one-dimensional transport in saturated soils can be applied in cases where advection is negligible, such as in low permeable clays, and solute transport is dominated by diffusive transport (Shackelford, 1991):

$$J_D = -D_0 \tau n \frac{da}{dx} \qquad [4.1]$$

where J_D is the diffusive mass flux of solute (M L^{-2} T^{-1}), a is mass activity of the solute (M L^{-3}), x is the distance of transport (L), τ is the dimensionless tortuosity factor, n is the total porosity of the clay, and D_o is the aqueous diffusion coefficient (L^2 T^{-1}) of the species of interest in free water. According to Shackelford (1991), the effective diffusion coefficient in soil (D^*) can be utilized in order to account for the tortuosity factor:

$$D^* = D_0 \tau \qquad [4.2]$$

Therefore, Fick's first law can be expressed as:

$$J_D = -D^* n \frac{da}{dx} \qquad [4.3]$$

The diffusive transport of a solute through clay is controlled both by the diffusive flux and chemical and/or biological reactions that retard the solutes movement. An adsorption isotherm can be sued to characterize these interactions by developing a relationship between the mass of species adsorbed to the soil solid, S (M M^{-1}) and the activity in solution, a. The slope of the adsorption isotherm is referred to as the distribution

function. A typical relationship used to describe non-linear distribution functions is the Freundlich isotherm, defined by Fetter (1988) as follows:

$$S = K_d a^b \qquad [4.4]$$

where *b* is a fitting coefficient.

In the case where the adsorption isotherm is linear the slope is described as the distribution function (K_d). In this case the attenuation provided by adsorption is independent of concentration and this gives rise to a dimensionless retardation factor, R_d defined as follows:

$$R_d = 1 + \left(\frac{\rho_b}{\mathrm{n}}\right)(\mathrm{K_d}) \qquad [4.5]$$

where ρ_b (M L^{-3}) is the dry bulk density, n is the porosity, and K_d is the distribution coefficient.

The use of the dimensionless retardation factor (R_d) allows the rate of transport for an attenuated species to be expressed as a ratio of the rate of transport for a non-reactive solute (such as chloride). Therefore, in a diffusion dominated system (such as a clay liner) Fick's second law can be used to calculate the rate diffusion (Shackelford, 1991):

$$\frac{\partial c}{\partial t} = \frac{D^*}{Rd}\frac{\delta^2 a}{\delta x^2} \qquad [4.6]$$

A series of one-dimensional diffusive transport simulations were conducted on the migration of H^+ in all diffusion cells, assuming either no adsorption or non-linear adsorption took place, to better understand the effect of mineral dissolution on the migration of H_2SO_4 in the cells. For all simulations a D* value of 6.54 x 10^{-9} m^2 s^{-1} was employed, which was calculated from the literature D_0 value (9.34 x 10^{-9} m^2 s^{-1}; 25°C; Lakatos, 2004) and an assumed tortuosity factor of 0.70. Source H^+ activities, calculated from the measured reservoir solution pH, of 9.65 x 10^1, 8.52 x 10^3, and 5.63 x 10^5 g m^{-3} were used in the pH 1.0, -1.0, and -3.0 simulations, respectively.

It is important to note that in this form of Fick's second law, it is assumed that there is the porosity of the domain is uniform and that the effective porosity for diffusion (e.g. Ficks' First Law) is the same as the porosity describing the accessible pore-space

available to the species of interest. The use of an adsorption relationship is also predicated on the assumption that the adsorption process is 'instantaneous' (e.g. 'fast' relative to chemical kinetics) and reversible.

To date, the scientific literature lacks a thermodynamic database that incorporates mineral dissolution and precipitation reactions within the pH ranges examined in the current study. Therefore, we were unable to use a geochemical transportation code to model the observed aqueous geochemical results from the diffusion cells. However, in an attempt to model the diffusive transport of H_2SO_4 through the cells, the observed pH profiles measured in the Kc and Km cells were simulated with CTRAN/W (GeoSlope International Ltd., 1991) using a backward-difference approximation for time integration. The finite-element model was set up as a cell with homogenous material properties for both Kc and Km. For the initial conditions, the boundary conditions of the reservoir nodes were set equal to the measured reservoir H^+ activities (9.65×10^1, 8.52×10^3, and 5.63×10^5 g m^{-3}), a D* value was calculated from the literature and an assumed tortuosity factor, and measured background H^+ activities for Kc (1.53×10^{-4} g m^{-3}) and Km (3.38×10^{-5} g m^{-3}) were used as input for all cell simulations.

4.4 Results and discussion

4.4.1 Acid buffering

Background pH values ranged from 6.3 to 6.9 and 7.2 to 7.5 in the Kc and Km cells. Background pH values were measured at depths ≥ 80, 193, and 210 mm, on day 216, in Kc_1, Kc_{-1}, and Kc_{-3}. For the Km experiments, background values were observed in Km1 (≥ 138 mm) while the pH front diffused ≥ 288 mm in Km_{-1} and Km_{-3}. Minimum pH values were measured in the uppermost samples of the Kc (pH = 2.2, -0.6, and -2.9; Fig. 4.1a) and Km (pH = 1.4, -0.6, -2.3; Fig. 4.2a) in the pH 1.0, -1.0, and -3.0 cells, respectively.

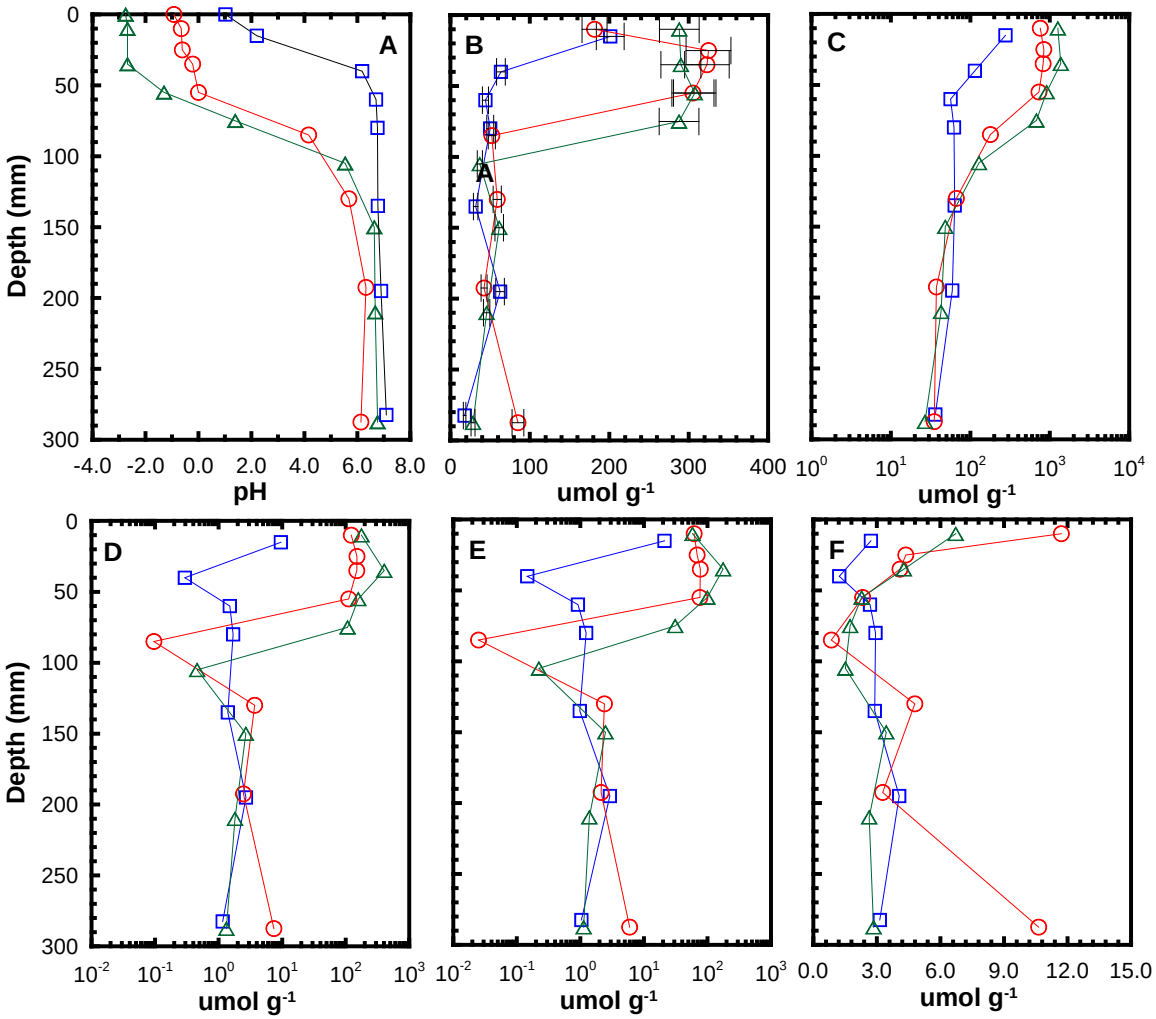

Figure 4.1. Depth profiles for Kc a) pH and 1:100 total soluble pore-water extracts for b) Ca, c) SO_4, d) Al, e) Fe, and f) Si for Kc_1 (□), Kc_{-1} (○), and Kc_{-3} (△).

The abrupt pH profile change with depth observed in all three Kc cells was characteristic of the presence of a buffering reaction. This transition gave rise to a pH plateau ranging between 6.3 and 6.8. The dissolution of carbonates occurs relatively rapidly and characteristically buffers acid pore-waters to values between pH 5.7 and 6.7 (Blowes and Ptacek 1994), which suggests the buffering in the current study can be attributed to dolomite present in the unaltered Kc (9.3 %; Table 4.1). Conversely, a carbonate buffering pH plateau was not observed in the Km cells (Fig. 4.2b) suggesting the buffering capacity of siderite in the unaltered samples (4.3 %; Table 4.1) was quickly exceeded in Km_1, Km_{-1}, and Km_{-3}, respectively. These observations were supported by the absence of dolomite and siderite peaks in the Kc_{-1}, Kc_{-3}, Km_{-1}, and Km_{-3}

diffractograms (Fig. 4.3a-d), which corresponded to maximum pH values of 1.4 and were well below the stability range of either carbonate (Blowes and Ptacek, 1994).

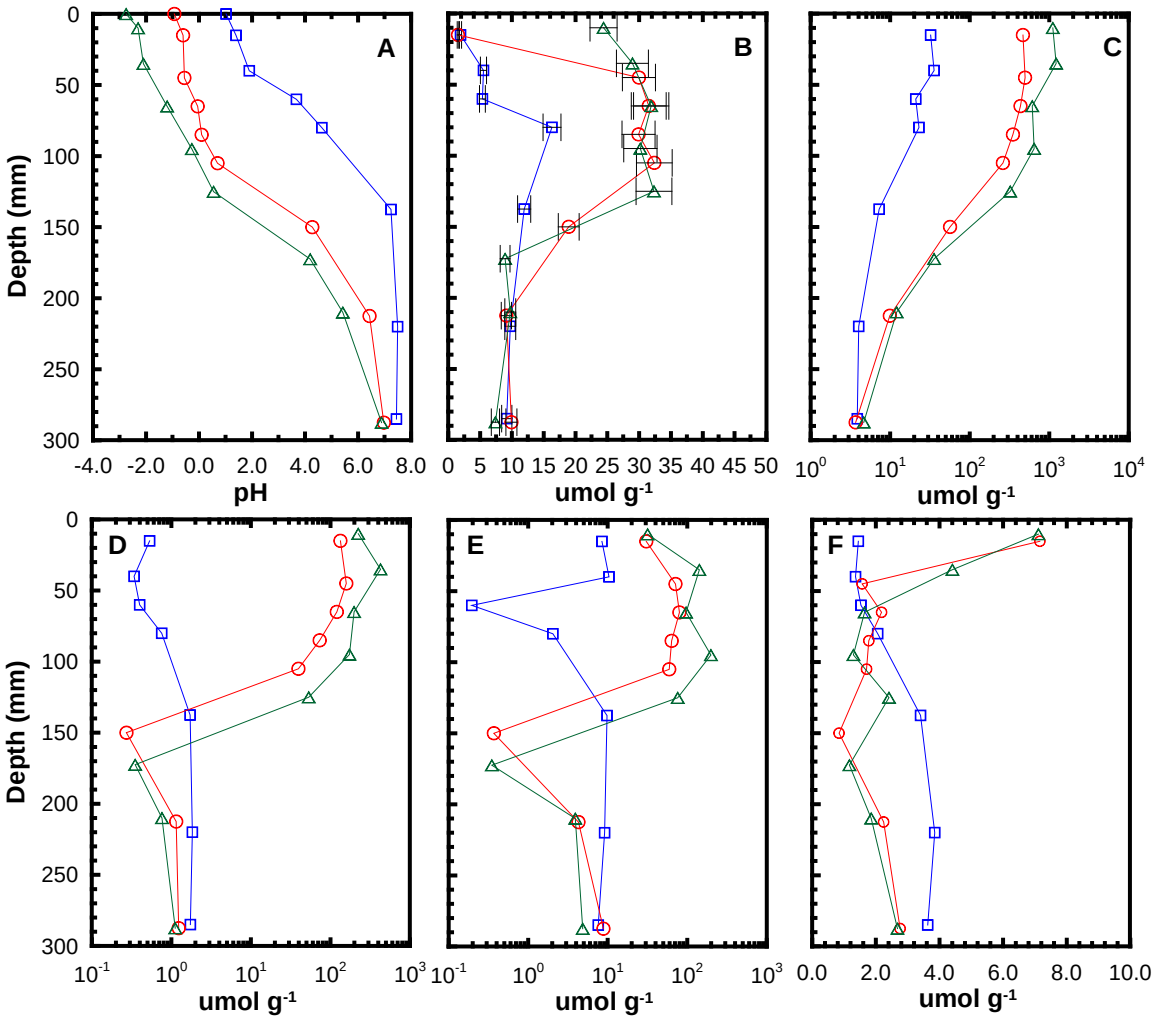

Figure 4.2. Depth profiles for Km a) pH and 1:100 total soluble pore-water extracts for b) Ca, c) SO_4, d) Al, e) Fe, and f) Si for Km_1 (□), Km_{-1} (○), and Km_{-3} (△).

Blowes and Ptacek (1994) observe that Fe and Al oxyhydroxides typically buffer pore-waters between pH 3.5 and 4.3. The absence of pH plateaus between 3.5 and 4.3 suggested that although Fe or Al oxyhydroxide buffering reactions may have occurred in the Kc and Km cells, they were overwhelmed by the large amount of acidity associated with the pH 1.0, -1.0, and -3.0 reservoir solutions. Moreover, Fe or Al oxyhydroxides were not observed in the unaltered Kc and Km diffractograms or the Kc_{-1}, Kc_{-3}, Km_{-1}, and Km_{-3} diffractograms (Fig. 4.3a-d). These observations are consistent with those of

Jurjovec et al. (2002), who suggest that, in the absence of primary oxyhydroxides phases, the amount of secondary oxyhydroxides that form are insufficient to adequately buffer the pore water pH.

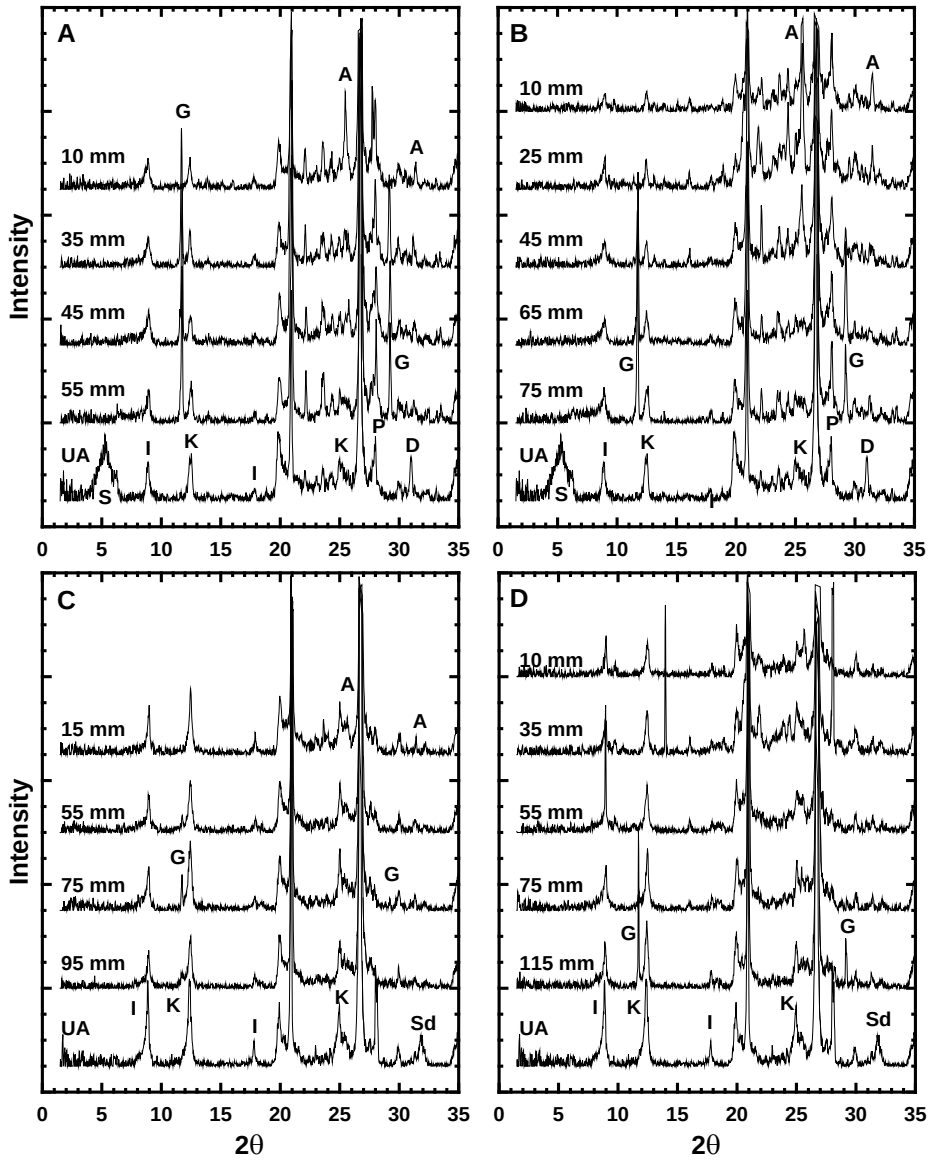

Figure 4.3. XRD diffractograms of unaltered and selected depth interval samples from a) Kc_{-1}, b) Kc_{-3}, c) Km_{-1}, and d) Km_{-3}, where Q = quartz, S = smectite, K = kaolinite, I = illite, D = dolomite, P = plagioclase, Sd = siderite, C = cristobalite and A = anhydrite. All Kc samples were glycolated.

Dubrovsky (1986), Blowes (1990), Blowes and Ptacek (1994), and Jurjovec et al. (2002), among others, indicate phyllosilicates weakly buffer the acidic porewaters to

approximately pH 1.3. The absence of a pH plateau at approximately pH 1.3 in any of the Kc or Km cells (Fig. 4.2a & b) suggests that the buffering capacity of the phyllosilicates were not enough to control the pore water pH. Kc_{-1} and Km_{-1} were characterized by pH plateaus between -0.55 and -0.65 at depths $\geq$ 25 and $\geq$ 35 mm (Fig. 4.1a & 4.2a), which suggested equilibrium or near-equilibrium phyllosilicate dissolution was controlling the pore-water pH at these depths. However, the presence of such a reaction could not be confirmed with the available data.

XRD results reveal that the strong diffractogram peak associated with dolomite (31.0°) in the unaltered Kc was not present at depths $\leq$ 55 and $\leq$ 75 mm in the Kc_{-1} and Kc_{-3} diffractograms (Fig. 4.3a & b). Similarly, the characteristic siderite peak (31.8°) in the unaltered Km was absent at depths $\leq$ 95 and $\leq$ 115 mm in the Km_{-1} and Km_{-3} diffractograms (Fig. 4.3c & d). In the Kc_{-1} and Kc_{-3} diffractograms, the main smectite peak (5.3°) observed in the unaltered clay was not present at depths $\leq$ 55 and $\leq$ 75 mm (Fig. 4.3a & b). Conversely, the primary illite (8.9°) and kaolinite (12.5°) peaks were observed in the Kc_{-1} and Kc_{-3} diffractograms at all examined depth intervals, but peak intensities decreased with decreased depth from surface (Fig. 4.3a-d). Moreover, secondary illite (18.0°) and kaolinite (24.9°) peaks persisted within the Kc_{-1}, Kc_{-3}, Km_{-1}, and Km_{-3} diffractograms (Fig. 4.3a-d). Finally, the intensity of the primary quartz peak (26.7°) remained unchanged at all examined depths in the Kc_{-1}, Kc_{-3}, Km_{-1}, and Km_{-3} diffractograms (Fig. 4.3a-d).

Shaw et al. (in submission) used Si K-edge XANES to determine the chemical and structural changes that occur during acidic dissolution of the Kc and Km clays in a series of batch experiments. The authors described the observed changes in the altered Kc and Km clay spectra using the known properties of a series of silicate and phyllosilicate standard spectra. Selected Si K-edge TEY and FY spectra for the Kc and Km diffusion cells are presented in Figures 4.4 and 4.5. The major peak features of the unaltered Kc and Km TEY spectra correlated well with the kaolinite standard spectrum (Shaw et al., in submission). This observation was in good agreement with the mineralogical composition of the unaltered Kc and Km samples (Table 4.1). The unaltered Kc and Km Si K-edge FY spectra, representative of the altered portion of the diffusion cells, indicated a combination of strong quartz and phyllosilicate peak signatures initially noted by Shaw et

al. (in submission) (Fig. 4.4 & Fig 4.5). The TEY and FY spectra demonstrated a clear alteration of the Si structure with decreasing depth in Kc_{-3} and Km_{-3}, to a lesser degree in Kc_{-1} and Km_{-1}, and nearly undetectable in Kc_1 and Km_1 (Fig. 4.4 & 4.5). In the TEY and FY spectra, a substantial decrease in the intensities of peaks D and F and increase in the intensity of peak E were observed. Additionally, the onset energy increased from 1846.50 to 1846.75 eV.

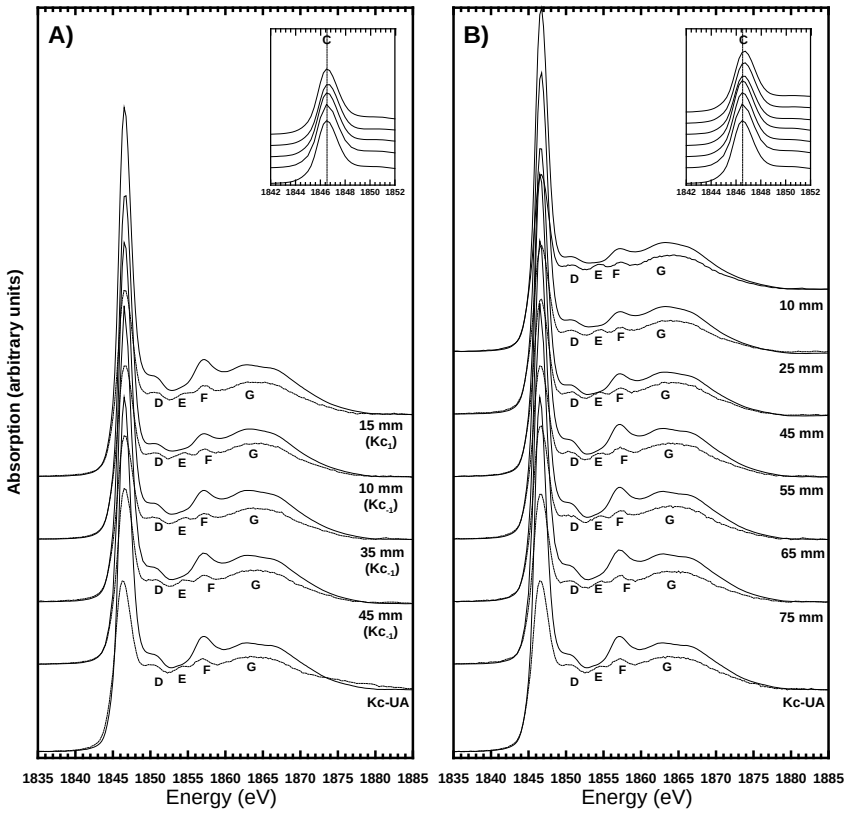

Figure 4.4. Si K-edge TEY (solid) and FY (dashed) spectra of unaltered (UA) and altered samples taken from discreet depth intervals from a) Kc_1 and Kc_{-1}, and b) Kc_{-3}.

In the Kc_{-3} and Km_{-3} FY spectra, the alteration of peaks C, D, E, and F suggested the development of a quartz-like peak signature (Fig. 4.4b & 4.5b), which was also observed to a lesser degree in Kc_{-1} and Km_{-1} (Fig. 4.4a & 4.5a). Conversely, the shift of peak C to higher energies in the Kc_{-3} and Km_{-3} TEY spectra was indicative of an increase in Si polymerization from Q^3 to Q^4 (Li et al., 1995a), while the decreased intensity of peaks D and F suggested a decrease in the medium-range Si order (Neuville et al., 2004).

These spectra alterations were well correlated to those observed by Shaw et al. (in submission). However, the extent of the alteration of the TEY and FY spectra was much more pronounced for both Kc and Km samples in Shaw et al. (in submission) than in the current study, even when compared with the uppermost samples from Kc_{-3} and Km_{-3} (Fig. 4.4b & Fig. 4.5b). Combined, the TEY and FY XANES results suggested that the Kc and Km primary phyllosilicate phases underwent dissolution and that this dissolution was more pronounced in samples collected from shallower depths in all diffusion cells.

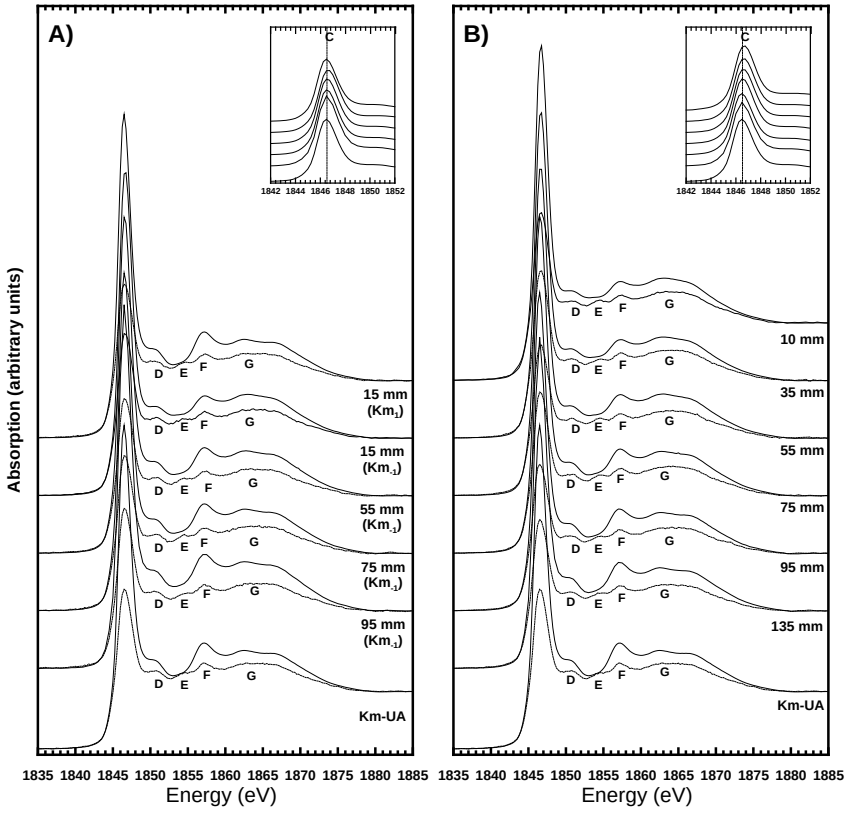

Figure 4.5. Si K-edge TEY (solid) and FY (dashed) spectra of unaltered (UA) and altered samples taken from discreet depth intervals from a) Km_1 and Km_{-1}, and b) Km_{-3}.

4.4.2 Metal mobilization

Background Al, Fe, and Si concentrations ranging from 1.8 to 2.7, 1.4 to 2.9, and 2.6 to 4.0 μmol g^{-1} were observed in Kc_1, Kc_{-1}, and Kc_{-3}, respectively (Fig. 4.1d-f), while background levels of 1.8, 9.1, 3.9 μmol g^{-1} were measured in Km_1, Km_{-1}, and Km_{-3}, respectively (Fig. 4.2d-f). In Kc_1, Kc_{-1}, and Kc_{-3}, peak Al concentrations of 9.5, 150, and

403 μmol g^{-1} and Fe concentrations of 21.0, 77.2, and 176 μmol g^{-1} were observed at respective depths of 15, 55, and 75 mm (Fig. 4.1d & e). These values were associated with elevated Al and Fe concentrations, operationally defined as being significantly increased relative to the back-ground concentration levels in each cell, measured at depths ≤ 40, ≤ 85, and ≤ 105 mm, respectively (Fig. 4d & e). Conversely, dissolved Si concentrations remained at or below background concentrations (1.2 to 4.5 μmol g^{-1}) throughout Kc_1 (Fig. 4.1f). In Kc_{-1} and Kc_{-3}, peak Si values of 11.7 and 6.7 μmol g^{-1} were measured at depths ≤ 55 mm (Fig. 4.1f).

In Km_1, Km_{-1}, and Km_{-3}, above-background Al and Fe values were observed at depths ≤ 60, ≤ 150 and ≤ 175 mm, respectively (Fig. 4.2d & e). Peak dissolved Al concentrations of 9.52, 158, and 426 μmol g^{-1} (15, 45, and 35 mm; Fig. 4.2d) and peak Fe values of 9.77, 79.7, and 199 μmol g^{-1} (138, 65, and 95 mm; Fig. 4.2e) were measured in Km_1, Km_{-1}, and Km_{-3}, respectively. Above-background Si concentrations were observed to depths of ≤ 45 and ≤ 65 mm, with peak values of 7.2 and 7.1 μmol g^{-1}, in Km_{-1} and Km_{-3}, while the Si concentrations remained below-background (0.84 and 3.8 μmol g^{-1}) throughout Km_1 (Fig. 4.2f).

Shaw and Hendry (accepted), determine that the Al and Fe present in the Kc and Km solid phases are primarily associated with phyllosilicates (smectite, illite, and kaolinite; Table 4.1). Similarly, several previous studies of acidic mineral dissolution in systems characterized by pH values ≤ 1.0, primarily attribute increased dissolved Al concentrations to phyllosilicate dissolution (e.g. Warren et al., 1992b; McGregor et al., 1998; Jurjovec et al., 2002; Moncur et al., 2005; Gunsinger et al., 2006). Additionally, Shaw and Hendry (accepted) show that phyllosilicates in the Kc and Km clays undergo acidic dissolution at pH ≤ 1.0 for exposure periods (t) ≥ 14 d. These observations support the data in the current study, where decreased intensity of the illite and kaolinite peaks and loss of smectite peaks were observed in the Kc_{-1}, Kc_{-3}, Km_{-1}, and Km_{-3} XRD diffractograms (Fig. 4.3a-d) and above-background dissolved Al and Fe values were observed in all Kc and Km cells (Fig. 4.1 & 4.2). The depth at which above-background Al and Fe values were measured increased with increasing acidity of the Kc and Km reservoir solutions (Fig. 4.1 & 4.2). These dissolved values were observed at greater depths in the Km cell compared to the Kc cell, for all three reservoir solutions examined.

These observations are well correlated with the Si K-edge TEY XANES results, where the decreased intensity of peaks D and F in sample spectra taken from depths associated with above-background Al and Fe concentrations suggested dissolution of the primary phyllosilicate minerals in all of the Kc and Km diffusion cells (Fig. 4.4 & 4.5). Similarly, the increased intensity of peaks D, E, and F, indicative of quartz, in the FY spectra further suggested the dissolution of phyllosilicates in the Kc and Km bulk sample.

In all cells, the maximum depths that above-background Al and Fe concentrations were measured corresponded with pH values between 3.7 and 6.2 (Fig. 4.1 & 4.2). Previous investigations into acidic dissolution of pure-phase phyllosilicates demonstrate that dissolution rates increase by several orders of magnitude between pH values of 5.0, 3.0, and 1.0 (Cama et al., 2002; Brandt et al., 2003; Kohler et al., 2003; Amram et al., 2005), which correlated well with the dissolved Al and Fe concentrations in the current study. This implies that the increase in peak Al and Fe concentrations between the pH 1.0, -1.0, and -3.0 Kc and Km cells can be attributed to increased solubility of phyllosilicates with increased H^+ concentrations. However, in Kc and Km batch experiments conducted at pH 1.0, -1.0, and -3.0 over 180 d, Shaw and Hendry (accepted) observe peak dissolved Al and Fe concentrations (298, 926, and 1.04 x 10^3 μmol g^{-1}) that exceed those observed (9.52, 158, and 426 μmol g^{-1}) in the current study by one to three orders of magnitude.

In all diffusion cells, above-background Si concentrations were measured to shallower depths than either Al or Fe (Fig. 4.1 & 4.2). Quartz, although present in large amounts in unaltered Kc and Km (Table 4.1), was assumed to remain relatively unreactive in all cells. This assumption is supported by the literature (Barrios et al., 1995; Breen et al., 1997; Madejova et al., 1998; Belver et al., 2002; Komadel, 2003; Wu and Ming, 2006; Shaw and Hendry, accepted) and by the persistence of quartz peaks at all depths in Kc_{-1}, Kc_{-3}, Km_{-1}, and Km_{-3} (Fig. 4.3a-d). Moreover, the development of quartz peak features at shallow depths in the Kc_{-1}, Kc_{-3}, Km_{-1}, and Km_{-3} FY XANES spectra (Fig. 4.4 & 4.5) corresponded to these observations. Previous studies, focused on the effects of acid mine drainage, indicate elevated Si concentrations primarily result from phyllosilicate dissolution (Blowes and Ptacek, 2003; Moncur et al., 2005; Gunsinger et al., 2006; Shaw and Hendry, accepted). In a series of acidic dissolution batch tests

conducted on the Kc and Km clays, Shaw and Hendry (accepted) observe Si concentrations (0.81 – 119 μmol g^{-1}) that are an order of magnitude greater than those observed in the current study (0.84 – 11.7 μmol g^{-1}). Additionally, Shaw et al. (submitted) demonstrate more intense alterations of the phyllosilicate peak features in Si K-edge FY and TEY spectra for both the Kc and Km batch experiment samples than observed in samples from the shallowest depths of all cells in the current study (Fig. 4.4 & 4.5). This can be attributed to the different experimental conditions; the batch tests performed by Shaw and Hendry (accepted) were conducted at a 20:1 (aqueous: solid) ratio, a ratio that was greatly reduced in the current diffusion cell experiments. Assuming an identical rate of mineral dissolution between the two experiments, the decrease in dissolved species can be attributed to a combination of decreased clay surface area or additional secondary phase precipitation in the diffusion cells.

4.4.3 Secondary phase precipitation

The maximum above-background Ca concentrations measured in the 1:100 (Fig. 4.1b & 4.2b) exceeded the 1:1 (Fig. 4.6a & c) values by up to an order of magnitude, for Kc_1, Kc_{-1}, and Kc_{-3} (201 to 325; 15.2 to 15.7 μmol g^{-1}) and Km_1, Km_{-1}, and Km_{-3} (16.3 to 32.4; 5.85 to 15.3 μmol g^{-1}). Peak SO_4 concentrations in the 1:100 (Fig. 4.1c & 4.2c) were, on average, an order of magnitude greater than the 1:1 (Fig. 4.6b & d) extracts in the Kc (277 to 1.38 x 10^3; 45.7 to 950 μmol g^{-1}) and Km (35.6 to 1.22 x 10^3; 33.7 to 926 μmol g^{-1}) cells. A similar trend was also evident between the 1:100 and 1:1 extracts for Al in Kc_1, Kc_{-1}, Kc_{-3} (9.52 to 403; 4.64 to 108 μmol g^{-1}) and Km_1, Km_{-1}, Km_{-3} (1.84 to 426; 7.67 to 151 μmol g^{-1}) samples characterized by above-background concentrations (1:100 extracts), but not for the corresponding dissolved Fe values, which remained relatively unchanged (data not shown).

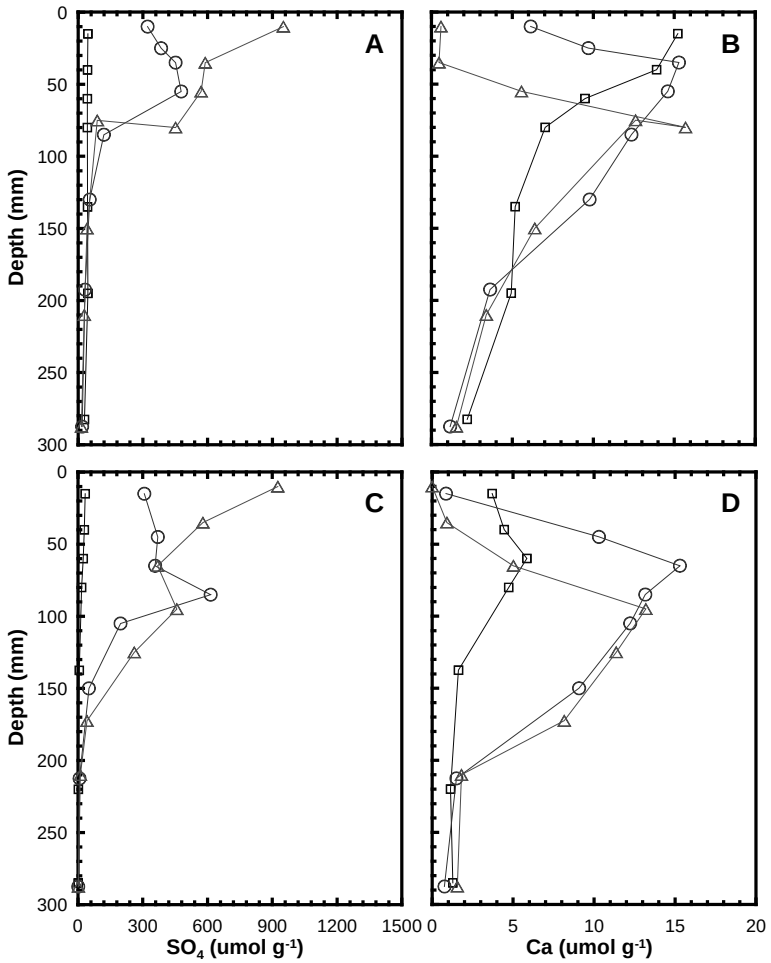

Figure 4.6. Ca and SO_4 depth profile concentrations for 1:1 pore-water extracts for the Kc (a & b) and Km (c & d) pH 1.0 (□), -1.0 (○), and -3.0 (△) cells.

The 1:100 extracts were assumed to be representative of the total soluble phases in the Kc and Km samples; therefore, the increased recovery of Ca and SO_4 from these extracts is due to the dissolution of a soluble Ca and SO_4-bearing phase or phases. These observations were supported by characteristic anhydrite (25.5° and 31.3°) and gypsum (11.6° and 29.1°) peaks observed to depths ≤ 55 and ≤ 95 mm (pH -1.0) and ≤ 75 and ≤ 115 mm (pH -3.0) in the Kc and Km diffractograms (Fig. 4.3a-d). Precipitation of gypsum and anhydrite is commonly associated with AMD settings because of the characteristically high dissolved SO_4 and Ca concentrations (e.g. Dubrovsky et al., 1985; Blowes and Ptacek, 1994; Al et al., 2000; Jurjovec et al., 2002; Moncur et al., 2005). Gypsum has also been observed to be associated with Ca-rich acidified soils, characterized by pH values between 1.6 and 2.9, adjacent to a 25 year old S^0 storage

block (Warren and Dudas, 1992a). Moreover, Shaw and Hendry (accepted) observe gypsum and anhydrite peaks in diffractograms for Kc clay at pH ≤ -1.0 and t ≥ 90 but not in the corresponding Km diffractograms.

The relationship between Al concentrations from 1:100 and 1:1 extracts suggested the formation of a readily soluble Al-bearing phase at depths associated with above-background Al concentrations, in Kc_1, Kc_{-1}, and Kc_{-3} (≤ 40, ≤ 85 and ≤ 105 mm) and Km_1, Km_{-1}, and Km_{-3} (≤ 60, ≤ 105 and ≤ 173 mm). Additionally, three unknown peaks (9.7, 16.1, and 18.9°) were observed in the Kc_{-1} and Kc_{-3} (≤ 10 and ≤ 25 mm) and Km_{-1} and Km_{-3} (≤55 and 75 mm) diffractograms (Fig. 4.3a-d), which were well correlated to the major peaks associated with aluminite (9.7 and 18.9°; $Al_2[SO_4][OH]_4 \bullet 7H_2O$) and aluminocoapiapite (9.7, 16.1°; $Al_{0.66}Fe_4[SO_4]_6[OH]_2 \bullet 20H_2O$). Shaw and Hendry (accepted) show identical peaks in Kc and Km diffractograms from batch experiments at pH ≤ -1.0, while Shaw et al., (in submission) confirm the presence of an Al-SO_4-rich phase in the same samples using x-ray near edge spectroscopy methods. Furthermore, XRD analyses suggested that halotrichite ($Fe^{II}[Al,Fe^{III}]_2[SO_4]_4 \bullet 22H_2O$) occurred as a massive, amorphous, secondary precipitate within distinct intervals in Kc_{-3} (25 to 45 mm; -2.9 ≤ pH ≤ -1.3) and Km_{-3} (25 to 55 mm; -2.1 ≤ pH ≤ -1.5) (data not shown). Espana et al. (2005) and Hammarstrom (2005) indicate that halotrichite is commonly associated with AMD settings. In addition, Nordstrom and Alpers (1999) document its occurrence at Iron Mountain, which is characterized by the lowest pH value recorded for an AMD setting (≥ -3.6; Nordstrom et al., 2000). Secondary sulfate mineral phases are commonly associated with elevated Al, Fe and SO_4 concentrations typical of AMD settings (Bigham and Nordstrom, 2000; Jambor et al., 2000). Together, these observations suggest that the precipitation of secondary gypsum and anhydrite represented a significant solid-phase sink for both Ca (mobilized from primary mineral dissolution) and SO_4 within all cells. However, as demonstrated from the 1:100 extract results, these phases are labile and there was a strong potential for remobilization of this Al, Ca and SO_4 to the aqueous phase.

Several studies show that acidic dissolution of phyllosilicates at pH≤ 0.0 leads to the formation of amorphous silica (a-SiO_2; Mendioroz et al., 1987; Pesquera et al., 1992; Vincente et al., 1996; Madejova et al., 1998; Gates et al., 2002; Nguetnkam et al., 2005;

Shaw and Hendry, accepted). Amorphous silica can be identified by a broad band of intensity between 18 and 30° in XRD diffractograms (Belver et al., 2002; Van Rompaey et al., 2002; Shaw and Hendry, accepted). This characteristic signature was absent from the Kc_{-1}, Kc_{-3}, Km_{-1}, and Km_{-3} diffractograms (Fig. 4.3a-d). Additionally, the development of a-SiO_2 peak features in the TEY XANES spectra at pH < 0.0 noted by Shaw et al. (in submission) were absent from all spectra in the current study (Fig. 4.4 & 4.5). Dissolved Al, Fe, and Si concentrations from the 1:100 extracts suggested that phyllosilicate dissolution was significantly less than observed by Shaw and Hendry (accepted) in their series of batch experiments on the Kc and Km clays. Therefore, the absence of a-SiO_2 may have resulted from a state of undersaturation with respect to dissolved Si concentrations in the Kc and Km pH 1.0, -1.0, and -3.0 cells.

4.4.4 Transport modeling

To account for the consumption of H^+ by mineral dissolution reactions, the assumption was made that H^+ consumption could be represented by adsorption of H^+. This assumption allowed for the use of an adsorption isotherm to estimate the retardation of H^+ due to geochemical reactions within each cell. The amount of H^+ ions consumed (S) as a function of the equilibrium H^+ activity (*a*) were calculated from the Kc and Km pH 5.0, 3.0, and 1.0 batch experiments data of Shaw and Hendry (accepted) (Table 4.2). H^+ consumption could not be calculated from the pH -1.0 and -3.0 batch test results. Shaw and Hendry (accepted) observe increased phyllosilicate dissolution between pH 1.0 and -3.0, which suggests H^+ consumption also increases at pH < 1.0. Therefore, in order to simulate the consumption of H^+ in the current study, it was assumed that the amount of H^+ consumption calculated for the pH 1.0 tests were representative of the consumption at pH < 1.0 (Table 4.2).

A comparison of the measured H^+ activity profiles and the simulated profiles are presented in Figure 4.7 and 4.8. For all cells, simulation results with no retardation were poorly correlated to the measured H^+ activity profiles, confirming that the diffusion of H^+ was inhibited by one or more geochemical mechanisms. The incorporation of non-linear H^+ adsorption (Fig. 4.7a & 4.8a) effectively simulated the steep concentration gradients measured in Kc_1 and Km_1. However, in the simulations that included non-linear

adsorption the depth to the diffusive fronts were overestimated and the ability to simulate the measured activities became progressively poorer as the source pH decreased for both clays (Fig. 4.7b-c & 4.8b-c).

Table 4.2. Average *a* and S values, calculated from Kc and Km pH 5.0, 3.0, and 1.0 batch tests results, conducted by Shaw and Hendry (accepted). The S values for pH 1.0 were assumed to represent the pH -1.0 and -3.0 values for both clays.

Batch Test pH	Kc		Km	
	a	**S**	***a***	**S**
	(g m^{-3})	***(g g^{-1})***	***(g m^{-3})***	***(g g^{-1})***
5.0	2.45×10^{-2}	1.03×10^{-3}	1.25×10^{-2}	1.74×10^{-4}
3.0	9.77×10^{-1}	1.03×10^{-3}	1.34	4.78×10^{-4}
1.0	9.65×10^{1}	3.14×10^{-3}	9.65×10^{1}	1.55×10^{-3}
-1.0	8.52×10^{3}	3.14×10^{-3}	8.52×10^{3}	1.55×10^{-3}
-3.0	5.63×10^{5}	3.14×10^{-3}	5.63×10^{5}	1.55×10^{-3}

The relationship between measured and modeled results placed our initial assumption that H^+ consumption at pH 1.0 was representative of consumption at pH -1.0 and -3.0 into question. Additionally, the increased divergence between measured and modeled H^+ activities in all cells indicated that the amount of H^+ consumption increased with decreasing pore water pH. This conclusion is supported by Shaw and Hendry (accepted), who observe continuously increasing dissolved Al concentrations, associated with phyllosilicate dissolution, with decreasing pH, between pH 1.0 and -3.0. However, the increased depth of the model H^+ diffusion front in Kc_1 and Km_1 indicated that the batch test results potentially underestimate the measured H^+ consumption. This implies an increase in the amount of mineral dissolution in the cells compared to the batch test results of Shaw and Hendry (accepted); however, the dissolved Al, Fe, and Si pore water concentrations suggested that mineral dissolution decreased. Therefore, additional mechanisms besides consumption reactions possibly controlled the migration of H^+ in the current study.

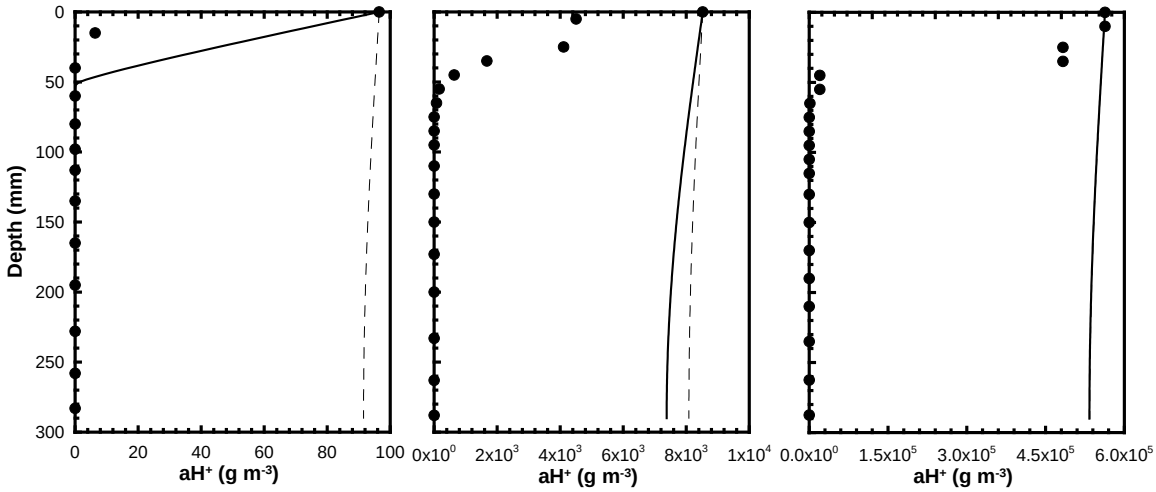

Figure 4.7. Comparison of measured (●) and modeled H^+ activity (aH^+) profiles assuming no retardation (dashed line) and non-linear retardation (solid line) for Kc a) pH 1.0, b) pH -3.0, and c) pH -3.0 cells.

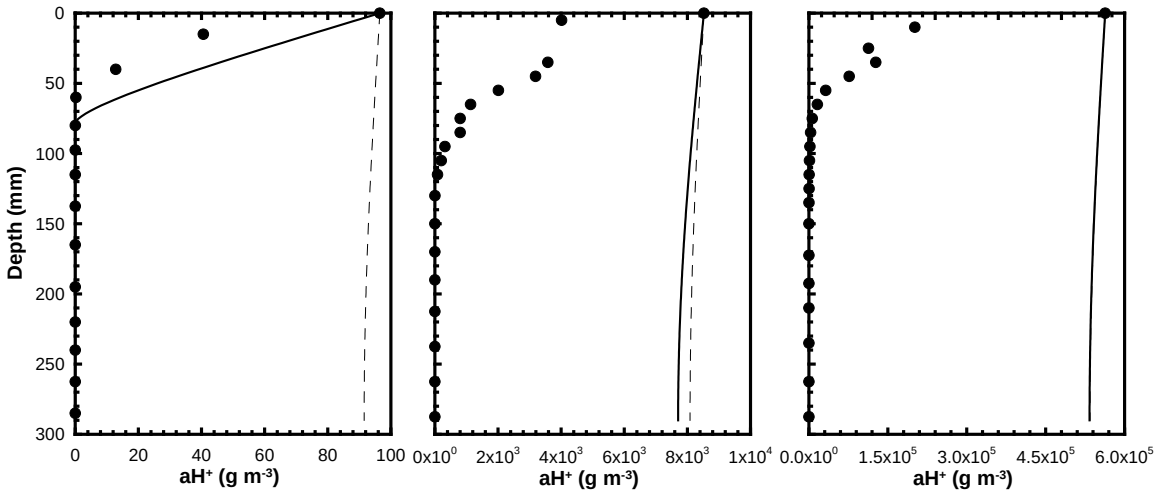

Figure 4.8. Comparison of measured (●) and modeled H^+ activity (aH^+) profiles assuming no retardation (dashed line) and non-linear retardation (solid line) for Km a) pH 1.0, b) pH -3.0, and c) pH -3.0 cells.

Alternatively, the poor fit of the CTRAN model to the observed H^+ activity profiles in all cells potentially resulted from an overestimation of D*. Specifically, the calculation of D* did not incorporate the effect of concentrated solutions on the diffusive transport of H^+. Two possible effects that would potentially result in a decrease of D* are the relaxation and electrophoretic effects (Wright, 2007). The relaxation effect states that around each central ion exists a symmetric ionic atmosphere (Wright, 2007). However, as the ion is displaced to an external field, such as diffusion, the ionic atmosphere must both

build up in front of the moving ion and decay behind it, which cannot occur instantaneously; thus, slowing down the movement of the ion (Wright, 2007). Additionally, in order to satisfy Columb's law, as H+ diffuses through the cells it will be slowed down viscous drag created by the diffusion of other ions at slower rates in both the same and opposite direction to that of the H^+ ion (Wright, 2007).

4.5 Conclusions

In this study, the diffusive transport of H_2SO_4 in two mineralogically distinct clays was studied for source reservoir concentrations of pH 1.0, -1.0, and -3.0. Study results showed that the Kc cells buffered a greater amount of H_2SO_4 than the Km clay at pH 1.0, -1.0, and -3.0, which was most likely due to differences in carbonate mineralogy observed via XRD. The presence of dolomite was observed in Kc compared to a small amount of siderite in Km. XRD diffractograms also suggested that Fe or Al oxyhydroxides did not exert a measureable influence on H_2SO_4 migration. Additionally, pore water extract and XRD results indicated that phyllosilicate dissolution did not appear to provide measureable buffering to H_2SO_4 migration in all cells. Both XRD and Si K-edge XANES results indicated phyllosilicate dissolution at depth intervals characterized by pH < 1.0. However, unlike previous studies, the precipitation of an a-SiO_2 phase was not observed in either set of results.

The magnitude and depth at which above background concentrations were measured for dissolved Al, Fe, Ca, and Si increased with increasing reservoir acidity for both Kc and Km. Moreover, a comparison of the 1:1 pore water extracts, total pore water extracts, and XRD diffractograms showed precipitation of large amounts of anhydrite and gypsum. The diffractograms also showed the precipitation of potential Al-SO_4-rich phases within intervals in the Kc and Km clays associated with pH ≤ -1.0.

One-dimensional diffusive transport simulations were conducted in an attempt to model the measured pH depth profiles in the Kc and Km cells, in the absence of the ability to model the results using a geochemical transport code. The control of H^+ consumption through acidic dissolution of mineral phases was modeled through the use of adsorption isotherms, calculated from batch experiments conducted between pH 5.0 and 1.0 on the Kc and Km clay in a previous study. The model results predicted the

relative shape of the H^+ activity gradients for Kc_1 and Km_1 but underestimated the H^+ consumption measured in all Kc and Km cells. The discrepancy between measured and modeled results was attributed to several possible factors including underestimation of H^+ consumption at pH < 1.0, overestimation of D*, and the inability to quantify the electrochemical effects associated with concentrated.

The results of this study suggested that, despite the extreme pH values, the geochemical and mineralogical impacts of H_2SO_4 diffusion through the Kc and Km clays are similar to the processes associated with AMD settings typically characterized by pH > 1.0. More practically, they suggest that the diffusion of H_2SO_4 solutions will be greatly retarded in clays through the addition of a strong acid neutralizing mineral phase, such as dolomite.

4.6 Acknowledgements

The authors would like to thank A. Jansen for assistance with transport modeling and T. Al and V. Reddy of the University of New Brunswick's Microscopy and Microanalysis facility for their assistance with the XRD analysis. Funding was provided by Syncrude Canada Limited and NSERC through a Collaborative Research and Development Grant.

4.7 References

Al, T. A., Martin, C. J., and Blowes, D. W., 2000. Carbonate-mineral/water interactions in sulfide-rich mine tailings. *Geochim. Cosmochim. Acta*. 64, 3933-3948.

Amram, K. and Ganor, J., 2005. The combined effect of pH and temperature on smectite dissolution rate under acidic conditions. *Geochim. Cosmochim. Acta* 69, 2535-2546.

Barrios, M. S., Gonzalez, L. V. F., Rodriguez, M. A. V., and Pozas, J. M. M., 1995. Acid activation of a palygorskite with HCl - Development of physicochemical, textural and surface-properties. *Appl. Clay Sci.* 10, 247-258.

Belver, C., Munoz, M. A. B., and Vicente, M. A., 2002. Chemical activation of a kaolinite under acid and alkaline conditions. *Chem. Mater* 14, 2033-2043.

Bigham, J. M. and Nordstrom, D. K. (2000) Iron and aluminum hydroxysulfates from acid sulfate waters. In C.N. Alpers, J.L. Jambor, D.K. Nordstrom, Eds., Sulfate Minerals—Crystallography, Geochemistry, and Environmental Significance, vol. 40, p.

351–403. Reviews in Mineralogy and Geochemistry, Mineralogical Society America, Chantilly, Virginia.

Blowes, D. W. and Jambor, J. L., 1990. The pore-water geochemistry and the mineralogy of the vadose zone of sulfide tailings, Waite-Amulet, Quebec, Canada. *Appl. Geochem.* 5, 327-346.

Blowes, D. W., Reardon, E. J., Jambor, J. L., and Cherry, J. A., 1991. The formation and potential importance of cemented layers in inactive sulfide mine tailings. *Geochim. Cosmochim. Acta* 55, 965-978.

Blowes, D. W. and Ptacek, C. J., 1994. Acid-neutralization mechanisms in inactive mine tailings. In: *The Environmental Geochemistry of Sulfide Mine-Wastes, Short Course Handbook 22* (eds. D.W. Blowes and J.L. Jambor), Mineralogical Association of Canada Short Course 22, pp. 271-292.

Blowes, D.W., Ptacek, C.J. and Jurjovec, J., 2003. Mill tailings: Hydrogeology and geochemistry. In: Blowes, D.W., Jambor, J.L. and Ritchie, A.I.M. (Eds.), The Environmental Geochemistry of Sulfide Mine-Wastes, Short Course Handbook 31, pp. 95-116.

Breen, C., Zahoor, F. D., Madejova, J., and Komadel, P., 1997. Characterization and catalytic activity of acid-treated, size-fractionated smectites. *J. Phys. Chem. B* 101, 5324-5331.

Cama, J., Metz, V. and Ganor, J., 2002. The effect of pH and temperature on kaolinite dissolution rate under acidic conditions. *Geochim. Cosmochim. Acta* 66, 3913-3926.

Dubrovsky, N. M., Cherry, J. A., Reardon, E. J., and Vivyurka, A. J., 1985. Geochemical evolution of inactive pyritic tailings in the Elliot Lake Uranium District. *Can. Geotech. J.* 22, 110-128.

Espana, J. S., Pamo, E. L., Santofimia, E., Aduvire, O., Reyes, J., and Barettino, D., 2005. Acid mine drainage in the Iberian Pyrite Belt (Odiel river watershed, Huelva, SW Spain): Geochemistry, mineralogy and environmental implications. *Appl. Geochem.* 20, 1320-1356.

Fetter, C. W., 1988. *Applied hydrogeology*, 2nd ed., Merrill Publishing Company; Columbus, 592p.

Gates, W. P., Anderson, J. S., Raven, M. D., and Churchman, G. J., 2002. Mineralogy of a bentonite from Miles, Queensland, Australia and characterization of its acid activation products. *Appl. Clay Sci*. 20, 189-197.

Geo-Slope International Ltd., 1991. CTRAN/W users manual, version 2. Geo-Slope International Ltd., Calgary, Alta.

Gunsinger, M. R., Ptacek, C. J., Blowes, D. W., Jambor, J. L., and Moncur, M. C., 2006. Mechanisms controlling acid neutralization and metal mobility within a Ni-rich tailings impoundment. *Appl. Geochem.* 21, 1301-1321.

Hammarstrom, J.M., Sibrell, P.L. and Belkin, H.E., 2003. Characterization of limestone reacted with acid-mine drainage in a pulsed limestone bed treatment system at the Friendship Hill National Historical Site, Pennsylvania, USA. *Appl. Geochem*. 18, 1705-1721.

Hammarstrom, J.M., Seal, R.R., Meier, A.L. and Kornfeld, J.M., 2005. Secondary sulfate minerals associated with acid drainage in the eastern US: recycling of metals and acidity in surficial environments. *Chem. Geol.* 215,407-431.

Jambor, J.L., Nordstrom, D.K., and Alpers, C.N., 2000. Metal-sulfate salts from sulfide mineral oxidation. In C.N. Alpers, J.L. Jambor, D.K. Nordstrom, Eds., Sulfate Minerals—Crystallography, Geochemistry, and Environmental Significance. *Rev. Mineral. Geochem*. 40, pp. 303-350.

Jambor, J. L., Dutrizac, J. E., Groat, L. A., and Raudsepp, M., 2002. Static tests of neutralization potentials of silicates and phyllosilicate minerals. *Environ. Geol.* 43, 1-117.

Jurjovec, J., Ptacek, C.J. and Blowes, D.W., 2002. Acid neutralization mechanisms and metal release in mine tailings: A laboratory column experiment. *Geochim. Cosmochim. Acta* 66, 1511-1523.

Kashir, M. and Yanful, E. K., 2001. Hydraulic conductivity of bentonite permeated with acid mine drainage. *Can. Geotech. J*. 38, 1034-1048.

Kohler, S.J., Dufaud, F. and Oelkers, E.H., 2003. An experimental study of illite dissolution kinetics as a function of pH from 1.4 to 12.4 and temperature from 5 to 50 degrees C. *Geochim. Cosmochim. Acta* 67, 3583-3594.

Komadel, P., Madejova, J., Janek, M., Gates, W. P., Kirkpatrick, R. J., and Stucki, J. W., 1996. Dissolution of hectorite in inorganic acids. *Clays Clay Miner*. 44, 228-236.

Komadel, P. 2003. Chemically modified smectites. *Clay Min.* 38, 127-138.

Madejova, J., Bujdak, J., Janek, M. and Komadel, P., 1998. Comparative FT-IR study of structural modifications during acid treatment of dioctahedral smectites and hectorite. *Spectrochim. Acta, Part A* 54, 1397-1406.

McGregor, R. G., Blowes, D. W., Jambor, J. L., and Robertson, W. D., 1998. Mobilization and attenuation of heavy metals within a nickel mine tailings impoundment near Sudbury, Ontario, Canada. *Environ. Geol.* 36, 305-319.

Mendioroz, S., Pajares, J. A., Benito, I., Pesquera, C., Gonzalez, F., and Blanco, C., 1987. Texture evolution of montmorillonite under progressive acid treatment - change from H-3 to H2 type of hysteresis. *Langmuir* 3, 676-681.

Moncur, M.C., Ptacek, C.J., Blowes, D.W. and Jambor, J.L., 2005. Release, transport and attenuation of metals from an old tailings impoundment. *Appl. Geochem*. 20, 639-659.

Morin, K. A., and Cherry, J. A., 1985. Trace amounts of siderite near a uranium-tailings impoundment, Elliot Lake, Ontario, Canada, and its implication in controlling contaminant migration in a sand aquifer. *Chem. Geol.* 56, 117-134.

Morin, K. A., Cherry, J. A., Dave, N. K., Lim, T. P., and Vivyurka, A. J., 1988. Migration of acidic groundwater seepage from uranium-tailings impoundments, 1. Field study and conceptual hyrodgeochemical model. *J. Contam. Hydrol.* 2, 271-303.

Nguetnkam, J.P. et al., 2005. Assessment of the surface areas of silica and clay in acid-leached clay materials using concepts of adsorption on heterogeneous surfaces. *J. Colloid Interface Sci.* 289, 104-115.

Nordstrom, D.K. and Alpers, C.N., 1999. Negative pH, efflorescent mineralogy, and consequences for environmental restoration at the Iron Mountain Superfund site, California. Proc. Nat. Acad. Sci. U.S.A. 96, 3455-3462.

Nordstrom, D.K., Alpers, C.N., Ptacek, C.J. and Blowes, D.W., 2000. Negative pH and extremely acidic mine waters from Iron Mountain, California. *Env. Sci. Technol.* 34, 254-258.

Pesquera, C., Gonzalez, F., Benito, I., Blanco, C., Mendioroz, S. and Pajares, J., 1992. Passivation of a Montmorillonite by the Silica Created in Acid Activation. *J. Mater.Chem.* 2, 907-911.

Pitzer K.S., Roy, R. N., Silvester, L. F., 1977. Thermodynamics of electrolytes. 7. Sulfuric acid. *J. Am. Chem. Soc.* 99, 4930-4936.

Schuring, J., Kolling, M. and Schulz, H.D., 1997. The potential formation of acid mine drainage in pyrite-bearing hard-coal tailings under water-saturated conditions: An experimental approach. *Env. Geol.* 31, 59-65.

Shackelford, C. D., 1991. Laboratory diffusion testing for waste disposal – A review. *J. Contam. Hydrol.* 7, 177-217.

Shaw, S. A. and Hendry J. M., accepted. Geochemical and mineralogical impacts of H_2SO_4 on clays between pH 5.0 and -3.0. *Appl. Geochem.*

Shaw S. A., Peak, D. and Hendry M. J., in submission. Application of Si and Al x-ray absorption near edge structure to acidic dissolution of mixed clays between pH 1.0 and -3.0. *Geochim. Cosmochim. Acta*

Van Rompaey, K., Van Ranst, E., De Coninck, F. and Vindevogel, N., 2002. Dissolution characteristics of hectorite in inorganic acids. *Appl. Clay Sci.* 21, 241-256.

Vicente, M.A., Suarez, M., LopezGonzalez, J.D.D. and Banares-Munoz, M.A., 1996. Characterization, surface area, and porosity analyses of the solids obtained by acid leaching of a saponite. *Langmuir* 12, 566-572.

Warren, C. J., and Dudas, M. J., 1992. Acidification adjacent to an elemental sulfur stockpile: I. Mineral weathering. *Can. J. Soil Sci.* 72, 113-126.

Warren, C. J., Dudas, M. J., and Abboud, S. A., 1992. Effects of acidification on the chemical composition and layer charge of smectite from calcareous till. *Clays Clay Miner*. 40, 731-739.

Wright, M. R., 2007. An introduction to aqueous electrolyte solutions, John Wiley and Sons; New York, 574p.

Wu, P.X. and Ming, C., 2006. The relationship between acidic activation and microstructural changes in montmorillonite from Heping, China. *Spectrochim. Acta, Part A* 63, 85-90.

5.0 SUMMARY AND CONCLUSIONS

The goal of this thesis was to investigate the long-term impacts of H_2SO_4 diffusion through clays. Specifically, the objectives were to (i) determine the mineralogical alterations resulting from the interaction of clays with H_2SO_4 solutions between pH 5.0 and -3.0; (ii) determine the aqueous geochemistry of the major elemental constituents associated with these interactions and, iii) determine the long-term geochemical and mineralogical impacts of H_2SO_4 diffusion through clay liners.

The study site for this research was the above-ground S^0 blocks at the Syncrude Mildred Lake Oilsands facility, located approximately 60 km North of Fort McMurray, Alberta, Canada. However, due to the long-term objectives of the thesis, the experiments were conducted in the laboratory setting. Kc clay, which was rich in montmorillonite, illite, kaolinite, and dolomite, was selected for its use as a liner material beneath existing above ground S^0 blocks in the Alberta Oilsands. Km clay was rich in kaolinite and illite and was chosen because of its very low carbonate content and potential use as a liner material for future S^0 blocks in the Alberta Oilsands. Finally, the BK, a pure Na-montmorillonite, was selected to provide a basis of comparison for the more complex, mixed, Kc and Km clays.

The summary and conclusions for each of these objectives and a global synthesis of the entire thesis are presented below.

5.1 Characterization of the mineralogical effects of H_2SO_4 on clays

In order to characterize the effects of H_2SO_4 on the mineralogy of clays between pH 5.0 and -3.0 a series of long-term batch experiments were conducted on three mineralogically distinct clays. In order to determine the mineralogy of the unaltered clays a series of analyses were performed, including grain size analyses, semi-quantitative x-ray diffraction (XRD), sequential extractions, B.E.T. surface area, total digestions, and total carbonate. The mineralogical alterations of the acid impacted samples were determined using both XRD and Si and Al x-ray absorption near edge structure (XANES) spectroscopy and compared to the unaltered samples. Results indicated that the three clays were characterized by distinct mineralogical compositions, such that Kc was rich in

quartz, montmorillonite, illite, kaolinite, and dolomite; Km was rich in quartz, kaolinite, illite, and siderite; while BK was rich in montmorillonite and quartz.

For the altered samples, XRD analyses showed (i) the complete loss of carbonates at pH $\leq$ 5.0, the dissolution of montmorillonite at pH $\leq$ 1.0, (ii) the progressive decrease of kaolinite and illite peaks between pH 1.0 and -3.0, (iii) the unreactive nature of quartz to a pH $\geq$ -3.0, (iv) the formation of amorphous silica (a-SiO_2) at pH $\leq$ 0.0, (v) the precipitation of anhydrite/gypsum, and (vi) the precipitation of an Al-SO_4-rich phase at pH $\leq$ -1.0. These results also showed that the major aluminosilicate phases preferentially undergo acidic dissolution in the order of montmorillonite > illite $\geq$ kaolinite. Additionally, the precipitation of a-SiO_2 corresponded to the findings of previous studies, which show the preferential dissolution of aluminosilicate Al-octahedral layers and the subsequent polymerization of the unaltered Si-tetrahedral layers that form an a-SiO_2 phase.

The Si XANES results showed the preferential dissolution of phyllosilicates (referred to as aluminosilicates here) and the acid resistance of quartz initially observed in the XRD results. Additionally, Si TEY and FY results demonstrated the formation of a surface specific a-SiO_2-like precipitate. The Si $L_{2,3}$-edge, Al K-edge, and Al $L_{2,3}$-edge spectra indicated an increase in the relative amount of four-fold coordinated Al (^{4}Al), which was attributed to the persistence of illite relative to montmorillonite and kaolinite. Finally, the formation of an Al-SO_4-like phase was evident from the Al K- and L2,3-edge spectra in all three clays at pH $\leq$ 0.0. The coupling of XANES analyses with XRD provided additional mineralogical information that could not normally be derived from XRD analyses alone. XANES spectroscopy provided information specific to the surface and bulk portions of the clay samples, which were not evident from the initial XRD results.

The results of this study indicate that a large amount of the clays primary mineral phases will undergo acidic dissolution in H_2SO_4 solutions characterized by pH < 1.0. These reactions include complete dissolution of carbonates, including dolomite and siderite, and the partial dissolution of aluminosilicates. However, quartz was shown to remain relatively unreactive even under the most extreme acidic conditions considered.

Furthermore, several secondary mineral phases were observed to precipitate at pH < 1.0, including anhydrite, gypsum, Al-SO_4-rich phases, and a-SiO_2.

5.2 Characterization of the geochemical effects of H_2SO_4 on clays

In order to characterize the geochemical effects of H_2SO_4 on clays between pH 5.0 and -3.0 a series of long-term batch experiments were conducted on three mineralogically distinct clays. Geochemical studies on the dissolution of clays at pH < 1.0 are extremely limited in the current scientific literature. The large spread of the batch experiments (pH = 5.0, 3.0, 1.0, 0.0, -1.0, -2.0, and -3.0; time = 14, 90, 180, and 365 d) represented the first attempt to systematically characterize the associated geochemistry of H_2SO_4 interaction with clays between pH 5.0 and -3.0. Geochemical results indicated increasing mobilization of Al and Fe with both decreasing pH and increasing exposure time, which was attributed to the dissolution of aluminosilicate Al-octahedral layers. Conversely, results demonstrated increasing Ca concentrations over the same range of conditions in the Kc and BK clays, which was associated with the precipitation of anhydrite and gypsum. Additionally, the precipitation of a-SiO_2 observed in the mineralogical analyses was supported by decreased dissolved Si values at pH ≤ 0.0 for all three clays. Geochemical speciation calculations, a fundamental component of geochemical studies, could not be conducted on batch experiments samples at pH < 1.0, as the current knowledge-base does not extend to the conditions examined in this thesis. While a limited thermodynamic database (PHRQPITZ) exists, it lacks datasets for Si and Al, the key elements identified from the geochemical results.

Calculated global Al and Si dissolution rates (R_{Al}, R_{Si}) show a general decrease in reaction rates with increasing exposure period, which was indicative of ultrafine phase dissolution. Additionally, these results suggested that the dissolution mechanism(s) for all three clays were strongly pH dependent at pH > 1.0 and pH independent at pH < 1.0. Contrary to previously published results, the calculated R_{Al} values for the multimineralic Kc, Km, and BK samples corresponded well to monomineralic (montmorillonite, illite, and kaolinite) dissolution rates in the literature, suggesting that monomineralic rates can be applied to complex multimineralic samples based on their dominant mineral phases.

Furthermore, R_{Si} values indicated that the precipitation of a-SiO_2 was pH dependent at pH $\leq$ 1.0.

Si and Al XANES results corresponded to the aqueous geochemical data for all three clays. Specifically, Al K-edge spectra indicated the progressive loss of Al relative to Si with decreasing pH, which corresponded to the observed large mobilization of Al to the aqueous phase. Moreover, Si and Al K- and $L_{2,3}$-edge spectra showed the persistence of aluminosilicates and the precipitation of Al-SO_4-like phases, which corresponded to the persistence of solid-phase Al to between 41 and 57 % in the three clays under the most extreme conditions examined (pH -3.0, 365 d). Additionally, Si K- and $L_{2,3}$-edge spectra indicate the formation of an a-SiO_2-like phase, which was matched the decreased aqueous Si concentrations at pH $\leq$ 1.0.

The results of this study clearly demonstrate that significant amounts of Al, Fe, Si and Ca will be mobilized into the surrounding pore waters through mineral dissolution reactions upon interaction with H_2SO_4 solutions with pH < 1.0. However, a large proportion of these species will subsequently be immobilized through secondary phase precipitation, such as anhydrite, gypsum, Al-SO_4-rich phases, and a-SiO_2.

5.3 Determine the long-term impact of H_2SO_4 diffusion through clays

To date, no studies have been conducted that investigate H_2SO_4 diffusion in clays at pH < 1.0. Understanding the geochemical and mineralogical impacts of long-term diffusion of H_2SO_4 in clays is important to understanding the long-term stability of clays and the environmental impacts that may potentially arise. The Kc and Km diffusion cell experiments conducted in this thesis, coupled with the batch experiment results, represented the first such study to address these concerns.

Modeled H^+ diffusion profiles assuming no consumption and non-linear consumption were unable to adequately simulate the measured pH profiles in all cells; although, the non-linear consumption model was able to account for the large concentration gradient measured in Kc_1 and Km_1. The assumption that the consumption of H^+ calculated from pH 5.0, 3.0, and 1.0 batch tests could be applied to consumption at pH -1.0 and -3.0 proved to be inaccurate. The amount of H^+ consumption measured in Kc_{-1}, Kc_{-3}, Km_{-1}, and Km_{-3} greatly exceeded the simulated amounts in all three model

cases. These results suggested that additional mechanisms were responsible for the consumption of H^+ in these cells. Alternatively, the value of D* could have been overestimated.

The results indicated that after 216 d above-background pH values were observed to depths of 80, 193, and 210 mm in the Kc pH 1.0, -1.0, and -3.0 cells and to depths of 138, $\leq$ 288, and $\leq$ 288 mm in the Km cells. These elevated pH intervals were characterized by above-ground Al, Fe, and Ca concentrations in the Kc and Km cells. Pore water extractions (1:100) showed above-background Ca, Al, Fe, Si, and SO_4 concentrations associated with elevated H^+ concentrations and XRD results indicated dissolution of carbonate and aluminosilicate phases, in the Kc and Km pH 1.0, -1.0, and -3.0 cells. Furthermore, XRD and 1:1 pore water extracts indicated the precipitation of secondary mineral phases, including anhydrite, gypsum, halotrichite, and an Al-SO_4 phase.

Comparing the depths of H^+ diffusion in the Kc and Km clays showed that H^+ diffusion was retarded in Kc_1, Kc_{-1}, and Kc_{-3} by factors of approximately 3.3, 1.5, and 1.5 relative to Km_1, Km_{-1}, and Km_{-3}.

5.4 Global conclusions

The individual results from the batch and diffusion cell experiments both yielded consistent findings. A large amount of primary phase dissolution, both carbonates and aluminosilicates, occurs at pH < 1.0. The dissolution of carbonates and cation exchange reactions mobilize Ca, Mg, and Na to the porewater, while preferential dissolution of aluminosilicate Al-octahedral layers results in high dissolved Al and Fe concentrations, associated with the preferential dissolution of the Al-octahedral layer. The corresponding Si-tetrahedral layers subsequently polymerize at pH$\leq$ 0.0, forming amorphous silica that is deposited as a surface coating on the unreacted clay. Moreover, large amount of soluble Ca and Al sulfate salts form through secondary phase precipitation reactions at pH $\leq$ 0.0. These reaction mechanisms are further summarized in the conceptual model illustrated in Figure 5.1.

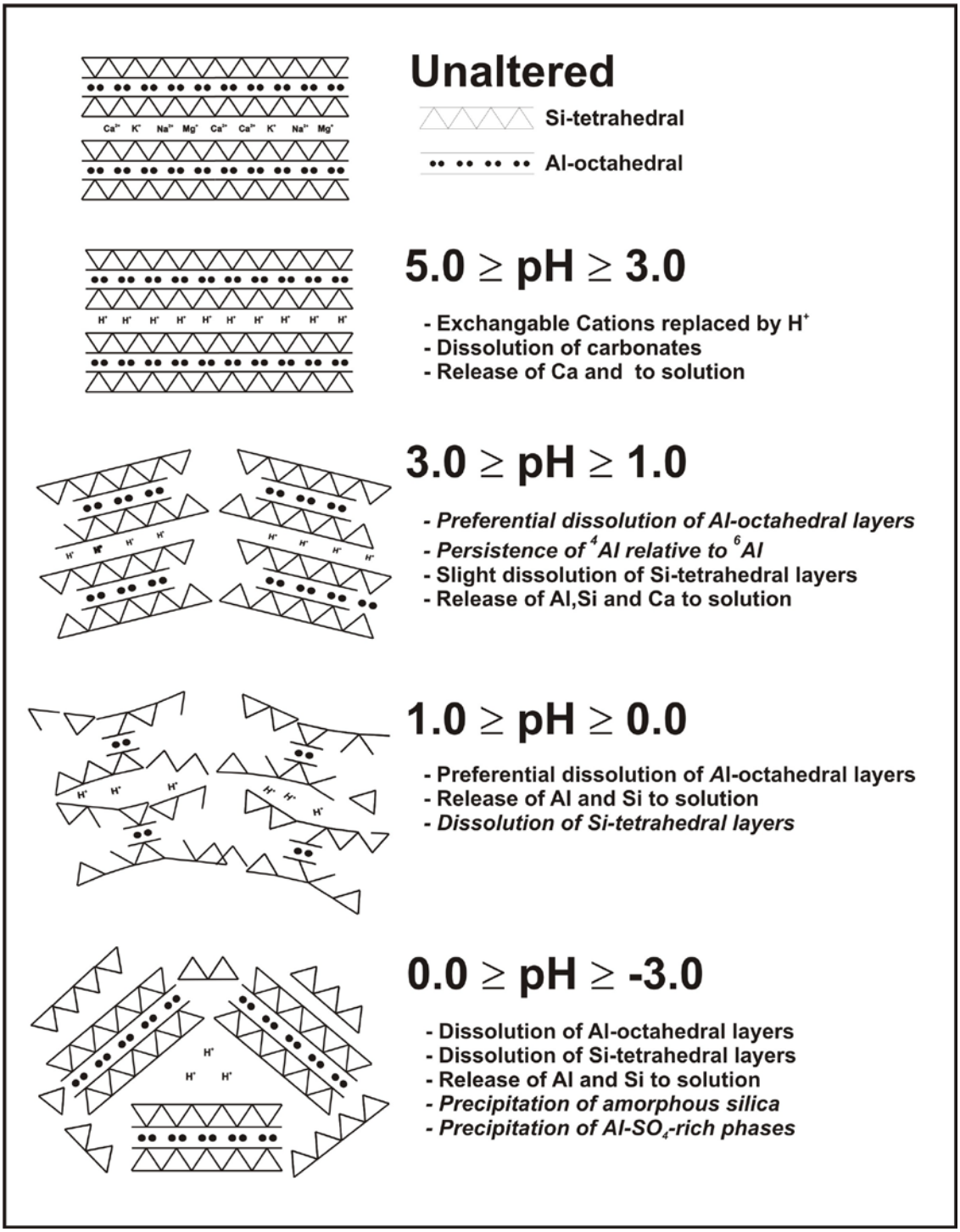

Figure 5.1. Conceptual model of phyllosilicate dissolution under extremely acidic conditions between pH 5.0 and -3.0.

The acidic dissolution of a substantial amount of primary mineral phases, such as carbonates and aluminosilicates, can have significant effect on the long-term geotechnical

stability of clay liners. These dissolution reactions could increase porosity and, therefore, increase the mobilization and transport of metals to the surrounding environment. Conversely, the dissolution of primary mineral phases could lead to increased consolidation of clay liners. Moreover, the observed precipitation of secondary phases, such as a-SiO_2, Al-SO_4, anhydrite, and gypsum could serve to counter-balance these effects through decreased porosity and the immobilization of metals. The results of the diffusion cell experiments demonstrate that, despite the extremely acidic H_2SO_4 solutions considered in this thesis, the incorporation of acid-buffering carbonates within clay liners still represents a significant barrier to the transport of acid impact pore-waters; resulting in the retardation of acid diffusion by a factor of 1.5 to 3.3 in the current study; a phenomena widely understood from the large number of AMD studies in the scientific literature.

6.0 RECOMENDATIONS FOR FUTURE WORK

The findings of the research presented in this thesis were obtained from laboratory-based experiments. However, the inherent problems of scaling laboratory results to in-situ field conditions are well documented. Attempts to characterize the impact of H_2SO_4 into a liner beneath an existing 15 year old above-ground S^0 block proved unsuccessful (data not presented) as no measurable impacts were observed within the collected samples. It is, therefore, recommended that investigations similar to those in this thesis be conducted on clay and/or geologic media situated beneath older S^0 blocks be considered to compare and contrast laboratory and field datasets. Alternatively, long-term acidic heap leach pads used by the mining industry could also be suitable for field investigations.

The measurement of pH is set, by convention, between 1.0 and 13.0. However, the lower limit of this convention only accounts for solution concentrations of approximately 0.1 M. Although the method used in this thesis to measure pH < 1.0 has proved robust and reproducible, the theoretical and uncertain nature of pH measurements below pH < 1.0 within the scientific community as a whole leaves them open to criticism. While not attempted in this thesis, the measurement of solution acidity represents one such possible unit of measurement widely applied within the scientific literature. Therefore, research should be conducted to correlate the negative pH measurements used in this thesis and other studies to the corresponding acidity measurements.

The batch experiment results showed dissolved Si concentrations that initially increased between pH 5.0 and 1.0 and subsequently decreased between pH 1.0 and -3.0. Through XRD and XANES analyses, as well as previous studies, the observed decrease was linked to the precipitation of an amorphous silica phase. While the possible controls of these processes are discussed within this thesis, they remain largely unknown. As such, future research should focus on the fundamental geochemical reactions and their underlying thermodynamics to better characterize the controls on aqueous Si concentrations at pH < 1.0.

The data collected from the diffusion cells, while relevant and valuable to the objectives of this thesis, lacked in some aspects. In particular, the inability to recover representative pore water samples through conventional means interfered with the ability to fully interpret the geochemical aspects of H_2SO_4 diffusion through clay. Therefore, additional diffusion cell experiments that are able to obtain representative pore waters should be considered.

The clays used in this thesis presented a considerable amount of complexity due to the presence of several mineral phases, including, quartz, cristabolite, dolomite, siderite, montmorillonite, illite, and kaolinite. The mechanisms and kinetics of acidic dissolution of monomineralic phases have been widely studied in the existing scientific literature at pH > 1.0, which have aided the interpretation of the acidic dissolution of multimineralic phases, such as the clays used in this thesis, However, acidic dissolution of monomineralic species at pH < 1.0 has not been widely studied and future research at these extreme solution pH values should be undertaken.

Similar to the previous recommendation, there is a lack of thermodynamic datasets for many of the aqueous species measured in this thesis, such as Al and Si. A limited dataset for concentrated solutions currently exists; however, the lack of thermodynamic data for Si and Al, in particular, limited the ability to perform even rudimentary geochemical modeling of the aqueous geochemical results in this research. Therefore, increasing the number of aqueous species that can be modeled by the PHRQPITZ database would greatly aide future studies.

In the Si and Al XANES study, time high resolution K- and $L_{2,3}$-edge analyses were conducted to understand the short-range structural and chemical alterations of H_2SO_4 on clay samples. As previously noted, the samples investigated in this thesis were complex clays containing several phyllosilicate species and an abundance of quartz. A more thorough investigation of the structural and chemical effects of H_2SO_4 on individual mineral phases would improve our understanding of specific processes presented in this thesis. Additionally, high resolution Si, Al, S, and Ca K- and $L_{2,3}$-edge XANES analyses

would improve our understanding of the effects of H_2SO_4 on the mixed clays examined in this thesis.

The model simulations of H^+ transport in the diffusion cell experiments assumed that pH values measured using conventional and negative pH methods could be equated to a known H^+ concentration. However, speciation data from previous studies indicates that at pH < 2.0 HSO_4^- is the dominant SO_4 species in solution. The fractionation of these species as a function of pH could not be incorporated into the model simulations; however, given the discrepancy between the measured and modeled H^+ consumption observed in all cells this mechanism requires further study.

The retardation of H^+ through consumption reactions in the Kc and Km clays was not well constrained in the current study. Therefore, additional work to determine the retardation of H^+ by these clays through batch tests or diffusion cells should be undertaken in future studies. Additionally, the D* of H^+ needs to be better constrained as a function of pH and pore water chemistry.

APPENDIX 1 Supplementary data for clays.

Appendix 1A - Unaltered Kc, Km, and BK total extract metal concentrations. Average values calculated from three sample replicates

Appendix 1B - Kc Sequential Extraction Totals. Calculated from three sample replicates

Appendix 1C - Km Sequential Extraction Totals. Calculated from three sample replicates

Appendix 1D - BK Sequential Extraction Totals. Calculated from three sample replicates

Appendix 1E - Kc, Km, and BK Cation Exchange Capacity (CEC) Calculations

Appendix 1A: Unaltered Kc, Km, and BK total extract metal concentrations. Average values calculated from three sample replicates.

Element	Kc			Km			BK		
	Average	Std. Dev.	RSD	Average	Std. Dev.	RSD	Average	Std. Dev.	RSD
	(µg g^{-1})	(µg g^{-1})	(%)	(µg g^{-1})	(µg g^{-1})	(%)	(µg g^{-1})	(µg g^{-1})	(%)
Ag	4.18E-01	5.89E-03	1.41	6.18E-01	3.25E-03	0.53	3.46E-02	0.00E+00	0.00
Al	7.59E+04	4.22E+03	5.56	6.68E+04	1.89E+03	2.83	1.19E+05	4.36E+03	3.68
As	2.08E+01	1.23E+00	5.91	3.43E+00	7.53E-01	21.9	6.90E+00	6.18E-01	8.96
Ba	7.39E+02	1.09E+01	1.48	3.23E+02	1.75E+00	0.54	8.39E+02	8.54E+00	1.02
Ca	1.66E+04	5.02E+02	3.02	1.58E+03	1.11E+01	0.70	1.40E+04	5.32E+02	3.80
Cd	3.55E-01	7.01E-02	19.8	4.51E-01	1.60E-01	35.5	2.94E-01	8.23E-02	28.0
Ce	7.30E+01	1.17E+00	1.60	9.03E+01	2.07E+00	2.29	1.00E+02	2.41E+00	2.40
Co	1.82E+01	3.45E-01	1.89	1.63E+01	2.17E-01	1.33	2.54E+00	8.60E-02	3.39
Cr	8.65E+01	1.27E+00	1.47	7.31E+01	4.41E+00	6.03	7.07E+00	4.53E-01	6.40
Cs	6.50E+00	1.72E-01	2.64	4.71E+00	2.07E-02	0.44	1.06E+00	6.49E-02	6.12
Cu	4.64E+01	2.31E+00	4.98	2.16E+01	5.29E-01	2.45	4.57E+00	1.48E+00	32.5
Dy	5.12E+00	6.83E-02	1.34	6.91E+00	8.96E-02	1.30	5.14E+00	2.31E-01	4.49
Er	2.92E+00	3.92E-02	1.34	4.15E+00	6.02E-02	1.45	2.63E+00	3.17E-02	1.21
Eu	1.46E+00	3.88E-02	2.66	1.59E+00	1.56E-02	0.99	6.97E-01	1.70E-02	2.44
Fe	2.87E+04	1.40E+03	4.88	2.18E+04	2.01E+02	0.92	3.03E+04	5.39E+02	1.78
Ga	1.68E+01	2.54E-01	1.51	1.56E+01	1.97E-01	1.26	2.69E+01	7.70E-01	2.87
Gd	6.04E+00	1.87E-02	0.31	7.26E+00	8.73E-02	1.20	6.13E+00	1.96E-01	3.19
Hf	4.37E+00	6.68E-02	1.53	1.17E+01	7.86E-01	6.72	6.77E+00	1.72E-01	2.53
La	3.41E+01	5.00E-01	1.47	4.00E+01	1.93E-01	0.48	4.77E+01	1.51E+00	3.16
Li	5.57E+01	3.04E+00	5.46	9.28E+01	8.17E-01	0.88	2.16E+01	1.46E+00	6.74
Lu	3.96E-01	9.76E-03	2.47	6.01E-01	2.61E-03	0.43	3.13E-01	5.26E-03	1.68
Mg	1.71E+04	8.77E+02	5.12	3.75E+03	8.68E+01	2.32	1.12E+04	9.42E+02	8.37
Mn	1.91E+02	6.51E+00	3.40	9.47E+02	7.05E+00	0.74	6.28E+02	4.13E+01	6.58
Mo	1.82E+00	9.95E-02	5.48	1.47E+00	3.39E-01	23.0	3.84E+00	2.88E-01	7.49
Nb	1.43E+01	1.77E-01	1.24	1.77E+01	2.71E+00	15.4	2.66E+01	1.09E+00	4.12
Nd	3.21E+01	4.73E-01	1.47	3.78E+01	3.33E-01	0.88	3.70E+01	5.84E-01	1.58
Ni	4.69E+01	2.44E-01	0.52	2.73E+01	5.36E-01	1.96	1.50E+00	7.40E-01	49.3
P	9.06E+02	2.70E+01	2.99	2.96E+02	8.04E+00	2.71	3.76E+02	3.19E+01	8.46
Pb	2.09E+01	4.22E-01	2.02	1.96E+01	4.93E-01	2.51	3.56E+01	2.98E+00	8.36
Pr	8.51E+00	9.98E-02	1.17	1.02E+01	7.66E-02	0.75	1.12E+01	1.67E-01	1.49
Rb	9.63E+01	1.98E+00	2.06	8.43E+01	1.46E+00	1.73	2.32E+01	7.29E-01	3.14
Sb	9.85E-01	1.08E-01	11.0	4.22E-01	3.22E-02	7.63	1.40E+00	1.63E-01	11.7
Sc	1.66E+01	6.87E-01	4.15	1.30E+01	2.13E+00	16.4	1.12E+01	1.36E+00	12.1
Sm	6.38E+00	1.47E-01	2.30	7.55E+00	8.79E-02	1.16	7.13E+00	6.44E-02	0.90
Sn	2.87E+00	7.10E-02	2.47	3.82E+00	1.00E+00	26.2	8.15E+00	4.26E-01	5.23
Sr	2.55E+02	4.20E+00	1.65	8.10E+01	1.34E+00	1.65	3.10E+02	1.66E+01	5.35
Ta	8.99E-01	8.10E-03	0.90	1.34E+00	4.89E-02	3.64	2.65E+00	9.23E-02	3.48
Tb	8.21E-01	1.46E-02	1.78	1.07E+00	1.51E-02	1.41	8.46E-01	2.15E-02	2.54
Th	1.02E+01	1.03E-01	1.01	1.21E+01	1.99E-01	1.64	3.28E+01	6.58E-01	2.01
Ti	4.15E+03	7.02E+01	1.69	6.51E+03	1.44E+02	2.21	1.38E+03	2.51E+01	1.82
Tl	6.54E-01	5.36E-02	8.21	4.05E-01	1.23E-02	3.05	3.15E-01	4.87E-02	15.5
Tm	4.26E-01	1.28E-02	3.00	6.25E-01	1.92E-02	3.07	3.66E-01	1.41E-02	3.86
U	3.33E+00	9.80E-02	2.95	3.25E+00	6.73E-02	2.07	1.09E+01	2.27E-01	2.08
V	1.80E+02	3.81E+00	2.12	8.86E+01	1.16E+00	1.31	9.35E+00	2.48E-01	2.66
W	1.57E+00	2.17E-01	13.8	2.41E+00	2.65E-01	11.0	3.00E-01	6.58E-02	22.0
Y	2.68E+01	3.21E-01	1.20	3.65E+01	5.42E-01	1.48	2.31E+01	7.51E-01	3.25
Yb	2.74E+00	9.14E-03	0.33	4.12E+00	8.60E-02	2.09	2.44E+00	9.50E-02	3.90
Zn	1.95E+02	7.94E+00	4.08	1.15E+02	4.43E+00	3.85	8.66E+01	1.07E+01	12.4
Zr	1.52E+02	2.34E+00	1.53	4.54E+02	7.02E+00	1.54	1.93E+02	1.99E+01	10.3

Appendix 1B: Kc Sequential Extraction Totals. Calculated from three sample replicates.

Element	Water Soluble	Exchangeable	Carbonate Bound	Al/Fe Oxy/Hydroxides	Organic Bound	Residual
	(%)	(%)	(%)	(%)	(%)	(%)
Ag	0.00	0.00	0.00	12.7	8.37	78.9
Al	0.02	0.00	0.03	2.65	1.13	96.2
As	0.52	0.00	4.99	59.2	31.9	3.43
Ba	0.13	15.8	3.47	1.86	0.80	77.9
Ca	0.54	11.3	31.1	45.6	0.35	11.1
Cd	0.96	1.78	13.4	15.9	0.00	67.9
Ce	0.14	0.03	2.89	16.5	17.3	63.1
Co	0.29	14.0	16.9	36.7	13.2	18.8
Cr	0.27	0.00	1.64	38.6	35.8	23.7
Cs	0.05	0.20	0.30	11.0	2.83	85.6
Cu	0.19	0.42	3.26	21.4	55.6	19.1
Dy	0.20	0.01	11.6	31.0	13.3	44.0
Er	0.14	0.00	11.2	26.9	10.8	51.0
Eu	0.20	0.30	9.5	29.7	16.1	44.2
Fe	0.03	0.02	0.11	22.7	29.1	48.1
Ga	0.03	0.00	0.00	4.97	2.67	92.3
Gd	0.19	0.01	11.1	33.9	18.3	36.4
Hf	0.09	0.00	0.02	3.15	1.62	95.1
Ho	0.17	0.00	12.1	29.1	11.1	47.6
La	0.12	0.16	2.26	13.6	13.6	70.3
Li	1.13	0.98	0.33	13.7	9.61	74.3
Lu	0.00	0.04	13.6	22.7	8.62	55.1
Mn	0.32	14.9	9.90	33.3	16.5	25.0
Mo	3.33	0.83	0.00	28.4	4.52	63.0
Nb	0.01	0.01	0.00	0.62	0.15	99.2
Nd	0.17	0.00	4.69	22.6	17.1	55.3
Ni	0.34	9.25	15.7	34.3	21.4	19.0
Pb	0.31	0.00	12.4	45.0	6.48	35.8
Pr	0.16	0.00	3.77	19.5	17.1	59.4
Rb	0.17	1.02	0.94	4.85	1.81	91.2
Sb	2.42	0.96	6.36	7.56	0.61	82.1
Sc	0.37	0.06	10.94	34.8	21.2	32.7
Sm	0.19	0.00	7.59	29.2	17.1	45.9
Sn	0.00	0.01	0.00	2.82	1.63	95.5
Sr	2.12	51.9	4.57	5.19	3.03	33.2
Ta	0.02	0.00	0.01	0.19	0.00	99.8
Th	0.23	0.00	2.37	1.72	47.1	48.5
Ti	0.01	0.00	0.01	0.47	0.06	99.4
Tl	0.05	0.28	1.27	5.45	9.65	83.3
Tm	0.00	0.00	9.63	23.7	8.93	57.7
U	0.21	0.10	9.60	8.48	24.0	57.6
V	0.10	0.00	0.28	12.4	6.14	81.1
W	0.00	0.00	0.00	0.66	0.00	99.3
Y	0.19	0.47	12.1	31.2	11.5	44.5
Yb	0.12	0.00	8.69	21.1	7.14	62.9
Zn	0.31	1.53	9.66	23.5	39.8	25.2
Zr	0.06	0.00	0.01	5.81	1.26	92.9

Appendix 1C: Km Sequential Extraction Totals. Calculated from three sample replicates.

Element	Water Soluble	Exchangeable	Carbonate Bound	Al/Fe Oxy/Hydroxides	Organic Bound	Residual
	(%)	(%)	(%)	(%)	(%)	(%)
Ag	0.00	0.00	0.00	1.42	0.00	98.6
Al	0.08	0.00	0.02	0.57	0.47	98.9
As	3.38	0.00	0.00	91.6	0.00	5.04
Ba	0.55	3.59	1.95	4.97	0.75	88.2
Ca	4.81	18.0	6.40	64.2	2.34	4.24
Cd	2.09	0.80	10.5	11.7	0.00	74.9
Ce	0.69	0.00	0.58	14.1	13.7	70.9
Co	7.67	13.3	16.7	34.0	3.86	24.4
Cr	0.38	0.00	2.15	53.8	0.00	43.6
Cs	0.17	0.17	0.41	10.3	2.06	86.9
Cu	4.02	0.12	8.45	35.4	1.81	50.2
Dy	0.49	0.00	2.25	19.1	6.30	71.9
Er	0.35	0.00	2.18	17.4	2.87	77.2
Eu	0.74	0.10	1.79	20.1	12.5	64.9
Fe	0.40	0.04	1.37	56.9	1.94	39.3
Ga	0.25	0.00	0.00	1.14	0.63	98.0
Gd	0.66	0.00	2.12	21.0	14.5	61.7
Hf	0.28	0.00	0.02	1.26	0.01	98.4
Ho	0.40	0.00	2.22	18.5	4.61	74.2
La	0.55	0.01	0.46	10.9	11.0	77.1
Li	0.90	0.65	0.45	3.41	0.00	94.6
Lu	0.03	0.28	3.37	15.9	9.46	71.0
Mn	0.89	5.89	6.78	84.0	1.03	1.44
Mo	1.15	0.00	0.00	20.5	2.81	75.6
Nb	0.02	0.00	0.01	0.31	0.63	99.0
Nd	0.74	0.00	0.93	14.8	12.6	70.9
Ni	6.27	8.43	15.2	30.1	5.13	34.9
Pb	3.88	0.00	8.55	42.6	6.41	38.6
Pr	0.72	0.00	0.69	13.87	12.9	71.8
Rb	0.45	1.12	0.83	3.71	1.13	92.8
Sb	1.50	0.11	1.95	2.08	0.00	94.3
Sc	1.23	0.16	10.2	44.8	0.00	43.6
Sm	0.76	0.00	1.48	18.2	12.2	67.4
Sn	0.53	0.00	0.00	5.42	0.00	94.0
Sr	3.20	20.3	3.62	11.9	23.7	37.2
Ta	0.01	0.00	0.00	0.10	0.00	99.9
Th	0.79	0.00	0.79	4.78	17.38	76.3
Ti	0.03	0.00	0.00	0.15	0.93	98.9
Tl	0.37	0.29	1.43	3.24	1.70	93.0
Tm	0.27	0.00	1.75	16.0	1.89	80.1
U	1.52	0.00	5.01	9.52	17.0	66.9
V	0.57	0.00	0.00	26.5	0.44	72.5
W	0.00	0.00	0.00	0.24	0.00	99.8
Y	0.46	0.08	2.41	19.1	3.67	74.3
Yb	0.25	0.00	1.82	15.3	2.82	79.8
Zn	4.08	1.78	7.61	13.8	0.86	71.8
Zr	0.14	0.00	0.03	2.08	0.31	97.5

Appendix 1D: BK Sequential Extraction Totals. Calculated from three sample replicates.

Element	Water Soluble	Exchangeable	Carbonate Bound	Al/Fe Oxy/Hydroxides	Organic Bound	Residual
	(%)	(%)	(%)	(%)	(%)	(%)
Ag	0.00	0.00	0.00	0.00	0.00	100.0
Al	0.06	0.00	0.16	0.40	1.70	97.7
As	10.0	4.99	13.9	0.00	38.8	32.3
Ba	0.01	11.3	9.59	29.8	11.3	37.9
Ca	0.17	18.7	29.3	9.91	2.01	39.9
Cd	4.82	3.04	60.0	38.7	36.8	-
Ce	0.02	0.00	1.88	5.82	57.2	35.1
Co	0.00	0.00	18.5	0.00	18.1	63.4
Cr	6.10	0.00	0.00	0.00	3.56	90.3
Cs	0.07	1.85	11.3	2.82	1.07	82.9
Cu	0.99	0.00	7.63	16.0	21.4	54.0
Dy	0.00	0.00	5.52	12.7	40.5	41.3
Er	0.00	0.00	7.74	13.0	30.4	48.9
Eu	0.00	0.00	3.93	8.82	33.2	54.1
Fe	0.09	0.08	0.65	8.34	7.21	83.6
Ga	0.23	0.26	0.50	1.08	1.66	96.3
Gd	0.00	0.00	3.74	13.6	48.4	34.3
Hf	0.09	0.00	0.01	5.53	0.00	94.4
Ho	0.00	0.00	6.57	13.3	35.2	44.9
La	0.02	0.07	2.23	5.38	55.6	36.7
Li	1.38	2.98	2.69	6.91	9.50	76.5
Lu	0.00	0.00	13.6	13.1	21.2	52.1
Mn	0.02	0.06	31.5	34.9	8.04	25.4
Mo	35.2	23.4	0.00	25.1	6.32	10.0
Nb	0.08	0.05	0.07	8.98	3.77	87.0
Nd	0.02	0.01	2.33	9.52	55.4	32.7
Ni	11.6	0.00	111.8	66.3	46.8	-
P	3.88	0.90	5.47	67.8	21.7	0.28
Pb	0.04	0.00	35.4	36.1	17.7	10.7
Pr	0.02	0.00	1.94	7.09	54.2	36.8
Rb	0.11	0.96	7.99	7.51	7.03	76.4
Sb	2.99	4.08	10.8	13.6	0.00	68.5
Sc	1.11	0.03	0.52	2.71	4.66	91.0
Sm	0.00	0.00	2.92	11.3	54.2	31.6
Sn	0.26	0.00	0.00	1.45	0.00	98.3
Sr	0.11	37.5	11.6	18.1	3.89	28.8
Ta	0.13	0.01	0.02	1.36	0.00	98.5
Th	0.02	0.00	0.45	0.78	56.4	42.4
Ti	0.06	0.03	0.11	0.00	1.79	98.0
Tl	0.00	0.00	6.64	13.5	45.3	34.6
Tm	0.00	0.00	9.25	11.8	26.5	52.4
U	0.49	0.72	9.06	5.06	42.3	42.4
V	7.57	1.42	3.60	0.00	11.0	76.4
W	4.11	0.00	0.00	8.73	0.00	87.2
Y	0.02	1.15	10.2	16.6	37.5	34.5
Yb	0.00	0.00	10.7	12.3	22.5	54.4
Zn	0.41	0.00	7.73	6.49	33.7	51.7
Zr	0.06	0.00	0.01	6.67	0.02	93.2

Appendix 1E: Kc, Km, and BK Cation Exchange Capacity (CEC) calculations.

Sample ID	Clay	Ca	Mg	Na	K	$BaCl_2$ Added	Ca	Mg	Na	K	Total	Average	Std. Dev.	RSD
	(g)	(mg L^{-1})	(mg L^{-1})	(mg L^{-1})	(mg L^{-1})	(mL)	(meq g^{-1})	(meq g^{-1})	(meq g^{-1})	(meq g^{-1})	(meq $100g^{-1}$)	(meq $100g^{-1}$)	(meq $100g^{-1}$)	(%)
KC-UA-1	0.50	20.2	11.7	60.3	7.36	30.24	0.061	0.058	0.159	0.011	28.9			
KC-UA-2	0.51	20.6	12.4	61.3	7.85	30.07	0.060	0.060	0.157	0.012	29.0	**28.5**	0.52	1.83
KC-UA-3	0.53	20.4	12.2	60.2	7.67	30.80	0.059	0.058	0.152	0.011	28.1			
KC-UA-4	0.53	19.9	12.4	60.1	7.67	30.80	0.058	0.059	0.152	0.011	28.0			
KM-UA-1	0.50	6.56	3.13	61.9	5.91	30.04	0.020	0.015	0.162	0.009	20.6			
KM-UA-2	0.49	5.93	3.02	59.6	5.99	30.00	0.018	0.015	0.159	0.009	20.1	**20.3**	0.24	1.20
KM-UA-3	0.53	5.93	3.04	59.4	5.93	32.63	0.018	0.015	0.159	0.009	20.2			
BK-UA-1	0.57	72.4	7.57	261	2.05	30.24	0.192	0.033	0.601	0.003	82.9			
BK-UA-2	0.51	64.1	6.69	229	1.71	30.94	0.194	0.033	0.603	0.003	83.3	**83.0**	0.28	0.34
BK-UA-3	0.56	69.6	7.40	259	2.02	30.05	0.186	0.033	0.605	0.003	82.7			
BK-UA-1	0.57	70.1	8.12	263	1.91	30.24	0.186	0.035	0.606	0.003	83.0			

Example Calculation:

$$\frac{meq}{g} = Ca\left(\frac{mg}{L}\right) \times BaCl_2\,Added(mL) \times \left(\frac{L}{1000mL}\right)\left(\frac{mol}{40.078g}\right)x\left(\frac{g}{1000mg}\right) \times \left(\frac{eq}{2mol}\right)x\left(\frac{1000meq}{eq}\right)x\left(\frac{1}{Clay(g)}\right)$$

APPENDIX 2 Supplementary data for Chapter 2.

Appendix 2A - Raw data for Kc batch experiments showing amount of clay, total H_2SO_4 and NaOH added, and final solution pH

Appendix 2B - Raw data for Km batch experiments showing amount of clay, total H_2SO_4 and NaOH added, and final solution pH

Appendix 2C - Raw data for BK batch experiments showing amount of clay, total H_2SO_4 and NaOH added, and final solution pH

Appendix 2D - Aqueous geochemistry analyses results for Kc (14d) batch experiment

Appendix 2E - Aqueous geochemistry analyses results for Kc (90d) batch experiment

Appendix 2F - Aqueous geochemistry analyses results for Kc (180d) batch experiment

Appendix 2G - Aqueous geochemistry analyses results for Kc (365d) batch experiment

Appendix 2H - Aqueous geochemistry analyses results for Km (14d) batch experiment

Appendix 2I - Aqueous geochemistry analyses results for Km (90d) batch experiment

Appendix 2J - Aqueous geochemistry analyses results for Km (180d) batch experiment

Appendix 2K - Aqueous geochemistry analyses results for Km (365d) batch experiment

Appendix 2L - Aqueous geochemistry analyses results for BK (14d) batch experiment

Appendix 2M - Aqueous geochemistry analyses results for BK (90d) batch experiment

Appendix 2N - Aqueous geochemistry analyses results for BK (180d) batch experiment

Appendix 2O - Aqueous geochemistry analyses results for BK (365d) batch experiment

Appendix 2P - Percent of Al, Fe, and Ca remaining in altered Kc solid phase

Appendix 2Q - Percent of Al, Fe, and Ca remaining in altered Km solid phase

Appendix 2R - Percent of Al, Fe, and Ca remaining in altered BK solid phase

Appendix 2S - Calculated Kc Al and Si dissolution rates

Appendix 2T - Calculated Km Al and Si dissolution rates

Appendix 2U - Calculated BK Al and Si dissolution rates

Appendix 2V - Diffractograms for pH 5.0 to -3.0, 14 d exposure time, a) Kc, b) Km, c) BK batch experiments.

Appendix 2A: Raw data for Kc batch experiments showing amount of clay, total H_2SO_4 and NaOH added, and final solution pH.

Sample ID	pH	Clay	H_2SO_4 Added	NaOH Added
		(g)	(mmol)	(mmol)
KC1-BE1-14d	4.60	5.08	2.305	
KC-BE1-90d	4.77	5.01	2.251	
KC-BE1-180d	4.81	5.10	2.346	0.000
KC-BE1-365d	4.40	5.08	4.216	1.464
KC1-BE2-14d	3.05	5.05	2.270	
KC2-BE2-14d	3.03	5.11	2.490	
KC-BE2-90d	3.01	5.05	3.032	0.753
KC-BE2-180d	2.98	5.16	2.904	0.865
KC-BE2-365d	3.00	5.00	3.458	0.771
KC1-BE3-14d	1.02	5.08	18.16	
KC2-BE3-14d	1.00	5.01	17.60	
KC-BE3-90d	1.02	5.02	17.17	
KC-BE3-180d	1.04	5.08	15.98	
KC-BE3-365d	1.11	5.05	18.24	
KC1-BE6-14d	-0.12	5.03	86.52	
KC2-BE6-14d	-0.12	5.15	86.52	
KC-BE6-90d	-0.05	5.01	97.21	
KC-BE6-180d	-0.20	5.01	86.16	
KC-BE6-365d	0.05	5.08	85.96	
KC1-BE4-14d	-1.10	5.09	209.7	
KC2-BE4-14d	-1.10	5.03	210.4	
KC-BE4-90d	-1.15	5.03	254.7	
KC-BE4-180d	-1.20	5.16	244.5	
KC-BE4-365d	-1.10	5.13	230.4	
KC1-BE7-14d	-1.97	5.03	412.8	
KC2-BE7-14d	-1.97	5.09	419.8	
KC-BE7-90d	-2.18	5.11	387.2	
KC-BE7-180d	-2.30	5.08	344.7	
KC-BE7-365d	-1.80	5.06	324.2	
KC1-BE5-14d	-2.95	5.01	427.3	
KC2-BE5-14d	-2.95	5.08	422.1	
KC-BE5-90d	-3.00	5.10	428.2	
KC-BE5-180d	-2.95	5.23	418.8	
KC-BE5-365d	-3.10	5.07	449.9	

Appendix 2B: Raw data for Km batch experiments showing amount of clay, total H_2SO_4 and NaOH added, and final solution pH.

Sample ID	pH	Clay	H_2SO_4 Added	NaOH Added
		(g)	(mmol)	(mmol)
KM1-BE1-14d	5.00	5.03	0.321	
KM2-BE1-14d	4.99	5.13	0.347	
KM-BE1-90d	4.85	5.16	0.636	
KM-BE1-180d	4.82	5.02	0.572	0.155
KM-BE1-365d	4.90	5.10	0.442	0.078
KM1-BE2-14d	2.55	5.02	1.585	
KM2-BE2-14d	2.99	5.03	1.661	
KM-BE2-90d	3.05	5.01	1.680	1.379
KM-BE2-180d	3.00	5.21	1.597	1.243
KM-BE2-365d	3.05	5.01	1.618	1.162
KM1-BE3-14d	1.00	5.15	14.33	
KM2-BE3-14d	1.00	5.15	14.33	
KM-BE3-90d	1.01	5.03	14.63	
KM-BE3-180d	1.00	5.06	12.53	
KM-BE3-365d	1.10	5.10	13.23	
KM1-BE6-14d	-0.12	5.05	86.25	
KM2-BE6-14d	-0.12	5.03	88.18	
KM-BE6-90d	-0.05	5.04	94.80	
KM-BE6-180d	-0.20	5.02	86.42	
KM-BE6-365d	0.05	5.08	85.71	
KM1-BE4-14d	-1.10	5.10	210.1	
KM2-BE4-14d	-1.10	5.13	209.8	
KM-BE4-90d	-1.15	5.11	242.8	
KM-BE4-180d	-1.20	5.11	247.5	
KM-BE4-365d	-1.10	5.00	230.3	
KM1-BE7-14d	-1.97	5.04	410.4	
KM2-BE7-14d	-1.97	5.07	410.3	
KM-BE7-90d	-2.18	5.01	377.6	
KM-BE7-180d	-2.30	5.12	329.1	
KM-BE7-365d	-1.80	5.08	325.6	
KM1-BE5-14d	-2.95	5.06	425.5	
KM2-BE5-14d	-2.95	5.19	425.8	
KM-BE5-90d	-2.90	5.21	414.0	
KM-BE5-180d	-3.00	5.01	419.6	
KM-BE5-365d	-3.10	5.01	450.2	

Appendix 2C: Raw data for BK batch experiments showing amount of clay, total H_2SO_4 and NaOH added, and final solution pH.

Sample ID	pH	Clay	H_2SO_4 Added	NaOH Added
		(g)	(mmol)	(mmol)
BK1-BE1-14d	5.07	5.14	1.273	
BK2-BE1-14d	4.81	5.03	1.243	
BK-BE1-90d	5.00	5.08	1.458	
BK-BE1-180d	5.10	5.15	1.460	0.000
BK-BE1-365d	4.69	5.07	1.385	0.000
BK1-BE2-14d	3.06	5.04	2.072	
BK2-BE2-14d	3.05	5.02	2.128	
BK-BE2-90d	2.96	5.06	2.222	
BK-BE2-180d	3.04	5.11	2.262	0.191
BK-BE2-365d	2.95	5.05	2.237	0.105
BK1-BE3-14d	1.03	5.14	16.41	
BK2-BE3-14d	1.03	5.12	16.38	
BK-BE3-90d	1.00	5.02	17.59	
BK-BE3-180d	0.97	5.07	15.20	
BK-BE3-365d	1.13	5.14	15.15	
BK1-BE6-14d	-0.12	5.07	87.57	
BK2-BE6-14d	-0.12	5.01	86.38	
BK-BE6-90d	-0.05	5.03	91.06	
BK-BE6-180d	-0.20	5.11	87.37	
BK-BE6-365d	0.05	5.04	85.88	
BK1-BE4-14d	-1.10	5.05	211.0	
BK2-BE4-14d	-1.10	5.17	209.8	
BK-BE4-90d	-1.15	5.06	252.5	
BK-BE4-180d	-1.20	5.00	247.2	
BK-BE4-365d	-1.10	5.13	230.8	
BK1-BE7-14d	-1.97	5.02	409.3	
BK2-BE7-14d	-1.97	5.12	409.8	
BK-BE7-90d	-2.18	5.06	362.7	
BK-BE7-180d	-2.30	5.04	331.9	
BK-BE7-365d	-1.80	5.01	323.9	
BK1-BE5-14d	-2.95	5.13	443.6	
BK2-BE5-14d	-2.95	5.15	447.6	
BK-BE5-90d	-2.90	5.02	419.4	
BK-BE5-180d	-3.05	5.09	412.2	
BK-BE5-365d	-3.15	5.08	439.7	

Appendix 2D: Aqueous geochemistry analyses results for Kc (14d) batch experiment.

Sample ID	BE1	BE2	BE3	BE6	BE4	BE7	BE5
	(mol L^{-1} g^{-1})	(mol L^{-1} g^{-1})	(mol L^{-1} g^{-1})	(mol L^{-1} g^{-1})	(mol L^{-1} g^{-1})	(mol L^{-1} g^{-1})	(mol L^{-1} g^{-1})
pH	5.00	3.00	1.00	0.00	-1.00	-2.00	-3.00
pe	8.53	11.89	11.08	11.54	11.91	12.05	12.21
Clay	5.15	5.08	5.05	5.09	5.06	5.06	5.05
Density (g mL^{-1})	1.01	1.01	1.01	1.07	1.14	1.21	1.30
Al	5.54E-06	1.07E-04	1.49E-03	2.39E-03	2.95E-03	3.91E-03	4.42E-03
Ba	-4.24E-09	3.01E-08	3.32E-08	5.45E-08	5.14E-08	4.34E-08	3.38E-08
Be	0.00E+00	3.17E-07	5.17E-07	6.91E-07	7.17E-07	8.82E-07	1.03E-06
B	2.31E-05	2.35E-05	2.17E-05	2.69E-05	2.46E-05	2.66E-05	2.32E-05
Cd	1.38E-08	1.31E-08	3.17E-08	2.96E-08	5.18E-09	1.77E-08	0.00E+00
Cr	0.00E+00	4.35E-08	1.54E-06	2.56E-06	2.83E-06	4.01E-06	3.99E-06
Co	8.56E-07	1.24E-06	1.93E-06	2.33E-06	2.59E-06	2.76E-06	3.07E-06
Cu	3.97E-08	9.60E-07	3.13E-06	3.86E-06	2.78E-06	4.53E-06	3.17E-06
Fe	3.27E-06	4.23E-05	1.64E-03	2.24E-03	2.56E-03	2.87E-03	2.80E-03
Pb	-1.87E-09	2.28E-08	2.11E-07	2.24E-07	1.65E-07	2.01E-07	1.01E-07
Mn	6.85E-06	9.23E-06	2.08E-05	2.71E-05	2.93E-05	3.35E-05	3.59E-05
Mo	0.00E+00	1.71E-09	8.43E-09	2.11E-08	8.01E-08	6.77E-08	1.18E-07
Ni	1.64E-06	2.64E-06	4.47E-06	5.45E-06	6.09E-06	6.60E-06	6.75E-06
P	0.00E+00	2.26E-06	1.85E-04	2.27E-04	2.66E-04	2.60E-04	3.07E-04
Si	8.95E-05	2.04E-04	1.33E-03	1.06E-03	4.54E-04	1.04E-04	2.77E-05
Ag	0.00E+00	0.00E+00	0.00E+00	0.00E+00	-3.23E-08	0.00E+00	-4.25E-08
Sr	8.56E-06	8.13E-06	8.90E-06	1.08E-05	1.30E-05	1.01E-05	6.75E-06
Ti	2.03E-08	1.44E-08	8.24E-07	4.67E-06	1.56E-05	2.24E-05	3.01E-05
V	0.00E+00	2.45E-07	4.36E-06	6.03E-06	6.92E-06	9.16E-06	9.56E-06
Zn	2.73E-06	8.26E-06	1.44E-05	1.84E-05	2.07E-05	2.19E-05	2.36E-05
Zr	4.25E-09	1.09E-08	3.15E-08	2.20E-06	2.73E-06	3.72E-06	3.51E-06
Ca	1.94E-03	1.79E-03	2.22E-03	2.33E-03	1.58E-03	4.98E-04	1.76E-04
Mg	1.87E-03	1.70E-03	3.10E-03	3.83E-03	5.33E-03	4.59E-03	5.76E-03
Na	1.41E-03	1.87E-03	1.89E-03	2.05E-03	1.99E-03	2.27E-03	2.18E-03
K	8.11E-04	1.13E-04	2.35E-04	3.17E-04	4.96E-04	5.80E-04	6.27E-04
Cl	8.58E-04	0.00E+00	0.00E+00	0.00E+00	0.00E+00	0.00E+00	0.00E+00
NO_3	0.00E+00	0.00E+00	0.00E+00	0.00E+00	0.00E+00	0.00E+00	0.00E+00
SO_4	4.56E-03	5.07E-03	3.32E-02	1.65E-01	4.51E-01	7.16E-01	9.95E-01

Appendix 2E: Aqueous geochemistry analyses results for Kc (90d) batch experiment

Sample ID	BE1	BE2	BE3	BE6	BE4	BE7	BE5
	(mol L^{-1} g^{-1})	(mol L^{-1} g^{-1})	(mol L^{-1} g^{-1})	(mol L^{-1} g^{-1})	(mol L^{-1} g^{-1})	(mol L^{-1} g^{-1})	(mol L^{-1} g^{-1})
pH	5.00	3.00	1.00	0.00	-1.00	-2.00	-3.00
pe	8.53	11.89	11.08	11.54	11.91	12.05	12.21
Clay	5.01	5.05	5.02	5.01	5.03	5.11	5.10
Density (g mL^{-1})	1.00	1.01	1.02	1.06	1.17	1.24	1.30
Al	7.40E-06	2.03E-04	2.43E-03	4.26E-03	7.50E-03	9.60E-03	1.17E-02
Ba	2.91E-08	7.21E-09	2.66E-08	4.28E-08	4.47E-08	4.53E-08	5.05E-08
Be	0.00E+00	3.74E-07	6.07E-07	9.32E-07	1.22E-06	1.38E-06	1.54E-06
B	2.40E-05	2.20E-05	1.57E-05	2.87E-05	3.63E-05	4.03E-05	3.85E-05
Cd	7.10E-09	1.41E-08	3.96E-08	5.23E-08	3.27E-08	5.53E-08	2.06E-08
Cr	0.00E+00	2.02E-07	2.42E-06	4.36E-06	6.60E-06	7.97E-06	8.89E-06
Co	8.47E-07	1.41E-06	2.20E-06	2.71E-06	2.91E-06	3.06E-06	3.10E-06
Cu	5.03E-08	2.21E-06	4.37E-06	5.02E-06	5.40E-06	5.87E-06	5.82E-06
Fe	4.65E-07	1.24E-04	2.54E-03	3.23E-03	4.08E-03	4.53E-03	4.84E-03
Pb	0.00E+00	0.00E+00	1.66E-07	2.23E-07	1.72E-07	1.00E-07	4.46E-08
Mn	7.34E-06	1.08E-05	2.50E-05	3.15E-05	3.50E-05	3.81E-05	3.87E-05
Mo	3.40E-09	3.37E-09	1.04E-08	4.29E-08	8.36E-08	1.06E-07	7.88E-08
Ni	1.77E-06	3.27E-06	5.56E-06	6.44E-06	7.10E-06	7.41E-06	7.48E-06
P	6.44E-06	2.05E-06	2.12E-04	2.71E-04	2.93E-04	3.08E-04	3.06E-04
Si	8.24E-05	2.43E-04	1.15E-03	9.27E-04	1.48E-04	5.31E-05	2.47E-05
Ag	0.00E+00	0.00E+00	0.00E+00	0.00E+00	0.00E+00	0.00E+00	0.00E+00
Sr	7.40E-06	7.16E-06	9.64E-06	1.21E-05	1.16E-05	9.46E-06	5.54E-06
Ti	8.34E-09	1.24E-08	6.77E-07	7.19E-06	3.20E-05	5.11E-05	6.71E-05
V	7.84E-09	3.89E-09	5.57E-06	9.56E-06	1.42E-05	1.75E-05	1.91E-05
Zn	3.66E-06	1.03E-05	1.67E-05	2.06E-05	2.25E-05	2.41E-05	2.51E-05
Zr	0.00E+00	4.34E-09	5.33E-08	2.58E-06	4.03E-06	4.32E-06	4.81E-06
Ca	2.03E-03	2.19E-03	2.71E-03	2.85E-03	1.31E-03	3.90E-04	1.65E-04
Mg	1.95E-03	2.15E-03	4.19E-03	4.72E-03	4.43E-03	6.15E-03	5.97E-03
Na	1.02E-03	1.75E-03	1.85E-03	1.98E-03	1.65E-03	2.30E-03	2.34E-03
K	1.33E-04	7.08E-06	3.15E-04	5.89E-04	4.12E-04	1.27E-03	1.46E-03
Cl	7.23E-05	5.75E-05	0.00E+00	0.00E+00	0.00E+00	0.00E+00	0.00E+00
NO_3	0.00E+00	0.00E+00	0.00E+00	0.00E+00	0.00E+00	0.00E+00	0.00E+00
SO_4	4.33E-03	5.69E-03	3.28E-02	1.50E-01	4.47E-01	6.52E-01	8.32E-01

Appendix 2F: Aqueous geochemistry analyses results for Kc (180d) batch experiment

Sample ID	BE1	BE2	BE3	BE6	BE4	BE7	BE5
	(mol L^{-1} g^{-1})	(mol L^{-1} g^{-1})	(mol L^{-1} g^{-1})	(mol L^{-1} g^{-1})	(mol L^{-1} g^{-1})	(mol L^{-1} g^{-1})	(mol L^{-1} g^{-1})
pH	5.00	3.00	1.00	0.00	-1.00	-2.00	-3.00
pe	10.31	13.32	11.11	11.58	11.89	12.11	12.30
Clay	5.10	5.16	5.08	5.01	5.16	5.08	5.23
Density (g mL^{-1})	1.00	1.01	1.02	1.08	1.19	1.26	1.30
Al	1.08E-05	2.22E-04	2.93E-03	6.52E-03	1.09E-02	1.22E-02	1.32E-02
Ba	2.14E-08	1.13E-08	2.49E-08	4.79E-08	5.16E-08	6.00E-08	4.84E-08
Be	2.18E-08	4.95E-07	6.70E-07	1.28E-06	1.44E-06	1.60E-06	1.47E-06
B	2.90E-05	2.69E-05	1.79E-05	3.73E-05	4.92E-05	5.14E-05	4.92E-05
Cd	8.72E-09	1.90E-08	5.37E-08	5.12E-08	5.25E-08	3.66E-08	1.97E-08
Cr	0.00E+00	1.57E-07	2.83E-06	5.85E-06	8.18E-06	9.11E-06	9.80E-06
Co	1.06E-06	1.74E-06	2.60E-06	3.21E-06	3.21E-06	3.21E-06	3.12E-06
Cu	4.63E-08	1.95E-06	3.99E-06	4.66E-06	4.83E-06	4.86E-06	4.53E-06
Fe	7.20E-07	5.06E-05	3.93E-03	4.71E-03	5.29E-03	5.24E-03	5.12E-03
Pb	0.00E+00	1.22E-08	1.94E-07	2.22E-07	1.25E-07	3.98E-08	0.00E+00
Mn	1.37E-05	2.65E-05	4.11E-05	5.28E-05	5.42E-05	5.47E-05	5.36E-05
Mo	1.34E-08	9.91E-09	1.72E-08	5.60E-08	1.41E-07	1.75E-07	1.13E-07
Ni	2.24E-06	4.09E-06	6.18E-06	7.70E-06	8.05E-06	8.07E-06	7.92E-06
P	1.08E-05	6.88E-07	2.31E-04	3.11E-04	3.13E-04	3.06E-04	3.00E-04
Si	7.71E-05	2.38E-04	1.10E-03	9.13E-04	1.01E-04	4.07E-05	2.13E-05
Ag	3.64E-09	0.00E+00	0.00E+00	0.00E+00	0.00E+00	0.00E+00	0.00E+00
Sr	9.33E-06	9.62E-06	1.06E-05	1.43E-05	1.21E-05	8.93E-06	4.30E-06
Ti	1.23E-08	2.43E-08	9.26E-07	1.31E-05	4.57E-05	6.45E-05	7.68E-05
V	0.00E+00	0.00E+00	6.80E-06	1.31E-05	1.83E-05	2.06E-05	2.17E-05
Zn	4.75E-06	1.15E-05	1.88E-05	2.51E-05	2.53E-05	2.55E-05	2.51E-05
Zr	1.29E-08	1.06E-08	5.08E-08	3.42E-06	4.40E-06	4.74E-06	4.61E-06
Ca	2.44E-03	2.20E-03	2.39E-03	3.11E-03	7.52E-04	2.83E-04	1.37E-04
Mg	2.49E-03	2.72E-03	4.91E-03	5.93E-03	6.63E-03	6.45E-03	6.33E-03
Na	1.91E-03	2.12E-03	2.02E-03	2.22E-03	2.24E-03	2.09E-03	2.10E-03
K	1.97E-04	3.01E-05	3.47E-04	8.60E-04	1.42E-03	1.60E-03	1.69E-03
Cl	1.82E-04	1.37E-04	0.00E+00	0.00E+00	0.00E+00	0.00E+00	0.00E+00
NO_3	6.17E-06	0.00E+00	0.00E+00	0.00E+00	0.00E+00	0.00E+00	0.00E+00
SO_4	5.21E-03	6.68E-03	3.77E-02	1.84E-01	4.87E-01	7.40E-01	8.68E-01

Appendix 2G: Aqueous geochemistry analyses results for Kc (365d) batch experiment

Sample ID	BE1	BE2	BE3	BE6	BE4	BE7	BE5
	(mol L^{-1} g^{-1})	(mol L^{-1} g^{-1})	(mol L^{-1} g^{-1})	(mol L^{-1} g^{-1})	(mol L^{-1} g^{-1})	(mol L^{-1} g^{-1})	(mol L^{-1} g^{-1})
pH	5.00	3.00	1.00	0.00	-1.00	-2.00	-3.00
pe	10.62	13.27	11.08	11.56	11.65	12.04	12.23
Clay	5.08	5.00	5.05	5.08	5.13	5.06	5.07
Density (g mL^{-1})	1.00	1.01	1.01	1.07	1.17	1.23	1.36
Al	7.95E-06	2.83E-04	3.08E-03	9.00E-03	1.38E-02	1.81E-02	2.04E-02
Ba	1.86E-08	8.74E-09	2.34E-08	4.81E-08	6.01E-08	7.45E-08	6.92E-08
Be	4.37E-08	3.77E-07	6.45E-07	1.28E-06	1.44E-06	1.82E-06	1.84E-06
B	4.55E-05	2.77E-05	1.43E-05	4.35E-05	6.00E-05	7.57E-05	7.69E-05
Cd	8.76E-09	1.42E-08	5.53E-08	5.88E-08	6.29E-08	7.28E-08	8.45E-08
Cr	0.00E+00	8.85E-08	2.97E-06	6.67E-06	8.39E-06	1.14E-05	1.28E-05
Co	1.07E-06	1.60E-06	1.97E-06	2.52E-06	2.80E-06	3.02E-06	3.59E-06
Cu	1.67E-07	1.10E-06	3.98E-06	5.07E-06	3.34E-06	5.80E-06	4.11E-06
Fe	3.17E-08	1.17E-05	2.85E-03	4.41E-03	5.17E-03	5.72E-03	6.12E-03
Pb	0.00E+00	0.00E+00	1.94E-07	1.55E-07	7.40E-08	3.95E-08	0.00E+00
Mn	8.81E-06	1.21E-05	2.30E-05	3.19E-05	3.37E-05	3.88E-05	4.41E-05
Mo	0.00E+00	0.00E+00	1.02E-08	4.22E-08	1.00E-07	1.40E-07	8.09E-08
Ni	2.31E-06	3.61E-06	4.71E-06	6.33E-06	6.83E-06	7.67E-06	8.90E-06
P	3.18E-07	6.46E-07	1.63E-04	2.37E-04	2.82E-04	2.71E-04	3.68E-04
Si	1.12E-04	3.24E-04	1.01E-03	8.20E-04	1.21E-04	4.99E-05	1.06E-05
Ag	0.00E+00	0.00E+00	0.00E+00	0.00E+00	0.00E+00	0.00E+00	0.00E+00
Sr	9.21E-06	7.28E-06	9.06E-06	1.16E-05	1.24E-05	8.18E-06	1.68E-06
Ti	0.00E+00	1.67E-08	5.86E-07	1.45E-05	6.11E-05	9.11E-05	1.21E-04
V	0.00E+00	0.00E+00	6.93E-06	1.59E-05	2.11E-05	2.77E-05	3.17E-05
Zn	5.37E-06	9.44E-06	1.41E-05	1.89E-05	2.16E-05	2.25E-05	2.86E-05
Zr	0.00E+00	0.00E+00	3.08E-08	3.17E-06	4.01E-06	5.39E-06	5.47E-06
Ca	2.34E-03	2.30E-03	2.40E-03	2.48E-03	1.11E-03	7.18E-04	1.09E-04
Mg	2.31E-03	2.56E-03	3.56E-03	4.90E-03	6.43E-03	6.18E-03	8.11E-03
Na	2.09E-03	2.52E-03	1.75E-03	2.18E-03	1.90E-03	2.45E-03	2.25E-03
K	2.11E-03	4.16E-04	5.05E-04	1.22E-03	1.73E-03	2.17E-03	2.79E-03
Cl	0.00E+00	0.00E+00	0.00E+00	0.00E+00	0.00E+00	0.00E+00	0.00E+00
NO_3	0.00E+00	0.00E+00	0.00E+00	0.00E+00	0.00E+00	0.00E+00	0.00E+00
SO_4	5.76E-03	6.23E-03	2.79E-02	1.51E-01	4.04E-01	5.92E-01	9.56E-01

Appendix 2H: Aqueous geochemistry analyses results for Km (14d) batch experiment

Sample ID	BE1	BE2	BE3	BE6	BE4	BE7	BE5
	(mol L^{-1} g^{-1})	(mol L^{-1} g^{-1})	(mol L^{-1} g^{-1})	(mol L^{-1} g^{-1})	(mol L^{-1} g^{-1})	(mol L^{-1} g^{-1})	(mol L^{-1} g^{-1})
pH	5.00	3.00	1.00	0.00	-1.00	-2.00	-3.00
pe	12.34	12.89	11.02	11.28	11.46	11.66	11.79
Clay	5.08	5.03	5.15	5.04	5.12	5.06	5.13
Density (g mL^{-1})	1.01	0.99	1.03	1.06	1.15	1.21	1.29
Al	3.18E-07	9.50E-05	4.53E-04	7.86E-04	1.05E-03	1.58E-03	1.85E-03
Ba	7.67E-08	5.07E-08	3.11E-08	4.92E-08	3.75E-08	3.60E-08	3.28E-08
Be	0.00E+00	4.97E-07	6.46E-07	7.50E-07	8.25E-07	8.78E-07	9.99E-07
B	3.07E-05	2.29E-05	2.49E-05	2.85E-05	2.81E-05	2.93E-05	2.87E-05
Cd	1.75E-09	2.04E-08	4.23E-08	2.63E-08	-1.02E-08	1.76E-08	0.00E+00
Cr	0.00E+00	1.85E-07	1.23E-06	1.38E-06	1.57E-06	2.19E-06	2.42E-06
Co	6.35E-07	1.27E-06	2.09E-06	2.29E-06	2.52E-06	2.62E-06	2.82E-06
Cu	-6.20E-09	1.94E-06	2.98E-06	2.39E-06	1.79E-06	2.68E-06	2.05E-06
Fe	7.83E-07	1.07E-03	2.61E-03	3.00E-03	3.15E-03	3.57E-03	3.67E-03
Pb	-1.90E-09	5.17E-08	2.49E-07	3.24E-07	1.74E-07	2.48E-07	1.30E-07
Mn	6.69E-05	1.56E-04	1.75E-04	1.76E-04	1.81E-04	2.04E-04	2.10E-04
Mo	0.00E+00	0.00E+00	3.33E-09	0.00E+00	3.90E-08	3.37E-08	7.67E-08
Ni	7.08E-07	1.76E-06	3.06E-06	3.46E-06	3.68E-06	4.05E-06	4.06E-06
P	0.00E+00	7.97E-07	5.50E-05	6.82E-05	7.02E-05	7.67E-05	7.25E-05
Si	5.40E-05	1.42E-04	5.63E-04	7.75E-04	2.66E-04	1.00E-04	2.40E-05
Ag	0.00E+00	0.00E+00	0.00E+00	0.00E+00	-3.20E-08	0.00E+00	-4.18E-08
Sr	1.58E-06	2.84E-06	3.17E-06	3.91E-06	4.05E-06	4.07E-06	3.98E-06
Ti	0.00E+00	2.48E-08	9.70E-07	5.10E-06	1.04E-05	1.59E-05	1.43E-05
V	0.00E+00	1.63E-07	2.94E-06	3.48E-06	3.82E-06	4.27E-06	4.63E-06
Zn	8.13E-07	4.69E-06	6.49E-06	7.62E-06	8.40E-06	8.78E-06	9.46E-06
Zr	0.00E+00	1.31E-08	2.96E-07	2.89E-06	3.54E-06	4.03E-06	4.51E-06
Ca	1.41E-04	3.58E-04	3.62E-04	3.02E-04	1.37E-04	1.27E-04	5.39E-05
Mg	9.32E-05	2.20E-04	3.43E-04	4.29E-04	4.87E-04	5.51E-04	5.61E-04
Na	1.58E-03	1.56E-03	1.59E-03	1.75E-03	1.94E-03	2.03E-03	2.10E-03
K	2.06E-04	9.95E-05	1.59E-04	2.09E-04	2.93E-04	3.33E-04	3.97E-04
Cl	9.80E-04	8.03E-04	8.35E-04	0.00E+00	0.00E+00	0.00E+00	0.00E+00
NO_3	0.00E+00	0.00E+00	0.00E+00	0.00E+00	0.00E+00	0.00E+00	0.00E+00
SO_4	6.88E-04	2.76E-03	2.59E-02	1.65E-01	4.16E-01	7.10E-01	9.80E-01

Appendix 2I: Aqueous geochemistry analyses results for Km (90d) batch experiment

Sample ID	BE1	BE2	BE3	BE6	BE4	BE7	BE5
	(mol L^{-1} g^{-1})	(mol L^{-1} g^{-1})	(mol L^{-1} g^{-1})	(mol L^{-1} g^{-1})	(mol L^{-1} g^{-1})	(mol L^{-1} g^{-1})	(mol L^{-1} g^{-1})
pH	5.00	3.00	1.00	0.00	-1.00	-2.00	-3.00
pe	12.34	12.89	11.02	11.28	11.46	11.66	11.79
Clay	5.16	5.01	5.03	5.21	5.11	5.01	5.21
Density (g mL^{-1})	1.00	1.00	1.01	1.06	1.17	1.23	1.30
Al	7.90E-07	6.66E-05	8.26E-04	2.06E-03	5.12E-03	6.11E-03	7.56E-03
Ba	3.81E-08	1.89E-08	2.78E-08	3.54E-08	3.41E-08	2.99E-08	3.23E-08
Be	0.00E+00	5.32E-07	7.58E-07	8.98E-07	1.30E-06	1.37E-06	1.48E-06
B	2.87E-05	4.43E-05	2.79E-05	3.30E-05	3.90E-05	4.18E-05	4.10E-05
Cd	3.45E-09	1.07E-08	4.29E-08	5.04E-08	2.08E-08	5.49E-08	1.97E-08
Cr	0.00E+00	3.84E-08	1.27E-06	2.49E-06	4.28E-06	5.54E-06	5.97E-06
Co	6.58E-07	1.49E-06	2.32E-06	2.61E-06	2.98E-06	3.07E-06	3.16E-06
Cu	6.10E-09	5.65E-07	2.15E-06	2.55E-06	3.68E-06	4.53E-06	4.53E-06
Fe	4.86E-07	1.27E-05	2.91E-03	3.42E-03	4.55E-03	4.42E-03	4.68E-03
Pb	0.00E+00	2.89E-09	2.91E-07	3.60E-07	3.22E-07	2.48E-07	1.50E-07
Mn	9.45E-05	1.54E-04	1.90E-04	1.86E-04	2.10E-04	2.25E-04	2.31E-04
Mo	0.00E+00	0.00E+00	0.00E+00	0.00E+00	3.99E-08	3.50E-08	3.78E-08
Ni	8.92E-07	2.14E-06	3.35E-06	3.86E-06	4.39E-06	4.90E-06	4.91E-06
P	0.00E+00	1.29E-07	5.96E-05	7.58E-05	8.69E-05	9.29E-05	9.30E-05
Si	5.52E-05	1.93E-04	1.02E-03	5.77E-04	1.42E-04	5.34E-05	2.29E-05
Ag	0.00E+00	0.00E+00	0.00E+00	0.00E+00	0.00E+00	0.00E+00	0.00E+00
Sr	1.88E-06	2.71E-06	3.57E-06	4.44E-06	4.94E-06	4.69E-06	4.05E-06
Ti	0.00E+00	4.17E-09	7.55E-07	7.44E-06	2.40E-05	3.48E-05	4.44E-05
V	0.00E+00	0.00E+00	3.39E-06	4.45E-06	5.97E-06	6.86E-06	7.40E-06
Zn	5.93E-07	3.97E-06	7.37E-06	8.54E-06	9.48E-06	1.04E-05	1.05E-05
Zr	0.00E+00	0.00E+00	1.14E-07	3.37E-06	4.62E-06	4.96E-06	5.34E-06
Ca	2.02E-04	2.92E-04	3.78E-04	3.14E-04	1.39E-04	2.01E-04	1.49E-04
Mg	1.41E-04	1.99E-04	4.13E-04	5.70E-04	4.92E-04	9.49E-04	1.02E-03
Na	1.95E-03	1.79E-03	1.67E-03	1.83E-03	1.96E-03	2.20E-03	2.33E-03
K	2.30E-04	1.07E-04	2.01E-04	3.66E-04	2.96E-04	8.56E-04	9.79E-04
Cl	9.43E-04	7.89E-04	6.62E-04	0.00E+00	0.00E+00	0.00E+00	0.00E+00
NO_3	0.00E+00	0.00E+00	0.00E+00	0.00E+00	0.00E+00	0.00E+00	0.00E+00
SO_4	1.07E-03	2.28E-03	2.43E-02	1.49E-01	4.20E-01	6.68E-01	8.26E-01

Appendix 2J: Aqueous geochemistry analyses results for Km (180d) batch experiment

Sample ID	BE1	BE2	BE3	BE6	BE4	BE7	BE5
	(mol L^{-1} g^{-1})	(mol L^{-1} g^{-1})	(mol L^{-1} g^{-1})	(mol L^{-1} g^{-1})	(mol L^{-1} g^{-1})	(mol L^{-1} g^{-1})	(mol L^{-1} g^{-1})
pH	5.00	3.00	1.00	0.00	-1.00	-2.00	-3.00
pe	10.33	13.38	11.05	11.30	11.57	11.77	11.94
Clay	5.02	5.21	5.06	5.02	5.11	5.12	5.01
Density (g mL^{-1})	1.01	1.00	1.02	1.08	1.17	1.25	1.30
Al	9.60E-07	5.62E-05	1.18E-03	4.02E-03	7.11E-03	9.73E-03	1.04E-02
Ba	3.77E-08	1.93E-08	2.64E-08	3.70E-08	4.37E-08	4.48E-08	3.40E-08
Be	2.21E-08	5.89E-07	8.73E-07	1.32E-06	1.46E-06	1.82E-06	1.55E-06
B	3.32E-05	4.39E-05	3.17E-05	4.55E-05	4.88E-05	5.31E-05	4.97E-05
Cd	5.32E-09	1.35E-08	6.46E-08	3.77E-08	3.20E-08	3.65E-08	2.08E-08
Cr	0.00E+00	4.74E-08	2.06E-06	4.57E-06	6.00E-06	7.49E-06	7.63E-06
Co	8.45E-07	1.67E-06	2.74E-06	3.45E-06	3.05E-06	3.44E-06	3.25E-06
Cu	1.57E-08	8.96E-07	3.46E-06	4.27E-06	3.96E-06	4.19E-06	4.04E-06
Fe	4.10E-07	1.62E-05	3.76E-03	4.48E-03	4.49E-03	5.07E-03	4.89E-03
Pb	2.40E-08	7.33E-09	3.12E-07	3.89E-07	2.49E-07	1.29E-07	9.01E-08
Mn	1.31E-04	1.65E-04	2.24E-04	2.33E-04	2.20E-04	2.44E-04	2.28E-04
Mo	0.00E+00	1.29E-08	3.44E-09	2.89E-08	1.02E-07	1.05E-07	7.96E-08
Ni	1.19E-06	2.62E-06	4.13E-06	5.20E-06	5.11E-06	5.59E-06	5.57E-06
P	1.29E-07	6.13E-08	7.04E-05	9.85E-05	9.29E-05	9.93E-05	9.80E-05
Si	5.21E-05	1.67E-04	1.09E-03	5.52E-04	1.11E-04	3.69E-05	2.83E-05
Ag	0.00E+00	0.00E+00	0.00E+00	0.00E+00	0.00E+00	0.00E+00	0.00E+00
Sr	2.27E-06	2.97E-06	4.17E-06	5.71E-06	5.34E-06	5.38E-06	4.26E-06
Ti	8.32E-09	7.93E-09	7.59E-07	1.22E-05	3.08E-05	4.84E-05	5.61E-05
V	0.00E+00	0.00E+00	4.08E-06	6.32E-06	7.30E-06	8.85E-06	8.71E-06
Zn	7.46E-07	4.60E-06	8.95E-06	1.10E-05	1.05E-05	1.19E-05	1.11E-05
Zr	0.00E+00	6.24E-09	1.35E-07	4.46E-06	5.65E-06	5.84E-06	5.37E-06
Ca	2.74E-04	3.48E-04	4.56E-04	9.47E-05	4.94E-04	1.93E-04	1.51E-04
Mg	1.75E-04	2.12E-04	5.29E-04	6.72E-04	1.20E-03	1.17E-03	1.13E-03
Na	2.19E-03	1.89E-03	2.07E-03	1.55E-03	3.20E-03	2.38E-03	2.28E-03
K	1.22E-04	1.26E-04	2.50E-04	6.34E-04	8.65E-04	1.12E-03	1.14E-03
Cl	1.01E-03	8.87E-04	9.67E-04	0.00E+00	0.00E+00	0.00E+00	0.00E+00
NO_3	0.00E+00	0.00E+00	0.00E+00	0.00E+00	0.00E+00	0.00E+00	0.00E+00
SO_4	1.09E-03	2.30E-03	2.92E-02	1.88E-01	4.61E-01	7.45E-01	9.16E-01

Appendix 2K: Aqueous geochemistry analyses results for Km (365d) batch experiment

Sample ID	BE1	BE2	BE3	BE6	BE4	BE7	BE5
	(mol L^{-1} g^{-1})	(mol L^{-1} g^{-1})	(mol L^{-1} g^{-1})	(mol L^{-1} g^{-1})	(mol L^{-1} g^{-1})	(mol L^{-1} g^{-1})	(mol L^{-1} g^{-1})
pH	5.00	3.00	1.00	0.00	-1.00	-2.00	-3.00
pe	10.63	13.27	11.15	11.41	11.44	11.81	11.81
Clay	5.10	5.01	5.10	5.08	5.00	5.08	5.01
Density (g mL^{-1})	1.00	1.00	1.01	1.06	1.16	1.23	1.34
Al	5.52E-07	6.21E-05	1.50E-03	5.41E-03	9.73E-03	1.25E-02	1.49E-02
Ba	3.43E-08	0.00E+00	2.31E-08	3.64E-08	5.17E-08	4.20E-08	5.21E-08
Be	0.00E+00	5.09E-07	8.14E-07	1.20E-06	1.58E-06	1.71E-06	1.85E-06
B	2.36E-05	3.32E-05	2.93E-05	4.32E-05	5.25E-05	5.69E-05	5.74E-05
Cd	3.49E-09	1.07E-08	6.70E-08	5.94E-08	6.31E-08	6.84E-08	6.37E-08
Cr	0.00E+00	3.84E-08	2.33E-06	4.97E-06	5.69E-06	7.77E-06	7.80E-06
Co	5.66E-07	1.46E-06	2.42E-06	2.69E-06	2.81E-06	3.10E-06	3.24E-06
Cu	0.00E+00	3.77E-07	3.65E-06	4.20E-06	2.23E-06	4.84E-06	2.63E-06
Fe	4.92E-08	9.13E-06	3.12E-03	3.69E-03	4.09E-03	4.61E-03	5.00E-03
Pb	0.00E+00	1.93E-09	3.35E-07	3.34E-07	2.40E-07	1.21E-07	2.30E-08
Mn	8.78E-05	1.35E-04	1.90E-04	1.91E-04	1.90E-04	2.17E-04	2.27E-04
Mo	0.00E+00	0.00E+00	0.00E+00	0.00E+00	6.05E-08	6.55E-08	4.07E-08
Ni	8.02E-07	2.07E-06	3.58E-06	4.26E-06	4.43E-06	5.24E-06	5.29E-06
P	0.00E+00	0.00E+00	5.89E-05	7.81E-05	8.40E-05	9.31E-05	1.00E-04
Si	5.20E-05	1.60E-04	7.76E-04	5.97E-04	1.30E-04	5.10E-05	1.07E-05
Ag	0.00E+00	0.00E+00	0.00E+00	0.00E+00	0.00E+00	0.00E+00	0.00E+00
Sr	1.72E-06	2.05E-06	3.64E-06	4.66E-06	4.86E-06	4.61E-06	3.54E-06
Ti	0.00E+00	4.17E-09	5.80E-07	1.31E-05	4.15E-05	5.75E-05	8.18E-05
V	0.00E+00	0.00E+00	3.97E-06	6.22E-06	7.66E-06	9.06E-06	1.03E-05
Zn	4.95E-07	3.92E-06	7.53E-06	9.14E-06	9.36E-06	1.05E-05	1.13E-05
Zr	0.00E+00	0.00E+00	8.69E-08	3.75E-06	4.67E-06	5.27E-06	5.76E-06
Ca	1.98E-04	2.92E-04	3.92E-04	3.92E-04	1.65E-03	2.99E-04	9.41E-05
Mg	1.24E-04	1.73E-04	4.92E-04	8.15E-04	2.62E-03	1.22E-03	1.25E-03
Na	1.53E-03	1.20E-03	1.74E-03	1.82E-03	7.75E-03	2.05E-03	2.23E-03
K	2.84E-04	4.75E-05	2.99E-04	7.08E-04	4.56E-04	1.31E-03	1.59E-03
Cl	0.00E+00	0.00E+00	0.00E+00	0.00E+00	0.00E+00	0.00E+00	0.00E+00
NO_3	0.00E+00	0.00E+00	0.00E+00	0.00E+00	0.00E+00	0.00E+00	0.00E+00
SO_4	7.12E-04	1.82E-03	2.05E-02	1.30E-01	3.91E-01	5.81E-01	9.23E-01

Appendix 2L: Aqueous geochemistry analyses results for BK (14d) batch experiment

Sample ID	BE1	BE2	BE3	BE6	BE4	BE7	BE5
	(mol L^{-1} g^{-1})	(mol L^{-1} g^{-1})	(mol L^{-1} g^{-1})	(mol L^{-1} g^{-1})	(mol L^{-1} g^{-1})	(mol L^{-1} g^{-1})	(mol L^{-1} g^{-1})
pH	5.00	3.00	1.00	0.00	-1.00	-2.00	-3.00
pe	8.37	10.52	11.26	11.70	12.06	12.34	12.48
Clay	5.09	5.03	5.13	5.04	5.11	5.07	5.14
Density (g mL^{-1})	1.01	1.01	1.02	1.06	1.14	1.21	1.29
Al	4.43E-06	5.26E-05	6.72E-04	1.56E-03	2.20E-03	2.49E-03	2.43E-03
Ba	0.00E+00	2.90E-08	3.26E-08	5.52E-08	5.92E-08	2.94E-08	1.63E-08
Be	0.00E+00	6.18E-07	1.12E-06	1.45E-06	1.74E-06	1.68E-06	1.74E-06
B	1.18E-05	8.04E-06	7.12E-06	1.05E-05	1.01E-05	1.11E-05	8.28E-06
Cd	8.89E-10	5.31E-09	1.65E-08	1.50E-08	1.04E-08	1.80E-08	9.93E-09
Cr	0.00E+00	1.34E-08	9.18E-08	1.30E-07	1.34E-07	1.75E-07	1.94E-07
Co	2.83E-08	7.94E-08	1.70E-07	2.43E-07	3.05E-07	2.91E-07	2.85E-07
Cu	4.57E-09	1.13E-07	3.01E-07	3.98E-07	5.30E-07	4.45E-07	4.22E-07
Fe	6.76E-06	7.21E-05	7.69E-04	1.11E-03	1.29E-03	1.33E-03	1.35E-03
Pb	5.71E-09	1.49E-08	2.50E-07	3.60E-07	3.87E-07	3.32E-07	1.24E-07
Mn	1.64E-05	3.80E-05	7.22E-05	9.23E-05	1.17E-04	1.12E-04	1.11E-04
Mo	3.01E-08	5.12E-09	6.97E-08	3.30E-07	6.43E-07	6.71E-07	6.86E-07
Ni	3.85E-08	7.47E-08	2.71E-07	3.52E-07	6.14E-07	4.65E-07	3.80E-07
P	2.86E-07	1.49E-06	8.64E-05	1.11E-04	1.41E-04	1.30E-04	1.26E-04
Si	1.75E-04	4.54E-04	1.11E-03	7.63E-04	3.03E-04	9.14E-05	2.19E-05
Ag	0.00E+00	0.00E+00	0.00E+00	0.00E+00	-3.20E-08	0.00E+00	-4.17E-08
Sr	3.38E-06	5.66E-06	1.06E-05	1.47E-05	1.70E-05	1.34E-05	9.45E-06
Ti	2.86E-08	1.25E-08	1.62E-06	7.90E-06	2.78E-05	4.66E-05	6.47E-05
V	0.00E+00	2.87E-08	4.78E-07	7.03E-07	9.11E-07	8.53E-07	9.00E-07
Zn	2.96E-07	1.47E-06	5.02E-06	7.02E-06	9.50E-06	9.89E-06	9.92E-06
Zr	0.00E+00	0.00E+00	8.33E-08	2.42E-06	3.84E-06	3.35E-06	3.14E-06
Ca	7.31E-04	1.11E-03	1.98E-03	2.41E-03	2.13E-03	4.97E-04	1.69E-04
Mg	1.69E-04	2.73E-04	6.15E-04	8.83E-04	1.03E-03	1.15E-03	1.12E-03
Na	6.62E-03	5.21E-03	6.25E-03	7.16E-03	7.75E-03	8.25E-03	8.63E-03
K	3.34E-05	1.97E-05	1.52E-04	3.14E-04	4.61E-04	4.25E-04	4.32E-04
Cl	0.00E+00	0.00E+00	0.00E+00	0.00E+00	0.00E+00	0.00E+00	0.00E+00
NO_3	0.00E+00	0.00E+00	0.00E+00	0.00E+00	0.00E+00	0.00E+00	0.00E+00
SO_4	3.53E-03	4.57E-03	2.93E-02	1.64E-01	4.31E-01	6.87E-01	9.67E-01

Appendix 2M: Aqueous geochemistry analyses results for BK (90d) batch experiment

Sample ID	BE1	BE2	BE3	BE6	BE4	BE7	BE5
	(mol L^{-1} g^{-1})	(mol L^{-1} g^{-1})	(mol L^{-1} g^{-1})	(mol L^{-1} g^{-1})	(mol L^{-1} g^{-1})	(mol L^{-1} g^{-1})	(mol L^{-1} g^{-1})
pH	5.00	3.00	1.00	0.00	-1.00	-2.00	-3.00
pe	8.37	10.52	11.26	11.70	12.06	12.34	12.48
Clay	5.08	5.06	5.02	5.03	5.06	5.06	5.02
Density (g mL^{-1})	1.01	1.00	1.01	1.06	1.16	1.23	1.29
Al	1.02E-06	6.74E-05	1.50E-03	3.90E-03	7.32E-03	7.55E-03	8.82E-03
Ba	2.15E-08	2.45E-08	2.64E-08	3.74E-08	3.53E-08	1.44E-08	1.62E-08
Be	0.00E+00	7.24E-07	1.28E-06	1.61E-06	1.75E-06	1.97E-06	1.97E-06
B	1.17E-05	6.22E-06	5.23E-06	9.50E-06	9.64E-06	1.23E-05	9.67E-06
Cd	1.75E-09	7.03E-09	2.15E-08	3.05E-08	2.16E-08	3.52E-08	1.98E-08
Cr	0.00E+00	3.80E-08	1.20E-07	1.81E-07	1.86E-07	1.90E-07	2.14E-07
Co	3.67E-08	8.72E-08	2.23E-07	2.76E-07	2.88E-07	3.02E-07	3.40E-07
Cu	3.10E-09	1.80E-07	5.08E-07	4.72E-07	4.77E-07	5.29E-07	5.25E-07
Fe	1.66E-06	4.32E-05	1.18E-03	1.75E-03	1.79E-03	1.94E-03	2.20E-03
Pb	5.70E-09	1.81E-08	2.24E-07	3.26E-07	2.98E-07	2.58E-07	1.07E-07
Mn	2.04E-05	3.96E-05	7.31E-05	9.79E-05	1.02E-04	1.09E-04	1.15E-04
Mo	2.68E-08	6.73E-09	6.19E-08	3.35E-07	4.95E-07	6.06E-07	6.44E-07
Ni	7.71E-08	1.72E-07	4.47E-07	4.52E-07	4.54E-07	4.72E-07	4.93E-07
P	5.72E-07	6.38E-07	1.08E-04	1.35E-04	1.37E-04	1.47E-04	1.51E-04
Si	1.24E-04	4.34E-04	9.05E-04	7.04E-04	1.68E-04	5.70E-05	2.30E-05
Ag	0.00E+00	3.66E-09	0.00E+00	0.00E+00	0.00E+00	0.00E+00	0.00E+00
Sr	3.10E-06	5.19E-06	1.13E-05	1.56E-05	1.47E-05	1.29E-05	7.87E-06
Ti	8.22E-09	8.26E-09	1.60E-06	8.23E-06	3.19E-05	6.73E-05	1.04E-04
V	0.00E+00	0.00E+00	7.13E-07	9.75E-07	1.07E-06	1.13E-06	1.27E-06
Zn	3.91E-07	2.36E-06	7.41E-06	9.03E-06	1.06E-05	1.15E-05	1.36E-05
Zr	0.00E+00	0.00E+00	9.51E-08	2.63E-06	3.98E-06	4.12E-06	4.63E-06
Ca	6.63E-04	1.25E-03	2.29E-03	2.77E-03	2.53E-03	4.00E-04	1.47E-04
Mg	1.86E-04	3.45E-04	9.83E-04	1.45E-03	1.22E-03	1.93E-03	2.12E-03
Na	5.31E-03	5.65E-03	6.60E-03	7.41E-03	9.21E-03	7.96E-03	8.35E-03
K	4.29E-05	1.28E-04	2.33E-04	4.63E-04	5.48E-04	6.05E-04	5.78E-04
Cl	1.21E-04	3.46E-04	0.00E+00	0.00E+00	0.00E+00	0.00E+00	0.00E+00
NO_3	1.85E-05	0.00E+00	0.00E+00	0.00E+00	0.00E+00	0.00E+00	0.00E+00
SO_4	2.95E-03	4.01E-03	2.97E-02	1.48E-01	4.13E-01	6.45E-01	8.48E-01

Appendix 2N: Aqueous geochemistry analyses results for BK (180d) batch experiment

Sample ID	BE1	BE2	BE3	BE6	BE4	BE7	BE5
	(mol L^{-1} g^{-1})	(mol L^{-1} g^{-1})	(mol L^{-1} g^{-1})	(mol L^{-1} g^{-1})	(mol L^{-1} g^{-1})	(mol L^{-1} g^{-1})	(mol L^{-1} g^{-1})
pH	5.00	3.00	1.00	0.00	-1.00	-2.00	-3.00
pe	7.94	13.17	11.31	11.82	12.09	12.33	12.54
Clay	5.15	5.11	5.07	5.11	5.00	5.04	5.09
Density (g mL^{-1})	1.01	1.01	1.02	1.08	1.18	1.24	1.31
Al	7.92E-08	1.07E-04	2.37E-03	6.97E-03	1.16E-02	1.16E-02	1.39E-02
Ba	1.27E-08	2.00E-08	2.82E-08	3.82E-08	2.71E-08	1.49E-08	1.64E-08
Be	0.00E+00	9.55E-07	1.53E-06	2.13E-06	2.06E-06	2.26E-06	2.00E-06
B	1.02E-05	8.69E-06	5.97E-06	1.21E-05	1.61E-05	1.55E-05	1.27E-05
Cd	0.00E+00	1.04E-08	2.30E-08	3.11E-08	2.21E-08	3.63E-08	2.01E-08
Cr	0.00E+00	2.26E-08	2.15E-07	2.69E-07	2.38E-07	2.75E-07	2.60E-07
Co	2.97E-08	1.20E-07	2.77E-07	3.56E-07	3.15E-07	3.46E-07	3.44E-07
Cu	0.00E+00	2.34E-07	5.08E-07	6.19E-07	5.66E-07	5.78E-07	6.39E-07
Fe	1.48E-06	1.55E-05	1.57E-03	2.46E-03	2.89E-03	2.94E-03	3.23E-03
Pb	8.43E-09	1.32E-08	2.28E-07	4.05E-07	2.57E-07	2.66E-07	3.26E-08
Mn	2.11E-05	5.13E-05	9.08E-05	1.22E-04	1.16E-04	1.23E-04	1.22E-04
Mo	0.00E+00	0.00E+00	7.33E-08	4.47E-07	5.70E-07	6.95E-07	6.91E-07
Ni	3.97E-08	2.87E-07	4.84E-07	6.26E-07	5.49E-07	5.56E-07	6.15E-07
P	1.88E-07	1.01E-06	1.35E-04	1.67E-04	1.60E-04	1.58E-04	1.67E-04
Si	9.30E-05	5.14E-04	7.92E-04	7.03E-04	1.28E-04	4.83E-05	2.25E-05
Ag	0.00E+00	0.00E+00	0.00E+00	0.00E+00	0.00E+00	0.00E+00	0.00E+00
Sr	3.06E-06	6.48E-06	1.35E-05	2.03E-05	1.66E-05	1.40E-05	4.63E-06
Ti	0.00E+00	8.18E-09	2.16E-06	1.22E-05	4.79E-05	9.21E-05	1.26E-04
V	0.00E+00	0.00E+00	9.29E-07	1.30E-06	1.36E-06	1.44E-06	1.50E-06
Zn	3.65E-07	4.44E-06	1.18E-05	1.19E-05	1.18E-05	1.37E-05	1.24E-05
Zr	0.00E+00	0.00E+00	1.41E-07	3.74E-06	5.03E-06	5.14E-06	5.44E-06
Ca	2.00E-04	7.33E-04	1.32E-03	3.22E-03	1.21E-03	3.01E-04	1.27E-04
Mg	5.22E-05	2.11E-04	6.16E-04	2.07E-03	2.61E-03	2.55E-03	2.81E-03
Na	1.63E-03	3.24E-03	3.75E-03	8.90E-03	8.80E-03	8.81E-03	8.97E-03
K	8.30E-06	2.17E-05	1.39E-04	5.90E-04	6.13E-04	6.22E-04	6.52E-04
Cl	6.68E-05	1.01E-04	0.00E+00	0.00E+00	0.00E+00	0.00E+00	0.00E+00
NO_3	2.03E-05	1.89E-05	0.00E+00	0.00E+00	0.00E+00	0.00E+00	0.00E+00
SO_4	3.59E-03	5.43E-03	3.70E-02	1.76E-01	4.81E-01	7.27E-01	9.34E-01

Appendix 2O: Aqueous geochemistry analyses results for BK (365d) batch experiment

Sample ID	BE1	BE2	BE3	BE6	BE4	BE7	BE5
	(mol L^{-1} g^{-1})	(mol L^{-1} g^{-1})	(mol L^{-1} g^{-1})	(mol L^{-1} g^{-1})	(mol L^{-1} g^{-1})	(mol L^{-1} g^{-1})	(mol L^{-1} g^{-1})
pH	5.00	3.00	1.00	0.00	-1.00	-2.00	-3.00
pe	9.84	13.14	11.33	11.86	11.97	12.35	12.29
Clay	5.07	5.05	5.14	5.04	5.13	5.01	5.08
Density (g mL^{-1})	1.00	1.01	1.01	1.06	1.16	1.22	1.35
Al	1.46E-06	9.02E-05	2.43E-03	8.98E-03	1.62E-02	1.66E-02	2.32E-02
Ba	1.58E-08	2.02E-08	2.29E-08	3.66E-08	3.47E-08	2.90E-08	1.73E-08
Be	4.38E-08	7.69E-07	1.24E-06	1.68E-06	1.85E-06	1.99E-06	2.38E-06
B	1.44E-05	9.16E-06	4.72E-06	1.47E-05	2.53E-05	2.58E-05	2.64E-05
Cd	1.75E-09	8.81E-09	3.14E-08	4.48E-08	5.30E-08	5.32E-08	6.35E-08
Cr	0.00E+00	4.57E-08	1.66E-07	2.26E-07	2.52E-07	3.07E-07	5.49E-07
Co	4.02E-08	9.74E-08	2.07E-07	2.70E-07	2.83E-07	3.05E-07	3.63E-07
Cu	0.00E+00	1.71E-07	4.63E-07	6.20E-07	6.56E-07	6.91E-07	8.62E-07
Fe	0.00E+00	1.66E-05	1.22E-03	2.40E-03	3.26E-03	3.40E-03	4.48E-03
Pb	4.76E-09	1.53E-08	2.46E-07	3.85E-07	3.57E-07	1.16E-07	1.49E-07
Mn	2.33E-05	4.33E-05	7.18E-05	1.02E-04	1.07E-04	1.17E-04	1.39E-04
Mo	0.00E+00	0.00E+00	3.34E-08	2.57E-07	4.47E-07	4.08E-07	5.27E-07
Ni	7.39E-08	1.79E-07	3.28E-07	4.29E-07	4.47E-07	4.42E-07	5.27E-07
P	2.55E-07	6.39E-07	9.00E-05	1.22E-04	1.27E-04	1.35E-04	1.61E-04
Si	9.45E-05	4.34E-04	7.82E-04	8.21E-04	1.40E-04	6.07E-05	1.07E-05
Ag	0.00E+00	0.00E+00	0.00E+00	0.00E+00	0.00E+00	0.00E+00	0.00E+00
Sr	2.81E-06	5.11E-06	1.19E-05	1.84E-05	1.74E-05	1.39E-05	4.07E-06
Ti	0.00E+00	4.14E-09	8.61E-07	8.76E-06	5.48E-05	1.02E-04	1.60E-04
V	0.00E+00	0.00E+00	6.55E-07	1.04E-06	1.24E-06	1.33E-06	1.68E-06
Zn	4.68E-07	3.59E-06	6.86E-06	9.96E-06	1.11E-05	1.09E-05	1.38E-05
Zr	0.00E+00	0.00E+00	9.25E-08	3.40E-06	6.01E-06	6.34E-06	8.61E-06
Ca	6.07E-04	1.20E-03	2.16E-03	2.66E-03	1.66E-03	7.95E-04	7.84E-05
Mg	1.45E-04	3.00E-04	8.94E-04	1.81E-03	2.62E-03	2.69E-03	3.67E-03
Na	4.87E-03	5.51E-03	6.03E-03	7.67E-03	8.00E-03	8.07E-03	9.28E-03
K	5.99E-05	4.01E-05	1.73E-04	3.70E-04	4.48E-04	5.23E-04	5.70E-04
Cl	0.00E+00	0.00E+00	0.00E+00	0.00E+00	0.00E+00	0.00E+00	0.00E+00
NO_3	0.00E+00	0.00E+00	0.00E+00	0.00E+00	0.00E+00	0.00E+00	0.00E+00
SO_4	2.50E-03	4.31E-03	2.24E-02	1.45E-01	3.84E-01	5.90E-01	9.47E-01

Appendix 2P: Percent of Al, Fe, and Ca remaining in altered Kc solid phase.

Sample ID	Al	Fe	Ca
	(% solid)	(% solid)	(% solid)
Total (μmol g^{-1})	2.81E+03	514	414
KC-BE1-14d	1.00	1.00	0.41
KC-BE1-90d	1.00	1.00	0.47
KC-BE1-180d	1.00	1.00	0.37
KC-BE1-365d	1.00	1.00	0.25
KC-BE2-14d	1.00	0.99	0.57
KC-BE2-90d	0.99	0.97	0.39
KC-BE2-180d	0.99	0.99	0.43
KC-BE2-365d	0.99	1.00	0.41
KC-BE3-14d	0.95	0.67	0.45
KC-BE3-90d	0.91	0.49	0.33
KC-BE3-180d	0.89	0.22	0.41
KC-BE3-365d	0.89	0.43	0.41
KC-BE6-14d	0.92	0.59	0.48
KC-BE6-90d	0.85	0.36	0.30
KC-BE6-180d	0.78	0.14	0.35
KC-BE6-365d	0.69	0.17	0.44
KC-BE4-14d	0.91	0.55	0.67
KC-BE4-90d	0.76	0.28	0.71
KC-BE4-180d	0.67	0.13	0.85
KC-BE4-365d	0.56	0.10	0.77
KC-BE7-14d	0.88	0.53	0.90
KC-BE7-90d	0.70	0.23	0.92
KC-BE7-180d	0.64	0.15	0.94
KC-BE7-365d	0.47	0.08	0.86
KC-BE5-14d	0.88	0.57	0.97
KC-BE5-90d	0.67	0.25	0.97
KC-BE5-180d	0.63	0.22	0.97
KC-BE5-365d	0.41	0.03	0.98

Appendix 2Q: Percent of Al, Fe, and Ca remaining in altered Km solid phase.

Sample ID	Al	Fe	Ca
	(% solid)	(% solid)	(% solid)
Total (μmol g^{-1})	2.48E+03	390	39.4
KM-BE1-14d	1.00	1.00	0.63
KM-BE1-90d	1.00	1.00	0.47
KM-BE1-180d	1.00	1.00	0.29
KM-BE1-365d	1.00	1.00	0.47
KM-BE2-14d	1.00	1.00	0.07
KM-BE2-90d	1.00	1.00	0.22
KM-BE2-180d	1.00	1.00	0.07
KM-BE2-365d	1.00	1.00	0.24
KM-BE3-14d	0.98	0.33	0.06
KM-BE3-90d	0.97	0.25	0.03
KM-BE3-180d	0.95	0.03	0.00
KM-BE3-365d	0.94	0.20	0.00
KM-BE6-14d	0.97	0.26	0.31
KM-BE6-90d	0.92	0.10	0.19
KM-BE6-180d	0.85	0.00	0.79
KM-BE6-365d	0.79	0.09	0.06
KM-BE4-14d	0.96	0.27	0.69
KM-BE4-90d	0.82	0.00	0.69
KM-BE4-180d	0.75	0.00	0.00
KM-BE4-365d	0.65	0.07	0.00
KM-BE7-14d	0.95	0.24	0.73
KM-BE7-90d	0.79	0.03	0.56
KM-BE7-180d	0.69	0.00	0.61
KM-BE7-365d	0.58	0.02	0.38
KM-BE5-14d	0.94	0.26	0.89
KM-BE5-90d	0.76	0.07	0.71
KM-BE5-180d	0.67	0.02	0.70
KM-BE5-365d	0.51	0.00	0.81

Appendix 2R: Percent of Al, Fe, and Ca remaining in altered BK solid phase.

Sample ID	Al	Fe	Ca
	(% solid)	(% solid)	(% solid)
Total (μmol g^{-1})	4.39E+03	543	350
BK-BE1-14d	1.00	1.00	0.77
BK-BE1-90d	1.00	1.00	0.80
BK-BE1-180d	1.00	1.00	0.94
BK-BE1-365d	1.00	1.00	0.80
BK-BE2-14d	1.00	0.99	0.66
BK-BE2-90d	1.00	0.99	0.62
BK-BE2-180d	1.00	1.00	0.78
BK-BE2-365d	1.00	1.00	0.65
BK-BE3-14d	0.98	0.86	0.41
BK-BE3-90d	0.97	0.78	0.34
BK-BE3-180d	0.95	0.71	0.62
BK-BE3-365d	0.94	0.77	0.37
BK-BE6-14d	0.97	0.81	0.36
BK-BE6-90d	0.92	0.69	0.25
BK-BE6-180d	0.85	0.57	0.19
BK-BE6-365d	0.80	0.57	0.28
BK-BE4-14d	0.96	0.79	0.45
BK-BE4-90d	0.85	0.70	0.35
BK-BE4-180d	0.77	0.54	0.70
BK-BE4-365d	0.67	0.46	0.59
BK-BE7-14d	0.95	0.80	0.88
BK-BE7-90d	0.86	0.71	0.91
BK-BE7-180d	0.79	0.56	0.93
BK-BE7-365d	0.69	0.48	0.81
BK-BE5-14d	0.95	0.80	0.96
BK-BE5-90d	0.84	0.68	0.97
BK-BE5-180d	0.76	0.55	0.97
BK-BE5-365d	0.57	0.33	0.98

Appendix 2S: Calculated Kc Al and Si dissolution rates.

Sample ID	pH	MacInnes Scaled aH^+	Al	Si
		(mol L^{-1})	(mol L^{-1} g^{-1} s^{-1})	(mol L^{-1} g^{-1} s^{-1})
KC-BE1-14d	5.00	9.99E-06	1.93E-14	3.12E-13
KC-BE2-14d	3.00	1.00E-03	3.18E-13	6.05E-13
KC-BE3-14d	1.00	0.10	4.38E-12	3.91E-12
KC-BE6-14d	0.00	1.00	6.37E-12	2.84E-12
KC-BE4-14d	-1.00	10.0	7.33E-12	1.13E-12
KC-BE7-14d	-2.00	100.1	9.26E-12	2.46E-13
KC-BE5-14d	-3.00	1001.5	9.84E-12	6.17E-14
KC-BE1-90d	5.00	9.99E-06	3.51E-15	3.91E-14
KC-BE2-90d	3.00	1.00E-03	1.09E-13	1.30E-13
KC-BE3-90d	1.00	0.10	1.09E-12	5.21E-13
KC-BE6-90d	0.00	1.00	1.90E-12	4.13E-13
KC-BE4-90d	-1.00	10.0	2.99E-12	5.91E-14
KC-BE7-90d	-2.00	100.1	3.67E-12	2.03E-14
KC-BE5-90d	-3.00	1001.5	4.12E-12	8.67E-15
KC-BE1-180d	5.00	9.99E-06	2.53E-15	1.80E-14
KC-BE2-180d	3.00	1.00E-03	5.24E-14	5.61E-14
KC-BE3-180d	1.00	0.10	6.55E-13	2.46E-13
KC-BE6-180d	0.00	1.00	1.33E-12	1.87E-13
KC-BE4-180d	-1.00	10.0	2.04E-12	1.88E-14
KC-BE7-180d	-2.00	100.1	2.23E-12	7.43E-15
KC-BE5-180d	-3.00	1001.5	2.28E-12	3.68E-15
KC-BE1-365d	5.00	9.99E-06	1.14E-15	1.61E-14
KC-BE2-365d	3.00	1.00E-03	3.26E-14	3.73E-14
KC-BE3-365d	1.00	0.10	3.41E-13	1.12E-13
KC-BE6-365d	0.00	1.00	9.17E-13	8.35E-14
KC-BE4-365d	-1.00	10.0	1.29E-12	1.13E-14
KC-BE7-365d	-2.00	100.1	1.59E-12	4.41E-15
KC-BE5-365d	-3.00	1001.5	1.67E-12	8.73E-16

Appendix 2T: Calculated Km Al and Si dissolution rates.

Sample ID	pH	MacInnes Scaled aH^+	Al	Si
		(mol L^{-1})	(mol L^{-1} g^{-1} s^{-1})	(mol L^{-1} g^{-1} s^{-1})
KM-BE1-14d	5.00	9.99E-06	1.18E-15	2.01E-13
KM-BE2-14d	3.00	1.00E-03	3.48E-13	5.18E-13
KM-BE3-14d	1.00	0.10	1.67E-12	2.08E-12
KM-BE6-14d	0.00	1.00	2.68E-12	2.64E-12
KM-BE4-14d	-1.00	10.0	3.32E-12	8.40E-13
KM-BE7-14d	-2.00	100.1	4.75E-12	3.00E-13
KM-BE5-14d	-3.00	1001.5	5.24E-12	6.80E-14
KM-BE1-90d	5.00	9.99E-06	4.63E-16	3.24E-14
KM-BE2-90d	3.00	1.00E-03	3.99E-14	1.15E-13
KM-BE3-90d	1.00	0.10	4.68E-13	5.79E-13
KM-BE6-90d	0.00	1.00	1.14E-12	3.19E-13
KM-BE4-90d	-1.00	10.0	2.49E-12	6.89E-14
KM-BE7-90d	-2.00	100.1	2.92E-12	2.55E-14
KM-BE5-90d	-3.00	1001.5	3.27E-12	9.90E-15
KM-BE1-180d	5.00	9.99E-06	2.75E-16	1.50E-14
KM-BE2-180d	3.00	1.00E-03	1.65E-14	4.90E-14
KM-BE3-180d	1.00	0.10	3.32E-13	3.06E-13
KM-BE6-180d	0.00	1.00	1.05E-12	1.44E-13
KM-BE4-180d	-1.00	10.0	1.74E-12	2.71E-14
KM-BE7-180d	-2.00	100.1	2.19E-12	8.29E-15
KM-BE5-180d	-3.00	1001.5	2.28E-12	6.22E-15
KM-BE1-365d	5.00	9.99E-06	8.00E-17	7.53E-15
KM-BE2-365d	3.00	1.00E-03	8.84E-15	2.28E-14
KM-BE3-365d	1.00	0.10	2.09E-13	1.08E-13
KM-BE6-365d	0.00	1.00	7.08E-13	7.81E-14
KM-BE4-365d	-1.00	10.0	1.17E-12	1.57E-14
KM-BE7-365d	-2.00	100.1	1.42E-12	5.82E-15
KM-BE5-365d	-3.00	1001.5	1.62E-12	1.16E-15

Appendix 2U: Calculated BK Al and Si dissolution rates.

Sample ID	pH	MacInnes Scaled aH^+	Al	Si
		(mol L^{-1})	(mol L^{-1} g^{-1} s^{-1})	(mol L^{-1} g^{-1} s^{-1})
BK-BE1-14d	5.00	9.99E-06	1.47E-14	5.80E-13
BK-BE2-14d	3.00	1.00E-03	1.64E-13	1.42E-12
BK-BE3-14d	1.00	0.10	2.05E-12	3.37E-12
BK-BE6-14d	0.00	1.00	4.43E-12	2.17E-12
BK-BE4-14d	-1.00	10.0	5.73E-12	7.90E-13
BK-BE7-14d	-2.00	100.1	6.09E-12	2.23E-13
BK-BE5-14d	-3.00	1001.5	5.81E-12	5.25E-14
BK-BE1-90d	5.00	9.99E-06	4.87E-16	5.91E-14
BK-BE2-90d	3.00	1.00E-03	3.30E-14	2.13E-13
BK-BE3-90d	1.00	0.10	6.99E-13	4.21E-13
BK-BE6-90d	0.00	1.00	1.70E-12	3.06E-13
BK-BE4-90d	-1.00	10.0	3.03E-12	6.97E-14
BK-BE7-90d	-2.00	100.1	2.85E-12	2.15E-14
BK-BE5-90d	-3.00	1001.5	3.17E-12	8.26E-15
BK-BE1-180d	5.00	9.99E-06	1.85E-17	2.17E-14
BK-BE2-180d	3.00	1.00E-03	2.57E-14	1.23E-13
BK-BE3-180d	1.00	0.10	5.46E-13	1.82E-13
BK-BE6-180d	0.00	1.00	1.50E-12	1.52E-13
BK-BE4-180d	-1.00	10.0	2.29E-12	2.53E-14
BK-BE7-180d	-2.00	100.1	2.16E-12	9.03E-15
BK-BE5-180d	-3.00	1001.5	2.43E-12	3.94E-15
BK-BE1-365d	5.00	9.99E-06	1.88E-16	1.22E-14
BK-BE2-365d	3.00	1.00E-03	1.05E-14	5.04E-14
BK-BE3-365d	1.00	0.10	2.78E-13	8.95E-14
BK-BE6-365d	0.00	1.00	9.65E-13	8.82E-14
BK-BE4-365d	-1.00	10.0	1.58E-12	1.37E-14
BK-BE7-365d	-2.00	100.1	1.53E-12	5.62E-15
BK-BE5-365d	-3.00	1001.5	1.98E-12	9.11E-16

Appendix 2V: Diffractograms for pH 5.0 to -3.0, 14 d exposure time, a) Kc, b) Km, c) BK batch experiments.

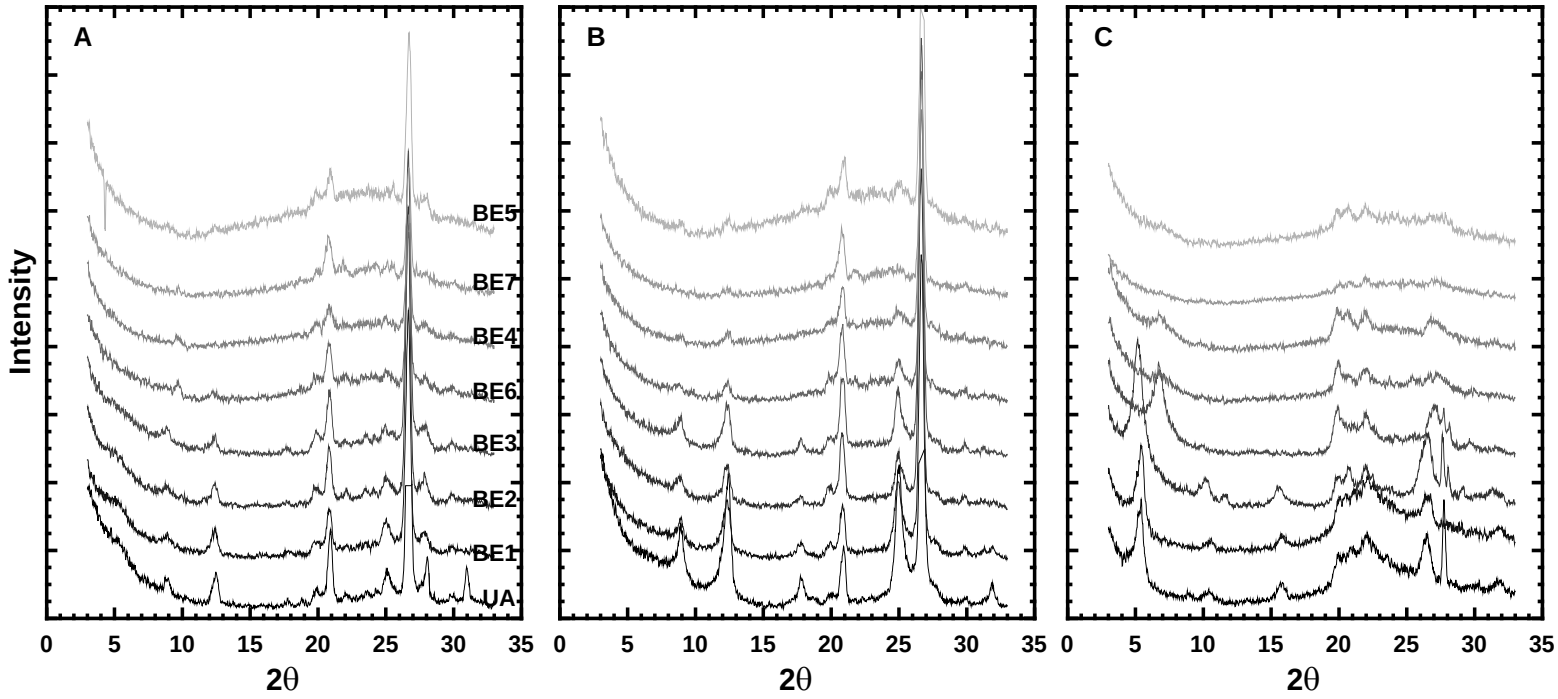

APPENDIX 3 Supplementary data for Chapter 3.

Appendix 3A - Si K-edge FY spectra of standard silicate minerals. The degree of polymerization (Q^n; where n represents number of shared oxygen atoms) of each mineral is listed

Appendix 3B - Si K-edge TEY (solid) and FY (dashed) spectra of unaltered (UA) and altered a) Kc, b) Km, and c) BK samples altered in a H_2SO_4 solution of pH -3.0 for durations of 14, 90, 180, and 365 days

Appendix 3C - Si $L_{2,3}$-edge FY spectra of unaltered (UA) and altered a) Kc, b) Km, and c) BK samples reacted in a H_2SO_4 solutions of pH -3.0 for durations of 14, 90, 180, and 365 days

Appendix 3D - Al K-edge FY spectra of Al-containing standard minerals

Appendix 3E - Al K-edge TEY spectra of unaltered (UA) and altered a) Kc, b) Km, and c) BK samples reacted in a H_2SO_4 solution of pH -3.0 for durations of 14, 90, 180 and 365 days

Appendix 3F - Al K-edge FY spectra of unaltered (UA) and altered Kc (A, D), Km (B, E), and BK (C, F) samples reacted in H_2SO_4 solutions of pH 1.0, 0.0, -1.0, and -3.0 for 365 days (A, B, & C) and reacted in a H_2SO_4 solution of pH -3.0 for 14, 90, 180, and 365 d (D, E, & F)

Appendix 3G - Al $L_{2,3}$-edge FY spectra of unaltered (UA) and altered a) Kc, b) Km, and c) BK samples reacted in a H_2SO_4 solutions of pH -3.0 for durations of 14, 90, 180, and 365 days

Appendix 3A: Si K-edge FY spectra of standard silicate minerals. The degree of polymerization (Q^n; where n represents number of shared oxygen atoms) of each mineral is listed.

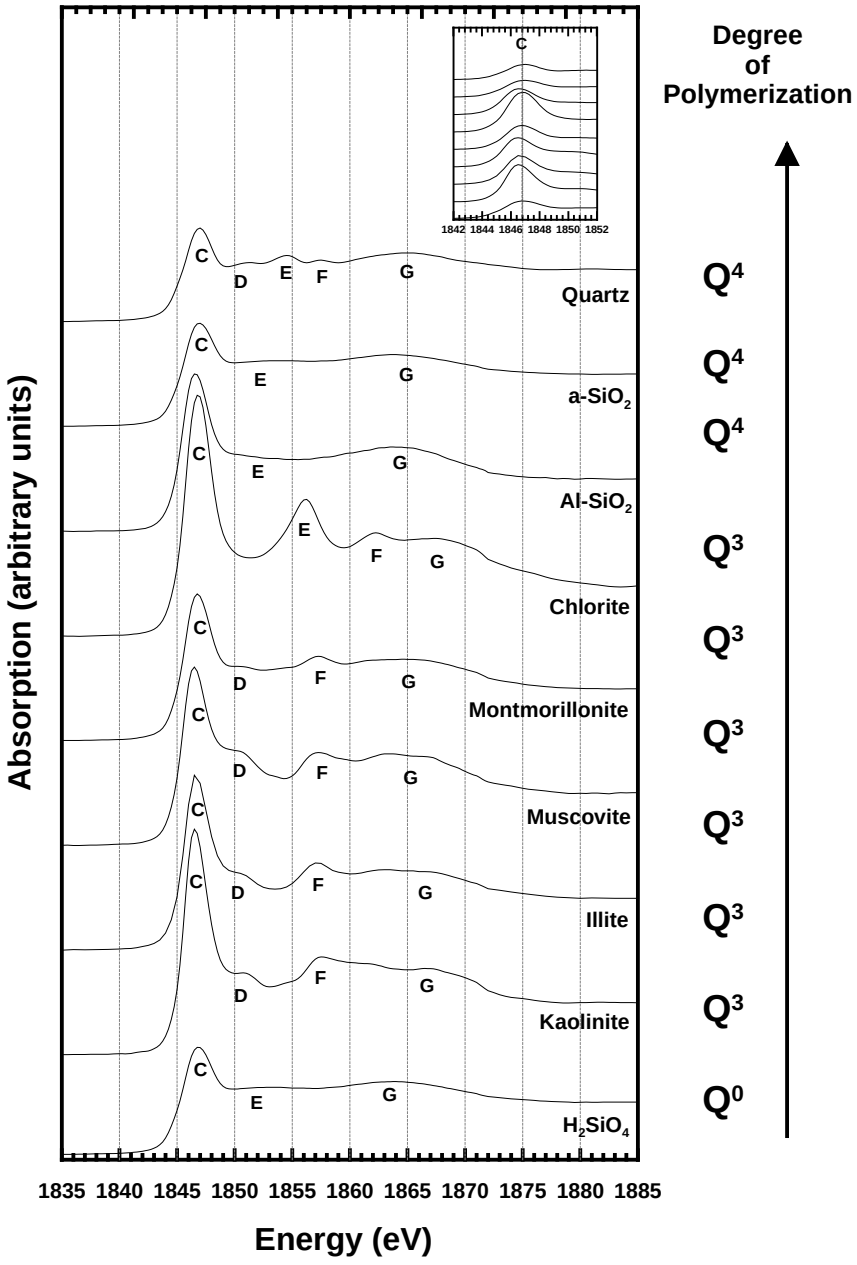

Appendix 3B: Si K-edge TEY (solid) and FY (dashed) spectra of unaltered (UA) and altered a) Kc, b) Km, and c) BK samples altered in a H_2SO_4 solution of pH -3.0 for durations of 14, 90, 180, and 365 days.

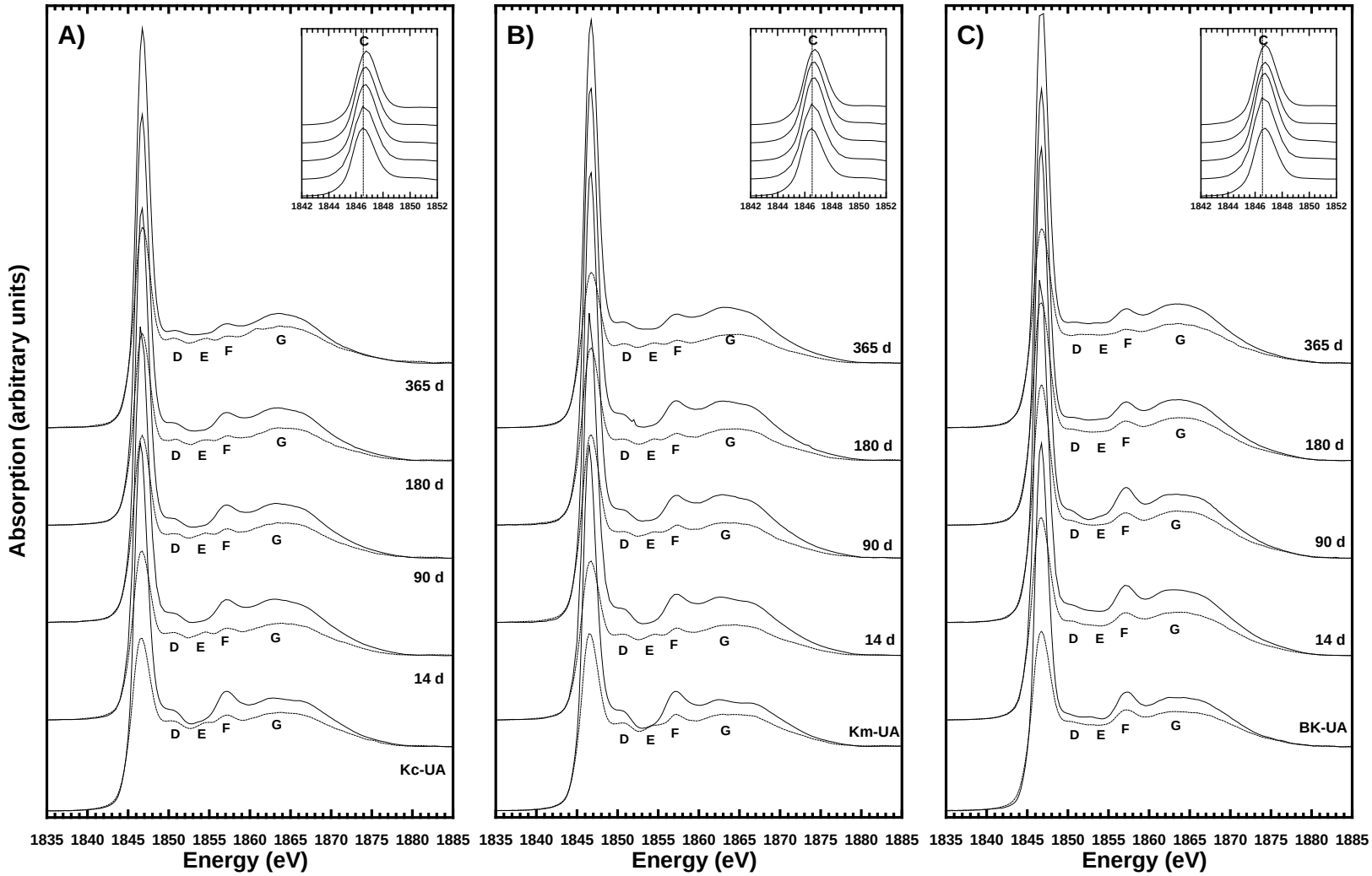

Appendix 3C: Si $L_{2,3}$-edge FY spectra of unaltered (UA) and altered a) Kc, b) Km, and c) BK samples reacted in a H_2SO_4 solutions of pH -3.0 for durations of 14, 90, 180, and 365 days.

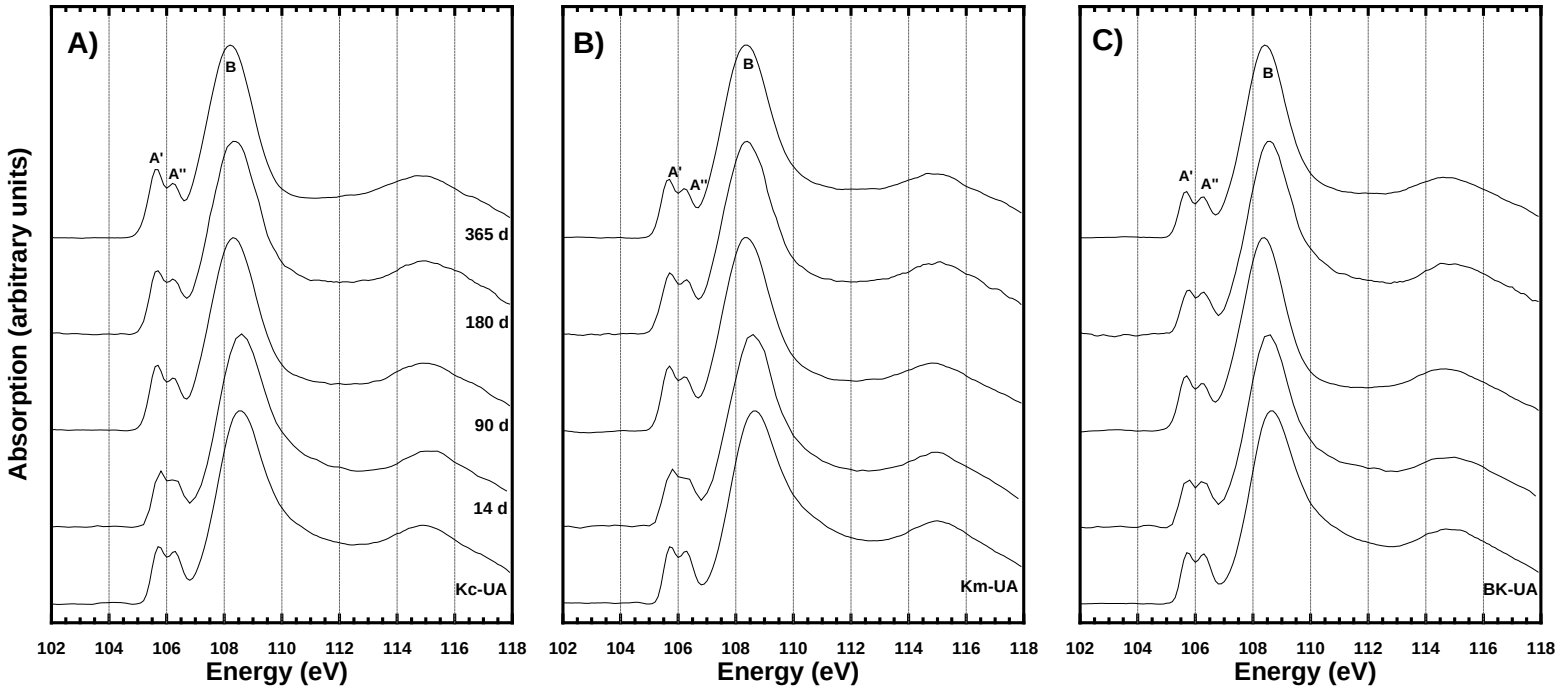

Appendix 3D: Al K-edge FY spectra of Al-containing standard minerals.

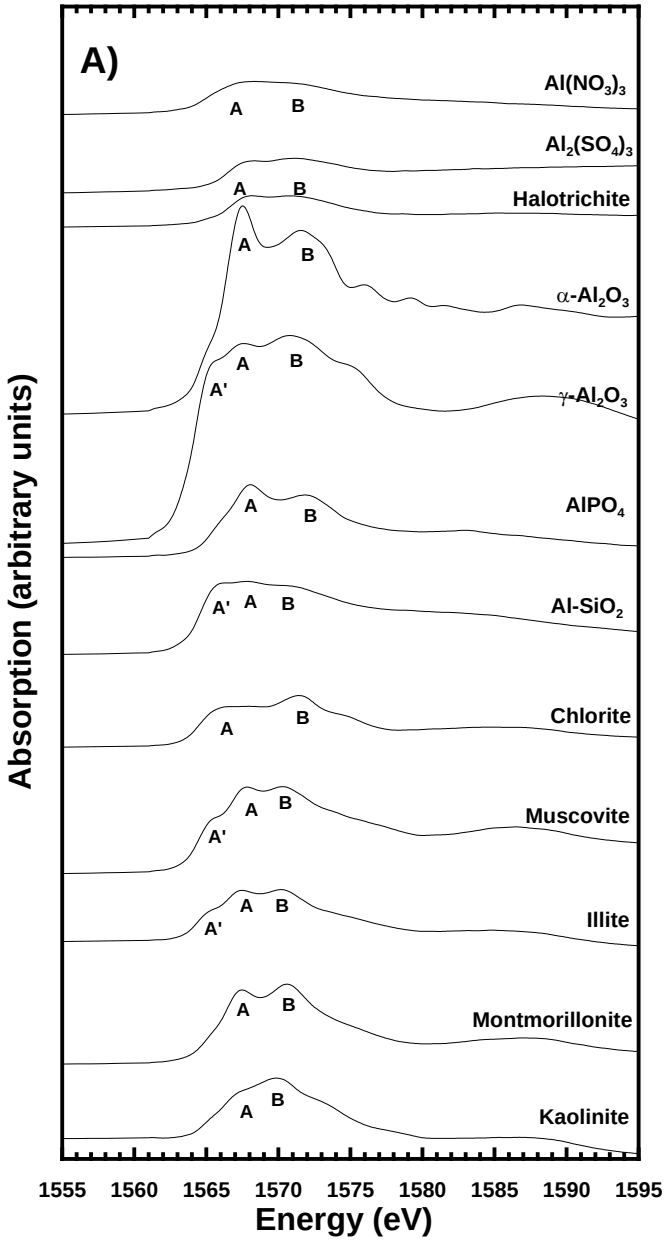

Appendix 3E: Al K-edge TEY spectra of unaltered (UA) and altered a) Kc, b) Km, and c) BK samples reacted in a H_2SO_4 solution of pH -3.0 for durations of 14, 90, 180 and 365 days.

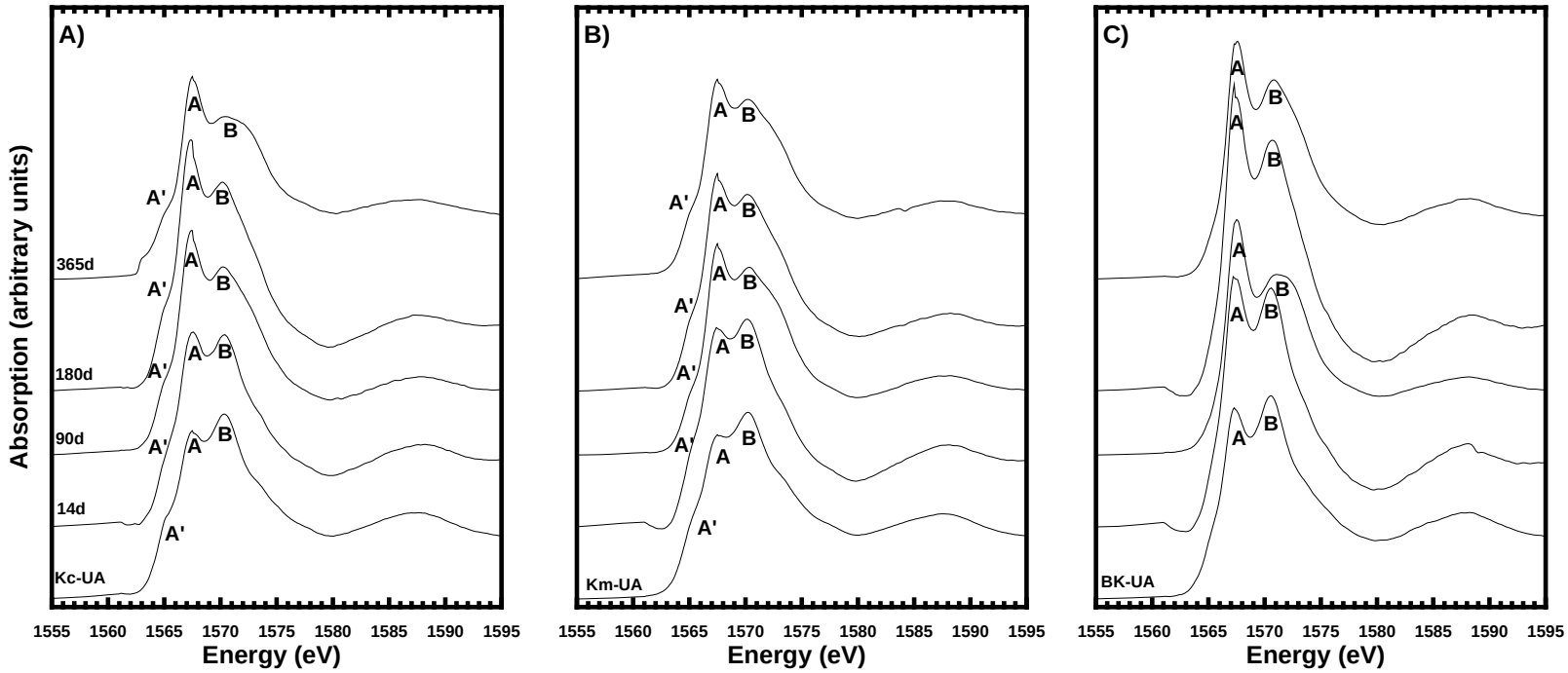

Appendix 3F: **Al K-edge FY spectra of unaltered (UA) and altered Kc (A, D), Km (B, E), and BK (C, F) samples reacted in H_2SO_4 solutions of pH 1.0, 0.0, -1.0, and -3.0 for 365 days (A, B, & C) and reacted in a H_2SO_4 solution of pH -3.0 for 14, 90, 180, and 365 d (D, E, & F).**

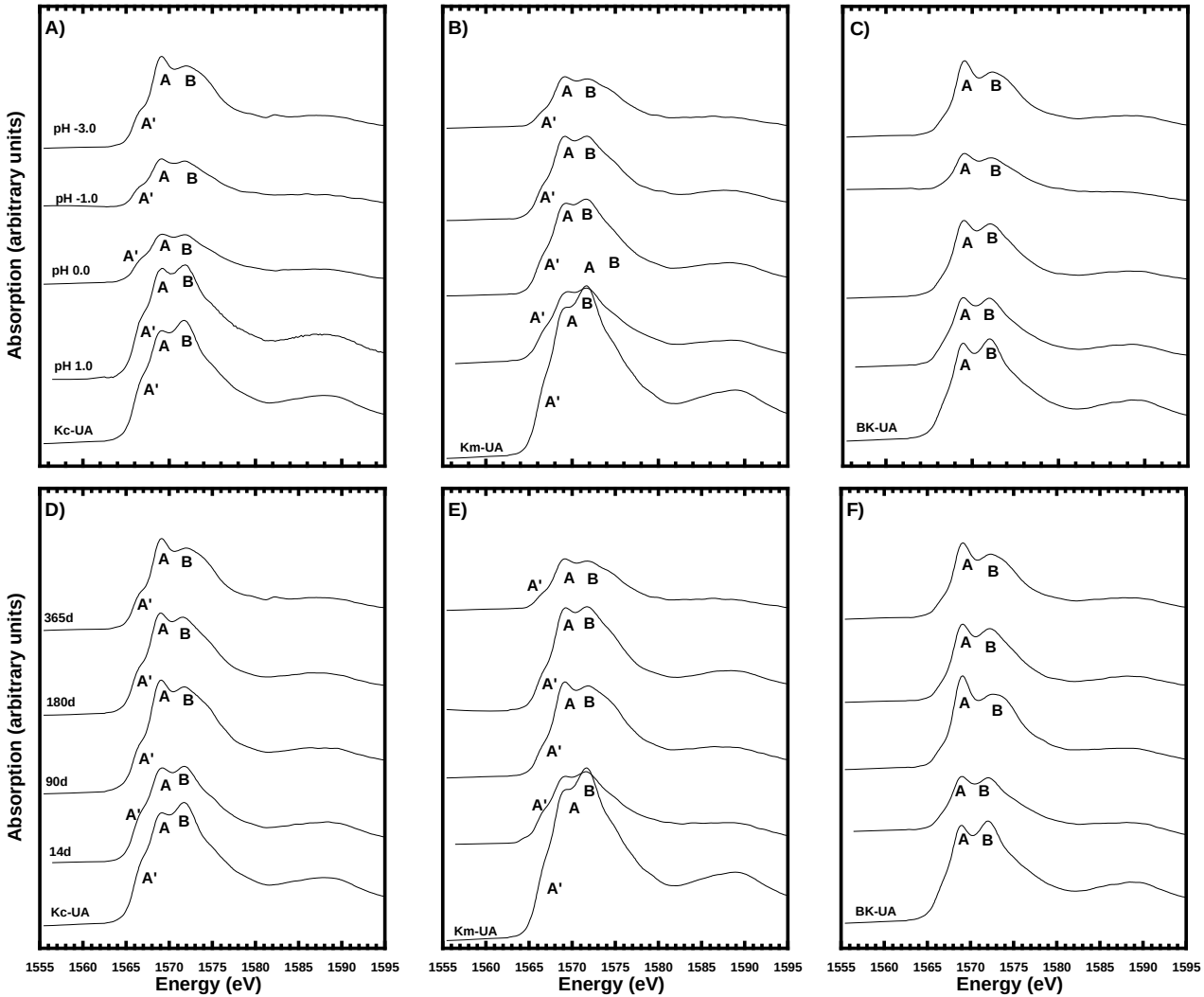

Appendix 3G: Al $L_{2,3}$-edge FY spectra of unaltered (UA) and altered a) Kc, b) Km, and c) BK samples reacted in a H_2SO_4 solutions of pH -3.0 for durations of 14, 90, 180, and 365 days.

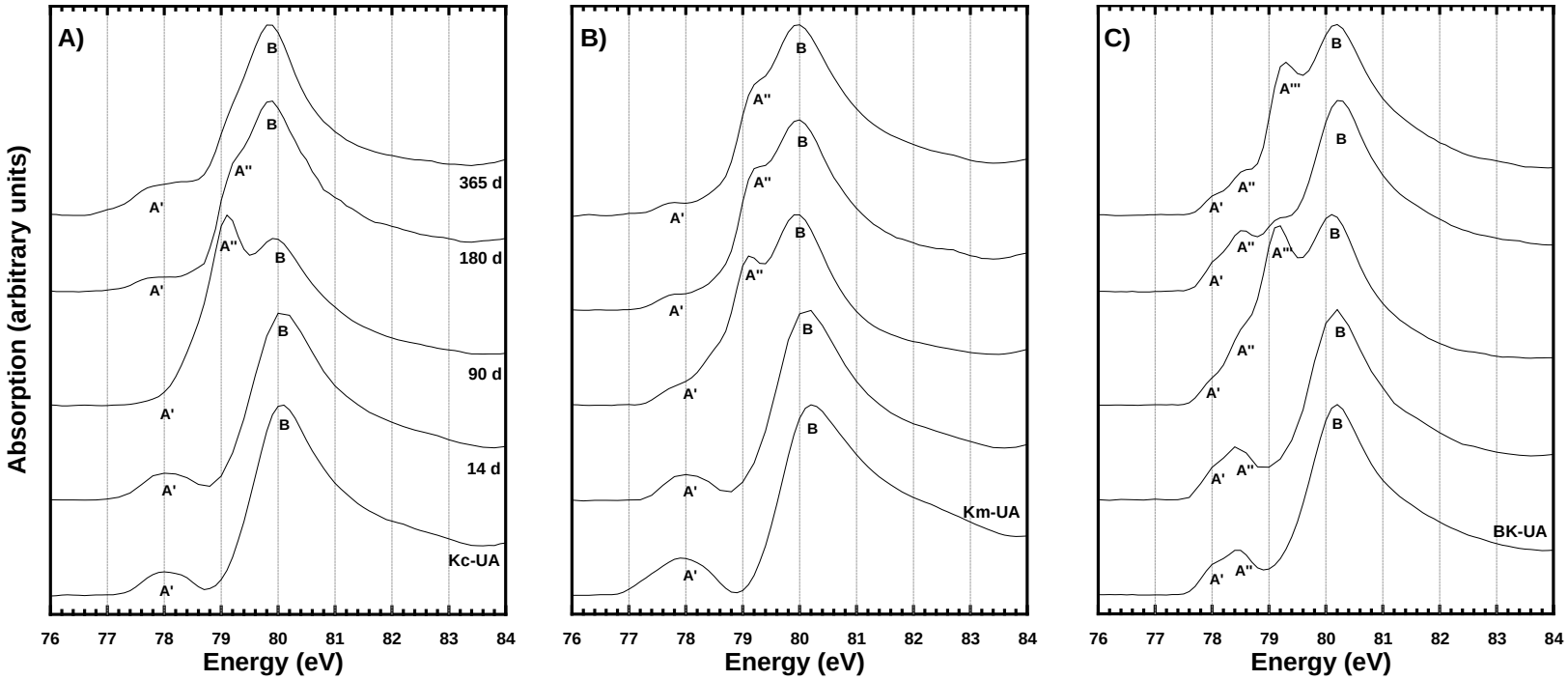

APPENDIX 4 Supplementary data for chapter 4.

Appendix 4A - Kc and Km diffusion cell schematic (to scale)

Appendix 4B - pH port data for Kc pH 3.0, 1.0, 0.0, -1.0, and -3.0 diffusion cells

Appendix 4C - pH port data for Km pH 3.0, 1.0, 0.0, -1.0, and -3.0 diffusion cells

Appendix 4D - Cumulative reservoir solutions for Kc pH 3.0, 1.0, 0.0, -1.0, and -3.0 diffusion cells. Each cumulative solution consisted of between two and six recovered reservoir solutions and the average solute concentration was determined on the cumulative solutions

Appendix 4E - Cumulative reservoir solutions for Kc pH 3.0, 1.0, 0.0, -1.0, and -3.0 diffusion cells. Each cumulative solution consisted of between two and six recovered reservoir solutions and the average solute concentration was determined on the cumulative solutions

Appendix 4F - Solute concentrations determined for 1:100 pore water extracts from the Kc pH 1.0, -1.0, and -3.0 diffusion cells

Appendix 4G - Dissolved aqueous concentrations determined for 1:100 pore water extracts from the Km pH 1.0, -1.0, and -3.0 diffusion cells

Appendix 4H - Dissolved aqueous concentrations determined for 1:1 pore water extracts from the Kc pH 3.0, 1.0, 0.0, -1.0, and -3.0 diffusion cells

Appendix 4I - Dissolved aqueous concentrations determined for 1:1 pore water extracts from the Km pH 3.0, 1.0, 0.0, -1.0, and -3.0 diffusion cells

Appendix 4J - Kc diffusion cell sub-sample physical parameters, including total sample mass (M_T), sample dry mass (M_D), sample water mass (M_W), dry bulk density (ρ_b), and volumetric water content (θ)

Appendix 4K - Km diffusion cell sub-sample physical parameters, including total sample mass (M_T), sample dry mass (M_D), sample water mass (M_W), dry bulk density (ρ_b), and volumetric water content (θ).

Appendix 4L - Kc absorption isotherm data calculated from the pH 5.0, 3.0, and 1.0 batch experiments results.

Appendix 4M - Km absorption isotherm data calculated from the pH 5.0, 3.0, and 1.0 batch experiments results.

Appendix 4N - Measured H^+ concentrations (g L^{-1}) for the Kc pH 1.0, -1.0, and -3.0 diffusion cells.

Appendix 4O - Measured H^+ concentrations (g L^{-1}) for the Km pH 1.0, -1.0, and -3.0 diffusion cells.

Appendix 4Q - Modled H^+ concentrations (g L^{-1}) for the Kc pH 1.0, -1.0, and -3.0 diffusion cells assuming no absorption.

Appendix 4R - Modled H^+ concentrations (g L^{-1}) for the Km pH 1.0, -1.0, and -3.0 diffusion cells assuming no absorption.

Appendix 4S - Modled H^+ concentrations (g L^{-1}) for the Kc pH 1.0, -1.0, and -3.0 diffusion cells assuming non-linear absorption.

Appendix 4T - Modled H^+ concentrations (g L^{-1}) for the Km pH 1.0, -1.0, and -3.0 diffusion cells assuming non-linear absorption.

Appendix 4A: Kc and Km diffusion cell schematic (to scale).

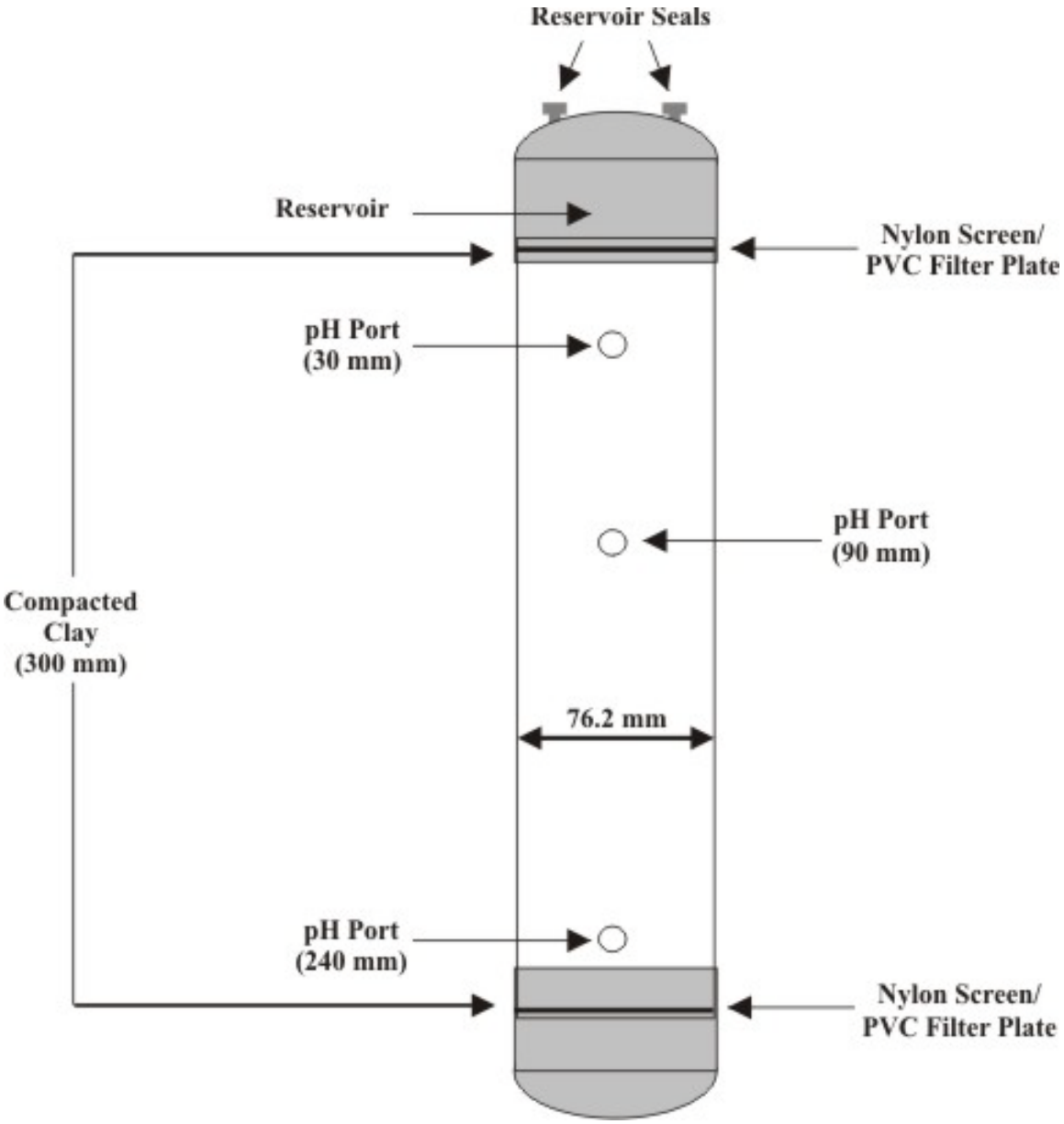

Appendix 4B: pH port data for Kc pH 3.0, 1.0, 0.0, -1.0, and -3.0 diffusion cells.

DC1	Port pH		
(d)	30 mm	90 mm	240 mm
59	6.43	6.21	6.48
66	6.34	6.36	6.34
73	6.50	6.42	6.42
80	6.50	6.42	6.36
87	6.57	6.40	6.30
94	6.40	6.14	6.21
108	6.24	6.40	6.21
115	6.33	6.26	6.39
122	6.24	6.26	6.11
145	6.12	6.30	6.10
157	6.30	6.15	6.05
164	6.20	6.10	6.08
171	6.20	6.15	6.14
178	6.38	6.43	6.57
185	6.38	6.30	6.35
192	6.21	6.10	6.20
199	6.41	6.51	6.90
206	6.26	6.25	6.45
216	6.32	6.21	6.19

DC2	Port pH		
(d)	30 mm	90 mm	240 mm
51	6.18	6.15	6.24
58	5.85	6.00	6.20
65	5.80	6.17	6.40
72	6.03	5.96	6.56
79	5.60	5.94	6.33
86	5.50	5.75	6.06
100	5.53	5.90	6.32
107	5.33	6.00	6.28
114	5.25	5.95	5.96
137	5.40	5.89	6.08
149	5.40	5.76	6.07
156	5.33	5.69	6.00
163	5.26	5.90	6.00
170	4.80	5.98	6.07
177	4.02	6.05	6.10
184	3.74	6.05	6.03
191	3.22	5.86	6.30
198	3.45	5.95	6.05
210	3.31	6.00	6.15
216	3.15	6.36	6.31

DC3	Port pH		
(d)	30 mm	90 mm	240 mm
42	3.73	5.75	6.13
49	3.49	5.87	6.20
56	2.62	5.85	6.30
63	1.80	6.02	6.00
70	1.48	5.88	6.11
77	1.27	5.66	5.94
91	0.99	5.70	5.83
98	0.93	5.50	5.85
105	0.96	5.49	5.87
128	0.80	5.34	5.74
140	0.70	5.49	5.89
147	0.60	5.50	5.85
154	0.60	5.48	5.90
161	0.57	5.39	5.95
168	0.50	5.04	5.91
175	0.60	4.90	6.02
182	0.60	4.24	6.15
189	0.60	5.05	6.00
201	0.70	4.22	6.63
209	0.70	3.86	6.04
216	0.70	3.76	6.18

Appendix 4B: Continued

DC4	Port pH		
(d)	30 mm	90 mm	240 mm
35	1.90	5.75	6.14
42	2.12	5.99	6.88
49	1.26	5.70	6.52
56	0.05	5.80	6.30
63	0.00	5.75	6.41
70	-0.05	5.65	6.30
84	0.05	5.63	6.10
91	-0.10	5.55	6.10
98	0.05	5.75	6.96
121	-0.25	4.95	6.55
133	-0.35	5.05	6.70
140	-0.15	5.13	6.60
147	-0.20	4.84	6.55
154	-0.25	4.64	6.10
161	-0.15	4.60	6.63
168	-0.20	4.70	6.82
175	-0.25	4.41	6.58
182	-0.25	4.20	6.66
194	-0.23	3.90	6.40
202	-0.23	3.90	6.82
211	-0.23	3.40	6.72
216	-0.23	3.50	7.24

DC5	Port pH		
(d)	30 mm	90 mm	240 mm
26	1.12	5.50	6.21
33	0.20	5.85	6.20
40	-0.52	5.89	6.85
47	-0.65	6.23	6.20
54	-1.35	6.00	6.10
61	-0.63	5.98	6.30
75	-0.85	5.06	6.49
82	-1.55	5.53	6.71
89	-0.95	5.30	6.26
112	-1.25	5.70	6.53
124	-2.10	5.60	6.70
131	-1.95	5.26	6.75
138	-1.60	4.70	6.63
145	-1.80	4.66	6.39
152	-1.70	4.62	6.40
159	-2.05	4.30	6.50
166	-1.65	4.00	6.65
173	-1.87	3.96	6.65
185	-2.77	4.20	6.40
193	-2.77	3.97	7.06
202	-2.77	3.88	6.7
209	-2.77	3.62	6.57
216	-2.77	3.52	6.92

Appendix 4C: pH port data for Km pH 3.0, 1.0, 0.0, -1.0, and -3.0 diffusion cells.

DC1 (d)	Port pH		
	30 mm	90 mm	240 mm
59	7.17	7.55	7.15
66	7.15	7.45	7.15
73	7.00	7.37	7.30
80	6.97	7.30	7.30
87	6.65	7.42	7.20
94	6.58	7.30	7.49
108	6.49	7.15	7.44
115	6.50	7.13	7.10
122	6.40	7.16	7.00
145	6.31	6.96	6.90
157	6.28	7.14	7.02
164	6.30	7.06	7.00
171	6.28	7.04	7.16
178	6.24	7.02	7.40
185	6.30	7.05	7.50
192	6.21	7.07	7.09
199	6.20	7.10	7.47
206	6.29	7.19	7.25
216	6.23	7.32	7.14

DC2 (d)	Port pH		
	30 mm	90 mm	240 mm
51	4.33	6.49	6.73
58	4.05	6.39	6.70
65	2.28	6.44	6.71
72	2.17	6.34	6.66
79	2.09	6.25	6.62
86	1.80	6.03	6.53
100	1.78	5.81	6.44
107	1.70	5.70	6.42
114	1.70	5.66	6.40
137	1.70	5.33	6.35
149	1.50	4.86	6.26
156	1.59	4.86	6.20
163	1.60	4.13	6.25
170	1.54	4.13	6.40
177	1.59	4.04	6.39
184	1.54	4.10	6.24
191	1.54	3.64	6.56
198	1.46	4.56	6.43
210	1.57	4.32	6.6
216	1.42	4.05	6.77

DC3 (d)	Port pH		
	30 mm	90 mm	240 mm
42	-	6.51	6.22
49	0.43	5.99	6.44
56	0.50	5.67	6.20
63	0.45	5.30	6.69
70	0.35	4.97	6.15
77	0.40	4.75	5.99
91	0.40	3.84	6.08
98	0.30	3.94	5.95
105	0.30	3.90	6.10
128	0.20	2.84	5.95
140	0.20	2.84	6.35
147	0.27	2.80	6.15
154	0.30	2.05	6.20
161	0.25	1.82	6.10
168	0.25	1.76	6.30
175	0.27	1.76	6.45
182	0.30	1.69	6.80
189	0.30	1.50	6.87
201	0.32	1.39	6.30
209	0.30	1.38	6.64
216	0.30	1.19	6.51

Appendix 4C: Continued

DC4	Port pH		
(d)	30 mm	90 mm	240 mm
35	-0.45	6.02	6.21
42	-0.40	5.80	6.33
49	-0.40	4.54	6.21
56	-0.48	4.14	6.26
63	-0.50	4.31	6.20
70	-0.40	3.65	6.22
84	-0.40	3.34	6.27
91	-0.40	1.85	6.10
98	-0.35	1.45	6.27
121	-0.50	0.99	6.09
133	-0.45	0.75	6.50
140	-0.20	0.68	6.25
147	-0.40	0.68	6.20
154	-0.47	0.58	6.10
161	-	0.58	6.20
168	-0.35	0.55	6.80
175	-0.42	0.60	6.76
182	-0.47	0.61	6.77
194	-0.45	0.52	6.70
202	-0.50	0.50	6.98
211	-0.50	0.45	6.58
216	-0.50	0.45	6.87

DC5	Port pH		
(d)	30 mm	90 mm	240 mm
26	-1.42	6.01	7.20
33	-1.27	3.55	7.20
40	-1.62	2.45	6.98
47	-1.45	2.45	6.65
54	-2.07	1.52	6.45
61	-1.67	1.15	6.40
75	-1.90	0.50	6.29
82	-2.07	0.47	6.40
89	-2.30	0.40	6.40
112	-2.90	0.20	6.40
124	-2.90	0.13	6.50
131	-2.90	0.13	6.70
138	-2.90	-0.05	6.45
145	-2.90	0.05	6.73
152	-2.90	0.10	6.85
159	-2.90	0.07	6.80
166	-2.90	-0.10	6.88
173	-2.90	-0.14	6.85
185	-2.80	-0.11	7.03
193	-2.90	-0.10	6.73
202	-2.90	-0.18	7.03
209	-2.90	-0.25	6.97
216	-2.90	-0.43	6.97

Appendix 4D: Cumulative reservoir solutions for Kc pH 3.0, 1.0, 0.0, -1.0, and -3.0 diffusion cells. Each cumulative solution consisted of between two and six recovered reservoir solutions and the average solute concentration was determined on the cumulative solutions.

Sample ID	Interval (d)	Al (umo L^{-1})	Si (umo L^{-1})	Fe (umo L^{-1})	Ca (umo L^{-1})	Mg (umo L^{-1})	Na (umo L^{-1})	K (umo L^{-1})
KC-DC1-1	**1-29**	0.00	30.08	1.52	338	375	8.19E+03	222
KC-DC1-2	**29-54**	0.00	42.76	5.38	418	434	6.04E+03	215
KC-DC1-3	**54-82**	0.00	21.93	2.98	202	243	5.25E+03	188
KC-DC1-4	**82-113**	0.00	21.03	0.72	216	273	5.17E+03	187
KC-DC1-5	**113-148**	0.00	20.12	0.29	237	279	5.36E+03	192
KC-DC1-6	**148-180**	0.00	19.22	0.19	246	301	5.47E+03	172
KC-DC1-7	**180-208**	0.00	17.41	1.72	218	249	4.74E+03	185
KC-DC1-8	**208-216**	0.00	37.33	3.67	240	289	5.29E+03	160
KC-DC2-1	**1-28**	1.26E+03	789	2.50E+03	2.73E+03	9.02E+03	1.69E+04	670
KC-DC2-2	**28-56**	3.53E+03	1.51E+03	5.89E+03	4.47E+03	1.45E+04	1.68E+04	779
KC-DC2-3	**56-84**	4.85E+03	1.59E+03	6.86E+03	5.01E+03	1.49E+04	1.68E+04	833
KC-DC2-4	**84-1137**	4.92E+03	1.45E+03	6.68E+03	4.69E+03	1.36E+04	1.42E+04	780
KC-DC2-6	**137-164**	7.40E+03	2.12E+03	9.30E+03	7.04E+03	1.99E+04	2.18E+04	1.11E+03
KC-DC2-7	**164-193**	7.89E+03	2.23E+03	9.33E+03	7.53E+03	2.02E+04	2.15E+04	1.16E+03
KC-DC2-8	**193-216**	7.65E+03	2.10E+03	8.73E+03	7.17E+03	1.92E+04	2.11E+04	1.11E+03
KC-DC3-1	**1-33**	1.51E+04	1.43E+03	2.29E+04	5.79E+03	5.10E+04	2.64E+04	2.45E+03
KC-DC3-2	**33-61**	1.68E+04	1.11E+03	1.72E+04	5.27E+03	3.98E+04	1.78E+04	2.20E+03
KC-DC3-3	**61-89**	1.54E+04	1.03E+03	2.06E+04	4.61E+03	3.18E+04	1.41E+04	2.01E+03
KC-DC3-4	**89-128**	2.38E+04	1.50E+03	2.45E+04	6.39E+03	4.40E+04	1.88E+04	3.04E+03
KC-DC3-5	**128-135**	2.80E+04	1.71E+03	2.67E+04	7.03E+03	4.98E+04	2.23E+04	3.90E+03
KC-DC3-6	**135-184**	1.98E+04	1.61E+03	2.29E+04	4.16E+03	2.40E+04	2.06E+04	3.21E+03
KC-DC3-7	**184-216**	2.95E+04	1.73E+03	2.49E+04	6.80E+03	4.47E+04	1.95E+04	4.11E+03
KC-DC4-1	**1-30**	2.88E+04	525	3.97E+04	4.37E+03	7.75E+04	3.13E+04	4.48E+03
KC-DC4-2	**30-58**	2.75E+04	428	2.71E+04	3.09E+03	4.68E+04	1.73E+04	4.00E+03
KC-DC4-3	**58-93**	3.28E+04	433	2.75E+04	3.06E+03	4.66E+04	1.69E+04	4.30E+03
KC-DC4-4	**93-121**	4.92E+04	518	3.61E+04	3.97E+03	6.19E+04	2.30E+04	6.51E+03
KC-DC4-5	**121-148**	5.14E+04	515	3.44E+04	3.71E+03	5.98E+04	2.25E+04	6.79E+03
KC-DC4-6	**148-177**	5.38E+04	516	3.37E+04	3.75E+03	5.73E+04	2.20E+04	7.08E+03
KC-DC4-7	**177-216**	5.17E+04	487	2.99E+04	3.22E+03	5.12E+04	1.99E+04	6.63E+03
KC-DC5-1	**1-28**	3.41E+04	338	4.12E+04	343	8.22E+04	3.37E+04	6.85E+03
KC-DC5-2	**28-63**	3.48E+04	302	2.44E+04	92.5	4.43E+04	1.68E+04	5.46E+03
KC-DC5-3	**63-96**	5.28E+04	322	3.09E+04	146	5.74E+04	2.13E+04	7.97E+03
KC-DC5-4	**96-126**	6.67E+04	298	3.77E+04	204	6.63E+04	2.50E+04	1.02E+04
KC-DC5-5	**126-153**	6.43E+04	323	3.34E+04	178	5.93E+04	2.25E+04	9.98E+03
KC-DC5-6	**153-186**	7.19E+04	326	3.58E+04	198	6.53E+04	2.49E+04	1.14E+04
KC-DC5-7	**186-216**	6.58E+04	321	3.14E+04	181	5.81E+04	2.24E+04	1.07E+04

Appendix 4E: Cumulative reservoir solutions for Km pH 3.0, 1.0, 0.0, -1.0, and -3.0 diffusion cells. Each cumulative solution consisted of between two and six recovered reservoir solutions and the average solute concentration was determined on the cumulative solutions.

Sample ID	Interval (d)	Al (umo L^{-1})	Si (umo L^{-1})	Fe (umo L^{-1})	Ca (umo L^{-1})	Mg (umo L^{-1})	Na (umo L^{-1})	K (umo L^{-1})
KM-DC1-1	**1-29**	0.00	12.8	31.8	103	119	1.22E+04	214
KM-DC1-2	**29-54**	0.00	15.5	37.3	68.4	81.5	8.92E+03	176
KM-DC1-3	**54-82**	0.00	10.1	27.8	79.6	86.6	6.86E+03	146
KM-DC1-4	**82-113**	0.00	19.1	26.8	79.6	85.0	7.29E+03	163
KM-DC1-5	**113-148**	0.00	20.9	19.3	82.0	87.0	7.04E+03	150
KM-DC1-6	**148-180**	0.00	25.4	18.7	86.0	88.6	6.93E+03	146
KM-DC1-7	**180-208**	0.00	21.8	17.6	81.2	79.5	5.97E+03	134
KM-DC1-8	**208-216**	0.00	32.6	17.2	86.0	86.6	6.38E+03	134
KM-DC2-1	**1-28**	862	673	1.30E+04	1.81E+03	1439.98	25534.77	724
KM-DC2-2	**28-56**	1.54E+03	1.15E+03	1.48E+04	1.82E+03	1711.25	21215.09	712
KM-DC2-3	**56-84**	1.82E+03	1.27E+03	1.38E+04	1.76E+03	1772.23	20319.37	733
KM-DC2-4	**84-1137**	1.91E+03	1.28E+03	1.25E+04	1.43E+03	1659.37	17932.87	726
KM-DC2-6	**137-164**	3.47E+03	2.04E+03	1.91E+04	2.37E+03	2754.85	27617.59	1.09E+03
KM-DC2-7	**164-193**	3.57E+03	2.08E+03	1.83E+04	2.28E+03	2695.87	26453.01	1.07E+03
KM-DC2-8	**193-216**	3.21E+03	1.82E+03	1.59E+04	1.91E+03	2329.18	22714.23	943
KM-DC3-1	**1-33**	5.69E+03	1.18E+03	3.92E+04	2.77E+03	5.09E+03	4.39E+04	2.04E+03
KM-DC3-2	**33-61**	7.58E+03	1.12E+03	2.77E+04	1.67E+03	4.27E+03	2.82E+04	1.84E+03
KM-DC3-3	**61-89**	7.65E+03	1.08E+03	2.19E+04	1.16E+03	3.44E+03	2.17E+04	1.61E+03
KM-DC3-4	**89-128**	1.41E+04	1.66E+03	3.22E+04	1.86E+03	5.48E+03	3.12E+04	2.64E+03
KM-DC3-5	**128-135**	1.62E+04	1.82E+03	3.16E+04	1.86E+03	5.64E+03	3.10E+04	3.04E+03
KM-DC3-6	**135-184**	9.89E+03	1.87E+03	2.82E+04	4.36E+03	2.55E+04	2.42E+04	3.52E+03
KM-DC3-7	**184-216**	1.93E+04	0.00	3.03E+04	1.70E+03	5.64E+03	2.87E+04	3.30E+03
KM-DC4-1	**1-30**	1.10E+04	653	5.65E+04	817	7.61E+03	5.70E+04	3.50E+03
KM-DC4-2	**30-58**	1.34E+04	544	3.14E+04	361	4.83E+03	2.87E+04	2.85E+03
KM-DC4-3	**58-93**	1.86E+04	569	3.00E+04	312	4.99E+03	2.57E+04	3.31E+03
KM-DC4-4	**93-121**	3.03E+04	697	3.85E+04	400	6.03E+03	2.93E+04	4.39E+03
KM-DC4-6	**121-177**	2.67E+04	639	2.67E+04	219	5.02E+03	2.05E+04	4.05E+03
KM-DC4-7	**177-216**	2.85E+04	517	2.32E+04	153	4.61E+03	1.81E+04	3.91E+03
KM-DC5-1	**1-28**	1.91E+04	397	6.98E+04	350	1.04E+04	6.92E+04	5.97E+03
KM-DC5-2	**28-63**	2.31E+04	339	3.07E+04	2.07	5.34E+03	2.71E+04	4.48E+03
KM-DC5-3	**63-96**	5.53E+04	339	4.44E+04	0.00	7.14E+03	2.86E+04	6.79E+03
KM-DC5-4	**96-126**	6.16E+04	353	3.92E+04	0.00	8.99E+03	3.18E+04	9.18E+03
KM-DC5-5	**126-153**	4.52E+03	358	2.48E+04	0.00	7.64E+03	2.59E+04	8.62E+03
KM-DC5-6	**153-186**	5.17E+03	359	2.63E+04	0.00	8.52E+03	2.82E+04	9.85E+03
KM-DC5-7	**186-216**	4.45E+03	378	2.13E+04	0.00	7.81E+03	2.49E+04	9.40E+03

Appendix F: Solute concentrations determined for 1:100 pore water extracts from the Kc pH 1.0, -1.0, and -3.0 diffusion cells.

Sample ID	Depth	pH	Clay	Al	Fe	Si	Ca	Mg	Na	SO_4
			(g)	(µmol g^{-1})	(µmol g^{-1})	(µmol g^{-1})	(µmol g^{-1})	(µmol g^{-1})	(µmol g^{-1})	(µmol g^{-1})
KC-DC2-1	1.5	2.20	1.00	9.52	21.0	2.72	201	32.0	14.9	277
KC-DC2-2	4.0	6.18	1.03	0.29	0.15	1.22	63.7	48.4	33.7	114
KC-DC2-3	6.0	6.71	1.02	1.50	0.91	2.68	44.1	43.7	57.0	56.4
KC-DC2-4	8.0	6.76	1.00	1.69	1.23	2.93	50.1	39.7	74.3	62.2
KC-DC2-7	13.5	6.78	1.02	1.40	0.98	2.90	31.8	23.8	98.1	63.5
KC-DC2-9	19.5	6.90	1.07	2.70	2.91	4.05	62.6	47.6	105	59.1
KC-DC2-12	28.3	7.10	1.01	1.16	1.04	3.14	17.9	15.6	80.3	36.3
KC-DC4-1	1	-0.65	1.09	182	46.7	11.1	123	61.8	11.7	760
KC-DC4-2	2.5	-0.61	1.06	325	67.0	15.0	150	68.8	4.36	842
KC-DC4-3	3.5	-0.22	1.04	323	100	22.4	150	77.2	4.09	826
KC-DC4-5	5.5	0.00	1.10	305	142	31.7	111	75.9	2.33	731
KC-DC4-8	8.5	4.16	1.01	52.2	115	52.0	0.10	0.02	0.85	179
KC-DC4-11	13	5.68	1.11	59.0	56.1	67.3	3.69	2.39	4.79	66.7
KC-DC4-14	19.25	6.33	1.00	42.4	24.7	69.6	2.46	2.12	3.27	37.4
KC-DC4-17	28.75	6.14	1.01	85.1	45.4	56.7	7.41	5.95	3.27	35.1
KC-DC5-1	1.0	-2.90	1.00	288	57.9	13.1	177	58.3	6.72	1.27E+03
KC-DC5-3	3.5	-2.68	1.06	290	166	28.2	403	176	4.28	1.38E+03
KC-DC5-5	5.5	-1.30	1.03	308	168	40.3	158	99.4	2.28	912
KC-DC5-7	7.5	1.39	1.02	288	213	31.6	107	31.2	1.74	680
KC-DC5-10	10.5	5.54	1.02	37.0	73.3	68.9	0.46	0.22	1.51	128
KC-DC5-13	15.0	6.64	1.02	61.5	44.6	72.9	2.69	2.48	3.44	48.3
KC-DC5-16	21.0	6.68	1.10	45.6	23.3	71.6	1.81	1.39	2.64	42.7
KC-DC5-19	28.8	6.77	1.00	28.4	16.2	54.1	1.32	1.12	2.84	26.9

Appendix G: Solute concentrations determined for 1:100 pore water extracts from the Km pH 1.0, -1.0, and -3.0 diffusion cells.

Sample ID	Depth	pH	Clay	Al	Fe	Si	Ca	Mg	Na	SO_4
			(g)	(µmol g^{-1})	(µmol g^{-1})	(µmol g^{-1})	(µmol g^{-1})	(µmol g^{-1})	(µmol g^{-1})	(µmol g^{-1})
KM-DC2-1	1.5	1.40	1.04	1.91	2.76	12.7	0.53	8.46	1.45	32.3
KM-DC2-2	4.0	1.90	1.01	5.53	3.31	21.5	0.34	10.4	1.36	35.6
KM-DC2-3	6.0	3.68	1.05	5.36	4.42	35.1	0.40	0.19	1.53	21.0
KM-DC2-4	8.0	4.64	1.08	16.3	9.74	53.5	0.75	2.04	2.06	23.0
KM-DC2-7	13.8	7.25	1.16	11.9	8.83	93.3	1.72	9.77	3.40	7.26
KM-DC2-10	22.0	7.50	1.00	9.74	7.00	100	1.84	9.13	3.85	4.01
KM-DC2-13	28.5	7.45	1.06	9.19	6.99	86.3	1.73	7.59	3.63	3.85
KM-DC4-1	1.5	-0.60	1.10	1.52	10.9	13.2	134	30.5	7.16	467
KM-DC4-3	4.5	-0.55	1.10	30.0	18.9	33.5	158	71.1	1.57	496
KM-DC4-5	6.5	-0.05	1.06	31.5	19.6	46.5	120	79.7	2.18	435
KM-DC4-7	8.5	0.10	0.98	29.9	20.1	56.5	73.3	63.7	1.78	350
KM-DC4-9	10.5	0.70	1.07	32.4	20.1	65.1	39.6	59.3	1.71	262
KM-DC4-12	15.0	4.28	1.03	18.9	14.3	75.7	0.27	0.37	0.84	56.6
KM-DC4-15	21.3	6.44	1.02	9.13	7.52	102	1.15	4.29	2.24	9.89
KM-DC4-18	28.8	6.98	1.02	9.92	7.36	82.2	1.23	8.82	2.76	3.67
KM-DC5-1	1.0	-2.30	1.11	24.4	12.0	14.9	223	31.8	7.11	1.11E+03
KM-DC5-3	3.5	-2.10	1.05	28.9	31.8	42.0	426	142	4.41	1.22E+03
KM-DC5-6	6.5	-1.20	1.02	31.9	26.3	64.1	198	96.8	1.65	611
KM-DC5-9	9.5	-0.27	1.01	30.2	36.5	96.5	173	199	1.29	646
KM-DC5-12	12.5	0.55	1.07	32.3	26.2	82.4	53.2	76.0	2.41	323
KM-DC5-15	17.3	4.20	1.11	8.93	12.7	86.5	0.35	0.35	1.17	35.7
KM-DC5-17	21.0	5.43	1.01	9.74	7.83	100	0.76	3.90	1.85	12.1
KM-DC5-20	28.8	6.89	1.07	7.41	5.70	86.1	1.12	4.85	2.68	4.65

Appendix H: Dissolved aqueous concentrations determined for 1:1 pore water extracts from the Kc pH 3.0, 1.0, 0.0, -1.0, and -3.0 diffusion cells.

Sample ID	Depth	pH	Clay	Al	Si	Fe	Ca	Mg	Na	K	SO_4
			(g)	(µmol g^{-1})	(µmol g^{-1})	(µmol g^{-1})	(µmol g^{-1})	(µmol g^{-1})	(µmol g^{-1})	(µmol g^{-1})	(µmol g^{-1})
KC-DC1-1	1.5	6.76	40.86	0.05	0.14	0.01	0.36	0.58	10.1	0.30	6.49
KC-DC1-2	4.0	6.79	40.35	0.11	0.16	0.03	0.75	0.87	18.4	0.45	13.8
KC-DC1-3	6.0	6.79	39.86	0.00	0.09	0.00	5.48	4.18	40.3	1.11	30.9
KC-DC1-4	8.5	6.82	40.72	0.00	0.09	0.00	4.97	4.27	50.5	3.58	37.4
KC-DC1-6	14.5	6.87	39.60	0.00	0.09	0.00	5.18	4.73	71.7	2.35	45.3
KC-DC1-8	20.3	6.79	40.09	0.00	0.09	0.00	5.24	4.84	76.3	1.52	46.5
KC-DC1-11	28.8	6.76	41.32	0.00	0.12	0.00	5.08	4.34	63.6	1.44	35.4
KC-DC2-1	1.5	2.20	43.63	4.64	1.47	2.67	15.2	13.3	10.5	0.72	45.7
KC-DC2-2	4.0	6.18	40.76	0.11	0.15	0.32	13.9	19.7	24.1	1.14	44.0
KC-DC2-3	6.0	6.71	39.66	0.11	0.12	0.31	9.48	13.3	40.5	1.51	42.6
KC-DC2-4	8.0	6.76	37.25	0.11	0.13	0.30	7.02	8.64	51.3	1.60	42.8
KC-DC2-7	13.5	6.78	40.89	0.02	0.08	0.00	5.18	4.67	66.2	1.57	43.5
KC-DC2-9	19.5	6.90	39.67	0.03	0.08	0.00	4.93	4.40	67.9	1.49	45.3
KC-DC2-12	28.3	7.10	42.81	0.02	0.08	0.00	2.22	2.02	44.8	1.07	29.3
KC-DC3-1	1.0	0.28	41.34	29.6	3.91	22.9	17.9	28.6	7.36	2.74	241
KC-DC3-2	3.0	0.57	40.86	39.2	2.49	40.0	16.9	58.5	14.8	2.60	314
KC-DC3-3	5.0	1.51	38.80	49.5	1.21	39.5	14.1	86.4	22.1	2.00	230
KC-DC3-4	7.0	4.50	37.22	0.00	0.08	0.00	12.2	81.3	32.0	2.06	111
KC-DC3-6	11.0	6.32	42.25	0.00	0.13	0.00	10.5	23.7	50.6	2.22	59.4
KC-DC3-8	15.0	6.63	41.06	0.00	0.08	0.00	5.29	6.10	56.9	1.83	41.8
KC-DC3-10	19.5	6.67	39.92	0.00	0.08	0.00	3.43	2.81	53.5	1.38	33.7
KC-DC3-13	28.8	6.48	41.17	0.00	0.07	0.00	1.19	1.14	37.2	0.90	20.6
KC-DC4-1	1.0	-0.65	39.17	57.3	4.08	28.2	6.13	37.4	8.77	4.93	322
KC-DC4-2	2.5	-0.61	29.24	79.6	4.03	43.4	9.70	62.9	13.5	5.41	384
KC-DC4-3	3.5	-0.22	30.51	80.7	3.07	61.9	15.3	44.1	19.2	5.39	452
KC-DC4-5	5.5	0.00	40.46	78.1	1.60	85.8	14.6	65.2	28.4	3.74	478
KC-DC4-8	8.5	4.16	33.92	0.22	0.11	0.61	12.4	85.9	41.3	2.42	119
KC-DC4-11	13.0	5.68	43.81	0.11	0.12	0.16	9.77	17.9	50.6	2.20	54.0
KC-DC4-14	19.3	6.33	41.24	0.02	0.06	0.00	3.63	2.67	48.3	1.41	31.8
KC-DC4-17	28.8	6.14	39.34	0.02	0.06	0.00	1.16	0.82	31.5	0.85	18.5
KC-DC5-1	1.0	-2.90	26.9	77.1	0.88	29.2	0.58	45.4	12.0	8.17	950
KC-DC5-3	3.5	-2.68	27.3	159	1.94	104	0.47	134	26.8	11.6	589
KC-DC5-5	5.5	-1.30	30.3	108	1.81	114	5.56	168	37.1	7.52	570
KC-DC5-7	7.5	1.39	31.2	87.9	1.88	112	15.7	193	43.4	2.17	452
KC-DC5-10	10.5	5.54	43.9	0.45	0.07	0.66	12.6	50.6	51.1	2.40	89.1
KC-DC5-13	15.0	6.64	40.9	0.11	0.09	0.29	6.38	8.09	52.9	1.92	40.8
KC-DC5-16	21.0	6.68	41.9	0.02	0.06	0.00	3.39	2.39	45.5	1.28	28.9
KC-DC5-19	28.8	6.77	41.9	0.02	0.07	0.00	1.55	1.04	29.9	0.84	15.7

Appendix 4I: Dissolved aqueous concentrations determined for 1:1 pore water extracts from the Km pH 3.0, 1.0, 0.0, -1.0, and -3.0 diffusion cells.

Sample ID	Depth	pH	Clay	Al	Si	Fe	Ca	Mg	Na	K	SO_4	Cl	NO_3
			(g)	(µmol g^{-1})	(µmol g^{-1})	(µmol g^{-1})	(µmol g^{-1})	(µmol g^{-1})	(µmol g^{-1})	(µmol g^{-1})	(µmol g^{-1})	(µmol g^{-1})	(µmol g^{-1})
KM-DC1-1	1.5	4.49	22.80	1.26	1.16	2.94	4.47	3.51	16.9	1.82	0.62	9.94	323
KM-DC1-2	4.5	6.63	38.95	1.51	2.00	1.21	2.26	2.41	25.3	1.57	0.46	6.29	191
KM-DC1-3	6.0	7.49	43.08	1.63	2.35	1.04	1.94	2.23	37.7	1.86	1.61	14.1	92.2
KM-DC1-4	8.5	7.86	40.11	2.61	0.00	13.2	9.08	6.39	67.1	2.98	0.36	19.1	93.3
KM-DC1-6	14.5	7.72	39.84	2.70	0.00	12.8	9.05	6.26	87.0	3.05	1.06	34.1	73.5
KM-DC1-9	23.5	7.59	42.18	0.80	2.04	0.79	1.35	1.57	57.7	1.75	1.03	36.0	93.7
KM-DC1-11	28.8	7.55	37.38	1.53	2.12	1.20	1.66	1.91	55.1	1.99	0.94	33.1	91.6
KM-DC2-1	1.5	1.40	35.16	7.67	1.41	11.5	3.71	2.95	18.1	2.34	5.30	0.36	33.7
KM-DC2-2	4.0	1.90	39.31	5.06	1.08	15.9	4.45	2.94	19.2	0.89	12.6	0.35	29.0
KM-DC2-3	6.0	3.68	39.77	0.44	0.59	5.96	5.85	3.97	29.7	0.65	23.7	0.12	23.9
KM-DC2-4	8.0	4.64	43.62	0.11	0.10	0.03	4.73	3.47	42.5	1.96	29.4	0.07	17.2
KM-DC2-7	13.8	7.25	39.94	0.74	1.16	0.52	1.62	1.77	62.6	1.70	39.6	65.5	5.38
KM-DC2-10	22.0	7.50	43.95	0.51	1.29	0.42	1.13	1.36	62.9	1.66	47.4	26.5	1.82
KM-DC2-13	28.5	7.45	38.04	0.64	1.59	0.67	1.28	1.46	54.1	1.76	31.2	107	0.97
KM-DC3-1	1.5	0.23	30.55	25.4	3.16	17.7	1.16	4.11	9.26	2.29	207	2.76	0.95
KM-DC3-2	3.8	0.35	37.64	29.2	2.66	34.7	6.78	6.91	18.4	2.85	205	7.33	0.94
KM-DC3-3	5.3	0.55	34.69	24.3	1.60	52.4	17.1	9.05	27.5	2.58	176	13.4	0.46
KM-DC3-5	8.3	1.04	29.37	18.8	1.14	79.0	11.0	11.8	40.2	2.55	153	29.7	0.83
KM-DC3-7	11.3	3.64	41.40	1.13	0.48	31.4	9.26	11.3	59.5	1.78	64.3	52.6	0.36
KM-DC3-9	15.0	4.97	41.76	0.00	0.12	0.00	3.98	4.22	74.6	2.68	22.1	53.7	0.08
KM-DC3-11	20.3	6.88	41.93	0.93	1.29	1.16	2.03	2.30	71.1	2.05	5.15	47.8	72.9
KM-DC3-14	28.8	6.93	41.94	0.95	1.50	1.19	1.95	2.10	55.2	2.05	1.76	34.0	55.5
KM-DC4-1	1.5	-0.60	34.24	50.1	4.37	23.5	0.86	6.40	11.4	4.00	3.51	2.81	307
KM-DC4-3	4.5	-0.55	33.23	68.2	3.14	68.2	10.3	13.7	27.8	5.58	7.39	1.86	370
KM-DC4-5	6.5	-0.05	37.35	62.0	2.35	99.2	15.3	17.0	41.1	5.20	16.6	0.79	357
KM-DC4-7	8.5	0.10	33.91	48.5	1.51	117	13.2	18.3	50.9	4.81	32.4	1.07	615
KM-DC4-9	10.5	0.70	27.76	28.4	0.99	119	12.2	17.7	58.0	3.98	49.3	0.36	197
KM-DC4-12	15.0	4.28	40.63	0.44	0.36	18.3	9.07	11.3	67.2	2.46	70.2	0.16	50.4
KM-DC4-15	21.3	6.44	43.59	0.14	0.53	0.08	1.50	1.87	69.7	1.52	51.7	36.6	7.25
KM-DC4-18	28.8	6.98	40.73	0.21	0.94	0.15	0.76	1.04	49.8	1.29	31.3	45.7	1.18
KM-DC5-1	1.0	-2.30	33.65	76.1	0.71	21.7	0.00	7.78	13.7	6.68	4.20	2.21	926
KM-DC5-3	3.5	-2.10	24.65	151	0.88	88.8	0.91	20.2	32.4	13.9	3.44	2.95	579
KM-DC5-6	6.5	-1.20	39.20	149	2.08	132	5.02	26.1	55.4	11.4	12.9	1.38	369
KM-DC5-9	9.5	-0.27	36.28	73.1	1.91	155	13.2	25.4	69.8	7.04	35.0	0.65	457
KM-DC5-12	12.5	0.55	41.42	35.3	0.91	65.2	11.4	21.1	71.9	4.77	74.2	0.36	260
KM-DC5-15	17.3	4.20	43.10	0.24	0.27	18.8	8.16	11.0	76.7	2.99	96.4	3.97	41.6
KM-DC5-17	21.0	5.43	43.41	0.02	0.07	0.00	1.81	2.44	77.2	1.62	71.9	0.07	10.8
KM-DC5-20	28.8	6.89	40.54	0.43	1.09	0.67	1.55	1.75	57.0	1.75	39.9	63.2	1.36

Appendix 4J: Kc Diffusion cell sub-sample physical parameters, including total sample mass (M_T), sample dry mass (M_D), sample water mass (M_W), dry bulk density (ρ_b), and volumetric water content (θ).

Sample ID	Interval	Depth	Length	V_T	M_T	M_D	M_w	ρ_b	θ
	(cm)	(cm)	(cm)	(cm^3)	(g)	(g)	(g)	(g cm^{-3})	(%)
KC-DC1-1	0.0 - 3.0	1.5	1.53	69.5	155	120	34.9	1.72	0.50
KC-DC1-2	3.0 - 5.0	4.0	1.90	86.6	168	132	36.3	1.52	0.42
KC-DC1-3	5.0 - 7.0	6.0	2.23	101	216	170	45.6	1.68	0.45
KC-DC1-4	7.0 - 10.0	8.5	2.70	123	261	223	37.5	1.81	0.30
KC-DC1-5	10.0 - 13.0	11.5	3.03	138	292	232	60.0	1.68	0.44
KC-DC1-6	13.0 - 16.0	14.5	3.03	138	292	231	60.4	1.68	0.44
KC-DC1-7	16.0 - 18.5	17.3	2.48	113	237	189	48.5	1.67	0.43
KC-DC1-8	18.5 - 22.0	20.3	3.58	163	338	268	69.6	1.65	0.43
KC-DC1-9	22.0 - 25.0	23.5	3.08	140	290	230	59.5	1.64	0.42
KC-DC1-10	25.0 - 27.5	26.3	2.50	107	208	165	42.7	1.54	0.40
KC-DC1-11	27.5 - 30.0	28.8	2.50	107	211	170	40.3	1.59	0.38

Sample ID	Interval	Depth	Length	V_T	M_T	M_D	M_w	ρ_b	θ
	(cm)	(cm)	(cm)	(cm^3)	(g)	(g)	(g)	(g cm^{-3})	(%)
KC-DC2-1	0.0 - 3.0	1.5	2.20	100	199	149	49.7	1.49	0.50
KC-DC2-2	3.0 - 5.0	4.0	2.25	103	207	160	46.7	1.56	0.45
KC-DC2-3	5.0 - 7.0	6.0	2.28	104	221	171	50.3	1.65	0.48
KC-DC2-4	7.0 - 9.0	8.0	1.63	74.1	156	120	35.6	1.62	0.48
KC-DC2-5	9.0 - 10.5	9.8	1.83	83.2	169	130	38.7	1.57	0.47
KC-DC2-6	10.5 - 12.0	11.3	1.55	70.7	150	116	34.6	1.64	0.49
KC-DC2-7	12.0 - 15.0	13.5	2.43	111	232	180	51.6	1.63	0.47
KC-DC2-8	15.0 - 18.0	16.5	3.30	150	306	238	67.8	1.58	0.45
KC-DC2-9	18.0 - 21.0	19.5	2.80	128	265	204	60.7	1.60	0.48
KC-DC2-10	21.0 - 24.5	22.8	3.65	166	343	264	78.9	1.59	0.47
KC-DC2-11	24.5 - 27.0	25.8	2.58	110	215	166	49.1	1.50	0.45
KC-DC2-12	27.0 - 29.5	28.3	2.45	105	207	162	44.8	1.54	0.43

Sample ID	Interval	Depth	Length	V_T	M_T	M_D	M_w	ρ_b	θ
	(cm)	(cm)	(cm)	(cm^3)	(g)	(g)	(g)	(g cm^{-3})	(%)
KC-DC3-1	0.0 - 2.0	1.0	1.40	63.8	141	104	36.6	1.63	0.57
KC-DC3-2	2.0 - 4.0	3.0	1.95	88.9	174	131	43.5	1.47	0.49
KC-DC3-3	4.0 - 6.0	5.0	1.83	83.6	170	131	39.1	1.57	0.47
KC-DC3-4	6.0 - 8.0	7.0	1.73	78.7	172	138	34.4	1.75	0.44
KC-DC3-5	8.0 - 10.0	9.0	2.33	106	225	179	45.6	1.69	0.43
KC-DC3-6	10.0 - 12.0	11.0	1.75	79.8	178	142	36.8	1.77	0.46
KC-DC3-7	12.0 - 14.0	13.0	1.90	86.6	184	145	39.0	1.68	0.45
KC-DC3-8	14.0 - 16.0	15.0	1.88	85.5	183	144	38.7	1.68	0.45
KC-DC3-9	16.0 - 18.0	17.0	2.13	96.9	202	159	42.5	1.64	0.44
KC-DC3-10	18.0 - 21.0	19.5	2.75	125	265	209	55.4	1.67	0.44
KC-DC3-11	21.0 - 25.0	23.0	3.80	173	361	283	77.1	1.64	0.45
KC-DC3-12	25.0 - 27.5	26.3	2.23	95.2	194	152	41.8	1.60	0.44
KC-DC3-13	27.5 - 30.0	28.8	3.00	128	251	199	51.6	1.55	0.40

Appendix 4J: Continued

Sample ID	Interval (cm)	Depth (cm)	Length (cm)	V_T (cm^3)	M_T (g)	M_D (g)	M_w (g)	ρ_b (g cm^{-3})	θ (%)
KC-DC4-1	0.0 - 2.0	1.0	1.08	49.0	114	88.4	25.8	1.80	0.30
KC-DC4-2	2.0 - 3.0	2.5	0.80	36.5	74.0	58.6	15.3	1.61	0.39
KC-DC4-3	3.0 - 4.0	3.5	1.08	49.0	106	84.2	21.4	1.72	0.37
KC-DC4-4	4.0 - 5.0	4.5	1.13	51.3	102	81.8	20.1	1.59	0.47
KC-DC4-5	5.0 - 6.0	5.5	0.90	41.0	98.1	78.8	19.3	1.92	0.36
KC-DC4-6	6.0 - 7.0	6.5	1.07	48.6	96.9	78.2	18.7	1.61	0.46
KC-DC4-7	7.0 - 8.0	7.5	1.08	49.4	98.3	81.7	16.6	1.65	0.42
KC-DC4-8	8.0 - 9.0	8.5	0.95	43.3	90.0	74.3	15.6	1.72	0.40
KC-DC4-9	9.0 - 10.0	9.5	0.83	37.6	81.8	68.2	13.6	1.81	0.38
KC-DC4-10	10.0 - 12.0	11.0	2.22	101	200	165	35.8	1.63	0.43
KC-DC4-11	12.0 - 14.0	13.0	1.68	76.4	157	128	28.8	1.67	0.42
KC-DC4-12	14.0 - 16.0	15.0	2.28	104	211	172	38.8	1.66	0.42
KC-DC4-13	16.0 - 18.0	17.0	2.53	115	232	188	43.8	1.64	0.42
KC-DC4-14	18.0 - 21.0	19.3	2.95	135	276	224	51.9	1.67	0.41
KC-DC4-15	21.0 - 25.0	23.0	3.40	155	323	261	61.9	1.68	0.41
KC-DC4-16	25.0 - 27.5	26.3	2.73	117	226	183	43.4	1.57	0.44
KC-DC4-17	27.5 - 30.0	28.8	2.40	103	217	178	38.3	1.74	0.39

Sample ID	Interval (cm)	Depth (cm)	Length (cm)	V_T (cm^3)	M_T (g)	M_D (g)	M_w (g)	ρ_b (g cm^{-3})	θ (%)
KC-DC5-1	0.0 - 2.0	1.0	1.05	47.9	96.4	76.7	19.7	1.60	0.43
KC-DC5-2	2.0 - 3.0	2.5	1.23	55.9	113	90.6	22.6	1.62	0.44
KC-DC5-3	3.0 - 4.0	3.5	0.88	39.9	80.9	65.9	15.1	1.65	0.42
KC-DC5-4	4.0 - 5.0	4.5	0.95	43.3	89.3	73.3	15.9	1.69	0.37
KC-DC5-5	5.0 - 6.0	5.5	1.00	45.6	96.3	78.6	17.6	1.72	0.42
KC-DC5-6	6.0 - 7.0	6.5	1.00	45.6	98.7	80.1	18.6	1.76	0.40
KC-DC5-7	7.0 - 8.0	7.5	1.03	46.7	99.4	73.1	26.3	1.56	0.49
KC-DC5-8	8.0 - 9.0	8.5	1.00	45.6	97.4	81.1	16.4	1.78	0.41
KC-DC5-9	9.0 - 10.0	9.5	1.05	47.9	97.8	81.5	16.3	1.70	0.41
KC-DC5-10	10.0 - 11.0	10.5	1.13	51.3	103	85.1	17.6	1.66	0.43
KC-DC5-11	11.0 - 12.0	11.5	1.00	45.6	94.5	76.5	17.9	1.68	0.43
KC-DC5-12	12.0 - 14.0	13.0	1.92	87.4	179	146	33.1	1.67	0.40
KC-DC5-13	14.0 - 16.0	15.0	2.05	93.5	197	160	36.8	1.72	0.40
KC-DC5-14	16.0 - 18.0	17.0	2.30	105	214	186	28.6	1.77	0.38
KC-DC5-15	18.0 - 20.0	19.0	2.12	96.5	174	141	32.7	1.47	0.49
KC-DC5-16	20.0 - 22.0	21.0	1.90	86.6	195	158	37.4	1.82	0.37
KC-DC5-17	22.0 - 25.0	23.5	3.12	142	295	239	56.4	1.68	0.40
KC-DC5-18	25.0 - 27.5	26.3	2.20	94.1	186	150	36.2	1.60	0.42
KC-DC5-19	27.5 - 30.0	28.8	2.53	108	215	175	40.5	1.62	0.42

Appendix 4K: Km Diffusion cell sub-sample physical parameters, including total sample mass (M_T), sample dry mass (M_D), sample water mass (M_W), dry bulk density (ρ_b), and volumetric water content (θ).

Sample ID	Interval	Depth	Length	V_T	M_T	M_D	M_w	ρ_b	θ
	(cm)	(cm)	(cm)	(cm^3)	(g)	(g)	(g)	(g/cm^3)	(%)
KM-DC1-1	0.0 - 3.0	1.5	1.15	52.4	115	92.2	22.5	1.76	0.43
KM-DC1-2	3.0 - 5.0	4.5	1.98	90.1	198	160	37.7	1.78	0.42
KM-DC1-3	5.0 - 7.0	6.0	1.75	79.8	178	144	33.4	1.81	0.42
KM-DC1-4	7.0 - 10.0	8.5	3.15	144	307	250	57.4	1.74	0.40
KM-DC1-5	10.0 - 13.0	11.5	2.85	130	290	235	54.3	1.81	0.42
KM-DC1-6	13.0 - 16.0	14.5	2.65	121	258	209	49.0	1.73	0.41
KM-DC1-7	16.0 - 18.5	17.3	2.50	114	255	207	47.9	1.82	0.42
KM-DC1-8	18.5 - 22.0	20.3	3.30	150	325	264	60.7	1.76	0.40
KM-DC1-9	22.0 - 25.0	23.5	2.80	128	253	205	47.5	1.61	0.37
KM-DC1-10	25.0 - 27.5	26.3	2.35	101	212	172	40.0	1.71	0.40
KM-DC1-11	27.5 - 30.0	28.8	2.50	107	204	168	36.0	1.57	0.34

Sample ID	Interval	Depth	Length	V_T	M_T	M_D	M_w	ρ_b	θ
	(cm)	(cm)	(cm)	(cm^3)	(g)	(g)	(g)	(g/cm^3)	(%)
KM-DC2-1	0.0 - 3.0	1.5	1.35	61.6	127	98.5	28.8	1.60	0.47
KM-DC2-2	3.0 - 5.0	4.0	2.00	91.2	179	140	38.8	1.54	0.43
KM-DC2-3	5.0 - 7.0	6.0	2.00	91.2	181	142	38.6	1.56	0.42
KM-DC2-4	7.0 - 9.0	8.0	1.93	87.8	179	142	37.9	1.61	0.43
KM-DC2-5	9.0 - 10.5	9.8	1.95	88.9	162	132	30.2	1.49	0.34
KM-DC2-6	10.5 - 12.5	11.5	1.98	90.1	184	145	39.3	1.61	0.44
KM-DC2-7	12.5 - 15.0	13.8	2.50	114	236	186	49.5	1.63	0.43
KM-DC2-8	15.0 - 18.0	16.5	3.05	139	286	226	59.7	1.63	0.43
KM-DC2-9	18.0 - 21.0	19.5	3.00	137	296	233	63.0	1.70	0.46
KM-DC2-10	21.0 - 23.0	22.0	2.05	93.5	186	145	40.1	1.56	0.43
KM-DC2-11	23.0 - 25.0	24.0	1.55	70.7	151	117	33.9	1.66	0.48
KM-DC2-12	25.0 - 27.5	26.3	2.30	98.4	208	162	46.4	1.65	0.47
KM-DC2-13	27.5 - 29.5	28.5	2.05	87.7	181	144	36.2	1.65	0.41

Sample ID	Interval	Depth	Length	V_T	M_T	M_D	M_w	ρ_b	θ
	(cm)	(cm)	(cm)	(cm^3)	(g)	(g)	(g)	(g/cm^3)	(%)
KM-DC3-1	0.0 - 3.0	1.5	1.40	63.8	115	90.2	25.0	1.41	0.50
KM-DC3-2	3.0 - 4.5	3.8	1.33	60.4	129	103	26.0	1.70	0.40
KM-DC3-3	4.5 - 6.0	5.3	1.60	73.0	144	116	28.3	1.58	0.43
KM-DC3-4	6.0 - 7.5	6.8	1.55	70.7	149	119	29.5	1.69	0.40
KM-DC3-5	7.5 - 9.0	8.3	1.43	65.0	133	107	26.4	1.64	0.40
KM-DC3-6	9.0 - 10.5	9.8	1.65	75.2	155	124	30.2	1.65	0.41
KM-DC3-7	10.5 - 12.0	11.3	1.75	79.8	156	126	30.4	1.58	0.42
KM-DC3-8	12.0 - 14.0	13.0	1.75	79.8	161	129	32.1	1.62	0.42
KM-DC3-9	14.0 - 16.0	15.0	2.28	104	210	167	42.8	1.61	0.41
KM-DC3-10	16.0 - 18.5	17.3	2.75	125	257	205	51.6	1.63	0.41
KM-DC3-11	18.5 - 22.0	20.3	3.00	137	285	227	57.9	1.66	0.40
KM-DC3-12	22.0 - 25.0	23.5	3.55	162	324	257	66.8	1.59	0.41
KM-DC3-13	25.0 - 27.5	26.3	2.43	104	201	160	41.6	1.54	0.44
KM-DC3-14	27.5 - 30.0	28.8	2.80	120	192	153	39.0	1.28	0.54

Appendix 4K: Continued

Sample ID	Interval (cm)	Depth (cm)	Length (cm)	V_T (cm^3)	M_T (g)	M_D (g)	M_w (g)	ρ_b (g/cm^3)	θ (%)
KM-DC4-1	0.0 - 3.0	1.5	1.50	68.4	143	117	26.8	1.70	0.36
KM-DC4-2	3.0 - 4.0	3.5	1.00	45.6	98.7	80.7	17.9	1.77	0.35
KM-DC4-3	4.0 - 5.0	4.5	0.95	43.3	92.2	76.2	16.0	1.76	0.35
KM-DC4-4	5.0 - 6.0	5.5	1.05	47.9	98.4	81.3	17.1	1.70	0.38
KM-DC4-5	6.0 - 7.0	6.5	1.05	47.9	96.1	79.4	16.7	1.66	0.42
KM-DC4-6	7.0 - 8.0	7.5	0.90	41.0	92.9	76.8	16.1	1.87	0.37
KM-DC4-7	8.0 - 9.0	8.5	0.73	33.4	72.3	59.8	12.5	1.79	0.39
KM-DC4-8	9.0 - 10.0	9.5	1.15	52.4	103	85.4	17.3	1.63	0.44
KM-DC4-9	10.0 - 11.0	10.5	1.15	52.4	106	87.5	18.6	1.67	0.42
KM-DC4-10	11.0 - 12.0	11.5	1.07	48.6	104	85.5	18.5	1.76	0.37
KM-DC4-11	12.0 - 14.0	13.0	1.98	90.1	166	137	29.3	1.52	0.48
KM-DC4-12	14.0 - 16.0	15.0	2.08	94.6	195	161	34.4	1.70	0.42
KM-DC4-13	16.0 - 18.0	17.0	1.98	90.1	185	152	33.2	1.69	0.41
KM-DC4-14	18.0 - 20.0	19.0	2.00	91.2	185	152	33.1	1.66	0.42
KM-DC4-15	20.0 - 22.5	21.3	2.60	119	239	194	44.4	1.64	0.43
KM-DC4-16	22.5 - 25.0	23.8	2.33	106	223	182	41.1	1.71	0.40
KM-DC4-17	25.0 - 27.5	26.3	2.55	109	204	166	37.8	1.52	0.47
KM-DC4-18	27.5 - 30.0	28.8	2.35	101	206	170	36.1	1.69	0.40

Sample ID	Interval (cm)	Depth (cm)	Length (cm)	V_T (cm^3)	M_T (g)	M_D (g)	M_w (g)	ρ_b (g/cm^3)	θ (%)
KM-DC5-1	0.0 - 2.0	1.0	1.15	52.4	116	92.7	23.0	1.77	0.32
KM-DC5-2	2.0 - 3.0	2.5	1.03	46.7	102	82.3	19.4	1.76	0.34
KM-DC5-3	3.0 - 4.0	3.5	1.00	45.6	93.0	87.2	5.8	1.91	0.27
KM-DC5-4	4.0 - 5.0	4.5	0.90	41.0	94.2	79.3	14.9	1.93	0.27
KM-DC5-5	5.0 - 6.0	5.5	0.93	42.2	97.7	81.5	16.2	1.93	0.29
KM-DC5-6	6.0 - 7.0	6.5	1.00	45.6	98.9	82.7	16.2	1.81	0.33
KM-DC5-7	7.0 - 8.0	7.5	1.05	47.9	97.5	81.6	16.0	1.70	0.38
KM-DC5-8	8.0 - 9.0	8.5	1.00	45.6	95.0	79.0	16.0	1.73	0.35
KM-DC5-9	9.0 - 10.0	9.5	1.05	47.9	93.4	78.0	15.4	1.63	0.40
KM-DC5-10	10.0 - 11.0	10.5	1.00	45.6	90.7	75.3	15.4	1.65	0.40
KM-DC5-11	11.0 - 12.0	11.5	1.05	47.9	93.3	76.9	16.4	1.61	0.39
KM-DC5-12	12.0 - 13.0	12.5	1.15	52.4	101	83.3	17.9	1.59	0.41
KM-DC5-13	13.0 - 14.0	13.5	0.95	43.3	83.7	68.7	15.0	1.59	0.40
KM-DC5-14	14.0 - 16.0	15.0	2.13	96.9	189	155	33.9	1.60	0.39
KM-DC5-15	16.0 - 18.5	17.3	2.25	103	204	168	36.0	1.63	0.39
KM-DC5-16	18.5 - 20.0	19.8	1.55	70.7	140	115	25.1	1.63	0.41
KM-DC5-17	20.0 - 22.0	21.0	2.10	95.8	188	153	34.2	1.60	0.42
KM-DC5-18	22.0 - 25.0	23.5	3.00	137	280	227	52.9	1.66	0.40
KM-DC5-19	25.0 - 27.5	26.3	2.20	94	177	143	34.0	1.51	0.45
KM-DC5-20	27.5 - 30.0	28.8	2.10	90	179	145	34.0	1.61	0.42

Appendix 4L: Kc absorption isotherm data calculated from the pH 5.0, 3.0, and 1.0 batch experiments results.

Kc Batch Test	Time	pH	Clay	H_2SO_4 Added	NaOH Added	H_2SO_4 Consumed	H+ Consumed	S (H^+ consumed)	C (H^+ in solution)	Average S	Average C
	(d)		(g)	(mmol)	(mmol)	(mmol)	(mmol)	($g\ g^{-1}$)	($g\ m^{-3}$)	($g\ g^{-1}$)	($g\ m^{-3}$)
pH 5.0	14	4.60	5.08	2.30	0.00	2.30	4.61	9.15E-04	2.53E-02	1.03E-03	2.45E-02
	90	4.77	5.01	2.25	0.00	2.25	4.50	9.06E-04	1.71E-02		
	180	4.81	5.10	2.35	0.00	2.35	4.69	9.27E-04	1.56E-02		
	365	4.40	5.08	4.21	1.46	3.48	6.97	1.38E-03	4.01E-02		
pH 3.0	14	3.05	5.05	2.27	0.00	2.27	4.54	9.06E-04	0.90	1.03E-03	9.77E-01
	14	3.03	5.11	2.49	0.00	2.49	4.98	9.82E-04	0.94		
	90	3.01	5.05	3.03	0.75	2.66	5.31	1.06E-03	0.98		
	180	2.98	5.16	2.90	0.86	2.47	4.94	9.66E-04	1.06		
	365	3.00	5.00	3.41	0.77	3.02	6.05	1.22E-03	1.01		
pH 1.0	14	1.02	5.08	7.71	0.00	7.71	15.42	3.06E-03	96.3	3.14E-03	92.7
	14	1.00	5.01	7.20	0.00	7.20	14.40	2.90E-03	100.8		
	90	1.02	5.02	8.67	0.00	8.67	17.34	3.48E-03	96.3		
	180	1.04	5.08	7.45	0.00	7.45	14.90	2.96E-03	91.9		
	365	1.11	5.05	8.23	0.00	8.23	16.45	3.28E-03	78.2		

Appendix 4M: Km absorption isotherm data calculated from the pH 5.0, 3.0, and 1.0 batch experiments results.

Km Batch Test	Time	pH	Clay	H_2SO_4 Added	NaOH Added	H_2SO_4 Consumed	H+ Consumed	S (H^+ consumed)	C (H^+ in solution)	Average S	Average C
	(d)		(g)	(mmol)	(mmol)	(mmol)	(mmol)	(g g^{-1})	(g m^{-3})	(g g^{-1})	(g m^{-3})
	14	5.00	5.03	0.32	0.00	0.32	0.64	1.28E-04	1.01E-02		
	14	4.99	5.13	0.35	0.00	0.35	0.69	1.36E-04	1.03E-02		
pH 5.0	**90**	4.85	5.16	0.64	0.00	0.64	1.27	2.49E-04	1.42E-02	1.74E-04	1.25E-02
	180	4.82	5.02	0.57	0.16	0.49	0.99	1.98E-04	1.53E-02		
	365	4.90	5.10	0.44	0.08	0.40	0.80	1.59E-04	1.27E-02		
	14	2.55	5.02	1.48	0.00	1.48	2.96	5.94E-04	2.84E+00		
	14	2.99	5.03	1.55	0.00	1.55	3.11	6.22E-04	1.03E+00		
pH 3.0	**90**	3.05	5.01	1.68	1.38	0.99	1.98	3.99E-04	8.98E-01	4.78E-04	1.34E+00
	180	3.00	5.21	1.60	1.24	0.98	1.95	3.78E-04	1.01E+00		
	365	3.05	5.01	1.57	1.16	0.99	1.97	3.97E-04	8.98E-01		
	14	1.00	5.15	3.86	0.00	3.86	7.71	1.51E-03	1.01E+02		
	14	1.00	5.15	3.86	0.00	3.86	7.71	1.51E-03	1.01E+02		
pH 1.0	**90**	1.01	5.03	4.61	0.00	4.61	9.21	1.85E-03	9.85E+01	1.55E-03	96.2
	180	1.00	5.06	4.06	0.00	4.06	8.13	1.62E-03	1.01E+02		
	365	1.10	5.10	3.21	0.00	3.21	6.43	1.27E-03	8.01E+01		

Appendix 4N: Measured H^+ concentrations (g L^{-1}) for the Kc pH 1.0, -1.0, and -3.0 diffusion cells.

Depth	Kc_1
(mm)	(g L^{-1})
15	6.36E-03
40	6.66E-07
60	1.99E-07
80	1.75E-07
97.5	1.53E-07
112.5	1.53E-07
135	1.69E-07
165	1.60E-07
195	1.28E-07
227.5	1.41E-07
257.5	1.67E-07
282.5	8.10E-08
Reservior	9.65E-02

Depth	Kc_{-1}
(mm)	(g L^{-1})
5	3.68
25	3.52
35	2.26
45	1.64
55	0.69
65	7.41E-02
75	1.20E-04
85	6.92E-05
95	6.76E-06
110	2.72E-06
130	2.09E-06
150	5.25E-07
172.5	5.19E-07
200	4.73E-07
232.5	7.24E-07
262.5	5.75E-07
287.5	7.33E-07
Reservior	4.69

Depth	Kc_{-3}
(mm)	(g L^{-1})
10	10.34
25	10.00
35	10.00
45	5.83
55	5.83
65	1.89
75	4.07E-02
85	6.31E-05
95	1.10E-05
105	2.88E-06
115	4.27E-07
130	4.52E-07
150	2.29E-07
170	2.99E-07
190	1.51E-07
210	2.11E-07
235	2.85E-07
262.5	1.93E-07
287.5	1.72E-07
Reservior	10.42

Appendix 4O: Measured H^+ concentrations (g L^{-1}) for the Km pH 1.0, -1.0, and -3.0 diffusion cells.

Depth	Kc_1
(mm)	(g L^{-1})
15.0	4.06E-02
40.0	1.28E-02
60.0	2.13E-04
80.0	2.34E-05
97.5	4.40E-06
115.0	4.50E-08
137.5	5.73E-08
165.0	2.39E-07
195.0	3.83E-08
220.0	3.22E-08
240.0	3.19E-08
262.5	3.11E-08
285.0	3.58E-08
Reservior	9.65E-02

Depth	Kc_{-1}
(mm)	(g L^{-1})
5	3.55
35	3.35
45	3.21
55	2.54
65	1.77
75	1.44
85	1.44
95	0.71
105	0.48
115	8.38E-02
130	1.79E-03
150	5.29E-05
170	2.47E-05
190	1.03E-05
212.5	3.66E-07
237.5	1.39E-07
262.5	1.33E-07
287.5	1.06E-07
Reservior	4.69

Depth	Kc_{-3}
(mm)	(g L^{-1})
10	8.79
25	8.13
35	8.04
45	7.74
55	6.49
65	5.48
75	4.60
85	3.18
95	2.40
105	1.69
115	0.81
125	0.64
135	9.12E-02
150	3.39E-03
172.5	6.31E-05
192.5	3.31E-05
210	3.72E-06
235	3.55E-07
262.5	1.51E-07
287.5	1.29E-07
Reservior	10.42

Appendix 4Q: Modeled H^+ concentrations (g L^{-1}) for the Kc pH 1.0, -1.0, and -3.0 diffusion cells assuming no absorption.

Depth	Kc_1	Kc_{-1}	Kc_{-3}	Depth	Kc_1	Kc_{-1}	Kc_{-3}
(mm)	(g L^{-1})	(g L^{-1})	(g L^{-1})	(mm)	(g L^{-1})	(g L^{-1})	(g L^{-1})
0.0	9.65E-02	4.69	9.88	94.7	9.41E-02	4.57	9.95
1.9	9.64E-02	4.69	9.88	96.7	9.40E-02	4.57	9.96
3.9	9.64E-02	4.68	9.88	98.6	9.40E-02	4.57	9.96
5.8	9.63E-02	4.68	9.88	100.5	9.39E-02	4.56	9.96
7.7	9.63E-02	4.68	9.88	102.5	9.39E-02	4.56	9.96
9.7	9.62E-02	4.68	9.88	104.4	9.38E-02	4.56	9.97
11.6	9.62E-02	4.67	9.88	106.3	9.38E-02	4.56	9.97
13.5	9.61E-02	4.67	9.88	108.3	9.37E-02	4.56	9.97
15.5	9.61E-02	4.67	9.88	110.2	9.37E-02	4.55	9.98
17.4	9.60E-02	4.67	9.89	112.1	9.37E-02	4.55	9.98
19.3	9.60E-02	4.66	9.89	114.1	9.36E-02	4.55	9.98
21.3	9.59E-02	4.66	9.89	116.0	9.36E-02	4.55	9.99
23.2	9.59E-02	4.66	9.89	117.9	9.35E-02	4.55	9.99
25.1	9.58E-02	4.66	9.89	119.9	9.35E-02	4.54	9.99
27.1	9.58E-02	4.65	9.89	121.8	9.35E-02	4.54	10.00
29.0	9.57E-02	4.65	9.89	123.7	9.34E-02	4.54	10.00
30.9	9.57E-02	4.65	9.89	125.7	9.34E-02	4.54	10.00
32.9	9.56E-02	4.65	9.89	127.6	9.33E-02	4.54	10.01
34.8	9.56E-02	4.64	9.89	129.5	9.33E-02	4.53	10.01
36.7	9.55E-02	4.64	9.89	131.5	9.33E-02	4.53	10.01
38.7	9.55E-02	4.64	9.89	133.4	9.32E-02	4.53	10.02
40.6	9.54E-02	4.64	9.90	135.3	9.32E-02	4.53	10.02
42.5	9.54E-02	4.63	9.90	137.3	9.31E-02	4.53	10.02
44.5	9.53E-02	4.63	9.90	139.2	9.31E-02	4.52	10.03
46.4	9.53E-02	4.63	9.90	141.1	9.31E-02	4.52	10.03
48.3	9.52E-02	4.63	9.90	143.1	9.30E-02	4.52	10.04
50.3	9.52E-02	4.63	9.90	145.0	9.30E-02	4.52	10.04
52.2	9.51E-02	4.62	9.90	146.9	9.29E-02	4.52	10.04
54.1	9.51E-02	4.62	9.91	148.9	9.29E-02	4.52	10.05
56.1	9.50E-02	4.62	9.91	150.8	9.29E-02	4.51	10.05
58.0	9.50E-02	4.62	9.91	152.7	9.28E-02	4.51	10.06
59.9	9.49E-02	4.61	9.91	154.7	9.28E-02	4.51	10.06
61.9	9.49E-02	4.61	9.91	156.6	9.28E-02	4.51	10.06
63.8	9.48E-02	4.61	9.91	158.5	9.27E-02	4.51	10.07
65.7	9.48E-02	4.61	9.92	160.5	9.27E-02	4.51	10.07
67.7	9.47E-02	4.60	9.92	162.4	9.27E-02	4.50	10.08
69.6	9.47E-02	4.60	9.92	164.3	9.26E-02	4.50	10.08
71.5	9.46E-02	4.60	9.92	166.3	9.26E-02	4.50	10.09
73.5	9.46E-02	4.60	9.93	168.2	9.26E-02	4.50	10.09
75.4	9.45E-02	4.59	9.93	170.1	9.25E-02	4.50	10.10
77.3	9.45E-02	4.59	9.93	172.1	9.25E-02	4.50	10.10
79.3	9.44E-02	4.59	9.93	174.0	9.25E-02	4.49	10.10
81.2	9.44E-02	4.59	9.93	175.9	9.24E-02	4.49	10.11
83.1	9.43E-02	4.58	9.94	177.9	9.24E-02	4.49	10.11
85.1	9.43E-02	4.58	9.94	179.8	9.24E-02	4.49	10.12
87.0	9.42E-02	4.58	9.94	181.7	9.24E-02	4.49	10.12
88.9	9.42E-02	4.58	9.94	183.7	9.23E-02	4.49	10.13
90.9	9.42E-02	4.58	9.95	185.6	9.23E-02	4.49	10.13
92.8	9.41E-02	4.57	9.95	187.5	9.23E-02	4.48	10.14

Appendix 4Q: Continued

Depth (mm)	Kc_1 ($g\ L^{-1}$)	Kc_{-1} ($g\ L^{-1}$)	Kc_{-3} ($g\ L^{-1}$)
189.5	9.22E-02	4.48	10.14
191.4	9.22E-02	4.48	10.15
193.3	9.22E-02	4.48	10.15
195.3	9.22E-02	4.48	10.16
197.2	9.21E-02	4.48	10.16
199.1	9.21E-02	4.48	10.17
201.1	9.21E-02	4.48	10.17
203.0	9.21E-02	4.47	10.18
204.9	9.20E-02	4.47	10.18
206.9	9.20E-02	4.47	10.19
208.8	9.20E-02	4.47	10.19
210.7	9.20E-02	4.47	10.20
212.7	9.20E-02	4.47	10.20
214.6	9.19E-02	4.47	10.21
216.5	9.19E-02	4.47	10.21
218.5	9.19E-02	4.47	10.22
220.4	9.19E-02	4.47	10.22
222.3	9.19E-02	4.46	10.23
224.3	9.18E-02	4.46	10.23
226.2	9.18E-02	4.46	10.24
228.1	9.18E-02	4.46	10.24
230.1	9.18E-02	4.46	10.25
232.0	9.18E-02	4.46	10.25
233.9	9.18E-02	4.46	10.26
235.9	9.17E-02	4.46	10.26
237.8	9.17E-02	4.46	10.27
239.7	9.17E-02	4.46	10.28
241.7	9.17E-02	4.46	10.28
243.6	9.17E-02	4.46	10.29
245.5	9.17E-02	4.46	10.29
247.5	9.17E-02	4.45	10.30
249.4	9.16E-02	4.45	10.30
251.3	9.16E-02	4.45	10.31
253.3	9.16E-02	4.45	10.31
255.2	9.16E-02	4.45	10.32
257.1	9.16E-02	4.45	10.32
259.1	9.16E-02	4.45	10.33
261.0	9.16E-02	4.45	10.34
262.9	9.16E-02	4.45	10.34
264.9	9.16E-02	4.45	10.35
266.8	9.16E-02	4.45	10.35
268.7	9.16E-02	4.45	10.36
270.7	9.16E-02	4.45	10.36
272.6	9.15E-02	4.45	10.37
274.5	9.15E-02	4.45	10.38
276.5	9.15E-02	4.45	10.38
278.4	9.15E-02	4.45	10.39
280.3	9.15E-02	4.45	10.39
282.3	9.15E-02	4.45	10.40
284.2	9.15E-02	4.45	10.40
286.1	9.15E-02	4.45	10.41
288.1	9.15E-02	4.45	10.41
290.0	9.15E-02	4.45	10.42

Appendix 4R: Modeled H^+ concentrations (g L^{-1}) for the Km pH 1.0, -1.0, and -3.0 diffusion cells assuming no absorption.

Depth	Kc_1	Kc_{-1}	Kc_{-3}	Depth	Kc_1	Kc_{-1}	Kc_{-3}
(mm)	(g L^{-1})	(g L^{-1})	(g L^{-1})	(mm)	(g L^{-1})	(g L^{-1})	(g L^{-1})
0.0	9.65E-02	4.69	10.42	94.7	8.93E-02	4.34	9.64
1.9	9.63E-02	4.68	10.40	96.7	8.92E-02	4.33	9.63
3.9	9.62E-02	4.68	10.39	98.6	8.90E-02	4.33	9.61
5.8	9.60E-02	4.67	10.37	100.5	8.89E-02	4.32	9.60
7.7	9.59E-02	4.66	10.35	102.5	8.88E-02	4.31	9.58
9.7	9.57E-02	4.65	10.34	104.4	8.86E-02	4.31	9.57
11.6	9.56E-02	4.65	10.32	106.3	8.85E-02	4.30	9.56
13.5	9.54E-02	4.64	10.30	108.3	8.84E-02	4.29	9.54
15.5	9.53E-02	4.63	10.29	110.2	8.82E-02	4.29	9.53
17.4	9.51E-02	4.62	10.27	112.1	8.81E-02	4.28	9.51
19.3	9.50E-02	4.62	10.25	114.1	8.80E-02	4.28	9.50
21.3	9.48E-02	4.61	10.24	116.0	8.79E-02	4.27	9.49
23.2	9.47E-02	4.60	10.22	117.9	8.77E-02	4.26	9.47
25.1	9.45E-02	4.59	10.20	119.9	8.76E-02	4.26	9.46
27.1	9.44E-02	4.59	10.19	121.8	8.75E-02	4.25	9.45
29.0	9.42E-02	4.58	10.17	123.7	8.74E-02	4.25	9.43
30.9	9.41E-02	4.57	10.16	125.7	8.73E-02	4.24	9.42
32.9	9.39E-02	4.56	10.14	127.6	8.71E-02	4.23	9.41
34.8	9.37E-02	4.56	10.12	129.5	8.70E-02	4.23	9.40
36.7	9.36E-02	4.55	10.11	131.5	8.69E-02	4.22	9.38
38.7	9.34E-02	4.54	10.09	133.4	8.68E-02	4.22	9.37
40.6	9.33E-02	4.53	10.07	135.3	8.67E-02	4.21	9.36
42.5	9.31E-02	4.53	10.06	137.3	8.66E-02	4.21	9.35
44.5	9.30E-02	4.52	10.04	139.2	8.64E-02	4.20	9.33
46.4	9.28E-02	4.51	10.03	141.1	8.63E-02	4.20	9.32
48.3	9.27E-02	4.51	10.01	143.1	8.62E-02	4.19	9.31
50.3	9.26E-02	4.50	9.99	145.0	8.61E-02	4.19	9.30
52.2	9.24E-02	4.49	9.98	146.9	8.60E-02	4.18	9.29
54.1	9.23E-02	4.48	9.96	148.9	8.59E-02	4.17	9.28
56.1	9.21E-02	4.48	9.95	150.8	8.58E-02	4.17	9.26
58.0	9.20E-02	4.47	9.93	152.7	8.57E-02	4.16	9.25
59.9	9.18E-02	4.46	9.91	154.7	8.56E-02	4.16	9.24
61.9	9.17E-02	4.46	9.90	156.6	8.55E-02	4.15	9.23
63.8	9.15E-02	4.45	9.88	158.5	8.54E-02	4.15	9.22
65.7	9.14E-02	4.44	9.87	160.5	8.53E-02	4.14	9.21
67.7	9.12E-02	4.43	9.85	162.4	8.52E-02	4.14	9.20
69.6	9.11E-02	4.43	9.84	164.3	8.51E-02	4.14	9.19
71.5	9.10E-02	4.42	9.82	166.3	8.50E-02	4.13	9.18
73.5	9.08E-02	4.41	9.81	168.2	8.49E-02	4.13	9.17
75.4	9.07E-02	4.41	9.79	170.1	8.48E-02	4.12	9.16
77.3	9.05E-02	4.40	9.77	172.1	8.47E-02	4.12	9.15
79.3	9.04E-02	4.39	9.76	174.0	8.46E-02	4.11	9.14
81.2	9.02E-02	4.39	9.74	175.9	8.45E-02	4.11	9.13
83.1	9.01E-02	4.38	9.73	177.9	8.44E-02	4.10	9.12
85.1	9.00E-02	4.37	9.71	179.8	8.44E-02	4.10	9.11
87.0	8.98E-02	4.37	9.70	181.7	8.43E-02	4.10	9.10
88.9	8.97E-02	4.36	9.69	183.7	8.42E-02	4.09	9.09
90.9	8.96E-02	4.35	9.67	185.6	8.41E-02	4.09	9.08
92.8	8.94E-02	4.35	9.66	187.5	8.40E-02	4.08	9.07

Appendix 4R: Continued

Depth	Kc_1	Kc_{-1}	Kc_{-3}
(mm)	(g L^{-1})	(g L^{-1})	(g L^{-1})
189.5	8.39E-02	4.08	9.06
191.4	8.39E-02	4.08	9.05
193.3	8.38E-02	4.07	9.05
195.3	8.37E-02	4.07	9.04
197.2	8.36E-02	4.06	9.03
199.1	8.36E-02	4.06	9.02
201.1	8.35E-02	4.06	9.01
203.0	8.34E-02	4.05	9.01
204.9	8.33E-02	4.05	9.00
206.9	8.33E-02	4.05	8.99
208.8	8.32E-02	4.04	8.98
210.7	8.31E-02	4.04	8.98
212.7	8.31E-02	4.04	8.97
214.6	8.30E-02	4.03	8.96
216.5	8.30E-02	4.03	8.96
218.5	8.29E-02	4.03	8.95
220.4	8.28E-02	4.03	8.95
222.3	8.28E-02	4.02	8.94
224.3	8.27E-02	4.02	8.93
226.2	8.27E-02	4.02	8.93
228.1	8.26E-02	4.02	8.92
230.1	8.26E-02	4.01	8.92
232.0	8.25E-02	4.01	8.91
233.9	8.25E-02	4.01	8.91
235.9	8.24E-02	4.01	8.90
237.8	8.24E-02	4.00	8.90
239.7	8.24E-02	4.00	8.89
241.7	8.23E-02	4.00	8.89
243.6	8.23E-02	4.00	8.88
245.5	8.22E-02	4.00	8.88
247.5	8.22E-02	4.00	8.88
249.4	8.22E-02	3.99	8.87
251.3	8.21E-02	3.99	8.87
253.3	8.21E-02	3.99	8.87
255.2	8.21E-02	3.99	8.86
257.1	8.20E-02	3.99	8.86
259.1	8.20E-02	3.99	8.86
261.0	8.20E-02	3.98	8.85
262.9	8.20E-02	3.98	8.85
264.9	8.19E-02	3.98	8.85
266.8	8.19E-02	3.98	8.85
268.7	8.19E-02	3.98	8.84
270.7	8.19E-02	3.98	8.84
272.6	8.19E-02	3.98	8.84
274.5	8.19E-02	3.98	8.84
276.5	8.19E-02	3.98	8.84
278.4	8.18E-02	3.98	8.84
280.3	8.18E-02	3.98	8.84
282.3	8.18E-02	3.98	8.84
284.2	8.18E-02	3.98	8.83
286.1	8.18E-02	3.98	8.83
288.1	8.18E-02	3.98	8.83
290.0	8.18E-02	3.98	8.83

Appendix 4S: Modeled H^+ concentrations (g L^{-1}) for the Kc pH 1.0, -1.0, and -3.0 diffusion cells assuming non-linear absorption.

Depth	Kc_1	Kc_{-1}	Kc_{-3}	Depth	Kc_1	Kc_{-1}	Kc_{-3}
(mm)	(g L^{-1})	(g L^{-1})	(g L^{-1})	(mm)	(g L^{-1})	(g L^{-1})	(g L^{-1})
0.0	9.65E-02	4.69	10.42	112.1	1.43E-07	3.08	9.31
1.9	9.25E-02	4.66	10.40	114.1	1.43E-07	3.05	9.29
3.9	8.85E-02	4.63	10.38	116.0	1.43E-07	3.03	9.27
5.8	8.45E-02	4.60	10.36	117.9	1.43E-07	3.00	9.26
7.7	8.05E-02	4.57	10.34	119.9	1.43E-07	2.98	9.24
9.7	7.66E-02	4.55	10.32	121.8	1.43E-07	2.95	9.23
11.6	7.26E-02	4.52	10.30	123.7	1.43E-07	2.93	9.21
13.5	6.86E-02	4.49	10.28	125.7	1.43E-07	2.90	9.19
15.5	6.47E-02	4.46	10.26	127.6	1.43E-07	2.88	9.18
17.4	6.07E-02	4.43	10.24	129.5	1.43E-07	2.85	9.16
19.3	5.68E-02	4.40	10.22	131.5	1.43E-07	2.83	9.15
21.3	5.29E-02	4.37	10.20	133.4	1.43E-07	2.81	9.13
23.2	4.90E-02	4.34	10.18	135.3	1.43E-07	2.78	9.12
25.1	4.52E-02	4.32	10.16	137.3	1.43E-07	2.76	9.10
27.1	4.13E-02	4.29	10.14	139.2	1.43E-07	2.73	9.09
29.0	3.75E-02	4.26	10.12	141.1	1.43E-07	2.71	9.07
30.9	3.38E-02	4.23	10.10	143.1	1.43E-07	2.69	9.06
32.9	3.00E-02	4.20	10.08	145.0	1.43E-07	2.66	9.04
34.8	2.64E-02	4.17	10.06	146.9	1.43E-07	2.64	9.03
36.7	2.28E-02	4.14	10.04	148.9	1.43E-07	2.62	9.01
38.7	1.92E-02	4.12	10.02	150.8	1.43E-07	2.60	9.00
40.6	1.58E-02	4.09	10.00	152.7	1.43E-07	2.57	8.98
42.5	1.24E-02	4.06	9.98	154.7	1.43E-07	2.55	8.97
44.5	9.23E-03	4.03	9.96	156.6	1.43E-07	2.53	8.96
46.4	6.18E-03	4.00	9.94	158.5	1.43E-07	2.51	8.94
48.3	3.38E-03	3.97	9.92	160.5	1.43E-07	2.49	8.93
50.3	1.04E-03	3.95	9.90	162.4	1.43E-07	2.46	8.92
52.2	1.71E-04	3.92	9.88	164.3	1.43E-07	2.44	8.90
54.1	2.80E-05	3.89	9.86	166.3	1.43E-07	2.42	8.89
56.1	4.66E-06	3.86	9.84	168.2	1.43E-07	2.40	8.88
58.0	8.76E-07	3.83	9.82	170.1	1.43E-07	2.38	8.87
59.9	2.61E-07	3.81	9.80	172.1	1.43E-07	2.36	8.85
61.9	1.62E-07	3.78	9.78	174.0	1.43E-07	2.34	8.84
63.8	1.46E-07	3.75	9.76	175.9	1.43E-07	2.32	8.83
65.7	1.43E-07	3.72	9.74	177.9	1.43E-07	2.30	8.82
67.7	1.43E-07	3.69	9.72	179.8	1.43E-07	2.28	8.81
69.6	1.43E-07	3.67	9.70	181.7	1.43E-07	2.26	8.80
71.5	1.43E-07	3.64	9.68	183.7	1.43E-07	2.24	8.78
73.5	1.43E-07	3.61	9.67	185.6	1.43E-07	2.22	8.77
75.4	1.43E-07	3.58	9.65	187.5	1.43E-07	2.20	8.76
77.3	1.43E-07	3.56	9.63	189.5	1.43E-07	2.18	8.75
79.3	1.43E-07	3.53	9.61	191.4	1.43E-07	2.17	8.74
81.2	1.43E-07	3.50	9.59	193.3	1.43E-07	2.15	8.73
83.1	1.43E-07	3.47	9.57	195.3	1.43E-07	2.13	8.72
85.1	1.43E-07	3.45	9.55	197.2	1.43E-07	2.11	8.71
87.0	1.43E-07	3.42	9.54	199.1	1.43E-07	2.10	8.70
88.9	1.43E-07	3.39	9.52	201.1	1.43E-07	2.08	8.69
90.9	1.43E-07	3.37	9.50	203.0	1.43E-07	2.06	8.68
92.8	1.43E-07	3.34	9.48	204.9	1.43E-07	2.05	8.67
94.7	1.43E-07	3.31	9.46	206.9	1.43E-07	2.03	8.66
96.7	1.43E-07	3.29	9.45	208.8	1.43E-07	2.02	8.66
98.6	1.43E-07	3.26	9.43	210.7	1.43E-07	2.00	8.65
100.5	1.43E-07	3.23	9.41	212.7	1.43E-07	1.98	8.64
102.5	1.43E-07	3.21	9.39	214.6	1.43E-07	1.97	8.63
104.4	1.43E-07	3.18	9.38	216.5	1.43E-07	1.96	8.62
106.3	1.43E-07	3.16	9.36	218.5	1.43E-07	1.94	8.61
108.3	1.43E-07	3.13	9.34	220.4	1.43E-07	1.93	8.61
110.2	1.43E-07	3.10	9.32	222.3	1.43E-07	1.91	8.60

Appendix 4U: Continued

Depth	Kc_1	Kc_{-1}	Kc_{-3}
(mm)	(g L^{-1})	(g L^{-1})	(g L^{-1})
224.3	1.43E-07	1.90	8.59
226.2	1.43E-07	1.89	8.58
228.1	1.43E-07	1.87	8.58
230.1	1.43E-07	1.86	8.57
232.0	1.43E-07	1.85	8.56
233.9	1.43E-07	1.84	8.56
235.9	1.43E-07	1.83	8.55
237.8	1.43E-07	1.82	8.55
239.7	1.43E-07	1.81	8.54
241.7	1.43E-07	1.80	8.54
243.6	1.43E-07	1.79	8.53
245.5	1.43E-07	1.78	8.53
247.5	1.43E-07	1.77	8.52
249.4	1.43E-07	1.76	8.52
251.3	1.43E-07	1.75	8.51
253.3	1.43E-07	1.74	8.51
255.2	1.43E-07	1.74	8.50
257.1	1.43E-07	1.73	8.50
259.1	1.43E-07	1.72	8.50
261.0	1.43E-07	1.71	8.49
262.9	1.43E-07	1.71	8.49
264.9	1.43E-07	1.70	8.49
266.8	1.43E-07	1.70	8.48
268.7	1.43E-07	1.69	8.48
270.7	1.43E-07	1.69	8.48
272.6	1.43E-07	1.68	8.48
274.5	1.43E-07	1.68	8.48
276.5	1.43E-07	1.68	8.47
278.4	1.43E-07	1.68	8.47
280.3	1.43E-07	1.67	8.47
282.3	1.43E-07	1.67	8.47
284.2	1.43E-07	1.67	8.47
286.1	1.43E-07	1.67	8.47
288.1	1.43E-07	1.67	8.47
290.0	1.43E-07	1.67	8.47

Appendix 4T: Modeled H^+ concentrations (g L^{-1}) for the Km pH 1.0, -1.0, and -3.0 diffusion cells assuming non-linear absorption.

Depth	Km_1	Km_{-1}	Km_{-3}	Depth	Km_1	Km_{-1}	Km_{-3}
(mm)	(g L^{-1})	(g L^{-1})	(g L^{-1})	(mm)	(g L^{-1})	(g L^{-1})	(g L^{-1})
0.0	9.65E-02	4.69	10.42	94.7	6.92E-08	4.15	9.42
1.9	9.37E-02	4.68	10.40	96.7	6.53E-08	4.14	9.41
3.9	9.08E-02	4.67	10.38	98.6	6.42E-08	4.13	9.39
5.8	8.80E-02	4.66	10.36	100.5	6.39E-08	4.12	9.37
7.7	8.51E-02	4.64	10.34	102.5	6.38E-08	4.11	9.35
9.7	8.23E-02	4.63	10.31	104.4	6.38E-08	4.10	9.33
11.6	7.95E-02	4.62	10.29	106.3	6.38E-08	4.10	9.31
13.5	7.67E-02	4.61	10.27	108.3	6.38E-08	4.09	9.30
15.5	7.39E-02	4.60	10.25	110.2	6.38E-08	4.08	9.28
17.4	7.10E-02	4.59	10.23	112.1	6.38E-08	4.07	9.26
19.3	6.82E-02	4.58	10.21	114.1	6.38E-08	4.06	9.24
21.3	6.55E-02	4.56	10.19	116.0	6.38E-08	4.05	9.23
23.2	6.27E-02	4.55	10.17	117.9	6.38E-08	4.04	9.21
25.1	5.99E-02	4.54	10.15	119.9	6.38E-08	4.03	9.19
27.1	5.72E-02	4.53	10.12	121.8	6.38E-08	4.02	9.18
29.0	5.44E-02	4.52	10.10	123.7	6.38E-08	4.01	9.16
30.9	5.17E-02	4.51	10.08	125.7	6.38E-08	4.00	9.14
32.9	4.90E-02	4.50	10.06	127.6	6.38E-08	3.99	9.13
34.8	4.63E-02	4.49	10.04	129.5	6.38E-08	3.98	9.11
36.7	4.36E-02	4.47	10.02	131.5	6.38E-08	3.98	9.09
38.7	4.10E-02	4.46	10.00	133.4	6.38E-08	3.97	9.08
40.6	3.84E-02	4.45	9.98	135.3	6.38E-08	3.96	9.06
42.5	3.58E-02	4.44	9.96	137.3	6.38E-08	3.95	9.05
44.5	3.33E-02	4.43	9.94	139.2	6.38E-08	3.94	9.03
46.4	3.08E-02	4.42	9.92	141.1	6.38E-08	3.93	9.01
48.3	2.83E-02	4.41	9.90	143.1	6.38E-08	3.92	9.00
50.3	2.59E-02	4.40	9.87	145.0	6.38E-08	3.92	8.98
52.2	2.35E-02	4.39	9.85	146.9	6.38E-08	3.91	8.97
54.1	2.12E-02	4.37	9.83	148.9	6.38E-08	3.90	8.95
56.1	1.89E-02	4.36	9.81	150.8	6.38E-08	3.89	8.94
58.0	1.67E-02	4.35	9.79	152.7	6.38E-08	3.88	8.93
59.9	1.45E-02	4.34	9.77	154.7	6.38E-08	3.88	8.91
61.9	1.24E-02	4.33	9.75	156.6	6.38E-08	3.87	8.90
63.8	1.04E-02	4.32	9.73	158.5	6.38E-08	3.86	8.88
65.7	8.50E-03	4.31	9.71	160.5	6.38E-08	3.85	8.87
67.7	6.70E-03	4.30	9.69	162.4	6.38E-08	3.85	8.86
69.6	5.02E-03	4.29	9.67	164.3	6.38E-08	3.84	8.84
71.5	3.49E-03	4.28	9.65	166.3	6.38E-08	3.83	8.83
73.5	2.15E-03	4.27	9.63	168.2	6.38E-08	3.82	8.82
75.4	1.05E-03	4.26	9.61	170.1	6.38E-08	3.82	8.80
77.3	3.55E-04	4.25	9.60	172.1	6.38E-08	3.81	8.79
79.3	1.05E-04	4.24	9.58	174.0	6.38E-08	3.80	8.78
81.2	3.08E-05	4.23	9.56	175.9	6.38E-08	3.80	8.76
83.1	9.02E-06	4.22	9.54	177.9	6.38E-08	3.79	8.75
85.1	2.67E-06	4.20	9.52	179.8	6.38E-08	3.78	8.74
87.0	8.22E-07	4.19	9.50	181.7	6.38E-08	3.78	8.73
88.9	2.84E-07	4.18	9.48	183.7	6.38E-08	3.77	8.72
90.9	1.28E-07	4.17	9.46	185.6	6.38E-08	3.76	8.70
92.8	8.23E-08	4.16	9.44	187.5	6.38E-08	3.76	8.69

Appendix 4V: Continued

Depth	Km_1	Km_{-1}	Km_3
(mm)	(g L^{-1})	(g L^{-1})	(g L^{-1})
189.5	6.38E-08	3.75	8.68
191.4	6.38E-08	3.75	8.67
193.3	6.38E-08	3.74	8.66
195.3	6.38E-08	3.73	8.65
197.2	6.38E-08	3.73	8.64
199.1	6.38E-08	3.72	8.63
201.1	6.38E-08	3.72	8.62
203.0	6.38E-08	3.71	8.61
204.9	6.38E-08	3.71	8.60
206.9	6.38E-08	3.70	8.59
208.8	6.38E-08	3.70	8.58
210.7	6.38E-08	3.69	8.57
212.7	6.38E-08	3.69	8.56
214.6	6.38E-08	3.68	8.56
216.5	6.38E-08	3.68	8.55
218.5	6.38E-08	3.67	8.54
220.4	6.38E-08	3.67	8.53
222.3	6.38E-08	3.66	8.52
224.3	6.38E-08	3.66	8.52
226.2	6.38E-08	3.66	8.51
228.1	6.38E-08	3.65	8.50
230.1	6.38E-08	3.65	8.49
232.0	6.38E-08	3.64	8.49
233.9	6.38E-08	3.64	8.48
235.9	6.38E-08	3.64	8.47
237.8	6.38E-08	3.63	8.47
239.7	6.38E-08	3.63	8.46
241.7	6.38E-08	3.63	8.46
243.6	6.38E-08	3.62	8.45
245.5	6.38E-08	3.62	8.45
247.5	6.38E-08	3.62	8.44
249.4	6.38E-08	3.62	8.44
251.3	6.38E-08	3.61	8.43
253.3	6.38E-08	3.61	8.43
255.2	6.38E-08	3.61	8.42
257.1	6.38E-08	3.61	8.42
259.1	6.38E-08	3.61	8.42
261.0	6.38E-08	3.60	8.41
262.9	6.38E-08	3.60	8.41
264.9	6.38E-08	3.60	8.41
266.8	6.38E-08	3.60	8.40
268.7	6.38E-08	3.60	8.40
270.7	6.38E-08	3.60	8.40
272.6	6.38E-08	3.59	8.40
274.5	6.38E-08	3.59	8.39
276.5	6.38E-08	3.59	8.39
278.4	6.38E-08	3.59	8.39
280.3	6.38E-08	3.59	8.39
282.3	6.38E-08	3.59	8.39
284.2	6.38E-08	3.59	8.39
286.1	6.38E-08	3.59	8.39
288.1	6.38E-08	3.59	8.39
290.0	6.38E-08	3.59	8.39

APPENDIX 5 Negative pH supplementary data.

Appendix 5A - Standardization titration and calculations for standard H_2SO_4 solutions

Appendix 5B - Standard H_2SO_4 solution molarity to molality conversion calculations

Appendix 5C - Input parameters used in PHRQPITZ to calculate MacInnes scaled pH values of standard H_2SO_4 solutions

Appendix 5D - MacInnes scaled pH values and activities for standard H_2SO_4 solutions calculated using PHRQPITZ

Appendix 5E - Comparison of calculated MacInnes scaled pH values between the current study and Nordstrom et al. (2000)

Appendix 5A: Standardization titration and calculations for standard H_2SO_4 solutions

Solution #	Na_2CO_3	Na_2CO_3	Na_2CO_3	H_2SO_4	H_2SO_4	Average H_2SO_4
	(g)	(mL)	(mol L^{-1})	(mL)	(mol L^{-1})	(mol L^{-1})
6	51.40 51.21	43.28 43.12	2.65 2.65	18.45 18.30	6.22 6.24	6.23
7	20.92 15.82	17.61 13.32	2.66 2.66	27.20 20.37	1.72 1.74	1.73
8	45.86 45.67	38.61 38.45	2.66 2.66	15.93 15.76	6.45 6.49	6.47
9	5.83 6.09	4.91 5.13	2.64 2.64	14.60 15.12	0.89 0.89	0.89
10	25.49 25.22	21.46 21.23	2.64 2.64	13.05 13.01	4.34 4.30	4.32
11	0.79 0.90	0.69 0.79	2.64 2.64	16.37 18.59	0.11 0.11	0.11
12	25.12 19.85	22.00 17.38	2.64 2.64	12.51 9.84	4.64 4.66	4.65
15	12.07 14.11	9.81 11.47	2.64 2.64	10.66 12.44	2.43 2.43	2.43
16	20.14 21.05	16.37 17.11	2.61 2.61	11.17 11.62	3.82 3.84	3.83
17	30.78 29.62	25.02 24.08	2.61 2.61	12.27 11.81	5.31 5.32	5.32
BE1	7.79 7.58	7.79 7.58	1.16E-03 1.16E-03	11.03 11.00	8.20E-04 7.99E-04	8.09E-04
BE2	0.77 0.90	0.65 0.76	2.59 2.59	20.25 23.15	0.08 0.08	0.08
BE5	40.23 34.66	33.87 29.18	2.66 2.66	17.25 14.86	5.22 5.22	5.22
BE7	0.64 0.66	0.54 0.56	2.65 2.65	13.54 14.26	0.11 0.10	0.104
BE9	18.41 19.13	15.50 16.11	2.65 2.65	15.98 16.61	2.57 2.57	2.57
BE10	5.11 6.34	4.30 5.34	2.63 2.63	12.78 15.91	0.89 0.88	0.88
DC2	1.18 1.41	1.05 1.26	1.27 1.27	13.79 16.49	0.10 0.10	0.097
DC3	10.52 11.50	9.40 10.27	1.27 1.27	15.03 16.49	0.79 0.79	0.79
DC4	14.90 15.04	12.11 12.23	2.61 2.61	13.59 13.70	2.32 2.33	2.32
DC5	31.25 30.86	25.41 25.09	2.61 2.61	12.82 12.63	5.16 5.18	5.17

Appendix 5B: Standard H_2SO_4 solution molarity to molality conversion calculations

Solution #	pH	H_2SO_4	Density	Assume 1L of Solution			
				Solution	Solute	Solvent	Molality
		(mol L^{-1})	(g mL^{-1})	(g)	(g)	(g)	(mol kg^{-1})
1	0.36	0.43	1.00	1000	41.8	958	0.44
2	-0.17	1.04	1.03	1034	102	932	1.11
3	-1.30	2.90	1.14	1135	285	850	3.41
4	-2.17	4.13	1.17	1171	405	766	5.39
5	-2.91	5.21	1.24	1236	511	725	7.18
6	-3.79	6.23	1.28	1284	611	673	9.25
7	-0.58	1.73	1.09	1089	170	919	1.88
8	-3.87	6.47	1.32	1319	634	685	9.44
9	-0.05	0.89	1.03	1035	87.3	948	0.94
10	-2.21	4.32	1.21	1209	424	786	5.50
11	0.96	0.11	1.00	1000	10.9	989	0.11
12	-2.46	4.65	1.22	1220	456	764	6.08
14	-0.03	0.86	1.03	1034	83.9	950	0.90
15	-1.09	2.43	1.12	1124	239	886	2.75
16	-1.84	3.83	1.20	1201	376	826	4.64
17	-2.94	5.32	1.26	1256	521	735	7.23
BE1	3.04	0.00	1.00	1000	0.05	1000	5.00E-04
BE2	1.07	0.08	1.00	1000	8.23	992	0.08
BE5	-2.82	2.65	1.14	1136	259	877	3.02
BE7	1.00	0.10	1.00	1000	9.82	990	0.10
BE9	-1.08	2.57	1.13	1130	252	878	2.93
BE10	-0.05	0.88	1.03	1028	86.7	941	0.94
DC2	1.02	0.10	1.00	1003	9.48	993	0.10
DC3	0.03	0.79	1.05	1046	77.7	968	0.82
DC4	-0.93	2.32	1.12	1121	228	893	2.60
DC5	-2.75	5.17	1.27	1271	507	764	6.77

Appendix 5C: Input parameters used in PHRQPITZ to calculate MacInnes scaled pH values of standard H_2SO_4 solutions. Adapted from PHRQPITZ manual (Plummer et al., 1988).

Input Parameter	Input Value	Description
IOPT(1)	1	Print the aqueous model data once during entire computer run
IOPT(2)	1	pH is adjusted in initial solutions to obtain charge balance
IOPT(3)	0	No reactions are modeled. Only the initial solution is solved (speciated)
IOPT(4)	0	The temperature of the reaction solution is (a) the same as the initial solution if adding a reaction, or (b) calculated linearly from the end members if mixing or titrating.
IOPT(5)	0	The pe of the initial solution is held constant
IOPT(6)	0	Activity coefficients are calculated according to the Pitzer model.
IOPT(7)	0	Do not save the aqueous phase composition at the end of a reaction for additional simulations
IOPT(8)	0	The debugging print routine is not called
IOPT(9)	0	No printout of each array to be solved
IOPT(10)	1	The individual-ion activity coefficients are scaled according to the MacInnes convention

Appendix 5D: MacInnes scaled pH values and activities for standard H_2SO_4 solutions calculated using PHRQPITZ

Sample ID	Molarity	Molality	Log Molality	Ionic Stregth	MacInnes Scaling		
					pH	Activity	Gamma
	(mol L^{-1})	(mol kg^{-1})		(mol L^{-1})			
1	0.426	0.44	-0.35	0.85	0.36	0.44	0.81
2	1.039	1.11	0.05	2.08	-0.17	1.46	1.06
3	2.903	3.41	0.53	5.81	-1.30	19.9	4.79
4	4.132	5.39	0.73	8.26	-2.17	147	23.8
5	5.208	7.18	0.86	10.4	-2.91	834	108
6	6.230	9.25	0.97	12.5	-3.79	6148	642
7	1.730	1.88	0.27	3.46	-0.58	3.81	1.62
8	6.467	9.44	0.98	12.9	-3.87	7422	762
9	0.890	0.94	-0.03	1.78	-0.05	1.13	0.98
10	4.319	5.50	0.74	8.64	-2.21	162	26.0
11	0.112	0.11	-0.95	0.22	0.96	0.11	0.77
12	4.647	6.08	0.78	9.29	-2.46	287	42.3
14	0.855	0.90	-0.05	1.71	-0.03	1.07	0.96
15	2.432	2.75	0.44	4.86	-1.09	12.2	3.32
16	3.830	4.64	0.67	7.66	-1.84	69.3	12.8
17	5.315	7.24	0.86	10.6	-2.94	877	112
BE1	0.001	0.00	-3.30	0.00	3.04	0.00	0.96
BE2	0.084	0.08	-1.07	0.17	1.07	0.08	0.77
BE5	5.221	6.94	0.84	10.4	-2.82	662	87.7
BE7	0.100	0.10	-1.00	0.20	1.00	0.10	0.77
BE9	2.571	2.93	0.47	5.14	-1.08	12.0	3.31
BE10	0.884	0.94	-0.03	1.77	-0.05	1.13	0.98
DC2	0.097	0.10	-1.01	0.19	1.02	0.10	0.77
DC3	0.792	0.82	-0.09	1.58	0.03	0.93	0.93
DC4	2.324	2.60	0.42	4.65	-0.93	8.45	2.61
DC5	5.171	6.77	0.83	10.3	-2.75	558	75.5

Appendix 5E: Comparison of calculated MacInnes scaled pH values between the current study and Nordstrom et al. (2000)